

MST13

**Proceedings of
the Thirteenth International Workshop on
Technical and Scientific Aspects of MST radar**

Kühlungsborn, Germany

19 – 23 March 2012

Edited by R. Latteck and W. Singer

MST13

Thirteenth International

Workshop

on Technical and Scientific Aspects of MST radar

Kühlungsborn, Germany

19 – 23 March 2012

Proceedings of

**the Thirteenth International Workshop on
Technical and Scientific Aspects of MST radar**

Edited by R. Latteck and W. Singer

Proceedings of the Thirteenth International Workshop on Technical and Scientific Aspects of
MST radar

Editors: R. Latteck and W. Singer

Published 2013

ISBN 978-3-00-044654-2

Distributed by

Leibniz-Institute of Atmospheric Physics at the Rostock University
18225 Kühlungsborn, Germany



For hard copies contact

Leibniz-Institute of Atmospheric Physics at the Rostock University
18225 Kühlungsborn, Germany
<http://www.iap-kborn.de/>

Hard copies will require reimbursement of shipping costs, packing and preparation of the book.
Prices will be negotiated on an individual basis at the time of request.

This work is subject to copyright. All rights are reserved, whether the whole or part of the
material is concerned, specifically all rights of translation, reprinting, reuse of illustrations,
recreations, reproduction on microfilm or in any other way.

Acknowledgements

The International Steering Committee of MST13 consisted of W. Singer and W.K. Hocking (co-chairs), D. Hooper, P. Chilson, E. Kudeki, I.M. Reid, and T. Tsuda. The ISC would like to thank the following sponsors for their support:

- Deutsche Forschungsgemeinschaft, Bonn, Germany
- Leibniz-Institute of Atmospheric Physics at the Rostock University, Kühlungsborn, Germany
- SCOSTEP (Scientific Committee on Solar-Terrestrial Physics).

Many thanks go to the Local Organizing Committee consisting of M. Rapp (chair), R. Latteck, M. Rosenthal, W. Singer, and G. Stober.

Special thanks go to Peter Schubert setting up the MST13 website, for arranging the online abstract submission and for taking care of online registration. The support of Peter Schubert and Tobias Zinau in organizing and performing the paper presentation at the venue site is greatly appreciated. Also, thanks to Monika Rosenthal for valuable support in all aspects of organizing and handling the requests of travel support. Thanks to Sophie Latteck, Vivien Matthias, and Manja Placke in many aspects of preparing the program booklet and the proceedings of the MST13 workshop. Thanks to the Upstalsboom Hotel Residence for its handling of the workshop and for its handling of the payment of registration fee. Finally, thanks to all who made the workshop to a very successful conference.

W. Singer

On behalf of the ISC



Attendees at MST13 in front of the venue hotel.

Introduction

MST workshops are held every two to three years around the world. The workshops are referred as “International Workshops on Scientific and Technical Aspects of MST Radar”, where “MST” stands for “Mesosphere, Stratosphere and Troposphere”. The start-up workshop (MST-0) was held in August 1978 at the Max-Planck-Institute for Aeronomy in Lindau, Germany, the home of the former SOUSY VHF Radar. The first regular workshop of the workshop series started one year later at the University of Illinois in the USA. The MST workshop series encompasses scientist, engineers, technical experts, theoreticians, and students. These all are united in one forum for radar studies of the troposphere, stratosphere, and mesosphere. The contributions to the workshops as well as the discussions during the workshops were helpful to scientists who use radar results in understanding the capabilities and limitations of the technique, and also to engineers and scientists in designing and constructing their own radar. The 13th workshop of the series, MST13, was held in Kühlungsborn, Germany on March 19 to 23, 2012, at the Upstalsboom Hotel Residence. The workshop was formally opened by Rainer Karl, the mayor of Kühlungsborn, and by Prof. Franz-Josef Lübken, the director of the Leibniz-Institute of Atmospheric Physics at the Rostock University, Kühlungsborn.

Approximately 111 participants attended, thereof 29 students, with 17 countries of origin as shown in Tab. 1. In total, 147 papers were presented (96 oral papers and 51 posters).

The workshop was supported by the German Research Foundation (DFG), the Leibniz-Institute of Atmospheric Physics (IAP) at the Rostock University, and the Scientific Committee on Solar-Terrestrial Physics (SCOSTEP). Basing on these supports of about 21 kEUR we were able to provide travel support, support of students, and reduced registration fees.

The scientific program has been developed by the International Steering Committee (ISC) in close cooperation with the Local Organizing Committee. The ISC consists of W. Singer and W. K. Hocking (co-chairs), P. Chilson, D. Hooper, E. Kudeki, I. M. Reid, and T. Tsuda. The Local Organizing Committee was formed by Markus Rapp, Ralph Latteck, Werner Singer and Gunter Stober.

Country	Participants
Australia	8
China	3
Germany	38
Finland	2
France	1
United Kingdom	7
India	11
Japan	12
Canada	3
Norway	4
Austria	1
Peru	1
Sweden	8
South Korea	1
Taiwan	1
Ukraine	1
USA	9
TOTAL	111

Tab. 1: Participants

Session	Invited paper (22 min.)	Regular paper (15 min.)	Tutorials (40 min.)	Poster
1 – Scattering, microscale processes	3	5		7
2 – New Instruments, signal processing	4	18	1	16
3 – Meteor studies with MST radar	3	3		6
4 – Plasma irregularities	4	4		4
5 - Meteorology, forecasting/nowcasting	5	18		12
6 – Middle Atmosphere Dynamics & Structure	5	22	1	6
TOTAL	24	70	2	51

Tab. 2: Presentation summary

The response to our call for papers was substantial. We received more than 160 contributions from 17 different countries which are finally furnished in 98 oral presentations and 51 posters. The contributions to the workshop were grouped into six sessions, the session chairs are added in brackets: (1) Scattering, calibration and microscale processes (Andreas Muschinski), (2) New instruments, signal processing and quality control (Iain Reid), (3) Meteor studies with MST radar (Phil Chilson), (4) Plasma irregularities (Erhan Kudeki), (5) Meteorology and forecasting/nowcasting (Wayne Hocking), (6) Middle Atmosphere Dynamics and Structure (Markus Rapp and Werner Singer). Here, 24 invited talks encompassing all sessions were arranged by the International Program Committee under guidance of the co-chairs Werner Singer and Wayne Hocking. In addition, two tutorial lectures could be arranged which dealt with “Radar Atmospheric Imaging Techniques” by Phillip Chilson and “Atmospheric processes and variability up to the lower thermosphere – numerical studies with HAMMONIA” given by Hauke Schmidt.

Selected papers of the 13th workshop will be published in the Journal of Atmospheric and Solar-Terrestrial Physics. The workshop proceedings contain the extended abstracts of about 30 % of the presentations only. The table of content presents the complete program of the workshop where the contributions to the proceedings are given in bold.

Table of content

Session 1: Scattering, calibration and microscale processes

VHF/UHF Radio-Wave Backscatter from Corrugated Sheets in the Stably Stratified Atmosphere **(invited)**

by Andreas Muschinski

An Investigation of Clear-air Scatter at Radio and Acoustic Frequencies

by Phillip Chilson, Charlotte Wainwright, Christopher Wilson, Timothy Bonin, Phillip Stepanian, Daniel Russell, Abraham Frei-Pearson, Robert Palmer, Evgeni Fedorovich, Danny Scipion

Quantify Atmospheric Turbulence – A Simple Signal Processing Approach for Turbulent Doppler Spectra

by C. F. Lee, G. Vaughan **2**

Small scale turbulence and instabilities observed simultaneously by radiosondes and the MU radar

by R. Wilson, H.Luce, H. Hashiguchi, F. Dalaudier, S. Fukao, T. Nakajo, Y. Shibagaki, M. Yabuki, J. Furumoto **8**

VHF Radar Scatter Microstructure Measured by Combined Spatial and Frequency Domain Interferometry: A developing approach (invited)

by Jürgen Röttger **13**

Momentum Flux Determination using the Multi-Beam Poker Flat Incoherent Scatter Radar (invited)

by Michael Nicolls, David Fritts, Diego Janches, Craig Heinselman

Performance Improvement in Momentum Flux Computation time using EV based Post Beamsteering Technique derived winds

by VK Anandan, Shridhar Kumar, VN Sureshbabu **27**

Validation of the receiving pattern of the MAARSY phased antenna array

by Toralf Renkwitz, Ralph Latteck, Werner Singer, Gunter Stober **32**

Poster

Observation of horizontal wind velocities in presence of convective system using multi receiver phased array MST radar system

by VK Anandan, VN Sureshbabu, S. Vijayabhaskara Rao **38**

Structure and dynamics of air inhomogeneities in the environment of a cirriform cloud from balloon and high-resolution radar measurements

by Hubert Luce, Shoichiro Fukao, Masayuki K. Yamamoto, Hiroyuki Hashiguchi, Tomoaki Mega, Takuya Tajiri, Masahisa Nakazato

'Sky noise' temperature recorded by the UK MST radar at 46.5 MHz

by Ivan Astin, Bala Goudar, David Hooper

Detecting low earth orbit (LEO) satellites using UK-based atmospheric radars
by Jon D. Eastment, David A. Hooper, Darcy N. Ladd, Chris J. Walden 43

A new field campaign for tropospheric turbulence studies with the MU radar and intensive insitu observations with RS92G Vaisala radiosondes.

by Hubert Luce, Richard Wilson, Francis Dalaudier, Noriyuki Nishi, Shoichiro Fukao, Masanori Yabuki, Hiroyuki Hashiguchi, Jun-ichi Furumoto, Yoshiaki Shibagaki, Tomoyuki Nakajo

Comparison of Calibrated C_n^2 Measurements and Determination of Kinetic Energy Dissipation Rates from a Relatively High-Density VHF Windprofiler Network in Canada
by N. Swarnalingam and W. K. Hocking

Rain kinetic energy measurement with a UHF wind profiler: application to soil erosion survey of a tropical volcanic island
by Bernard Campistron, Anne Réchou 47

Session 2: New instruments, signal processing, and quality control

Radar Atmospheric Imaging Techniques: An Overview **(tutorial)**
Phillip Chilson

EISCAT-3D: Volumetric imaging radar in Northern Scandinavia for studies of the atmospheric and geospace environment **(invited)**
by Esa Turunen et al.

Atmospheric radar reception using LOFAR technology **(invited)**
by Derek McKay-Bukowski

MAARSY - The new MST radar on Andøya: system description and first results **(invited)**
by Ralph Latteck, Werner Singer, Markus Rapp, Toralf Renkowitz, Gunter Stober, Marius Zecha

The program of the Antarctic Syowa MST/IS radar (PANSY) **(invited)**
by Kaoru Sato, Masaki Tsutsumi, Toru Sato, Takuji Nakamura, Akinori Saito, Yoshihiro Tomikawa, Koji Nishimura, Hisao Yamagishi, Takashi Yamanouchi

New Equipment and Data Processing Techniques at the University of Adelaide Field Site
by Iain Reid, Bronwyn Dolman, Joel Younger, Jens Lautenbach, Andrew MacKinnon

HCOPAR: Hainan VHF Coherent Scatter Phased Array Radar - System Description and First Results
by Jingye Yan, Jürgen Röttger, Sheping Shang, Jiankui Shi, Heguang Liu, Chi Wang, Ji Wu 54

The Colorado Software Defined Radar
by Cody Vaudrin, Scott Palo 59

Development of 53 MHz Multi-Mode Radar for Atmospheric Probing
by Parvatala Srinivasulu, Poliseti Yasodha, P. Kamaraj, Meka Durga Rao, S. Narayana Reddy, A. Jayaraman, PP Leena

Small Modular 449 MHz Wind Profiling Radar – First Results <i>by Bronwyn Dolman, Iain Reid, Robert Vincent, Andrew MacKinnon, Richard Mayo, Gary Jonas, Jonathan Woithe</i>	
Introduction to the Kunming atmospheric radar facility (KARF) and the initial results <i>by Jinsong Chen, Zhenwei Zhao, Na Li, Jian Wu, Jiyao Xu</i>	65
The transceiver-based approach to phased array radars – applications and advantages <i>by Brenton Vandeppeer, Pramod Aryal, Adrian Murphy, Daniel O'Connor, Brian Fuller</i>	
Boundary layer measurements by the MARA MST radar using a local bistatic technique. <i>by Sheila Kirkwood, Ingemar Wolf, Daria Mikhaylova</i>	
De-noising of atmospheric radar signals using Spectral based sub-space method <i>by VN Sureshbabu, VK Anandan, Toshitaka Tsuda, Jun-ichi Furumoto</i>	70
Quasi-coherent bistatic radar - implementation and observations <i>by Brenton Vandeppeer, Adrian Murphy, Daniel O'Connor, Brian Fuller</i>	
RASS optimisation for mid-latitude summers <i>by Andrew MacKinnon, Bronwyn Dolman, Lenard Pederick, Iain Reid</i>	
An FPGA-Based Wind Profiler Controller and Signal Processor <i>by Charles Martin, Eric Loew, Chris Burghart, William Brown, Brad Lindseth</i>	74
Adaptive beamforming technique for accurate vertical wind measurements with multi-channel MST radar <i>by Koji Nishimura, Takuji Nakamura, Toru Sato, Kaoru Sato</i>	
3D-measurement results by MAARSY using radar interferometry methods <i>by Marius Zecha, Ralph Latteck, Markus Rapp, Werner Singer, Gunter Stober, Toralf Renkwitz</i>	
Adaptive suppression of aircraft clutter with the PANSY radar training system <i>by Taishi Hashimoto, Koji Nishimura, Kaoru Sato, Toru Sato</i>	79
Development of digital radar receiver using software-defined radio technique <i>by Masayuki K. Yamamoto, Hiroyuki Hashiguchi, Noor Hafizah Binti Abdul Aziz, Youhei Wakisaka, Mamoru Yamamoto</i>	
New Developments and Innovations in VHF Radar <i>by Richard Mayo, Bronwyn Dolman, Gary Jonas, Iain Reid, Jonathan Woithe</i>	
Renovation of the Aberystwyth MST radar: Evaluation <i>by David A. Hooper, John Bradford, Les Dean, Jon D. Eastment, Marco Hess, Eric Hibbett, John Jacobs, Richard Mayo</i>	86

Poster

- Extraction of horizontal wind velocities from a multi receiver phased array radar system using post beam steering technique and efficiency of various beamforming methods**
by VK Anandan, VN Sureshbabu, Toshitaka Tsuda, Jun-ichi Furumoto 91
- A Mini VHF BLR and the known FCA Wind Magnitude Underestimation
by Bronwyn Dolman, Iain Reid, Andrew MacKinnon
- Separating sky and ground wave in indirect phase height measurements
by Dieter Keuer, Jörg Trautner
- Good Resolution at High Effective Power without Traditional Pulse-Coding**
by W.K. Hocking, A. Hocking, D.G. Hocking, M. Garbanzo-Salas 96
- The NCAR 449 MHz Modular Wind Profiler – Prototype and future plans**
by Stephen A. Cohn, William O.J. Brown, Bradley J. Lindseth, Charlie Martin 101
- Renovation of the Aberystwyth MST radar: Technical issues
by Richard Mayo, John Bradford, Les Dean, Jon Eastment, Marco Hess, Eric Hibbett, David Hooper, John Jacobs
- Implementation, Calibration, and Testing of Range Imaging on the Lindenberg 482-MHz Radar Wind Profiler
by Phillip Chilson, Volker Lehmann
- An inter-comparison of wind velocities in different observation approaches and signal processing techniques using multi receiver phased array MU radar system**
by Shridhar Kumar, VN Sureshbabu, VK Anandan, Toshitaka Tsuda, Jun-ichi Furumoto . . . 105
- Improved performance in Horizontal wind estimation from a multi receiver phased array atmospheric radar system using Spaced Antenna Drift Technique and signal processing approaches**
by Shridhar Kumar, VK Anandan, Toshitaka Tsuda, Jun-ichi Furumoto 110
- Performance analysis of optimum tilt angle with necessary beam configuration to minimize error in measurement of horizontal wind velocities derived by Post Beam Steering technique**
by VN Sureshbabu, VK Anandan, Toshitaka Tsuda, Jun-ichi Furumoto 115
- Conjuring a Gaussian: A new signal processing approach for turbulent Doppler spectra.
by Christopher Lee
- Development of turbulence detection and prediction techniques with wind profiler radar for aviation safety
by Hiroyuki Hashiguchi, Kuniaki Higashi, Seiji Kawamura, Ahoro Adachi, Yusuke Kajiwara, Kotaro Bessho, Masanobu Kurosu, Mamoru Yamamoto
- Development and Validation of L-band Active Array Lower Atmospheric Radar Wind Profilers at NARL
by Parvatala Srinivasulu, Poliseti Yasodha, P. Kamaraj, T. Narayana Rao, S. Narayana Reddy, A. Jayaraman, PP Leena

A Model Study on the Measurement Error of Wind Profiling Radar Observations in the Atmospheric Boundary Layer

by Makoto Matsuda, Toshitaka Tsuda, Kuniaki Higashi, Jun-ichi Furumoto

Advanced Capabilities and applications of the new Digisonde DPS-4D at Juliusruh

by Jens Mielich

Session 3 – Meteor studies with MST radar

Chemistry of meteor trail formation **(invited)**

by John Plane, Wuhu Feng, Diego Janches

60 years of meteor radar at Adelaide **(invited)**

by Iain Reid

The MU radar meteor head echo analysis technique and the 2009-2010 observation programme **(invited)**

by Johan Kero, Csilla Szasz, Takuji Nakamura, David Meisel, Toshio Terasawa, Yasunori Fujiwara, Masayoshi Ueda, Koji Nishimura, Jun-Ichi Watanabe

Atmospheric Density and the Height Distribution of Meteor Radar Detections

by Joel Younger, Iain Reid, Robert Vincent, Damian Murphy

The Effect of Aerosol Absorption on Meteor Decay Times at Different Wavelengths

by Joel Younger, Iain Reid, Robert Vincent, Damian Murphy

Radar observations of the Perseid meteor shower activity and meteoroid stream structure from the Gadanki MST radar

by Yellaiah Ganji, K. Chenna Reddy

Poster

The errors of meteor radar data

by Svitlana V. Kolomiyets

The Diffusion of Multiple Ionic Species in Meteor Trails

by Joel Younger, Iain Reid, Robert Vincent

Accuracy of Meteor Shower Velocity Estimates Obtained from the Fresnel Transform Method

by Joel Younger, Iain Reid, Robert Vincent, Damian Murphy

The Role of Sputtering in the Formation of Meteor Trails

by Joel Younger, Iain Reid, Robert Vincent

Interferometric measurements of meteor-head echoes with MAARSY

by Carsten Schult, Gunter Stober, Ralph Latteck, Werner Singer, Markus Rapp

Estimation of absolute meteor fluxes from specular meteor observations

by Carsten Baumann, Gunter Stober, Ralph Latteck, Werner Singer

Session 4: Plasma irregularities

Radar investigations of mesospheric clouds subjected to artificial electron heating—observations and theory **(invited)**

by Ove Havnes, Cesar La Hoz, Alexander Biebricher, Meseret Kassa, Jörg Gumbel

Active modification of the D-region ionosphere **(invited)**

by Antti Kero

ESRAD Radar observations of PMSE during the PHOCUS rocket campaign at ESRANGE on 21 July 2011 07 UTC: preliminary results of coherent radar imaging.

by Joel Arnault, Sheila Kirkwood

In-situ measurements of small-scale structures in neutrals and plasma species during ECOMA-2010

by Boris Strelnikov, Artur Szewczyk, Markus Rapp

Overview of VHF radar observations of equatorial mesosphere and ionosphere **(invited)**

by Erhan Kudeki, Gerald Lehmacher, Pablo Reyes, Marco Milla, Jorge Chau, Karim Kuyeng, Levent Gezer

Aperture synthesis radar imaging in coherent scatter radars: Results and lessons from Jicamarca **(invited)**

by Jorge Chau, D.L. Hysell, M. Urco

PMSE – a comparison between ESRAD in Arctic Sweden and MARA at Wasa, Antarctica.

by Sheila Kirkwood, Evgenia Belova, Peter Dalin, Maria Mihalikova, Daria Mikhaylova, Hans Nilsson, K. Satheesan, Ingemar Wolf

Spectral characteristics of incoherent scatter radar observations from the D-region

by Irina Strelnikova, Markus Rapp

Poster

Apparent electron density modulation under RF heating at EISCAT UHF and its application for estimating the electron-ion temperatures ratio

by Henry Pinedo, Cesar La Hoz, Ove Havnes, Mike Rietveld

Occurrence of mid-latitude field-aligned irregularities observed with VHF coherent scatter ionospheric radar in South Korea

by Tae-Yong Yang, Young-Sil Kwak, Jae-Jin Lee, Young-Deuk Park

A Low Power Software Defined Incoherent Scatter Radar System Design Concept for Continuous Sounding the Earth's Ionosphere

by Ming Yao

Predicting the occurrence of visual Noctilucent Clouds

by John Rowlands, Kerry A. Day, David A. Hooper, Nicholas J. Mitchell 120

Session 5: Meteorology and forecasting/nowcasting

Observation of turbulence and clouds in the tropics by the Equatorial Atmosphere Radar
(invited)

by Masayuki K. Yamamoto, Hiroyuki Hashiguchi, Mamoru Yamamoto, Shoichiro Fukao

Comparison of wind profiler radar measurements with Doppler Wind Lidar profiles
measurements at the Lindenberg GRUAN site

*by Ronny Leinweber, Stefan Emeis, Bernd Stiller, Simone Lolli, Matthias Mauder, Ludovic
Thobois, Volker Lehmann*

Climatological characteristics of tropospheric- and lower stratospheric- turbulence over
Kiruna, Sweden

by T. Narayana Rao, Sheila Kirkwood

**Vertical flow in atmospheric boundary layer observed by a lower troposphere radar
under clear air condition**

***by Tomoyuki Nakajo, Kenji Sasaki, Yuki Ogura, Yoichiro Saito, Hiroyuki Hashiguchi,
Manabu D. Yamanaka, Shoichiro Fukao* 126**

Response of tropical lower atmosphere to annular solar eclipse of 15 January, 2010

*by Gopa Dutta, P. Vinay Kumar, M. Venkat Ratnam, Salauddin Mohammad, M. C. Ajay
Kumar, P. V. Rao, H. Aleem Basha*

Further investigation on stratospheric air intrusion in to the troposphere during the
episode of tropical cyclone: Numerical simulation and MST radar observations

by Siddarth Shankar Das, S Sijikumar, Kizhathur Narasimhan Uma

Meso highs and Meso lows observed over the Indian region during Deep convective
conditions

by Nelli Narendra Reddy, Kusuma G. Rao

Impact of Meso-Network Observations on prediction of Extreme Rain Events of the Indian
Summer Monsoon during PRWONAM

by Kusuma G. Rao, Rani Jacob, Nelli Narendra Reddy

Ground-Based Wind Profiler Radar and Lidar Measurements of Marine Boundary Layer
evolution over PALAU in Pacific Ocean

by U.V.Murali Krishna, K.Krishna Reddy, R Shirooka

**Measurement of vertical air velocity and hydrometeor in stratiform precipitation by the
Equatorial Atmosphere Radar and polarization lidar**

***by Masayuki K. Yamamoto, Tomoaki Mega, Yasukuni Shibata, Makoto Abo, Hiroyuki
Hashiguchi, Toyoshi Shimomai, Yoshiaki Shibagaki, Mamoru Yamamoto, Manabu D.
Yamanaka, Shoichiro Fukao, Timbul Manik* 131**

Study of radar bright band and freezing level height

by Rajasri Sen Jaiswal, R. Fredrick Sonia, V. S. Neela, M. Rasheed, Zaveri Leena, V. Sowmya

Single- Compared to Dual-Frequency DSD Retrievals During TWP-ICE

by Bronwyn Dolman, Christopher Williams

Case-study of tropopause fold observation by MARA MST radar at Wasa, Antarctica – comparison with ECMWF and WRF model data.

by Maria Mihalikova, Sheila Kirkwood, Joel Arnault, Daria Mikhaylova

Higher application of wind profilers to forecasting/nowcasting severe convections and to aviation weather services **(invited)**

by Masahito Ishihara

Incorporation of O-QNet windprofiler data into numerical forecast models

***by W.K. Hocking, P. Taylor and A. Hocking* 136**

A VHF profiler network study: Upper level divergence and the SW Ontario tornadoes of Aug 2011.

by Matthew Corkum, Peter Taylor, ZhengQi Wang, Shama Sharma

Objectives and tasks of the EUMETNET Composite Observing System (EUCOS) **(invited)**

by Stefan Klink, Sabine Hafner, Tanja Kleinert, et al.

The challenge of providing continuous high-quality measurements with an operational radar wind profiler network

by Ronny Leinweber, Volker Lehmann

The usefulness of model-comparison statistics for wind-profiling radar operators (invited)

***by David A. Hooper, David M. Edwards, Gemma Holmes, Kevin Linklater, Tim Oakley, Colin Parrett, and Myles Turp* 141**

Australian Government Bureau of Meteorology Next Generation Wind Profiler Network

by Daniel McIntosh

Monitoring and data assimilation of Wind Profiler (invited)

***by Catherine Gaffard, David Simonin, Colin Parrett, Richard Marriott, Myles Turp, Dirk Klugmann* 151**

Water vapor analyses in mixed-phase clouds

by Edwin Campos

Diurnal wind variations in the lower-tropospheric wind over Japan as revealed with wind profilers and analysis/reanalysis data sets

by Takatoshi Sakazaki, Masatomo Fujiwara

Diurnal wind variations in the upper-tropospheric and lower stratospheric wind over Japan as revealed with MU radar and five reanalysis data sets

by Takatoshi Sakazaki, Masatomo Fujiwara, Hiroyuki Hashiguchi

Poster

Measurements of wind variation in surface boundary layer with tilted 1.3GHz wind profiler
by Kuniaki Higashi, Jun-ichi Furumoto, Hiroyuki Hashiguchi

Observations of atmospheric thermal structures during 2009 and 2010 solar eclipses
by S.B.Surendra Prasad, M.Venkatarami Reddy, A.Hari Krishna, K.Krishna Reddy, C.J Pan, U.V. Murali Krishna

Investigations on Tropospheric ducts by using wind profiler radar and Artificial Neural Network over PALAU in the Pacific Ocean
by Punyaseshudu Dupadu, Madhusudhana Kallu, K.Krishna Reddy, U.V. Murali Krishna

Accurate track prediction of cyclones over bay of Bengal using WRF model
by M.Venkatarami Reddy, S. Balaji Kumar, S.B. Surendra Prasad, K.Krishna Reddy, U.V. Murali Krishna

Observations and modeling studies on severe thunderstorms over north east region of India
by S.Balaji Kumar, U.V.Murali Krishna, M.Venkatarami Reddy, K.Krishna Reddy

The Tropospheric cooling and the Stratospheric warming at Tirunelveli during the Annular Solar Eclipse 15 January, 2010
by Kusuma G. Rao, Nelli Narendra Reddy, Raj Kumar Choudhary

A study of Indian Summer Monsoon clouds during drought and normal monsoon years using data Cloud Profiling Radar on CloudSat
***by M Muhsin and Kusuma G Rao* 160**

Impact of Total Solar Eclipse on troposphere and stratosphere thermal and wind structure at Dibrugarh on 22 July, 2009
by Kusuma G. Rao, Nelli Narendra Reddy

Shrinking of Tropical Tropopause Layer during Organized Deep Convection of Indian Summer Monsoon over the Bay of Bengal with JASMINE Measurements
***by Kusuma G Rao, Nelli-Narendra Reddy and Paquita Zuidema* 164**

Air quality measurements with Lidar, SODAR and tethered balloon profiling in the surface boundary layer over Shigaraki, Japan
by Masanori Yabuki, Kenshi Takahashi, Taichi Hayashi, Chikara Miyawaki, Makoto Matsuda, Toshitaka Tsuda

Session 6: Middle Atmosphere Dynamics and Structure

Satellite observations of gravity wave momentum flux and interpretation by global ray-tracing modeling **(invited)**

by Peter Preusse, Manfred Ern, Silvio Kalisch

Re-examination of observed gravity wave characteristics by using a high-resolution GCM **(invited)**

by Kaoru Sato

Characteristics of high frequency gravity waves observed using simultaneous high resolution radiosonde and MST radar observations

by PP Leena, M. Venkat Ratnam, B.V. Krishna Murthy

Frequency dependence of gravity wave momentum flux estimates in the lower atmosphere: First observations using MST radar wind data at Gadanki

by P Vinay Kumar, M.C. Ajay Kumar, P. V. Rao, Salauddin Mohammad, Gopa Dutta

The Wave-Driven Circulation and Variability of the Wintertime Arctic Middle Atmosphere

by Richard L. Collins, Amal Chandran, V. Lynn Harvey, Michael Gerding, Gerd Baumgarten, Franz-Josef Lübken, Kohei Mizutani, Anja Strømme, Rolando R. Garcia, Daniel R. Marsh, Brentha Thurairajah **170**

Seasonal characteristics of Kelvin-waves in the mesosphere and lower thermosphere (MLT) region over an equatorial station Thumba using SKiYMET meteor wind radar

by Siddarth Shankar Das, S Suheela, Anu Krishna

Winds, tides and waves in the mesosphere and lower thermosphere over Bear Lake Observatory (42N 111W)

by Kerry Day, Michael Taylor, Victoria Howells, Nicholas Mitchell

Annual and interannual variations of mesospheric gravity waves from radar, satellites and models

by Peter Hoffmann, Manfred Ern, Erich Becker, Peter Preusse, Markus Rapp

Simultaneous observations of small-scale structures in Mesosphere Lower Thermosphere winds and temperature using Meteor radar and OH day-glow photometer over Thumba (8.50 N, 770 E)

by Kishore Karanam Kumar, K.V. Subrahmanyam, C. Vineeth, T.K. Pant

High-latitude Observations of Atmospheric Gravity Waves in the Mesopause Region

by Dominique Pautet, M.J. Taylor, Y. Zhao, W.R. Pendleton Jr, Peter Hoffmann, Werner Singer

Comparison of mesospheric gravity wave momentum fluxes derived by MF Doppler radar and meteor radar measurements at 69°N

by Manja Placke, Peter Hoffmann, Markus Rapp, Werner Singer, and Ralph Latteck **175**

Main Characteristics of Polar Mesosphere Summer Echoes Observed with the MST Radar ESRAD, Kiruna, Sweden During 1997- 2011

by Evgenia Belova, Maria Smirnova, Sheila Kirkwood **180**

First three - dimensional observations of polar mesosphere winter echoes: Resolving space - time ambiguity
by Markus Rapp, Ralph Latteck, Gunter Stober, Peter Hoffmann, Werner Singer, Marius Zecha

Atmospheric processes and variability up to the lower thermosphere – Numerical studies with HAMMONIA **(tutorial)**
by Hauke Schmidt

Long-term variability and trends of mean winds in the mesosphere and lower thermosphere within $\pm 22^\circ$
by Venkateswara Rao Narukull, Toshitaka Tsuda, D. M. Riggan, S Gurubaran

Eureka meteor radar temperatures compared with AuraMLS
by Chris Meek, Alan Manson, and Wayne Hocking 185

Recent advances in radar turbulence studies with emphasis on in-situ comparisons **(invited)**
by Wayne Hocking, Arnim Dehghan

Solar diurnal tides in the middle atmosphere: Interactions with the zonal-mean flow, planetary waves and gravity waves **(invited)**
by Ulrich Achatz, Fabian Senf, Norbert Grieger, Thomas Kessemeier

Climatology of the 8-hour solar tide over Central Europe, Collm (51.3°N; 13.0°E)
by Christoph Jacobi, Tilo Fytterer 189

Characteristics of the “Hiccup” in the fall transition
by Vivien Matthias, Theodore G. Shepherd, Peter Hoffmann, Markus Rapp 194

Long-term variability of 16 day planetary wave in the equatorial mesosphere and lower thermosphere in relation with QBO and SSW events
by Sathishkumar Sundararaman, Sridharan Sundarajan, Gurubaran Subaramanian, et al.

Studying mesospheric dynamics from PMSE backscatter using velocity azimuth displays (VAD)
by Gunter Stober, Markus Rapp, Ralph Latteck, Werner Singer, Marius Zecha

Planetary wave activity during the summer months of 2007 over Gadanki
by M.C. Ajay Kumar, Gopa Dutta, et al.

Mesospheric vertical velocity and tilts
by Chris Meek, Alan Manson 198

Radar and lidar observations in the summer mesosphere at Davis, Antarctica **(invited)**
by Franz-Josef Lübken, Josef Höffner, Bernd Kaifler, Timo Viehl, Ray Morris

Semi-diurnal tidal coupling at low-latitudes during sudden stratospheric warming events
by S Sridharan, S Sathishkumar, S Gurubaran

Diurnal and Seasonal Variability of D-Region Electron Densities at 69°N
by Werner Singer, Martin Friedrich

Coordinated observations of mesospheric gravity waves with airglow imager, lidar, and radar

by Shin Suzuki, Takuji Nakamura, Matsumu K. Ejiri, Masaki Tsutsumi, Kazuo Shoikawa, Takuya D. Kawahara

PMSE observations with the EISCAT VHF and UHF-radars: Ice particles and their effect on ambient electron densities

by Qiang Li, Markus Rapp

Investigations on the variability of the tropical mesospheric echoes, winds, waves and associated momentum fluxes

by Sunkara Eswaraiah, M. Venkat Ratnam, B.V. Krishna Murthy, S. Vijaya Bhskara Rao

Poster

Dynamical influence of a gravity wave generated by the Vestfjella Mountains in Antarctica: radar observations, fine-scale modeling and kinetic energy budget analysis

by Joel Arnault, Sheila Kirkwood

Resonance lidar measurements of atomic energy states in the auroral E-Region

by Richard Collins, Xinzhao Chu, Zhibin Yu, Chester Gardner, Michael Nicolls

The climatology, propagation and excitation of ultra-fast Kelvin waves

by Robin Davis, Saburo Miyahara, Ying-Wen Chen, Nicholas Mitchell

Long-Term Trends of Upper Mesosphere Gravity Waves at Midlatitudes

***by Christoph Jacobi, Peter Hoffmann* 201**

Sodankylä-Leicester Ionospheric Coupling Experiment - Selected First Results

by Thomas Ulich, Juha Vierinen, Neil Arnold, Chris Thomas, Mark Lester

Session 1

Quantify Atmospheric Turbulence – A Simple Signal Processing Approach for Turbulent Doppler Spectra

C. F. Lee^{*,1}, G Vaughan

Centre for Atmospheric Science, University of Manchester, Manchester, UK.

¹ Now at Department of Meteorology, University of Reading, Berkshire, UK

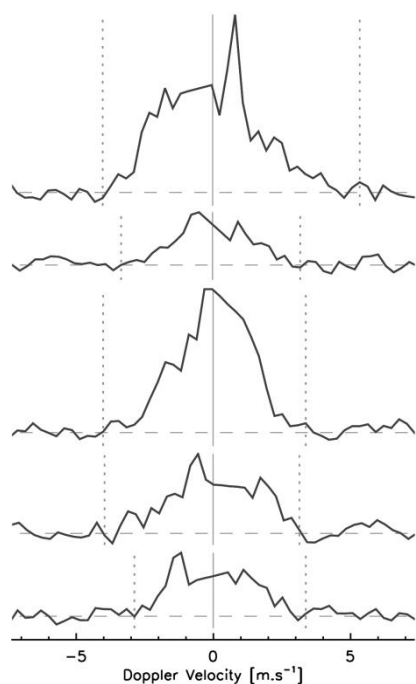
J. D. Price

Met Office Research Unit, Cardington, Bedfordshire, UK.

Abstract

Quantifying turbulence above the boundary layer, with a wind profiling radar, is often difficult because Doppler spectra do not have the expected Gaussian form. This study presents a new approach that combines consecutive Doppler spectra, improving the resolution of turbulence where measurements are otherwise sparse, for MST and boundary layer radar observations.

1. Introduction



The spectral width method is commonly used to quantify turbulence from measurements by wind profiling radars. In some regions of the atmosphere the method becomes unreliable, because a key assumption – that turbulence fills the pulse volume – is not met. Such conditions are typically found above the convective boundary layer, and in particular in the stratosphere (Pepler et al., 1998). To overcome the problem of sparse measurements, this study introduces a method that effectively increases the observation time of the radar (thereby quantifying more of the turbulent ensemble), by combining consecutive Doppler spectra.

The spectral width method relies on a broadening of the Doppler spectrum as the strength of turbulence increases. Where the ensemble of turbulent motions is adequately sampled, the Doppler spectrum is expected to be Gaussian in shape, with its spectral width proportional to turbulent kinetic energy.

Figure 1: Five FGAM Radar Doppler spectra from free troposphere combine to give a 'more Gaussian' composite (bottom); the light grey line is a Gaussian fit to the composite; signal limits are shown by the dotted lines. (Spectra taken from an off-vertical beam; range: 3256m; radial resolution: 187.5 m, recorded between 16:44:09 and 16:59:37UT on 01/04/08.)

* Corresponding Author: Department of Meteorology, University of Reading, Earley Gate, PO Box 243, Reading, RG6 6BB, UK

Even where echo signals are weak, wind velocities can usually be quantified from the Doppler spectrum (indeed most wind profiler algorithms have been tailored to optimise mean velocity retrieval); but spectral width calculations are more susceptible to non-Gaussian ‘perturbations’ – a particular problem given the highly specular nature of a typical free troposphere Doppler spectrum (for example, Figure 1).

Previous studies have sought to overcome this problem using a Gaussian fit to the Doppler spectrum (e.g. Murphy et al., 1994). Unfortunately, the clear-air signal may not be the only peak in the spectrum (for example, ground clutter signals – a particular problem for boundary layer profilers, and Rayleigh scatter from precipitation, may also be present); and simply fitting a Gaussian to the whole spectrum may not identify the correct peak.

Combining consecutive spectra was proposed by Hocking (1986), who joined in-phase (I) and quadrature (Q) radar signals, prior to Fourier transforming them into a single Doppler spectrum. Using a continuous I and Q time series for combination has two disadvantages: Firstly, the clear-air signal is shifted on the Doppler axis from dwell to dwell, because of changes in the background wind speed; creating a single Doppler spectrum from a long time series will include those (non-turbulent) variations in the spectral width (temporal broadening); secondly, I and Q measurements are not routinely recorded for most radars, and implementation of I and Q combination would require extensive changes to some acquisition systems.

To overcome the problems associated with I and Q combination and Gaussian fitting, this study proposes a more practical and reliable approach that: (a) couples Gaussian fitting with existing signal identification algorithms; (b) uses combination of Doppler spectra rather than I and Q time series. In doing so, this study answers the following questions:

- 1) Can we qualitatively identify a ‘Gaussian’ Doppler spectrum?
- 2) Does spectral combination improve our ability to resolve turbulence?

2. Methods

Instruments: The Natural Environment Research Council (NERC) MST radar is a VHF instrument (46.5 MHz), located at Capel Dewi, close to the coastal town of Aberystwyth, in West Wales. The Facility for Ground Based Atmospheric Measurements (FGAM) mobile Boundary Layer Wind Profiler is a UHF radar (1290 Mhz), manufactured by Degreane, and was located at Capel Dewi for this study. The NERC MST radar uses Doppler Beam Swinging with a vertical and four off-vertical beams (6° zenith) for this experiment. The boundary layer profiler has three fixed beams (one vertical, two off-vertical at 17.3° zeniths). A summary of each radar is given in Table 1.

	Beamwidth ¹	Pulse Shape	Pulse Length ²	Vertical Res.	Doppler Res.	Range
NERC MST	0.9°	Square	300m/600m	150m/300m	0.16 m.s ⁻¹	1.7 – 20 km
FGAM	2.55°	Gaussian	300m/750m	75m/750m	0.08 -0.31m.s ⁻¹	100m-4000m

¹Two-way one-sigma width

²Full-width at Half-Maximum

Table 1: Summary of NERC MST radar and FGAM Boundary Layer Wind Profiler.

Traditional Signal Processing: The results presented here use the current NERC MST radar algorithm (Hooper et al., 2008) to identify the clear-air signal for both radars, though the method can be used with any algorithm that returns the first moment of the clear-air signal and signal limits. NERC MST signal limits are identified using the following three criteria, with the noise level identified using the Hildebrand & Sekhon (1974) method:

1. The spectrum reaches the noise level.
2. The spectrum drops to 0.01 of the peak signal power.
3. A local spectral minimum is reached. (Defined as a point below 0.1 of the peak signal power, with larger signals to either side.)

Some smoothing of the Doppler spectrum is often needed to obtain reliable signal limits (a running mean with a rectangular window is used). Consensus algorithms are used by both the MST and FGAM radars, to reduce the identification of non-clear-air signals.

Spectral Combination: Spectral combination is performed by incoherently averaging consecutive Doppler spectra, to generate a single composite spectrum (Figure 1 - note that individual spectra are always from the same range gate). Spectra are aligned by their first moments, prior to averaging, to avoid temporal broadening.

Quantifying Spectral Width: To make the link between TKE and spectral width, it is assumed that the clear-air spectrum is a Gaussian, such that Equation 1 gives it's variance (σ^2 , where v is Doppler velocity, and S is signal power). Erroneous TKE measurements are obtained if the clear-air signal deviates from a Gaussian. Deviations are a particular problem at a signal's edges, because of the weighting of the second moment (the numerator in Equation 1) by the square of the distance from the mean. 'Low power tails' (elevated signal powers at the edge of the clear-air component) are common in Doppler spectra, but fitting a Gaussian to the clear air signal, and using it's width, rather than the second moment, reduces the their influence. (A least-squares Gaussian fit is used in this study.)

$$\sigma^2 = \frac{\int v'^2 \cdot S(v) dv}{\int S(v) dv} \quad \text{where } v' = v - \bar{v} \quad (1)$$

Identifying a 'Gaussian' Spectrum: A Gaussian with a 'poor' fit to the clear-air signal should not be used to quantify spectral width; to assess what constitutes a 'good' Gaussian fit, FGAM data have been examined by hand, with the 'Good' and 'Bad' Gaussians appropriately flagged. The hand-examined data set comprises 2600 spectra, recorded over three hours in the convective boundary layer (boundary layer spectra are expected to be 'close to Gaussian' in shape). Typically χ^2 statistics have been used to judge the 'quality' of a Gaussian fit (e.g. Murphy et al., 1994), but that approach more heavily weights low powers (i.e. the spectrum edges – note the denominator in Equation 2 – the sum is over all points in the spectrum, where G is the Gaussian fit, and S is the Doppler spectrum). In contrast, the root-mean-square (RMS) evenly weights the whole of the spectrum (Equation 3, where N is the number of points in the spectrum). Both statistics are calculated for each hand-examined spectrum, and are compared below. (The Gaussian fit and Doppler spectrum are normalised by their average total power, before χ^2 and RMS are calculated.)

$$\chi^2 = \sum \frac{(G - S)^2}{S} \quad (2) \qquad \text{RMS} = \sqrt{\sum \frac{(G - S)^2}{N}} \quad (3)$$

The Effects of Spectral Smoothing: The smoothing needed to identify atmospheric signal limits will broaden the Doppler spectrum. Since smoothing is simply a convolution between a rectangular window (width σ_{window}) and the un-smoothed Doppler spectrum (width $\sigma_{spec.}$), the associated broadening can be corrected using Equation 4 (where σ_{smooth} is the smoothed spectrum width).

$$\sigma_{spec.}^2 = \sigma_{smooth}^2 - \sigma_{window}^2 \quad (4)$$

3. Results and Discussion

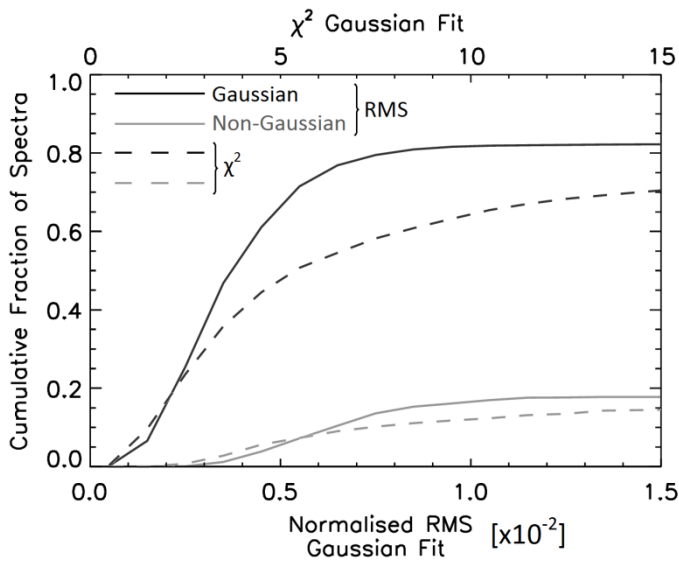


Figure 2: Comparison of RMS and χ^2 statistics for Gaussian fits to FGAM profiler Doppler spectra. Hand-picking identify spectra accurately represented by their Gaussian fits (labelled ‘Gaussian’). (Taken from 2600 FGAM profiler spectra from in the convective boundary layer on 01/04/08, between 13:00 and 14:30UTC, 1500m to 3000m in altitude, and from all three beams.)

Identifying Gaussian Spectra: Hand-examined spectra show no definite threshold in either RMS or χ^2 (Figure 2) separating ‘Gaussian’ and ‘non-Gaussian’ spectra. The ‘human’ element involved in the flagging inevitably introduces some noise, so the absence of a threshold is not surprising. Nevertheless, the overlap between ‘Gaussian’ and ‘non-Gaussian’ spectra shows that an RMS threshold will capture a higher proportion of Gaussian spectra than a χ^2 threshold.

In the absence of a clear threshold, the middle of the ‘transition region’ has been

adopted, such that an RMS of 0.65×10^{-2} indicates a ‘Gaussian’ spectrum. Any spectra falling above that threshold are taken to be non-Gaussian.

Effects of Spectral Combination: Spectral combination gives differing degrees of improvement (measured as an increase in the number of Gaussian spectra) depending on atmospheric conditions. Above the convective boundary layer, the number of

Gaussian spectra generally increases with wind speed (Figure 3). Stronger winds (larger beam broadening – see Abstract We-03 for more details), spread the Doppler spectrum over a greater range of velocity bins, reducing the influence of any non-Gaussian points in the spectrum.

Where wind speeds are low there is little beam broadening to generate Gaussian spectra; combined with the sparse nature of free tropospheric turbulence, most spectra are too narrow to give a reliable Gaussian fit. Very few Gaussian spectra are identified in low winds (Figure

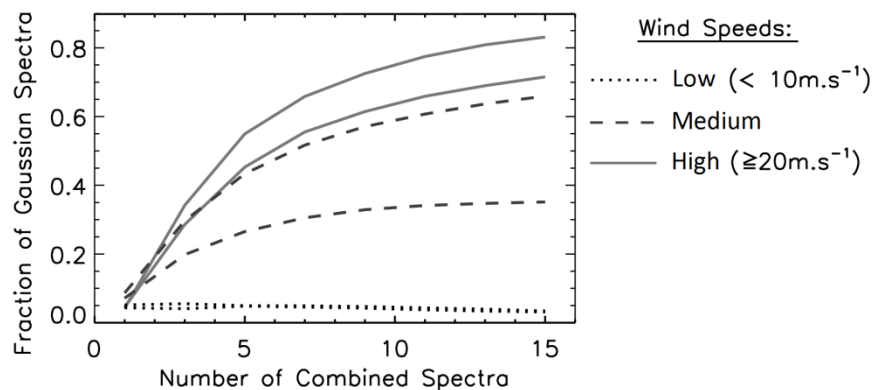


Figure 3: Fraction of Gaussian spectra ($\text{RMS} < 0.6 \times 10^{-2}$) for High ($>20\text{m.s}^{-1}$), Medium, and Low ($<10\text{m.s}^{-1}$) mean wind speeds in the free troposphere for different combination periods. (MST spectra between 10:00 and 16:00 UTC, 2000 m and 6000 m, and with five-bin smoothing.)

3). In contrast, broadening by convective boundary layer turbulence may dominate contributions from beam broadening:

Figure 3 shows the fraction of Gaussian spectra obtained in the daytime boundary layer for the periods as Figure 4. The fraction of Gaussian spectra (for large combination periods) is correlated with the convectively available potential energy (indicated qualitatively by the shading in the skew-t plots from sondes launched from the radar site - Figure 4).

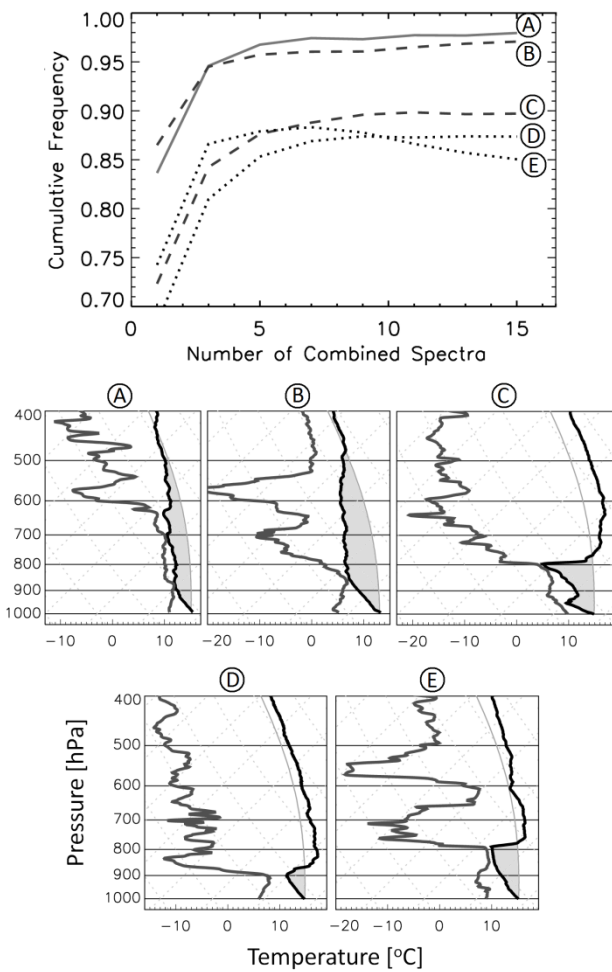


Figure 4: As Figure 3, but for FGAM daytime boundary layer spectra (500m to 2000m altitudes) (top), with corresponding Skew T-log p diagrams (bottom), indicating the magnitude of convectively available potential energy.

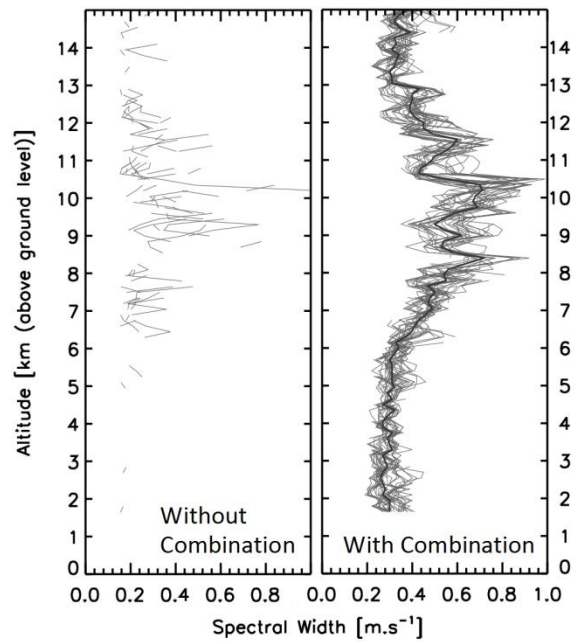


Figure 5: Comparison of Gaussian fit spectral width from vertical beam dwells, without spectral combination (left) and with combination of seven consecutive profiles (right), across a 30 minute period on 30/11/2011 centred on 09:30:00 (see abstract We-03 for more details). The thick line in the right hand plot indicates the median.

Improved Resolution of Turbulence: The improved resolution of turbulence in the free troposphere and stratosphere is evident from Figure 5, which compares spectral widths obtained with and without spectral combination, and Gaussian fitting for vertical beam MST observations on 30/11/2011.

4. Conclusions

Hand examination of Doppler spectra showed that the root-mean-squared difference between the Doppler spectrum and its Gaussian fit is a much better measure of 'Gaussian' Doppler spectra than the traditional χ^2 statistic. A threshold of 0.6×10^{-2} to identify a Gaussian fit.

Spectral combination was shown to dramatically improve the ability to resolve turbulence in the free troposphere and stratosphere, and to produce more Gaussian spectra – crucial for accurate quantification of turbulent kinetic energy.

References

- R. S. Hildebrand, P. H. Sekhon. Objective determination of noise-level in Doppler spectra. *Journal of Applied Meteorology*, 13(7):808-811, 1974.
- W. K. Hocking. Observation and measurement of turbulence in the middle atmosphere with a vhf radar. *Journal of Atmospheric and Terrestrial Physics*, 48(7):655-670, 1986.
- D. A. Hooper, J. Nash, T. Oakley, and M. Turp. Validation of a new signal processing scheme for the mst radar at aberystwyth. *Annales Geophysicae*, 26 (11):3253-3268.
- D. J. Murphy, W. K. Hocking, and D. C. Fritts. An assessment of the effect of gravity-waves on the width of radar doppler spectra. *Journal of Atmospheric and Terrestrial Physics*, 56(1):17-29, 1994. 17
- S. J. Pepler, G. Vaughan, and D. A. Hooper. Detection of turbulence around jet streams using a vhf radar. *Quarterly Journal of the Royal Meteorological Society*, 124(546):447-462, 1998. B.

Small scale turbulence and instabilities observed simultaneously by radiosondes and the MU radar

R. Wilson¹, H. Luce², H. Hashiguchi³, F. Dalaudier², S. Fukao⁴, T. Nakajo⁴, Y. Shibagaki⁵, M. Yabuki³, J. Furumoto³

¹ LATMOS-IPSL, UPMC Univ Paris 06, Univ. Versailles St-Quentin, CNRS/INSU, Paris, France.

² Université du Sud-Toulon Var, La Garde, France

³ Research Institute for Sustainable Humanosphere, Kyoto University, Uji, Japan

⁴ Department of Space Communication Engineering, Fukui University of Technology, Fukui, Japan

⁵ Osaka Electro-Communication University, Negagawa, Japan

Abstract

A Japanese-French field campaign devoted to study small-scale turbulence and instabilities in the lower atmosphere was conducted in September 2011 for three weeks at Shigaraki MU observatory (34.85N, 136.15E; Japan). The VHF MU radar was operated in range imaging mode (e.g. Luce et al., 2001) for turbulence observations at high temporal (24 s) and high range (typically 30 m) resolutions. In addition, 59 balloons instrumented with RS92SGP Vaisala radiosondes were successfully launched during the campaign when the radar was operated. Wilson et al. (2011, 2012) showed that turbulence can be detected from raw vertical profiles of temperature measured from standard radiosoundings through the detection of overturns using the so-called Thorpe analysis (Thorpe, 1977). In the present work, we shall present some comparison results between radiosonde and MU radar data.

1. Introduction

Soon after their conceptions, ST (Stratosphere-Troposphere) VHF radars have been used simultaneously with instrumented balloons for measuring atmospheric parameters. Intercomparisons improved our knowledge on the radar backscattering mechanisms at VHF which, in turn, provided some information on atmospheric dynamics and structures at various scales. A variety of methods was then developed for retrieving small-scale turbulence parameters from ST radars. However, the dominant sources and characteristics of the turbulent events detected by ST radars in the troposphere are still poorly documented partly due to the lack of temporal and range resolutions of these instruments (typically a few minutes and 150 m, respectively). Recently, the MU radar has been upgraded for being operated in range imaging mode (called Frequency domain radar Interferometry Imaging -FII-), allowing a range resolution of several ten meters and a time resolution of several ten seconds (e.g., Luce et al., 2001, 2006).

A Japanese-French field campaign devoted to the study of turbulence and instabilities in the free atmosphere with the MU radar in FII mode was carried out for three weeks in September 2011 at the Shigaraki MU Observatory (Japan). During this campaign, 59 radiosondes (Vaisala RS92SGP) were launched at the radar site. Turbulent events were detected from temperature/humidity profiles collected from radiosondes by applying the methods described by Wilson et al. (2011, 2012).

The dataset collected in September 2011 helped us to characterize the turbulent events detected by the MU radar and the background atmospheric conditions in which they occurred. We shall present some results of this campaign including direct comparisons between observables

collected simultaneously by radiosondes and MU radar.

2. Dataset

The 59 RS92SGP Vaisala radiosondes were launched every three hours mainly during night periods. The measurements consist of pressure, temperature, relative humidity (and horizontal wind) at a vertical sampling of 1 Hz (i.e. 3-5 m), the balloons being under-inflated. The MU radar is a flexible and fast beam-steering Doppler pulsed radar operating at 46.5 MHz (6.45-m radar wavelength, 3.5-MHz bandwidth and 1-MW peak output power) (e.g., Fukao et al., 1990). The radar beamwidth is 3.6°. The FII technique consists in transmitting several closely-spaced frequencies switched pulse to pulse.

The collected data at the various frequencies are processed using the adaptive Capon processing method (Luce et al., 2001). The radar was operated with five equally spaced frequencies from 46.0 MHz to 47.0 MHz (i.e., with a frequency spacing of 0.25 MHz). Range sampling was performed from 1.32 km up to 20.37 km ASL with a step of 5 m (the initial range resolution was 150 m). The radar antenna beam was steered into three directions (one vertical and two oblique directions at 10° off zenith toward North, East) so that winds could be estimated and echo powers between directions could be compared. The number of coherent integrations was set equal to 32 and one profile was acquired every 24.5 s at a time sampling of 6.14 s.

3. Balloon data processing method

The Thorpe method consists in comparing a measured potential temperature profile conserved during reversible dry or moist adiabatic motions to the sorted profile θ^s , used as a reference profile. Small scale turbulence is expected to induce local overturns within the θ profile. Identification of the turbulent layers is based on the identification of the overturns by subtracting the observed and sorted profiles (Figure 1). Such a method has been used mostly in oceanic studies, and more recently in an atmospheric context (Luce et al., 2002; Gavrillov et al., 2005, Nath et al, 2010, Alapatu et al., 2010, Kantha and Hocking, 2011). Wilson et al. (2010, 2011) proposed an objective method based on both an optimal filtering and on a statistical test making possible to reject artificial overturns produced by noise.

Water vapour saturation may significantly reduce the stability of the atmospheric stratification. The impact on turbulence detection in clouds from in situ measurements was recently considered by Wilson et al. (2012). According to the state of the air parcels probed by the sensors, dry (i.e. subsaturated) or saturated, the dry and moist (saturated) adiabatic lapse rates were estimated by using the derivations given by , e.g., Durran and Klemp (1982). Composite potential temperature profiles were calculated by a numerical integration of the vertical profiles of dry or saturated lapse rates (Wilson et al., 2012). The saturated (i.e. cloudy) layers were detected from the radiosonde measurements of relative humidity by applying an empirical multi-thresholds' method described by Zhang et al. (2010).

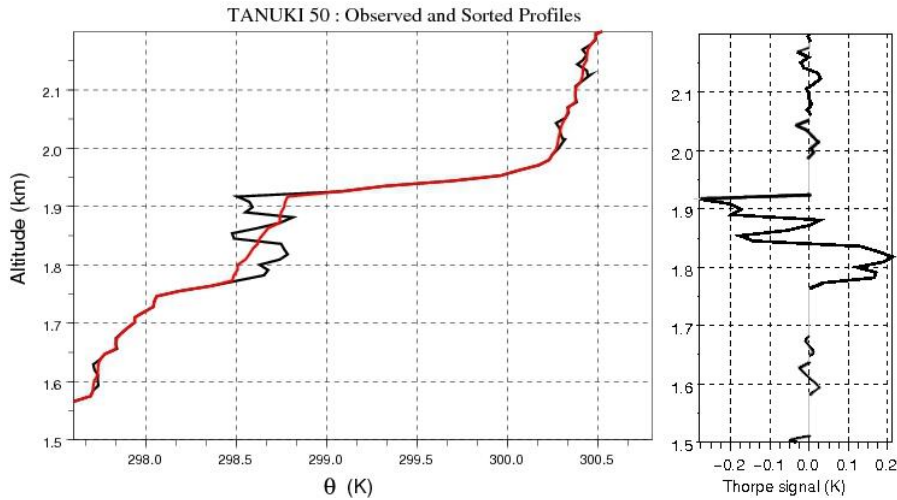


Figure 1: Example of detection of an overturn based on the Thorpe sorting.

4. A case study

Before 21 September 2011, summer anticyclonic conditions were met over Japan. Just after the passage of typhoon Roke over Japan (September 21st), the tropospheric jet-stream, initially running at higher latitudes, drifted southward. Autumnal weather conditions started from 22 September with negative temperature anomaly at tropospheric heights and the passage of an upper level frontal zone over Japan. We observed the passage of this front by both MUR and radiosondes. A very intense turbulent layer was detected by MUR during the night of September 25–26, corresponding to the passage of the upper level front (below the dashed line drawn in Figure 2a showing the location of the frontal zone). Echo intensities were similar in the three beam directions, indicating pure isotropic scattering in this layer (not shown). This turbulent event was probed by three radiosondes (51, 52 and 53) as shown by Figure 2a.

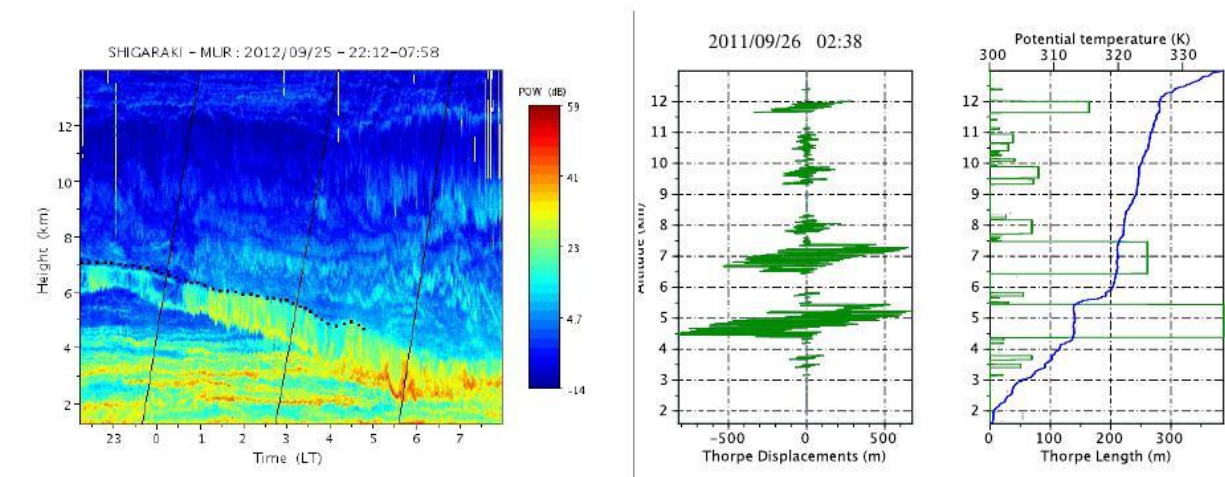


Figure 2: (a) Time-height cross-section of echo power from MU radar measurements in FII mode and at vertical incidence. The dashed line shows the height of the front and the continuous lines show the altitude versus time of the three balloons launched during this event. (b) The turbulent layers detected from the radiosounding 52. (Left) Thorpe displacements (Right) Thorpe lengths and potential temperature (blue line). The intense layer seen by the MU radar is within the height range 4.5–5.5 km.

Figure 2b shows the locations of the turbulent layers for balloon flight 52, the Thorpe displacements and Thorpe lengths. A 1-km deep turbulent layer was observed around the altitude of 5 km underneath the frontal zone, consistent with the radar observations in Figure 2a. The concurrent observations from MU radar and balloons makes thus possible to estimate the energetics of this turbulent event. Turbulent kinetic energy (TKE), estimated from the vertical velocity variance measured by the MU radar, reaches 3.5 J/kg in average. Turbulent potential energy (TPE) inferred from the Thorpe length and Brunt-Väisälä frequency calculated from balloon data, is 0.7 J/kg within the layer. The corresponding dissipation rates of kinetic energy, ϵ_k , and potential energy, ϵ_p , are very large: $\epsilon_k \sim 30$ mW/kg, $\epsilon_p \sim 9$ mW/kg. From these dissipation rates and the background stability of the stratification within the turbulent layer, a sensible heat flux $\rho c_p K_\theta d\theta/dz \approx 130$ W/m² is obtained.

5. Conclusions

The data collected in September 2011 were obtained during various meteorological conditions. In the present work, we focused on an intense turbulent event associated with a frontal zone. The turbulence layer was generated at a cloud base and extended well below the frontal zone. As already reported by Luce et al. (2010), turbulence was very likely produced by a convective instability due to evaporative cooling near the cloud base. In the present case, the data from four consecutive balloon flights confirmed the presence of a statically unstable layer ($N^2 < 0$) giving extra-credence to this interpretation. In addition, the presence of a turbulent layer of depth similar to the radar echo layer thickness (~ 1.0 km) was confirmed from the in situ profile by applying detection method of turbulence described by Wilson et al. (2010). Such a mechanism of turbulence generation is an alternative to dynamic shear instabilities, commonly proposed in the literature. The energetics associated with this event could be estimated using the standard approaches and extreme values of TKE, energy dissipation rates and heat flux were obtained. These results indicate that such turbulent events may have a strong impact on its environment. Further studies will be performed from this dataset and will aim at evaluating the agreement between the radar and balloon data and identifying the mechanisms of generation of turbulence in various weather conditions.

Acknowledgments

Financial support for the stay of two authors (R. Wilson and H. Luce) was provided by RISH during the field campaign. Part of this work was carried out during the stay of H. Luce at RISH founded by the National Institute of Information and of Communications Technology (NICT, Japan). Radiosondes were founded by LATMOS.

References

- Alappattu, D. P. and Kunhikrishnan, P. K.: First observations of turbulence parameters in the troposphere over the Bay of Bengal and the Arabian Sea using radiosonde, *J. Geophys. Res.*, 115, D06105, doi:10.1029/2009JD012916, 2010.–2896.
- Durrant, D. R. and J. Klemp, 1982: On the effects of moisture on the Brunt-Väisälä frequency. *J. Atmos. Sci.*, 39, 2152–2158.
- Fukao, S., T. Sato, T. Tsuda, M. Yamamoto, D. Tamanaka, and S. Kato, 1990: MU radar: New capabilities and system calibration. *Radio Sci.*, 25, 477–485.

- Gavrilov, N. M., H. Luce, M. Crochet, F. Dalaudier, and S. Fukao, 2005: Turbulence parameter estimation from high-resolution balloon temperature measurements of the MUTSI-2000 campaign. *Annales Geophysicae*, 23, 2401–2413.
- Kantha, L. and Hocking, W.: Dissipation rates of turbulence kinetic energy in the free atmosphere: MST radar and radiosondes, *J. Atmos. Sol-Terr. Phys.*, 73, 1043–1051, 2011.
- Luce, H., S. Fukao, F. Dalaudier, and M. Crochet, 2002: Strong mixing events observed near the tropopause with the MU radar and high-resolution balloon techniques. *J. Atmos. Sci.*, 59, 2885
- Luce, H., G. Hassenpflug, M. Yamamoto, and S. Fukao, 2006: High-resolution vertical imaging of the troposphere and lower stratosphere using the new mu radar system. *Ann. Geophys.*, 24, 791–804.
- Luce, H., M. Yamamoto, S. Fukao, D. Helal, and M. Crochet, 2001: A frequency domain radar interferometric imaging (fii) technique based on high-resolution methods. *J. Atmos. Sol. Terr. Phys.*, 61, 2885–2896.
- Luce, H., et al., 2010: Observations of kelvin-helmholtz instability at a cloud base with the middle and upper atmosphere (mu) and weather radars. *J. Geophys. Res.*, 115, doi:10.1029/2009JD013 519.
- Nath, D., Venkat Ratman, M., Patra, A. K., Krishna Murthy, B. V., and Bhaskar Rao, S. V.: Turbulence characteristics over tropical station Gadanki (13.5o N, 79.2o E) estimated using high-resolution GPS radiosonde data, *J. Geophys. Res.*, 115, D07102, doi:10.1029/2009JD012 347, 2010.
- Thorpe, S. A., 1977: Turbulence and mixing in a Scottish lock,. *Philos. Trans. Roy. Soc. London*, 286A, 125–181.
- Wilson, R., F. Dalaudier, and H. Luce, 2011: Can one detect small-scale turbulence from standard meteorological radiosondes? *Atmos. Meas. Tech.*, 4, 795–804, doi:10.5194/amt-4-795-2011.
- Wilson, R., H. Luce, F. Dalaudier, and J. Lefr`re, 2010: Turbulent patch identification in the potential-density/temperature profiles. *J. Atmos. Oceanic Technol.*, 26, 977–993.
- Wilson, R., H. Luce, H. Hashiguchi, and M. Shiotani, 2012: On the effect of moisture on the detection of tropospheric turbulence from in situ measurements. submitted to *Atmos. Meas. Tech.*
- Zhang, J., H. Chen, Z. Li, X. Fan, L. Peng, Y. Yu, and M. Cribb, 2010: Analysis of cloud layer structure in shouxian, china, using rs92 radiosonde aided by 95 ghz cloud radar. *J. Geophys. Res.*, 115, doi:10.1029/2010JD014 030.

VHF Radar Scatter Microstructure Measured by Combined Spatial and Frequency Domain Interferometry - SFDI -

A developing approach of three-dimensional interferometry with VHF Radar

Jürgen Röttger

c/o Max-Planck-Institute Solar System Research, Germany (roettger.jr@t-online.de)

Besides the VHF radar applications of the Spatial Domain Interferometry (SDI), measuring particularly variations in the horizontal structure, also the Frequency Domain Interferometry (FDI), measuring the line-of-site structure and velocity (mostly vertical), had been introduced successfully. Detailed descriptions and references to relevant radar interferometry publications are found in some tutorials (Röttger, 2000, 2003, 2010). This paper emanates from a series of publications on VHF radar interferometry, expands and extends these.

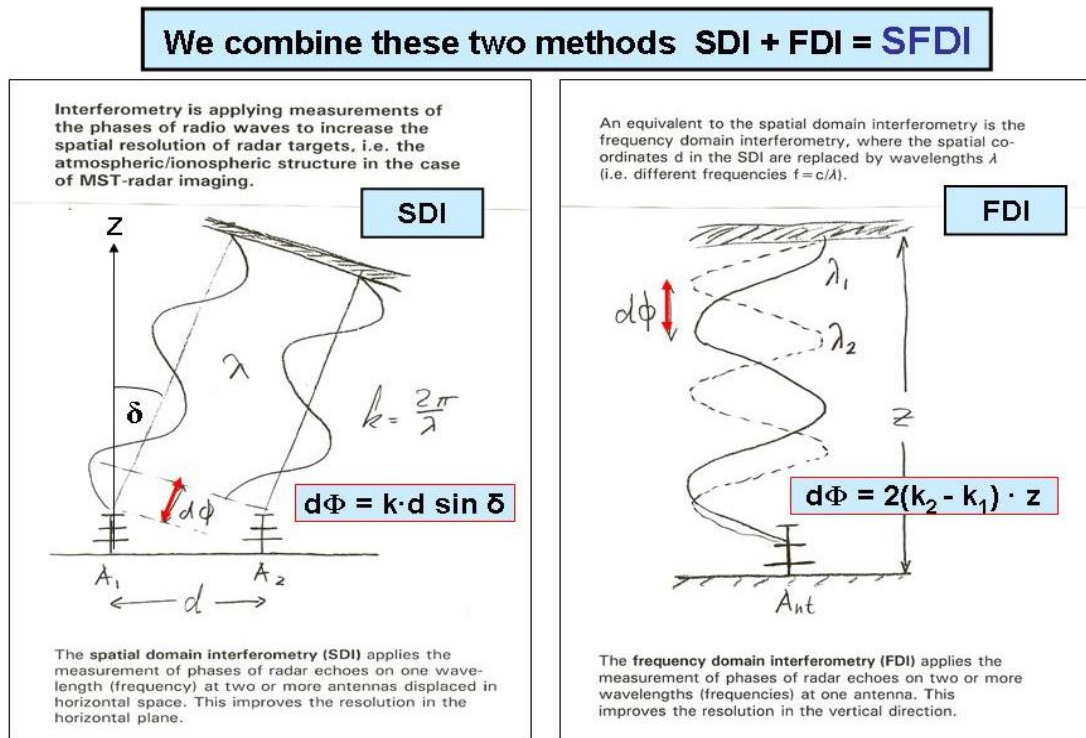


Figure 1: The Spatial Domain Interferometry **SDI** and Frequency Domain Interferometry **FDI**

The combination of these two methods, which is the main topic of this paper, allows determination of the development of the three-dimensional fine structure of the atmospheric radar refractivity. It will also be applied at high temporal resolution in the order of several seconds, and it allows range resolutions down to better than 50 meters. These are observational requirements to view and interpret the fine structure of atmospheric turbulence and stable laminae or sheets, which are the generators of the refractive index irregularities giving rise to VHF radar echoes.

This Extended Abstract for the MST13 Proceedings summarizes the author's development of SDI and FDI since its beginning in the early 1980s (see Röttger et al., 1985, 1996, 1998, 2000). It

describes the expansion to SFDI by combining these two approaches, basing on the same principle, which is presented first in this paper.

This novel way combining the Spatial and Frequency Domain Interferometry is called in short “SFDI”, and measures the main three parameters of position, bulk and fluctuating velocity of the refractivity distribution in three dimensions. The variation of these distribution functions show for instance that the velocity fluctuations (usually assumed to be a measure of turbulence) are not directly related to changes in radial position. The position variations can be interpreted as a measure of the roughness of moving, specular reflecting, corrugated refractive index surfaces and not necessarily as active turbulence. The consequences of these and some more new observations using this technique will be discussed, namely many MST VHF radar echoes are believed to be due to specular-type reflections from steep vertical gradients of the refractive index (given by humidity and temperature), which are horizontally extended and corrugated or rough.

In this and other papers the terms “scatter” and “reflection’ are used. Through their ultimate definition they describe two extrema, namely a random process and a deterministic process, respectively, which seldom occur in the atmosphere. We, thus, use both terms depending on which of both processes appear dominant in particular circumstances. The processes of reflection and scattering are initially treated for VHF radars by Röttger (1980a), basing on Atlas (1964).

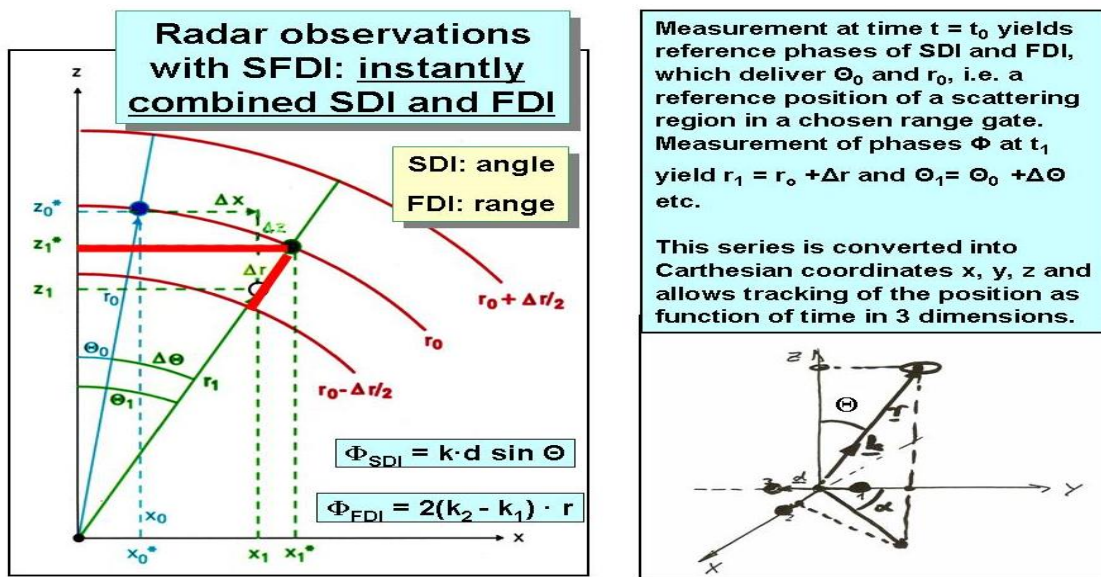


Figure 2: The principle of SFDI. $k = 2\pi / \lambda$ is the wavevector, d the distance between receiving antennas and Φ the measured phase difference.

Constrained optimization (Capon’s Method) using several in-pulse-bandwidth frequencies (FDI) to estimate or predict the higher frequency components of a pulse, is frequently applied to increase the range resolution (see Röttger, 2000, for references). The most advisable solution to study three-dimensional fine- and micro-structure of the atmosphere with VHF radars, is to use shortest pulses (wide frequency bandwidth) to improve range/altitude resolution and large-scale multiple antenna base-lines to improve the horizontal resolution (Woodman et al., 2007).

However, combining Frequency- and Spatial Domain Interferometry (FDI + SDI = SFDI) also provides us new information on small-scale variations in the atmosphere as we show now by using

data acquired on 6 October 1998 with the MU Radar in Japan. Details of the corresponding radar experiment operation and initial data treatment are found in Röttger et al. (2000).

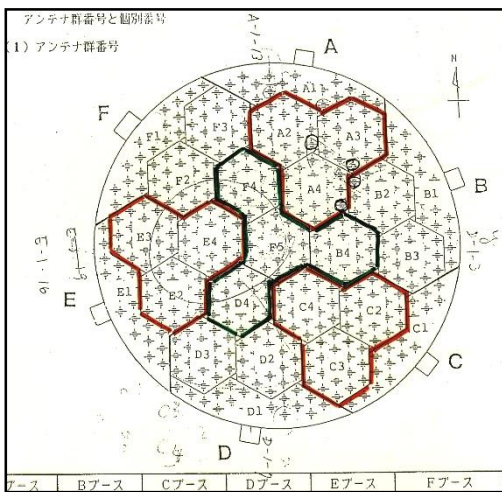


Figure 3:

TX: full antenna array of MUR.
 RX: 57 – 57 – 57 – 76, vertical beams;
 peak power: 1 MW. F1 = 46.25 MHz
 F2 = 46.75 MHz, range gate: 300 m

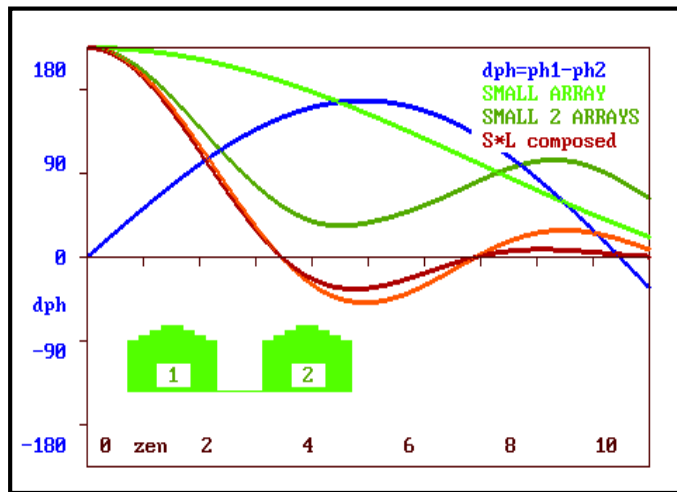


Figure 4:

The combined antenna diagram of two sectors and their weighting function 1 and 2 (green). In blue the phase difference as function of zenith angle zen. red and brown the effective beam pattern.

The combination of the full antenna array and smaller receiving arrays yields a combined pattern which allows unambiguous determination at zenith angles up to 5° , but the beam width of the main antenna limits that angle to $< 3^\circ$.

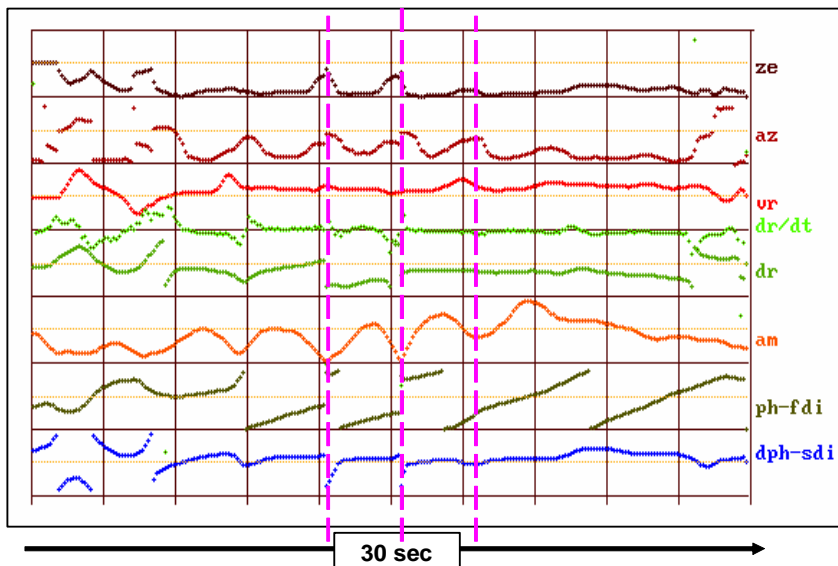


Figure 5: Phase difference between 2 SDI channels $dph-sdi$, and 2 FDI channels $ph-fdi$, amplitude am , relative radial position dr and its variation with time dr/dt , radial velocity vr , azimuth az and zenith angle ze in one range gate.

Minima of amplitude am occur regularly in connection with changes of the vertical position dr , zenith ze and azimuth az angles (marked by the hatched vertical red lines). There is also a connection to the radial velocity vr and dr/dt . These parameters are, thus, not independent, which let assume a deterministic but not a random process. The formers point towards a partial reflection process.

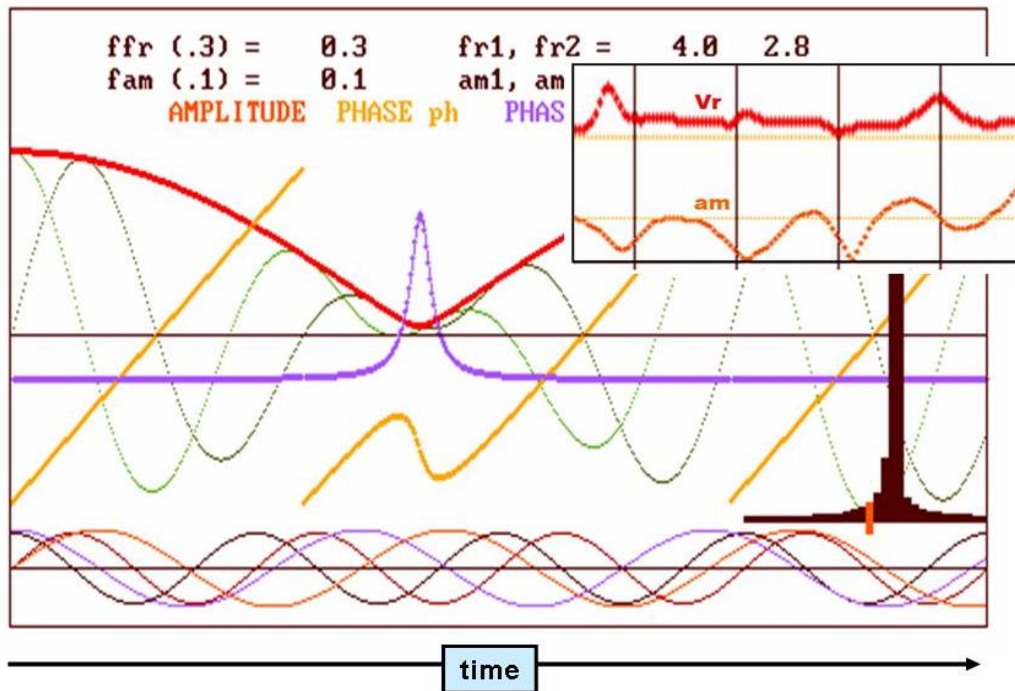


Figure 6: Complex superposition of two signals (lower 4 curves) their heterodyned amplitude (red) and phase derivative/change dph/dt (violet).

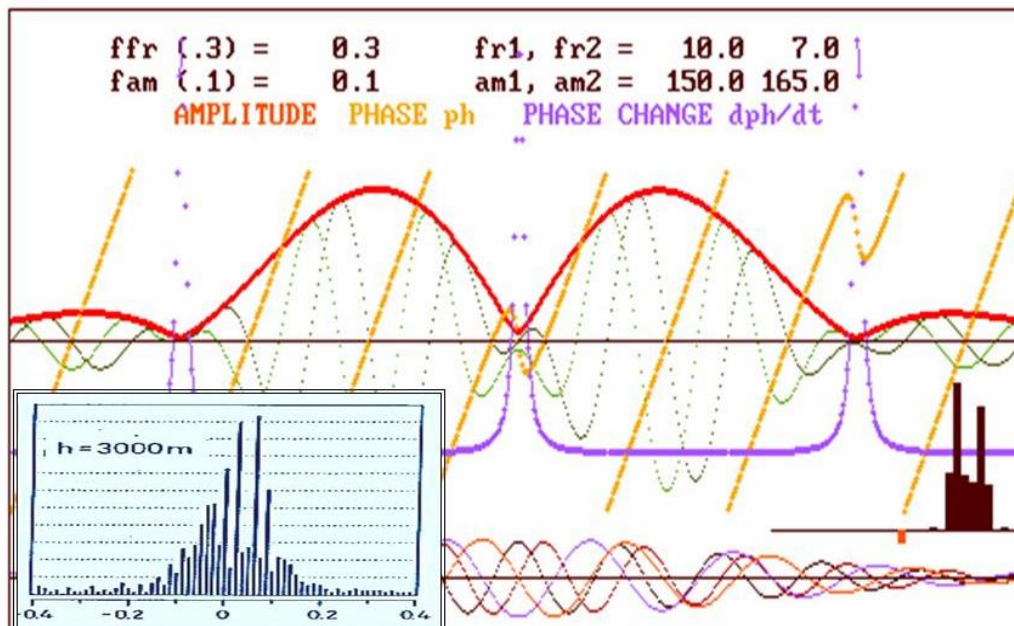


Figure 7: Same as Fig. 6 but for two signals with larger frequencies and unequal amplitudes. The Doppler spectrum shows two peaks (or more for larger number of interfering signals), as can be seen in VHF radar spectra (lower left-hand inset).

Simulation of superposition (heterodyning) of two signals (Fig. 6) with equal amplitude but different frequency and the corresponding change of amplitude and phase (difference). As in the observations (right-hand upper inset), the amplitude minimum occurs when the phase change, i.e. velocity is maximum. The Doppler spectrum of the composed signal (lower-right inset of Fig. 6)

shows a smooth shape, whereas in Fig. 7 examples are shown of a simulated and measured spiky spectrum.

These comparisons of observations and model simulation can prove that the signals scattered/reflected from irregularities of the refractive index have a deterministic behavior. This method, though, does not allow to separate the individual irregularity structure, but allows tracking of their mean position, strength and velocity.

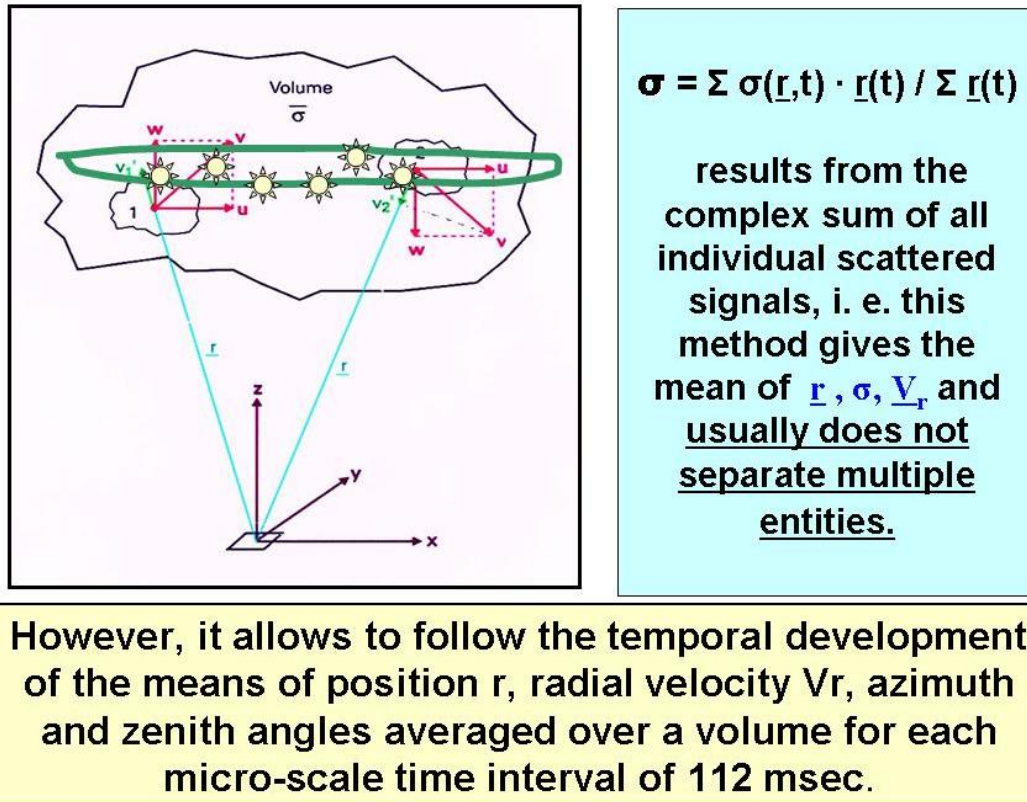


Figure 8: Sketch of individual scattering irregularities causing the VHF radar echo.

Mean position:

$$\underline{r} = \langle \underline{r}(x, y, z, t) \rangle = \Sigma \sigma(\underline{r}, t) \cdot \underline{r}(t) / \Sigma \sigma(\underline{r}, t)$$

Mean reflectivity

(scatter cross section per unit volume):

$$\sigma = \langle \sigma(x, y, z, t) \rangle = \Sigma \sigma(\underline{r}, t) \cdot \underline{r}(t) / \Sigma \underline{r}(t)$$

Mean radial velocity:

$$\underline{V}_r = \langle \underline{V}_r(x, y, z, t) \rangle = \underline{V}(\underline{r}, t) = \Sigma \underline{r}'(t) \cdot \sigma(\underline{r}, t) / \Sigma \sigma(\underline{r}, t)$$

After \underline{r} , σ , \underline{V}_r are measured using SFDI (SDI+FDI) with a time resolution of 112 msec. The samples of reflectivity σ (scatter cross section per unit volume or reflection coefficient) in vertical direction z are accumulated in 36 sub-range bins of 8.3 m thickness ($\Delta\Phi = 10^\circ$) over a period of $256 \times 112 \text{ msec} = 29 \text{ sec}$ (Fig.9). We also take an average of the vertical velocity component V_z

over these 29 sec. The basic micro-scale sample time period of the described data set is the coherent integration time of 112 milliseconds. This described analysis procedure is continued over suitable longer time periods (>15 min), as will now be presented.

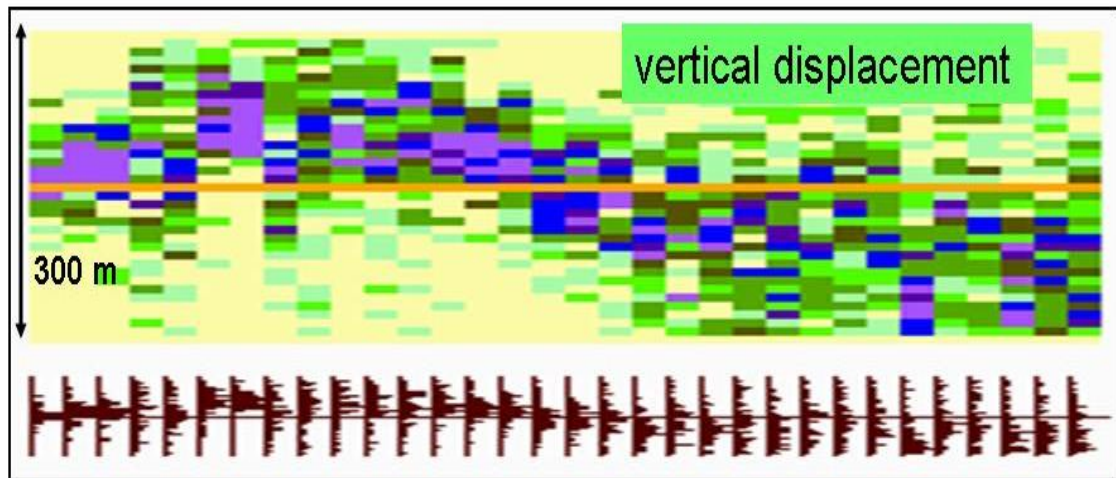


Figure 9: Distribution of vertical displacement of mean echo position in one range (height) gate over 15 minutes. The lower plot shows the distributions and the upper one the corresponding color plot.

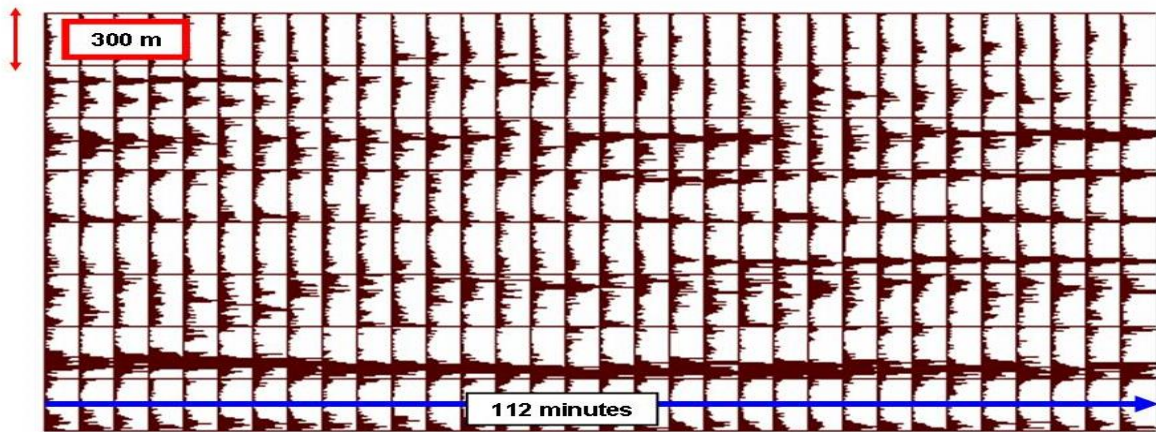


Figure 10: Distributions of vertical displacement of varying echo position in eight tropospheric height gates 4.6 – 6.7 km over 112 minutes

This method shows that the "range" (= height) distribution of the mean reflectivity is in the order of 1/5 to 1/2 narrower than the gate width (300 m), i.e. a significant improvement of the range resolution. The shortest micro-scale (averaging) time is – in the presented case - given by the coherent integration time (112 msec) of the radar experiment. There are times when 2 or more peaks occur. These are resulting from echoes occurring during different times in the accumulation period.

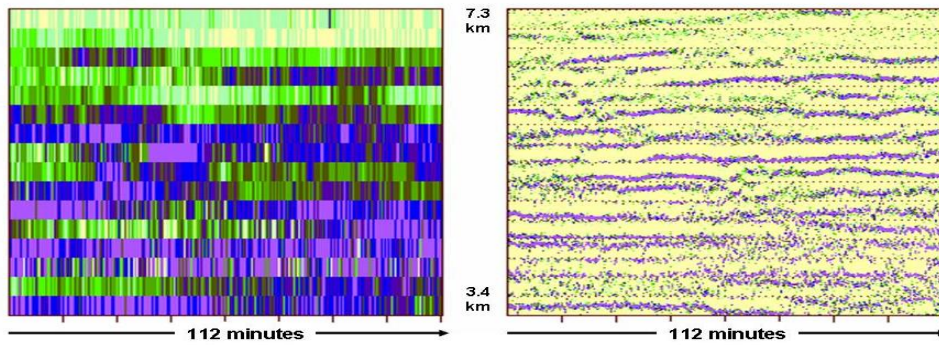


Figure 11:
 Left: normal HTI plot with 300 m range resolution
 Right: Location (in vertical direction) of irregularity center deduced with SFDI for the same data set

Fig. 11 shows the advantage of this SFDI method extracting the mean position of refractive index irregularities (also called refractivity) in the vertical direction with much higher resolution than the standard range gating.

In the following Fig. 12 the vertical position changes as shown in the right-hand side panel of Fig. 11 are color coded according to the sign of their vertical velocity, which is deduced from the variations of the phase with time. The “width” of the height distribution (Fig. 10) is not significantly correlated to the width of the Doppler spectrum (right hand panels of Fig. 12), which means that Doppler frequency fluctuations (usually assumed to be a measure of turbulence) are not directly related to changes in radial / vertical position. This lets the common assumption question that the width is a measure of random turbulent fluctuations of scattering irregularities. As argued further in the following, it is an indication of the roughness of a specular reflecting corrugated refractive index surfaces.

Fig. 12 also shows that the vertical velocity is usually not directly resulting from the vertical displacement (i.e. upward moving trace should always be red and v.v., see als Fig. 13). This is an indication that the mean position of the scattering center / rough reflecting surface changes due to variations of reflectivity (growth and decay) change but are not moving in bulk. The latter should result in a real velocity change. More work needs to be done to extract full information from these observations.

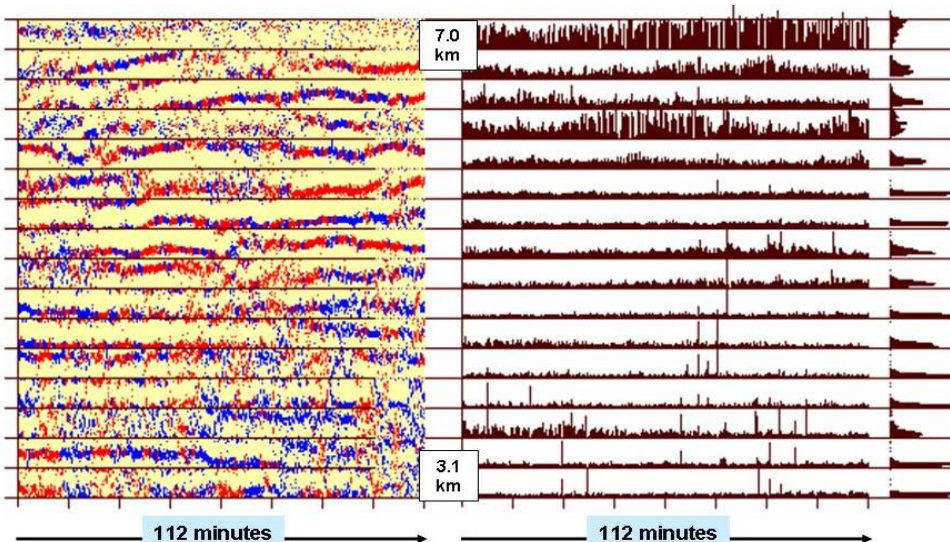


Figure 12:
 Left: Same as right of Fig. 11 but color-coded velocity sign (blue = upward, red = downward)
 Right: Variation and mean **width of Doppler spectrum** corresponding to left-hand side.

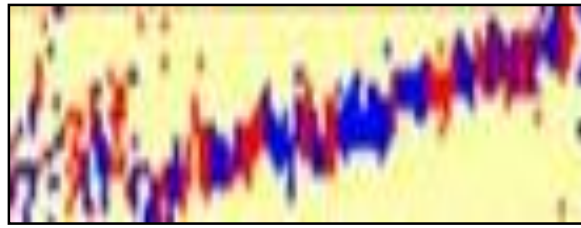


Figure 13: A blow-up from Fig. 12 of a mean upward displacement of a reflectivity sheet near 6.7 km, where besides upward (blue) also downward (red) velocities occur.

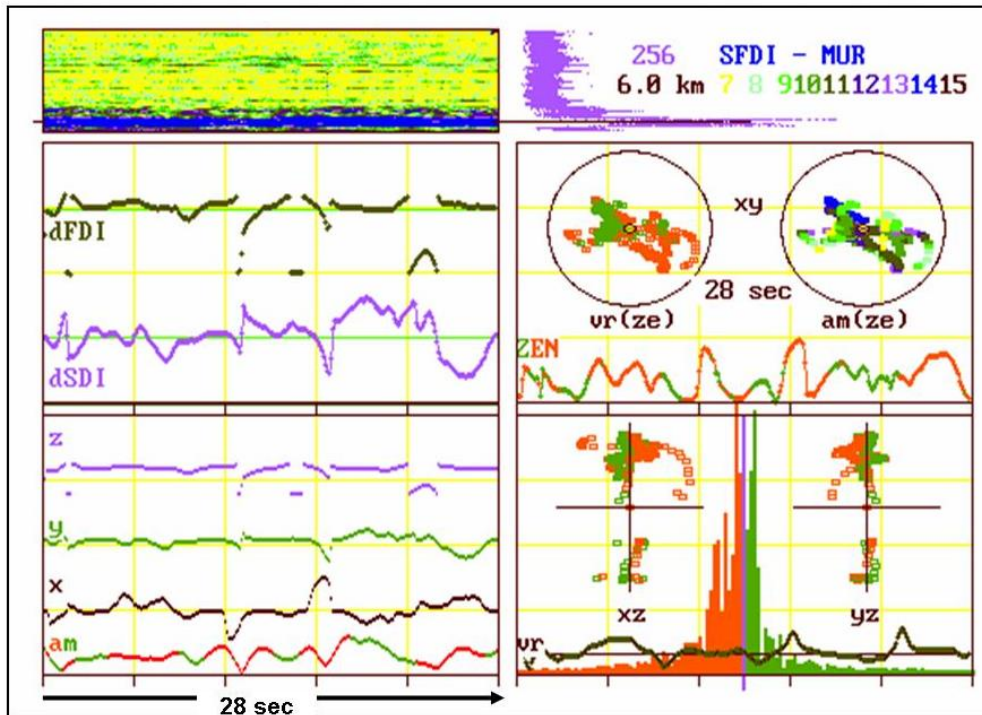


Figure 14: A summary of typical SFDI micro-scale observational results with the MUR
Left-hand side: Temporal developments over 28 (29) seconds (256 samples). Upper panel: Height-Time-Intensity plot of troposphere and tropopause echoes. Center panel: phase difference (+- 180 deg) of two frequencies dFDI and two spaced antenna sectors dSDI of the four recorded ones (Fig. 3). Lower panel: Location of scattering/reflecting centers in x,y,z coordinates and amplitude am in arbitrary scales (red and green color of the am line indicate up/downward velocity).
Right-hand side: Upper panel: Scatter plot of power profile (noise plus signal). The black line indicates the range gate ($z = 6.0$ km) of the parameters displayed in this figure. Center panel: Display of mean position projected in the xy plane (horizontal) over the 28 seconds. The center is the zenith direction ze. The circle indicates the -3 dB level of the transmitting antenna. The colour code of the radial velocity vr is red for upward velocity and green for downward velocity. In the lower line the temporal variation of the zenith angle (0 – 3 deg) is shown, also colour coded depending on the sign of the vertical velocity. In the right-hand circle the positions are displayed, using amplitude colour coding (highest power blue-magenta-black and smallest power green/yellow). Lower right-hand panel: Projections of the centres in the zonal / vertical xz and the meridional / vertical yz plane with velocity colour coding as before. The vertical lines indicate the vertical extent of the range gate of 300 m and the horizontal lines the -3 dB levels of the transmitting antenna. In addition the Doppler spectrum over the 256 points calculated within 28 sec is shown with the red colour for negative frequencies and the green for positive. The lower black line shows the temporal variation of the radial velocity vr in arbitrary unites.

The SFDI analysis delivers many parameters, the most essential ones are displayed in Fig. 5.

In Fig. 14 some indicative parameters are shown which are transformed into Cartesian coordinates. Due to space limitations in an Extended Abstract we can only extract some obvious highlights from this display, such as:

Changes of phases SDI and FDI often occur quickly at the same time, resulting in simultaneous changes of the derived parameters: position in 3-dimensions and velocity and their relations and changes, between the quick changes/jumps (within < seconds) there is a rather smooth behaviour. Often these quick changes in position are occurring with amplitude minima. Explanation of this can be the heterodyning presented in Figs. 6 and 7.

The physical reasons of these correlations are felt to be basically be understood by the super-positioning of two or more signals scattered/reflected from different positions and having different velocities. Indications from the position of structure on two sides of the zenith with opposite velocities are an indication of beam-width broadening. Thus, spectrum widening is not necessarily due to turbulence.

There is one more interesting feature observed in the right-hand panels of Fig. 14. The xy projection of locations with color coded velocities accumulates in the eastward part for positive velocities and in the westward part for negative velocities. This also shows up in the projection into the zonal and meridional plane as depicted in the following Fig. 15.

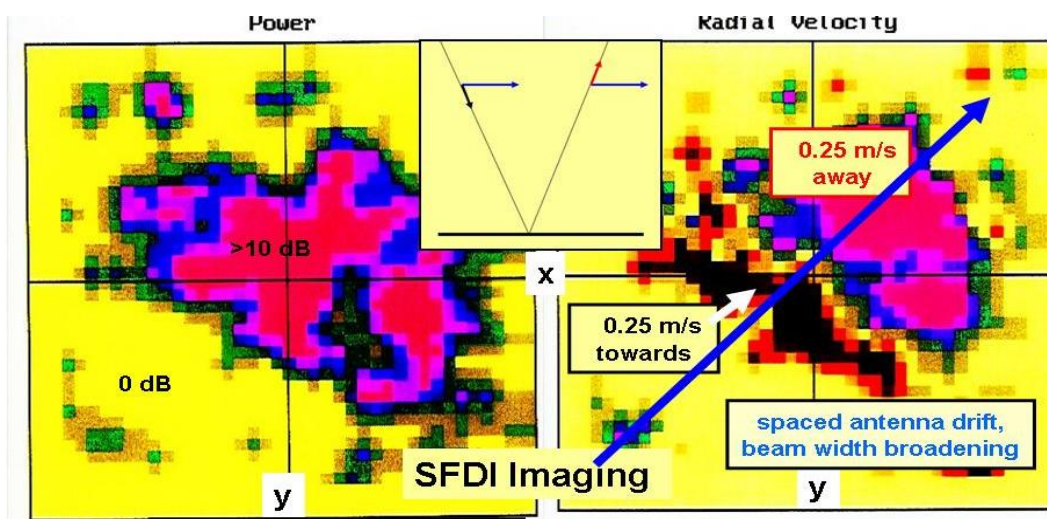


Figure 15: Left: power distribution in the horizontal xy plane at 8.1 km altitude. Right: radial velocity distribution in the same plane. Both displays are 28 sec averages over regions of a fraction of the Fresnel zone (3 km). The outer frames cover the -3 dB beam-width of the antenna.

The kind of imaging displayed in Fig. 15 shows the brightness of the irregularity structure and the irregularity drift in the right-hand side panel. That clearly shows the separation of negative and positive velocities on opposite sides of the zenith. This is an indication that the irregularities were carried through the antenna beam with given velocity. The measured velocity (in direction of the arrow) of about ± 0.25 m/s is the projection of the horizontal velocity as depicted in the center inset. This observation is a replica of the spaced antenna drift (SAD) method, which demonstrates its applicability by these means of SFDI radar imaging.

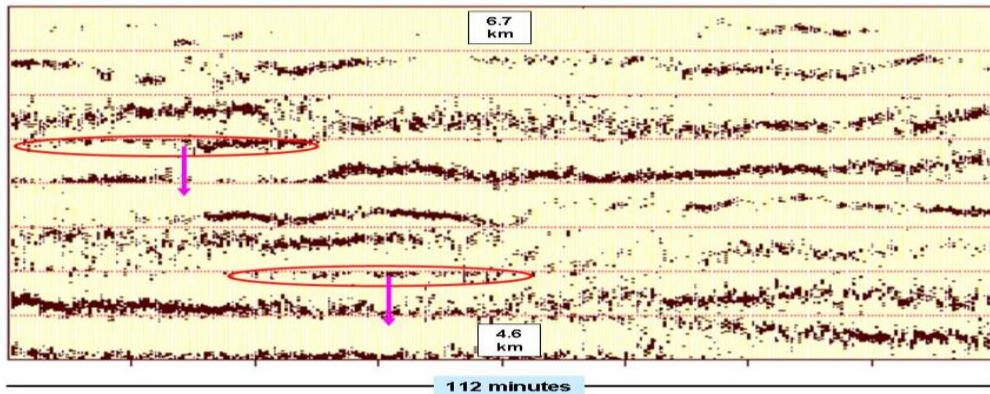


Figure 16: Range aliasing occurs in the red-framed parts and have to be shifted to the next lower range.

In the case of Fig. 15 we have to consider that here an average over one range gate of 300 m vertical extent and some kilometer in horizontal is calculated. It will be required in future to also display the position in the range gate by means of color coding. We have shown the thin structures of irregularities and their vertical displacement in Figs. 9 - 12. In this context we have to consider that there can be range aliasing occurring due to overlap of the 300 m wide range gates (these are Gaussian shaped). This is briefly indicated in Fig. 16, where two examples of range aliasing are highlighted in red color. This can be overcome by extending the range.

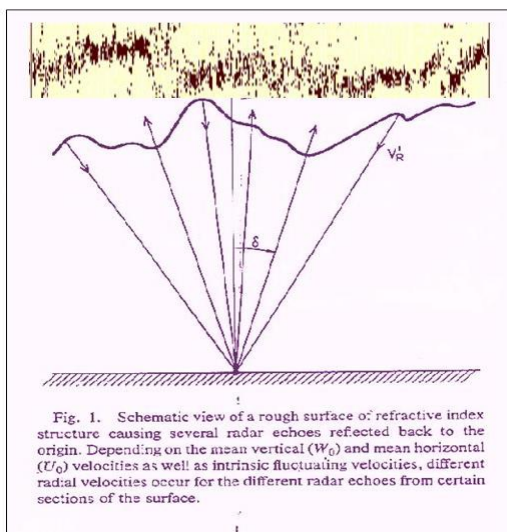


Fig. 1. Schematic view of a rough surface of refractive index structure causing several radar echoes reflected back to the origin. Depending on the mean vertical (W_0) and mean horizontal (U_0) velocities as well as intrinsic fluctuating velocities, different radial velocities occur for the different radar echoes from certain sections of the surface.

In Fig. 17 the distribution of reflectivity of irregularities in one range gate is shown. We note that here two jumps in vertical position occur and these are certainly not to range aliasing. The entire variation of this position distribution plot can be explained by spatial specular-type reflection from a rough surface as depicted in the lower part of Fig. 17. Such reflections occur from diversified positions on this surface, which also have different velocities as indicated by the arrows

Figure 17: Schematic view of a rough surface of refractive index structure causing radar echoes (from Röttger, 2000).

This figure shows an early potential interpretation how spikes in Doppler spectra and thin sheets and laminae could be explained resulting from longer lasting specular-type reflections at a rough surface of a sharp refractive index gradient. Such jumps in vertical position (Fig.17) are not uncommon and were also observed in Polar Mesosphere Summer Echoes (Röttger et al., 2007) and explained by Kelvin-Helmholtz Instability (KHI). See also Fig. 18.

This roughness can be caused by a spectrum of waves and turbulence, which, however, is not the particular scatterer/reflector itself. The view of locally rough surfaces of refractivity with specular reflection regions moving with given velocities can explain the shift and in particular the widening of the radar signal spectrum. The latter is usually assumed to be a proper estimate of turbulence, which may be questioned due to the shown specular-type reflection from quasi-horizontally stratified rough layers. These implications are supposed to be generally considered.

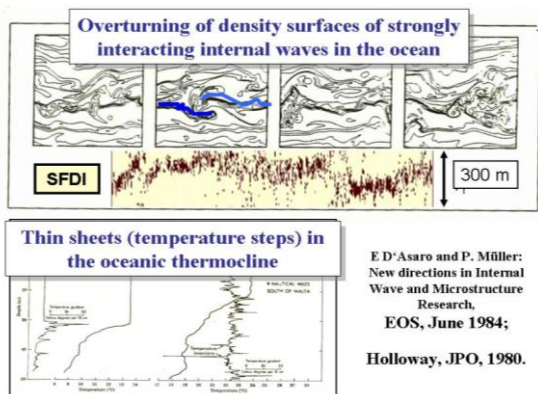


Figure 18: (in the left) shows an evident similarity of waves and turbulence in the ocean and the atmosphere. (Röttger, 1980b).

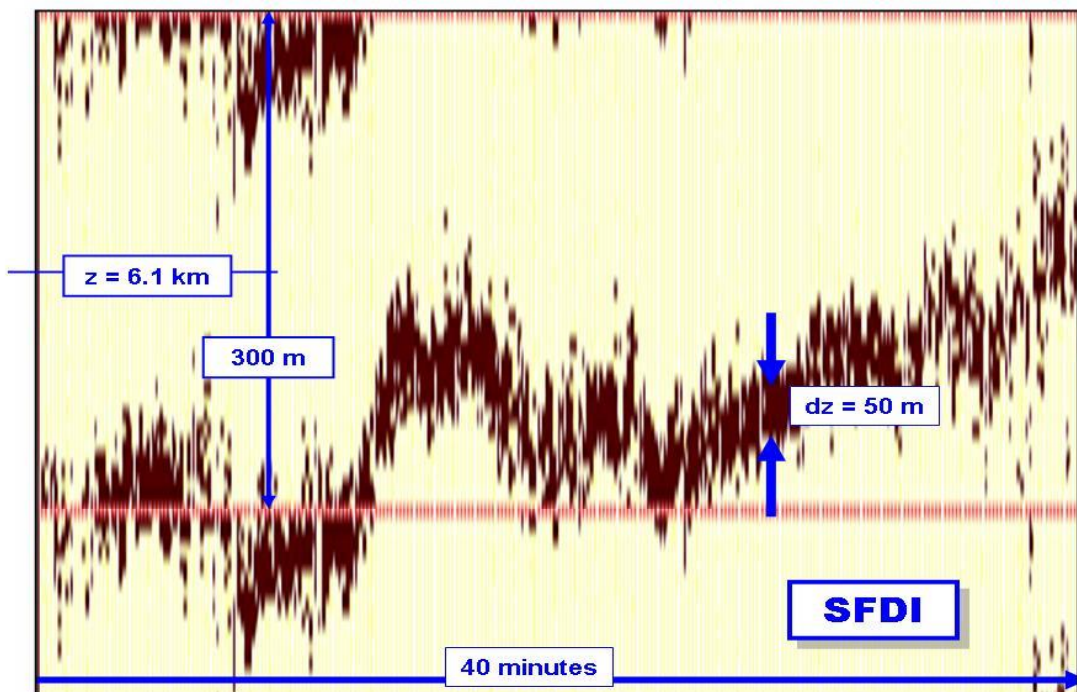


Figure 19: MY GRAND TOTAL

MST VHF radars are proper tools to continue studying the important dynamics and structure of the atmosphere, in particular applying three-dimensional imaging interferometry with high spatial and temporal resolution.

I did and do not believe that these thin, quasi-persistent structures, observed by VHF MST radars are caused by pure scattering from turbulence layers. I believe, and try to show it again in this paper, that they are due to specular-type partial reflections (Atlas, 1964) from steep quasi-vertical gradients of the refractive index (sheets and laminae), which can be tilted and slightly corrugated or rough. These steep vertical refractivity gradients can occur at the edges of active turbulence as first suggested by Bolgiano (1962, 1968), which develops into fossil turbulence, and keeping a roughness of the sheets and layers (Beckman and Spizzichino, 1963).

The width of a turbulence layer is usually defined as the half-power width of a Gaussian describing layered turbulent velocity fluctuations. The "width" dz (see Figure 19 above) as determined by this SFDI method is by no means such a "width of a turbulence layer". It is a measure of the roughness of thin refractivity sheets. Radial displacements due to three-dimensional velocity, which carries (by the generally accepted Taylor Hypothesis) the corrugated sheets or laminae of steep refractivity gradients and the growth and decay of refractivity structures causes further displacements. This results in spatial and temporal variations of the distributions of 3-dimensional locations of radar reflectivity as shown in this paper.

More research, - e.g. case studies, statistics, modeling, further advanced technology (such as wider bandwidth and multiple receiving antenna channels), novel processing, and finally a full physical interpretation – is welcome.

This Extended Abstract paper, published in the Proceedings of the MST13 Workshop, was originally presented orally at the International Symposium on the 25th Anniversary of the MU Radar at RISH, Kyoto University, Uji, Japan, on 23 September 2010. I thank all my colleagues of RISH and other places in Japan for the fruitful collaboration and hospitality during my visits to RASC, MUR, EAR, RISH etc. In particular I want to dedicate this paper to my good friend Shoichiro Fukao.

References

- Atlas, D, Advances in Radar Meteorology, in Adv. In Geophys., vol. 10, ed. H.E. Landsberg and J. Van Mieghem, p. 317-478. Academic Press NY, 1964.
- Beckman, P., and A. Spizzichino, The Scattering of Electromagnetic Waves from Rough Surfaces, Pergamon Press, 503 pp., 1963.
- Bolgiano, R., Structure of Turbulence in Stratified Media, J. Geophys. Res., vol. 67, p.3015-3023, 1962.
- Bolgiano, R., The General Theory of Turbulence in the Atmosphere, Proc. NATO Adv. Study Inst.,371-398, 1968.

- Röttger, J., Reflection and Scattering of VHF radar signals from Atmospheric Refractivity Structure, *Radio Sci.*, vol. 15, p. 259-276, 1980a.
- Röttger, J., Structure and Dynamics of the Stratosphere and Mesosphere Revealed by VHF Radar Investigations, *Pure and Appl. Geophys. (Pageoph)*, Vol. 118, Birkhäuser Verlag, Basel, p.494-527, 1980b.
- Röttger, J., and H.M. Ierkic, Postset Beam Steering and Interferometer Applications of VHF Radars to Study Winds, Waves and Turbulence in the Lower and Middle Atmosphere, *Radio Sci.*, vo. 20, 1461-1480, 1985.
- Röttger, J., C.J. Pan, C.H. Liu, S.Y. Su and J.C.H. Wu, VHF Radar Interferometer Observations of Lightning Echoes and Tropospheric Scattering Centers, *Proc. 7th International Workshop on Technical and Scientific Aspects of MST Radar MST7*, November 1995, Hilton Head, SC, USA, ed. B. Edwards, SCOSTEP Secretariat, NOAA, Boulder, CO, USA, p.368-371, 1996.
- Röttger, J., C.H. Liu, C.J. Pan and C.H. Wu, A Microscopic View on VHF Radar Returns from the Troposphere, *Proc. 8th International Workshop on Technical and Scientific Aspects of MST Radar MST8*, December 1997, Bangalore, India, ed. B. Edwards, SCOSTEP Secretariat, NOAA, Boulder, CO, USA, 1998. p. 21-24, 1998.
- Röttger, J., H. Luce, M. Yamamoto, S. Fukao, C.H. Liu, C.J. Pan, S.Y. Su and C.H. Wu, Combined High-Time Resolution SDI-FDI Experiments with VHF Radar, *Proc. 9th International Workshop on Technical and Scientific Aspects of MST Radar MST9 and COST-76*, March 2000, Toulouse, France, ed. B. Edwards, SCOSTEP, COST and Meteo France, c/o SCOSTEP Secretariat, NOAA, Boulder, CO, USA, 1998. p. 47-50, 2000.
- Röttger, J., S.Y. Su, C.J. Pan, C.H. Liu and C.H. Wu, SDI-FDI Detection of Lightning Echoes with the Chung-Li VHF Radar: Three-Dimensional Interferometry, *Proc. 9th International Workshop on Technical and Scientific Aspects of MST Radar MST9 and COST-76*, March 2000, Toulouse, France, ed. B. Edwards, SCOSTEP, COST and Meteo France, c/o SCOSTEP Secretariat, NOAA, Boulder, CO, USA, 1998. p. 51-54, 2000.
- Röttger, J., MST Radar Interferometry, *Invited Lectures The International School on Atmospheric Radar*, Tirupati, Dec. 1997, ed's. K.G. Rao and S.C. Chakravarty, Indian Space Research Organisation (ISRO), Bangalore-560094, p. 129-186, 2000.
- Röttger, J., What is Turbulence Seen by VHF Radars? *Proc. 10th International Workshop on Technical and Scientific Aspects of MST Radar MST10*, May 2003, Piura, Peru, ed's. J. Chau, J. Lau and J. Röttger, p.449-559, 2003.
- Röttger, J., M. Rapp, J. Trautner, A. Serafimovich and C. Hall, New PMSE Observations with the EISCAT 500-MHz Svalbard Radar and the Sousy 53.5-MHz Svalbard Radar, *Proc. 11th International Workshop on Technical and Scientific Aspects of MST Radar MST11*, December 2006, Gadanki, India, ed. V.K. Anandan, McMillan Delhi, ISBN 10:0230-63414-1, p.136-140, 2007.

Röttger, J., The Initial Decade of MST Radars: Looking back 30 - 40 Years 1971 - 1981, Proc. 12th International Workshop on Technical and Scientific Aspects of MST Radar MST12, May 2009, London (Ontario), Canada, ed's. S. Svarnalingam and W.K. Hocking, ISBN: 978-0-98867285-0-1, CAP, Ottawa, Canada, p. 27-65, 2010

Woodman, R.F., G. Michhue, J. Röttger and O. Castillo, The MPI-SOUSY-VHF Radar at Jicamarca: High Altitude Resolution Capabilities, Proc. 11th International Workshop on Technical and Scientific Aspects of MST Radar MST11, December 2006, Gadanki, India, ed. V.K. Anandan, McMillan Delhi, ISBN 10:0230-63414-1, p.334-337, 2007.

Performance Improvement in Momentum Flux Computation time using EV based Post Beamsteering Technique derived winds

VK Anandan, Shridhar Kumar, VN Sureshbabu

ISTRAC, Indian Space Research Organisation, Bangalore, India -560058 (anandanvk@hotmail.com)

Abstract

A study has been performed to derive zonal and meridional momentum fluxes from the vertically received beam of the Middle and upper atmospheric (MU) radar and co-synthesized beams within the transmit beamwidth. The main advantage of this work is that it demonstrates spatial-averaging of estimated flux in various directions in azimuth plane and that integration of fluxes over different time intervals has reduced the time of integration about 8-9 hours to minimize the error in flux estimation.

1. Introduction

Vertical flux of horizontal momentum of wind fluctuations has been key parameters for radar measurements in the lower and middle atmosphere. The reliability of these measurements is still uncertain. Detailed studies have been presented to perform error analysis and demonstrate statistical reliability on momentum. Basically, the symmetric beam radar method of Vincent and Reid [6] most common technique to measure momentum flux in the lower atmosphere. Kudeki and Franke [2] discussed the statistics of momentum flux estimation and concluded that to obtain statistically significant measurements of the momentum flux, long integration times are necessary since the flux is typically a small fraction of the mean energy. During the CADRE campaigns at Jicamarca, Riggin et al. [1] estimates the zonal and meridional momentum flux of range $0.01 - 0.04 \text{ (m/s)}^2$ using 10 hours of observations per day for 10 days between 20 and 27 km. The intrinsic uncertainties in the measurements of zonal momentum flux were on the order of $0.005 - 0.04 \text{ (m/s)}^2$ with slightly smaller values for meridional flux. Dutta et al. [4] estimated the momentum flux for short periods ($T < 2 \text{ hrs}$), integrated for different lengths of times to minimize the error and concluded that the optimum time of integration for estimation of momentum flux is about 15 - 16 hrs.

In this paper, using time series of vertical data collected from MU radar, the beam has been synthesized at the tilt angle of 1.5° with 32 equally separated azimuth angles using Post Beamsteering Technique (PBS). The obtained beams in various pointing directions constitute 8 set of beams (8X4), each of which includes 4 symmetric beams separated by 90° in azimuth. From each set of beams, momentum flux of short period ($< 2 \text{ hrs}$) is estimated using the symmetric beam method with modified to accommodate multiple beams along different pointing directions. The flux estimated from each set is averaged and integrated over different lengths of time up to 14 hrs (Jul 16, 2008, 1700LT- Jul 17, 2008, 0600 LT). This systematic method for the estimation of momentum flux reveals that spatial averaging of beams in azimuth and integration over different lengths of time have reduced the time of integration to about 8-9 hours to minimize the irreducible error in flux estimation period.

2. System Description and Data Analysis

The MU radar located in Shigaraki, Japan (34.85° N, 136.10°E) has a large circular antenna array with 475 crossed Yagi elements, peak transmission power of 1 MW. The antenna array is separated into 25 sub-arrays (channels). The observation were conducted with full array transmission (beamwidth 3.6°) in the vertical direction, 64 coherent integration, 320μs inter pulse period, 256 samples and 0.1024 sec sampling time interval.

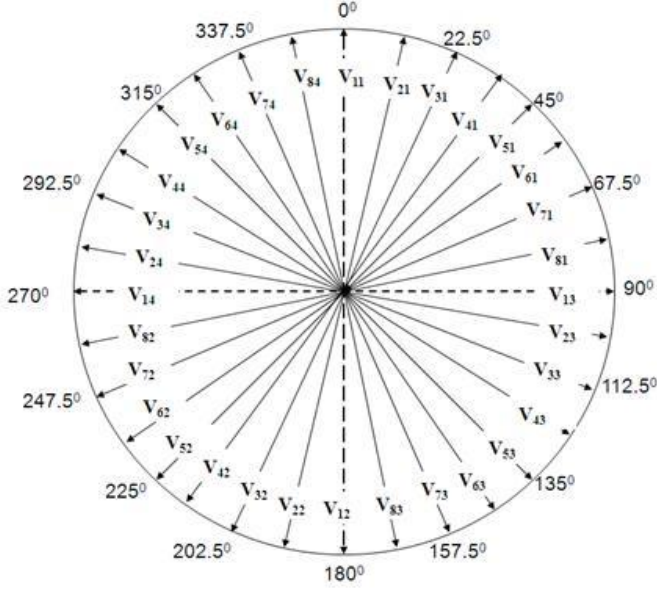


Fig.1 shows that representation of indices for radial velocities in different directions

In the present work, the data collected from 25 channels were analyzed using the adaptive Capon beamforming technique [5] to synthesize new beams in the desired directions (32 equally spaced azimuth positions at 1.5° zenith angle) within the transmit beamwidth. The power spectrum using the EV method [3], at a pointing direction is independently obtained for 5 overlapping sub-bands, and the sequence is repeated three times. In this way, 15 power spectra

have been obtained from one record. The average power spectrum is obtained to improve SNR. From the average spectra, the first moment is derived through the adaptive moment estimation method [7], and thus radial velocity is readily obtained in the direction of interest. The same process is continued to obtain the time series of radial velocities over time duration about 14 hrs. The time series of radial velocities is divided into 14 blocks of one hour each. The time series of radial velocities are detrended (by subtracting the mean) from each block. The same steps are used to obtain the time series of radial velocities along 32 equally separated beam pointing directions (Fig. 1). The vertical flux of horizontal momentum has been calculated with four off-zenith beams (separated by 90° in azimuth) using the symmetric beam method [6]. For each set, the expressions for zonal $u'w'$ and meridional $v'w'$ fluxes have been modified as follows:

$$u'w' = \frac{(V_{N1}^2 - V_{N2}^2) \sin \varphi_1 + (V_{N3}^2 - V_{N4}^2) \sin \varphi_3}{2 \sin 2\theta} \quad (1)$$

$$v'w' = \frac{(V_{N1}^2 - V_{N2}^2) \cos \varphi_1 + (V_{N3}^2 - V_{N4}^2) \cos \varphi_3}{2 \sin 2\theta} \quad (2)$$

where v and φ represent the radial velocity and azimuth angle, respectively. In the above expressions, the subscript N represents set number, and the subscripts 1, 2, 3 and 4 represent beam number in each set of beams. θ is the off-zenith angle. The symmetric beam pair in azimuth is used for estimating the momentum flux. The fluxes obtained from 8 sets are spatially averaged. Likewise, zonal and meridional momentum fluxes are obtained for each hour data block. After this,

the momentum flux profiles are smoothed by taking three-point moving averages and are then averaged over different lengths of time from one to 14 hours.

3. Results and Discussion

The momentum flux profiles averaged over 14 hours; flux per unit mass for zonal wind varies between $-0.026 \text{ m}^2\text{s}^{-2}$ and $0.080 \text{ m}^2\text{s}^{-2}$ and that for meridional wind it varies between $-0.021 \text{ m}^2\text{s}^{-2}$ and $0.054 \text{ m}^2\text{s}^{-2}$. We have estimated the momentum flux using the EV based Post beam steering (PBS) technique and averaged it for different lengths of time up to 14. The results for different lengths of time for both zonal and meridional flux are presented in Fig. 2, which shows that momentum flux profiles averaged over 4 to 8 hours show changes at several heights but profiles averaged from 8 hours or longer agrees better with each other. The little variability at the highest altitudes is due to poor SNR.

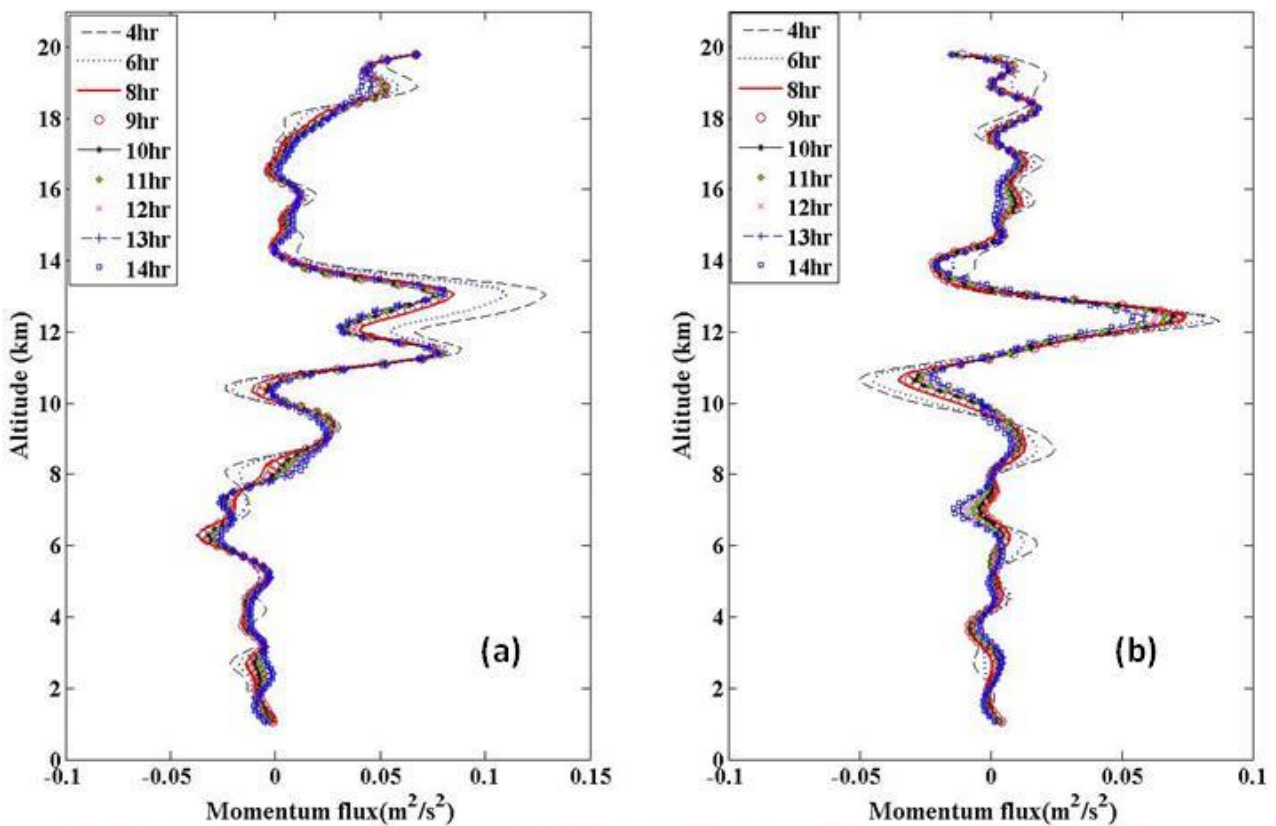


Fig.2 shows the vertical profile of momentum flux integrated over different length of times (a) Zonal flux (b) Meridional flux

The standard deviation of averaged momentum flux has been calculated to determine the variation of error in estimation with different lengths of time. The irreducible error in zonal flux is found to be $0.0049 \text{ m}^2\text{s}^{-2}$, $0.0081 \text{ m}^2\text{s}^{-2}$ and $0.0070 \text{ m}^2\text{s}^{-2}$ whereas in meridional flux it is $0.0020 \text{ m}^2\text{s}^{-2}$, $0.0060 \text{ m}^2\text{s}^{-2}$ and $0.0025 \text{ m}^2\text{s}^{-2}$ for the altitude ranges of 1.05-12 km, 12-16 km and 16-20 km respectively. Fig. 3 shows that irreducible error in flux estimation is consistent after 8 - 9 hours of integration.

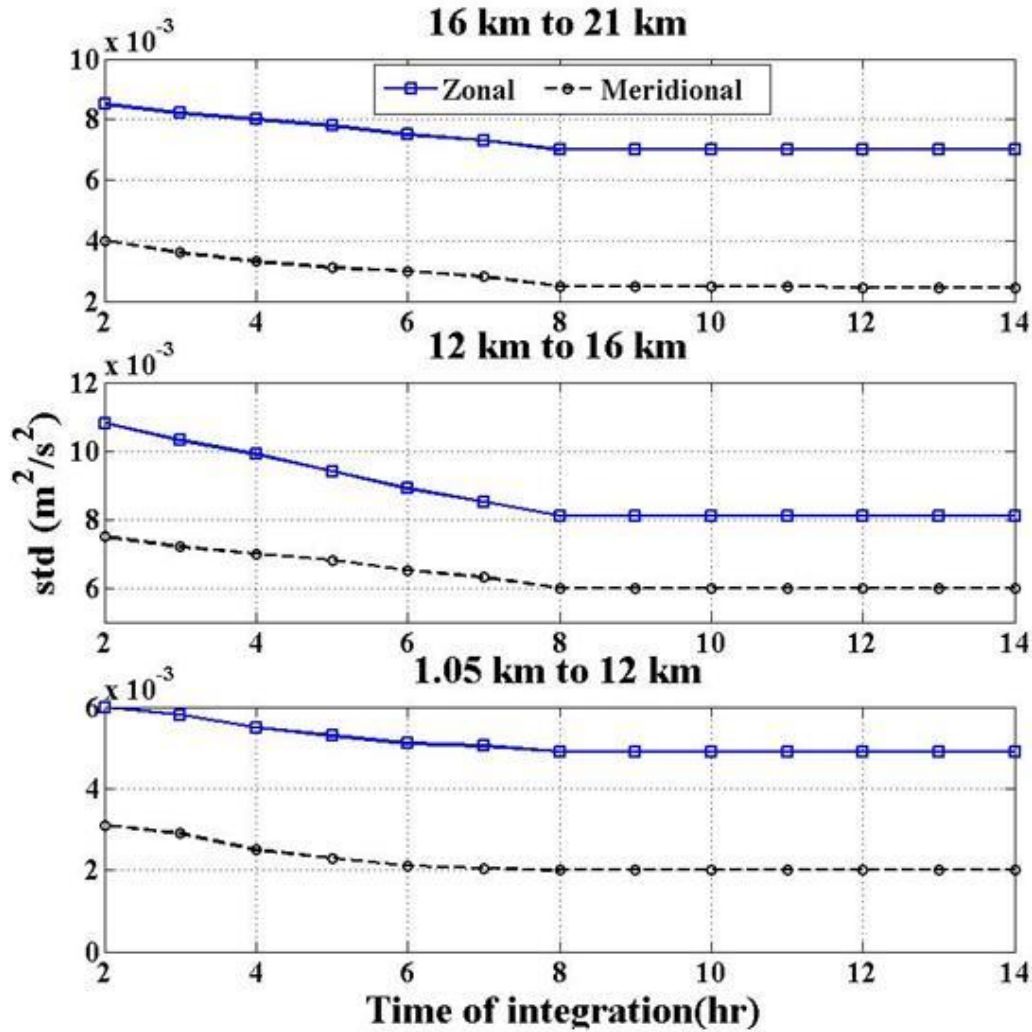


Fig.3 shows standard deviation of mean zonal and meridional fluxes with time of integration at different altitude zones.

4. Conclusion

In this work, a new approach to momentum flux estimation using the PBS technique has been demonstrated using the symmetric beam method with modification to accommodate multiple beams simultaneously synthesized by Capon beam forming and eigenvalue based power spectral analysis. This new approach to deriving velocities using multiple beams and estimating momentum flux is demonstrated to be more efficient to obtain reduce the of time integration to about 8-9 hours in deriving atmospheric parameters, compared to conventional approach which requires a minimum of 15-16 hours of radar observation and integration of estimated parameters.

Acknowledgement

This study was conducted by using the MU radar under a support of the Asia-Africa Science Platform Program (AA-SP) of JSPS, Japan and Indian Space Research Organization, Govt. of India.

References

- D. M. Riggan, D. C. Fritts, C. D. Fawcett, E. Kudeki, and M. H. Hitchman, "Radar observations of gravity waves over Jicamarca, Peru during the CADRE campaign," *J. Geophys. Res.*, vol. 102, pp. 26,263–26,282, 1997.
- [1] E. Kudeki and S. J. Frank, "Statistics of momentum flux estimation," *J. Atmos. Sol. Terr. Phys.*, vol.60, pp.1549–1553, 1998.
- [2] G. Bienvana and L. Kopp, "Optimality of high resolution array processing using the eigen system approach," *IEEE Trans. Acoustic, Speech, Signal processing*, vol. 34, pp. 1234-1248, 1983.
- [3] G. Dutta, P. V. Rao, M. C. Ajay Kumar, P. Vinay Kumar, and H. Aleem Basha, "On the optimum time of integration for estimation of momentum flux from VHF radar data," *GRL*, vol.32, 2005.
- [4] J. Capon, "High resolution frequency-wave number spectrum analysis," *Proc. IEEE*, vol. 57, pp.1408-1418, 1969.
- [5] R. A. Vincent and I. M. Reid, "HF Doppler measurements of mesospheric momentum fluxes," *J. Atmos. Sci.*, vol.40, pp.1321–1333, 1983.
- [6] V. K. Anandan, P. Balamuralidhar, P. B. Rao, A. R. Jain, and C. J. Pan, "An adaptive moments estimation technique applied to MST radar echoes," *J. Atmos. Oceanic Technol.*, vol. 22, pp. 396–408, 2005

Validation of the receiving pattern of the MAARSY phased antenna array

Toralf Renkwitz, Ralph Latteck, Werner Singer and Gunter Stober

Leibniz-Institut für Atmosphärenphysik an der Universität Rostock, Kühlungsborn
(email: renkwitz@iap-kborn.de, phone: +49 38293 680, fax: +49 38293 6850)

1. Introduction

In 2009/2010 the Leibniz-Institute of Atmospheric Physics (IAP) installed a new powerful VHF radar on the island Andoya in Northern Norway (69.30°N, 16.04°E). The **Middle Atmosphere Alomar Radar System** (MAARSY) is designed for improved studies of the Arctic atmosphere with high spatial and temporal resolution in the troposphere/lower stratosphere and in the mesosphere/lower thermosphere. The monostatic radar is operated at 53.5 MHz with an active phased array antenna consisting of 433 Yagi antennas. Each individual antenna is connected to its own transceiver with independent phase control and a scalable power output of up to 2 kW. These properties give the radar a very high flexibility of beam forming and beam steering. The MAARSY radar has been described in detail by Latteck et al. (2012).

During the design phase of MAARSY several model studies have been carried out in order to estimate the radiation pattern for various combinations of beam forming and steering. However, parameters like mutual coupling, active impedance and ground parameters may have an impact to the radiation pattern, but hardly can be measured. Hence, experimental methods need to be implied to verify the model results.

For this purpose, the radar has occasionally been exclusively used in passive mode, monitoring the noise power received from both distinct galactic noise sources like e.g., Cassiopeia A, Cygnus A and the complete diffuse galactic background noise. The analysis of the collected dataset enables us to verify beam forming and steering attempts. These results document the current status of the radar during its development and provide valuable information for further improvement.

2. Passive experiment observing cosmic radio noise

In earlier experiments (Renkwitz et al., 2012) we observed cosmic radio emissions with almost 80% of the MAARSY antenna array, named MAARSY343. The reason for this was the constraint of selectable antenna groups that may be connected to the receiver chain to generate a total radar beam by the coherent integration of the individual antenna groups. We used seven antenna groups, each composed of 49 antennas, resulting in 343 individual antennas in total. Nevertheless we were able to identify three distinct cosmic radio sources, Cassiopeia A, Cygnus A and Taurus A, and the signature of the Milky Way. For the analysis of beam pointing and categorizing the beam width we concentrated on the first two of these major radio sources that can be observed in lower VHF band on the northern hemisphere. Taurus A is generally out of the beam pointing cone of MAARSY as it is positioned at too low declination which results in about 48 degrees zenith angle. However, this radio source was also useful to verify the capability to steer our radar beam in this direction. Thus, under certain precautions MAARSY could even be used with such high off-zenith angles.

With these observations we focused on the angular and temporal power distribution originating from Supernova remnants, radio galaxies and the diffuse cosmic background radiation.

For this purpose we performed a scan between 0 and 34 degrees zenith angle and fixed 180 degrees azimuth. This experiment was scheduled with other experiments in sequence for a total observation time of few days.

Subsequently we compared our observations with the Global Sky noise temperature Maps by de Oliveira-Costa et al. (2008). This model is comprised of the eleven most accurate sky surveys and allows the generation of Quiet Day Curves for a specific frequency chosen by the user.

To adapt the native resolution of the GSM to our radar we convolved the GSM data with the radiation pattern. Furthermore we included the typical noise figure of the receiver front end and the losses in the coaxial cable to the antennas.

Finally, we found a very good agreement between the GSM data and our observations underlined by a correlation factor of 0.98. As the total received power is not only depending on the main beam, but on the total radiation pattern we were very confident that our current radiation pattern is very similar to what we have simulated afore. For more details of the experiment settings and analysis see Renkwitz et al (2012) and references therein.

To underline these findings, we planned to use the total antenna array for a campaign based cosmic radio noise observation. For this purpose we connected all groups of the antenna array on individual receiver channel. The simulated radiation pattern of the complete MAARSY antenna array with an overlay of the trajectory of Cassiopeia A is depicted in figure 1.

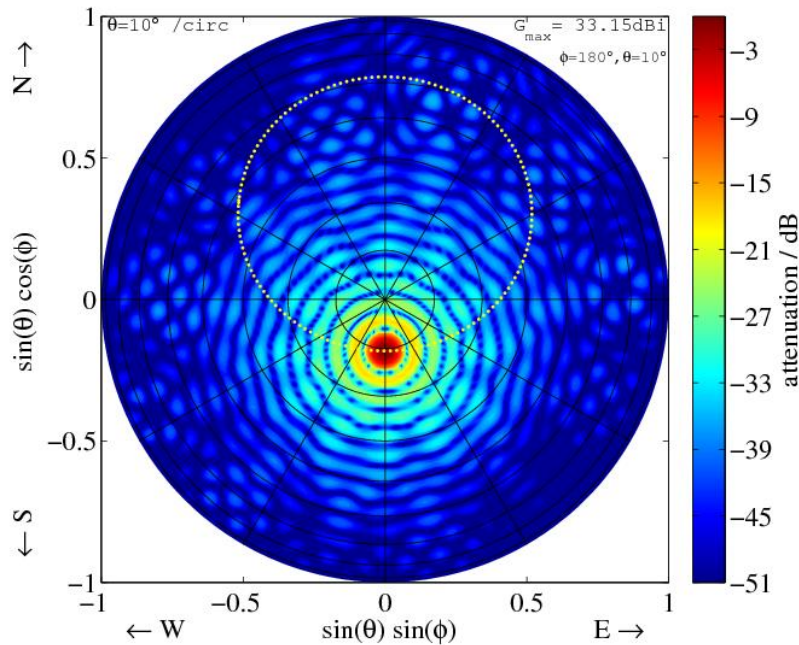


Figure 1: Radiation pattern of the complete MAARSY antenna array while pointing to the culmination of Cassiopeia A, presented in top view. The overlay of a yellow dotted circle corresponds to the trajectory of the radio source Cassiopeia A.

The objective of this experiment was to see a) more power from the distinct radio sources, b) decreased beam width and c) more dynamic range of the total input power over the full scan. In figure 2 we present the power distribution using 343 antennas (similar to the earlier experiments) in the upper panel and in the lower panel is shown the same scan, but with the total array of 433 antenna elements.

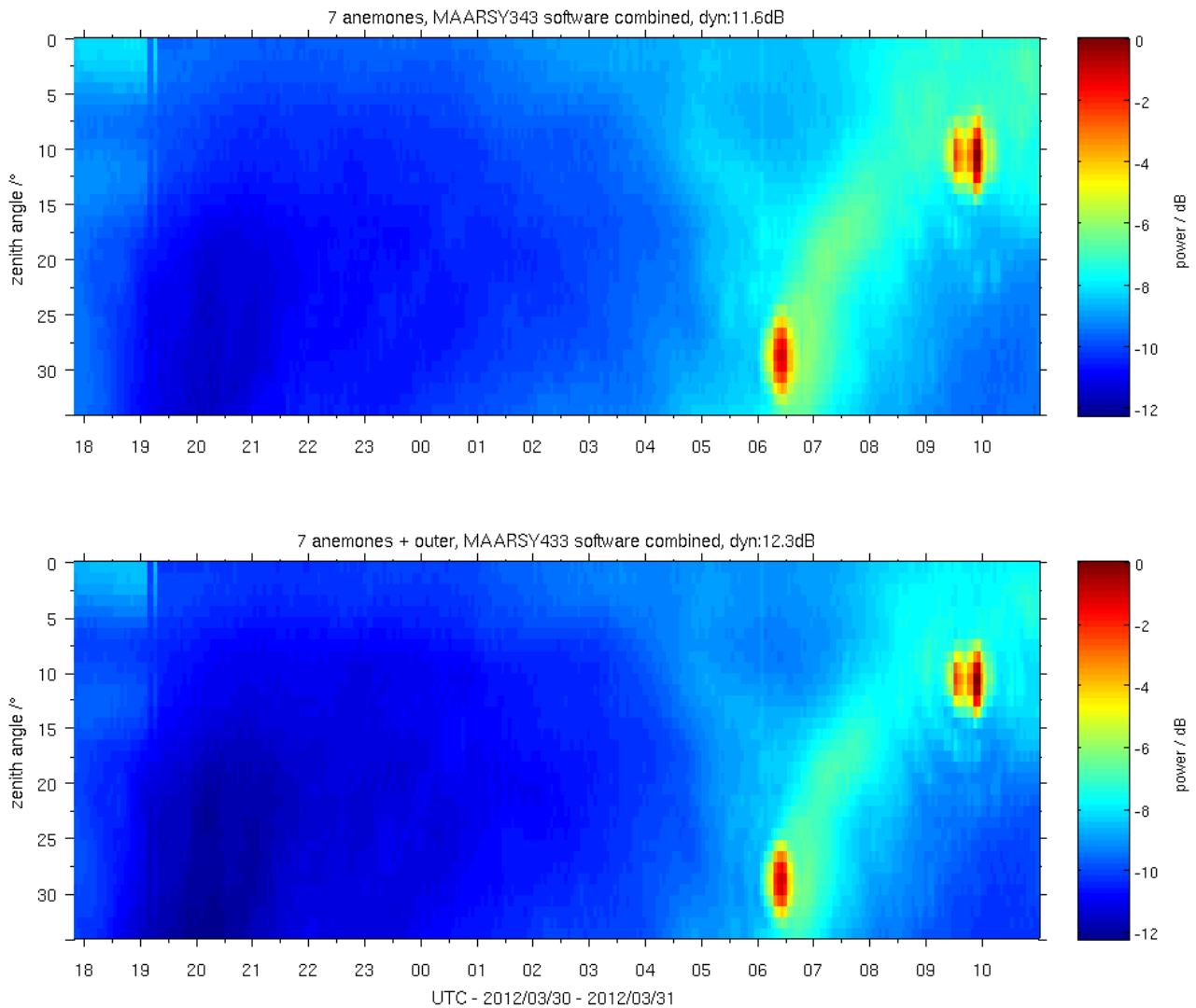


Figure 2: Distribution of incident noise power over time and zenith angle Θ for a scan within $\Phi=180^\circ$, $\Theta=0-34^\circ$. In the upper and lower panel are shown the received noise power using MAARSY343 and MAARSY433 respectively for the same observation time. The highlighted point-like radio sources are Cassiopeia A ($\Theta=10.5^\circ$) and Cygnus A ($\Theta=27.5^\circ$).

In figure 3 is shown the analysis of cross sections through the maximum incident power originating from Cassiopeia A. It can be seen that the beam width cannot be derived by simply analyzing the incident power as the total radiation pattern has to be considered. For this purpose we compare the cross section along the zenith angle of our observations with the GSM and find once again a good agreement. We actually cannot explain the secondary maximum at about 21 degrees zenith angle in the GSM, which is not prominent in our observations.

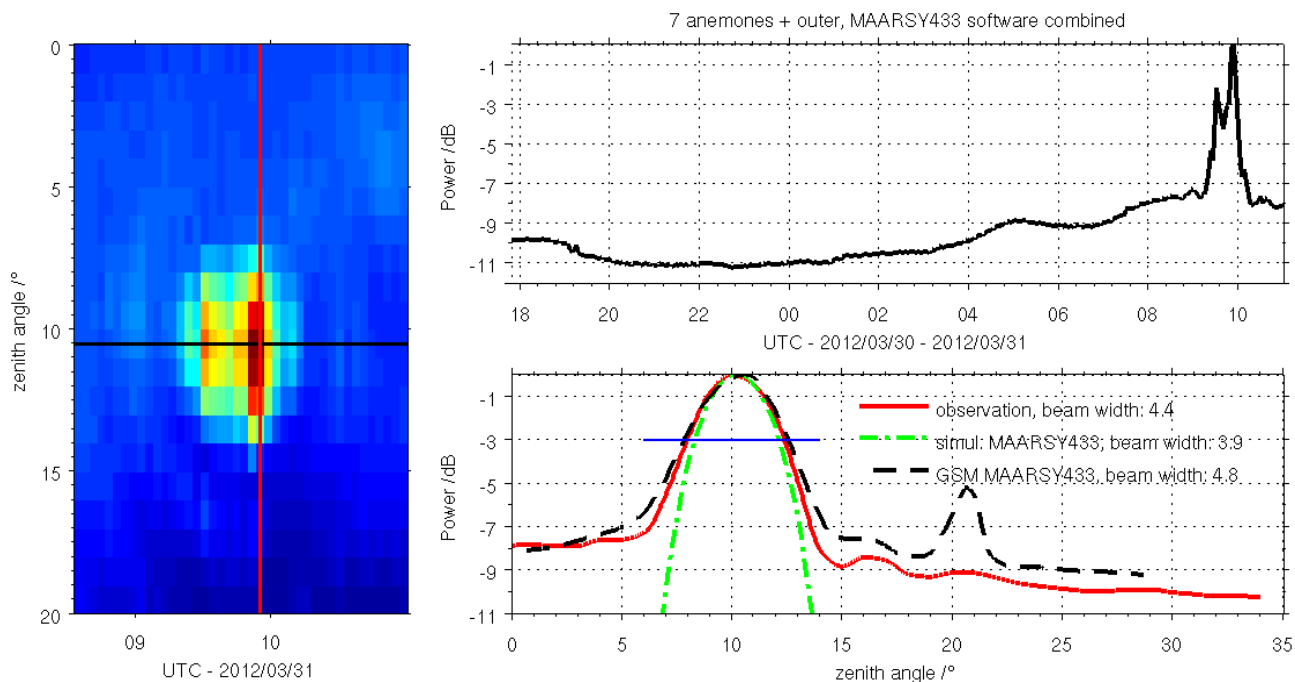


Figure 3: Analysis of cosmic noise observations to estimate the apparent time of passage of Cassiopeia A. The left panel depicts the detected intensities during the experiment, where the subsequent cross sections are used to determine the apparent time of passage and beam width, which are marked by lines in the corresponding colors. The upper right panel shows the time series for a fixed zenith angle where the maximum intensity of the radio source has been detected. The lower right panel presents the cross section in zenith angle through the radio source. The estimated apparent beam width during this experiment, the simulated beam pattern and the model data are marked in red, green and black, respectively.

Using the full antenna array we see a decreased apparent beam width (5.1° to 4.7°), an increase of power of the individual radio sources above the background and an increase of dynamic range of the cosmic radio noise in total (+0.7dB). Thus, we conclude that the radiation pattern using the full antenna array is superior to the MAARSY343 in terms of antenna gain, beam width and side lobe attenuation. These findings are naturally obvious from antenna array theory and modelling, but it is very profitable to underline this by observations. We finally are very confident about the shape and the positioning of the radar beam, to be less than one degree, using the complete MAARSY array on reception.

3. Active experiment as a first attempt to validate the two-way radiation pattern of MAARSY

The limitation of the earlier presented experiments is that they only provide information about the receiving system. The transmitting part of the radar needs to be investigated separately by other means.

For this purpose we prepared an experiment where we actively used the radar tracking the moon. During this experiment we used the full antenna array to transmit a 50 μ s long pulse and sampled between 250 and 350 km range, while for reception we used MAARSY343. Similarly to the prior presented cosmic noise experiments we performed a scan in zenithal direction in southern direction to see the passage of the moon. Unfortunately the moon doesn't reach above 45 degrees elevation in the polar region where MAARSY is located. We are aware about the generation of

grating lobes while pointing the radar beam at such zenith angle, however due to the range to the moon we are certain not to conflict with other targets. Inflicting targets like satellites may be rejected due to their apparent approach speed.

At the predicted time and zenith angle we finally found the signature of the moon, which is depicted in figure 4. Analyzing the slope of the moons echo, we derived an approach speed of approximately 205km/h, while the simulation showed 202km/h. We also found high variations in power of the moons echo, which may be related to fast Faraday rotation and absorption effects as at the time of this experiment the geomagnetic indices showed disturbances. Considering the beforehand limitations we could also estimate the beam pointing error within this experiment, which was found to be in the order of 1.5 degrees in azimuth and zenith. These findings are in agreement to the experiments observing the radio source Taurus A, which was observed at about the same zenith angle, see Renkwitz et al. (2012).

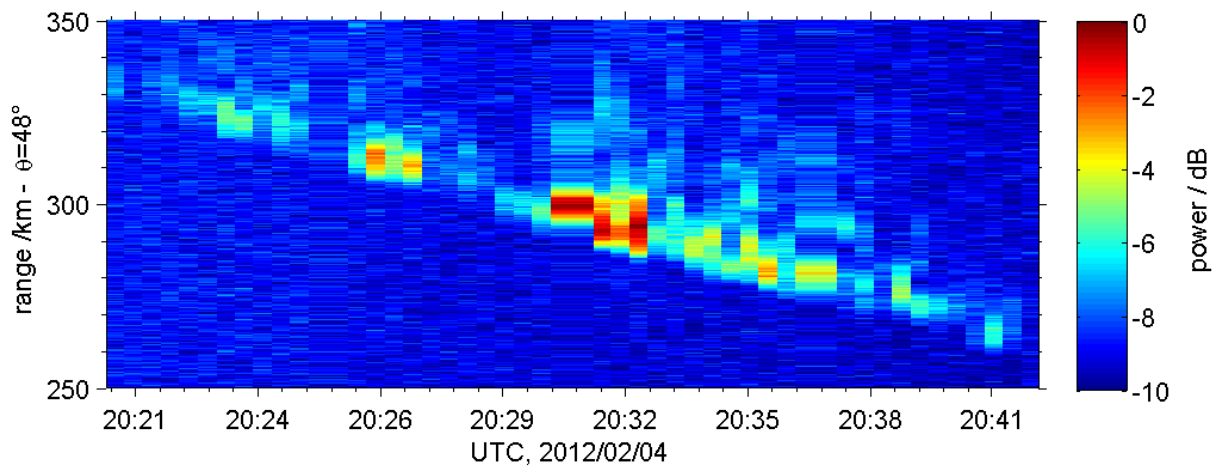


Figure 4: Range-time-intensity plot presenting the range varying echo generated for the passage of the moon for a fixed beam pointing of $\Phi=180^\circ$, $\Theta=48^\circ$.

The moon experiment could be improved by optimizing the experiments settings e.g. increasing the pulse length and pulse repetition frequency and limiting to a narrower range segment. Doing so, we should see an even stronger signature of the moon compared to the 8-10dB during this experiment.

With this active moon experiment we could verify the combined beam pointing for both, reception and transmission. As we estimated similar errors of beam pointing in the passive observation of a radio source and the active moon experiment we assume similar behavior of the radiation pattern for reception and transmission.

Nevertheless, until now we don't have any corroboration about the shape and the position of the side lobes during transmission. For this purpose we are planning an airborne electric field probe which shall be used to directly sample the radiation pattern in the far field region.

Bibliography

- de Oliveira-Costa, A., Tegmark, M., Gaensler, B. M., Jonas, J., Landecker, T. L., and Reich, P.: A Model of Diffuse Galactic Radio Emission from 10MHz to 100 GHz, *Mon. Not. R. Astron. Soc.*, 338, 247–260, doi:10.1111/j.1365-2966.2008.13376.x, 2008.
- Latteck, R., Singer, W., Rapp, M., Vandeppeer, B., Renkwitz, T., Zecha, M., and Stober, G.: MAARSY: The new MST radar on Andøya – System description and first results, *Radio Sci.*, 47, 1006–1024, doi:10.1029/2011RS004775, 2012.
- Renkwitz, T., Singer, W., Latteck, R., Stober, G., and Rapp, M.: Validation of the radiation pattern of the Middle Atmosphere Alomar Radar System (MAARSY), *Adv. Radio Sci.*, 10, 1–9, doi:10.5194/ars-10-1-2012, 2012

Observation of horizontal wind velocities in presence of convective system using multi receiver phased array MST radar system

VK Anandan¹, VN Sureshbabu¹, S. Vijayabhaskara Rao²

¹ ISTRAC, Indian Space Research Organisation, Bangalore -58, India (anandanvk@hotmail.com)

² Dept. of Physics, SV University, Tirupati, AP, India

Abstract

This paper demonstrates the potential of Postset Beam Steering (PBS) technique on VHF multi receiver profiler radar for studying convective processes within radar beam volume. Generally, it is difficult to study atmospheric processes by normal radar observational methods due to instantaneous changes in velocity field over the observation time. It is important to know vertical and horizontal wind velocities simultaneously to study the evolution of atmospheric processes and kinematics associated with it. PBS, as a means of software beam steering, sorts such difficulty to extract atmospheric wind parameters because of inherent signal processing works involved within the technique itself. Further, the advantages of PBS are revealed to monitor and study the fast changing wind fields, circulation patterns, structure, turbulence, and vortex during precipitate and convective processes. The study also helps for better understanding of atmospheric processes. The results obtained by PBS are much useful to investigate the impact of wind flow on atmospheric changes during atmospheric convection.

1. Introduction

The wind profilers operating in the low VHF range (~50 MHz) have proven as tools for studying the dynamics of the tropical atmosphere and tropical convection [1]. Several convective systems have been studied using VHF profilers by number of authors. Balsley et al. (1988) presented air motions in clear air and precipitation conditions at Pohnpei Island (7°N, 157°E) in the tropical western Pacific using a vertically pointing wind profiler. A recent study [3] reported drop size distribution and various precipitation events associated with typhoon passage. Further, a better understanding of wind dynamics by profilers during convective process is needed to investigate the relationship between convection and mixing processes, upper- air circulation patterns, wave generation and climate variability. This article is mainly concerned with the potential of PBS technique for extracting atmospheric parameters from Middle and Upper (MU) atmospheric radar data obtained during short convective period of about 30 minutes. In PBS, a phase shift is systematically introduced in the received signals from the corresponding array elements and then combined to produce the two-way beam pattern in the desired directions within the volume illuminated by transmit beam.

In the present study, PBS based wind estimation includes number of signal processing methods like beamforming; spectral estimation; adaptive moments estimation. In particular, we are reporting the accuracy of PBS wind estimates which mainly depends on the performance of spectral estimator, synthesized beam directions and adaptive moments estimation [2]. The systematic improvements and signal processing works done for PBS technique could be used to obtain radial wind velocities in many directions and thus wind measurement with high temporal resolution of about 26 seconds and height coverage of about 20 km. Such high temporal

estimations have revealed to be useful for studying the fast changing non-homogeneous wind fields during disturbed atmospheric condition such as convective and precipitate cases.

1. System description and data processing

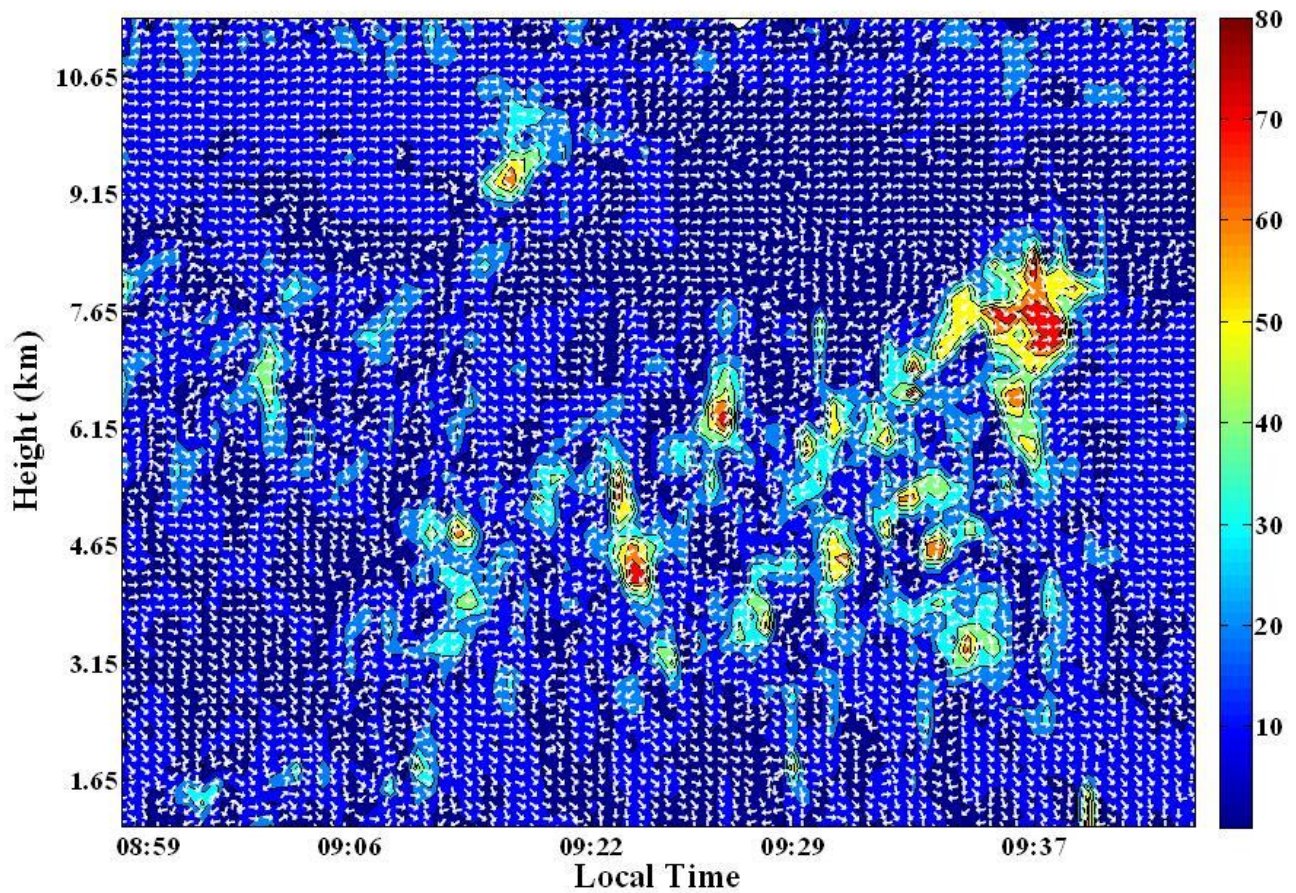
The system descriptions is given in the companion paper namely *“Extraction of horizontal wind velocities from a multi receiver phased array radar system using post beam steering technique and efficiency of various beamforming methods”*.

2. Profiler observations during convective processes

A. Evolution of 3-D wind structure measured by PBS during convective process

In general, profilers operating in DBS mode provide the atmospheric parameters along the beam directions. The wind dynamical parameters are obtained by measuring the radial wind components at 10° - 20° off-zenith direction with maximum of four azimuth planes i.e. north, east, south and west. For the large off-zenith angle usages, spatial separation is typically of the order of several hundred meters (lower altitude) to few kilo meters (higher altitude), transverse to vertically directed radar beam. In convective cases, the beam swinging nature of standard DBS technique precludes the evolution of individual convective regions, which pass directly through the radar beam. Further, profiler elapses the time (about a minute) in each direction for data collection so that instantaneous measurement of wind parameter simultaneously in other directions cannot be possible. Therefore, the average wind information provided by such type of techniques for profilers need not be completely reliable and precise to investigate the dynamics of winds and associated weather processes during atmospheric convection. Conversely, the possibility of instantaneous wind parameters simultaneously in the desired directions by PBS has been reported [4] and so the evolution of wind structure components can be understood in better sense compared to other classical observational methods. Of course, PBS permits atmospheric parameter extraction only within the vicinity of illuminated beam volume. For instance, figure-1 shows the 3-D wind vectors derived by PBS in presence of convective rain fall. The wind estimation is made with 16 equally spaced synthesized beams at 1.7° tilt angle, which is optimum tilt angle for 3.6° beam width usage [4]. The rain echoes in various synthesized beam directions have been separated in spectral domain during the moments computation [2].

In the figure-1, the fluctuations in horizontal winds over the time are due to the irregular and differential rotations of air column (in the height regions 2-9 km) caused by atmospheric waves generated by convective processes. However, the characteristics of associated waves are not discussed in this paper. The existence of arbitrary wind circulation (irregular and differential rotations of air column) observed in horizontal winds over profiler site and the time is shown in figure-1. The figure-1 shows the sign and magnitude changes in horizontal winds (altitude of 2-9 km) over the time. Further, the air column rotation (horizontal) can be understood by comparatively noticing directional changes in horizontal winds in figure-1. It has been also observed the enhancement in vertical lift with strength of horizontal rotation (figure not shown). In figure-1, the high winds are attributed with strong pressure gradient established during the process. The high winds noticed in high altitude regions are attributed due to waves generated by convective and mixing processes. The mixing process is ensured with horizontal wind circulation as well as vertical up and down motion (figure not shown).



The vertical profiles of wind speed and direction over the time observed by PBS. The wind field inside the closed contour exhibits arbitrary circulations (during convection) in various height regions over the time within the volume of profiler beam. The observations correspond to the radar data on Jul 18, 2008. In the figure, wind speed is represented in term of colour values and direction with single headed arrow.

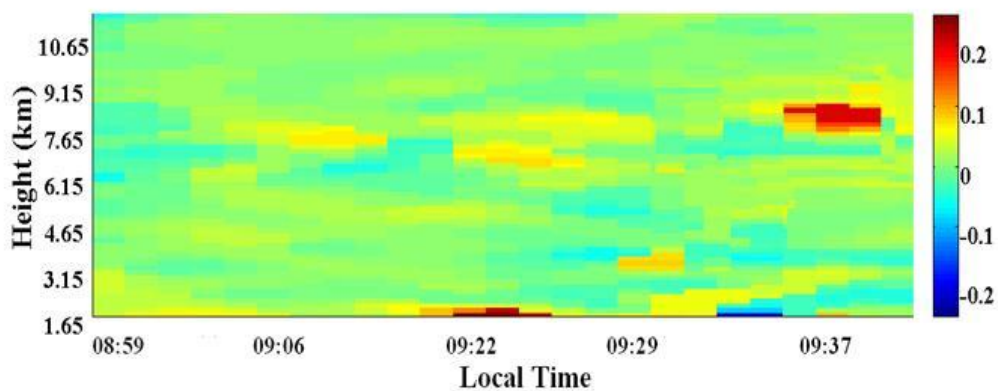


Figure shows the contour colour map of vertical profiles of relative vorticity derived from horizontal wind fields by PBS with 4 equally separated synthesized beams. The figure shows the relative vorticity of wind can be related with vertical lift and horizontal circulations in wind during convective processes. The observations correspond to the radar data on Jul 18, 2008.

B. Evolution of arbitrary wind circulation pattern deduced by PBS during convective processes

In the present study, the horizontal extent for 1.7° tilted beam is about 55 m to 1.05 km for lower and higher altitude regions respectively. The relative vorticity have been obtained using 4 equally separated azimuth beam positions. For example, the zonal velocities are obtained individually from east and west beams and meridional velocities from north and south beams. The relative vorticity is derived range bin wise and shown in figure-2.

In figure-2, the values of relative vorticity are arbitrary and very high. This is due to the fact that the horizontal extent considered for wind estimation at small tilt angle is very small. However, these arbitrary values can infer or monitor the useful information about the magnitude of wind flow and arbitrary circulations during convective process. In the case of clear air condition, the relative vorticity was of the order of about 10^{-2} - 10^{-3} s^{-1} . It is observed that the magnitude of relative vorticity more than 0.1 s^{-1} is associated with appreciable vertical lift (figure not shown) and horizontal circulation (orientation of arrows over the time in a range bin, i.e. figure-1). The relative vorticity more than 0.2 s^{-1} is associated with strong vertical lift and arbitrary circulations. Also, in the case of profiler observations, the high magnitude of relative vorticity more than 0.2 s^{-1} during convection could be related with rain fall intensity. This has been analyzed and realized with the data obtained in different date and time as given in table-1.

Observation	Horizontal wind velocity components		Vorticity value (s^{-1})
	Zonal (ms^{-1})	Meridional (ms^{-1})	
Jul 18, 2008 07:02-07:46 LT	~ (-45 to -40)	~ (-40 to +35)	~ (-0.12 to +0.09)
Jul 17, 2008 20:03-20:57 LT	~ (-63 to +45)	~ (-55 to +50)	~ (-0.32 to +0.17)

Table 1: The relative vorticity derived from horizontal wind fields (between the altitudes 1.05-10.5 km) by PBS with 4 equally separated synthesized beams at 1.7° tilt angle.

Thus, such a study on the evolution of vorticity can be useful to study the wind flow and associated weather processes (within radar illuminated volume) in convective processes. Besides, the potential of PBS for studying atmospheric winds can be still better for wide radar beam width usage.

2. Conclusion

PBS wind estimation technique, improved by various signal processing methods for high temporal (26 seconds) and maximum height coverage (~ 20 km), is used to monitor and study the evolution and impact of 3-D winds in convective processes. In this paper, the characteristics of fast changing 3-D wind fields over short time are examined during convective and precipitate processes with set of examples. The study has verified the existence of convective cores and their associated motion in connection with vertical wind updraft and down draft. Also, the relative vorticity (as arbitrary values) of wind field within radar beam volume has been investigated and the values are high (in the case of wind circulation triggered during convection) compared to that in clear air conditions. Besides, the study strongly suggests that potential of PBS technique can be used to monitor the wind flow in various atmospheric disturbed conditions. The study recommends that the applicability of PBS on profiler data can be a better way to verify various insights already reported in the field of fluid dynamics and to study the evolution of atmospheric wind patterns and the characteristics (and propagation) of atmospheric waves generated during convective processes.

References

- [1] Balsley, B. B., W. L. Ecklund, D. A. Carter, A. C. Riddle, and K. S. Gage, 1988: Average vertical motions in the tropical atmosphere observed by a radar wind profiler on Pohnpei (7°N latitude, 157°E longitude). *J. Atmos. Sci.*, *45*, 396-405.
- [2] Anandan, V. K., P. Balamuralidhar, P. B. Rao, A. R. Jain, C. J. Pan, 2005: An adaptive moments estimation technique applied to MST radar echoes. *J. Atmos. Oceanic Technol.*, *22*, 396–408.
- [3] Anandan V.K., C.J. Pan, K. Krishna Reddy, T. Narayana Rao, S.VijayaBhaskara Rao, 2010: Observation of precipitation and drop-size distribution associated with a typhoon using VHF Radar. *The Open Atmospheric Science Journal*, *4*, 114-125.
- [4] Sureshababu, V.N., V.K.Anandan, T. Tsuda, J.Furumoto, S.Vijayabhaskara Rao, 2012: Performance Analysis of Optimum Tilt Angle and Beam Configuration to Derive Horizontal Wind Velocities by Postset Beam Steering Technique. *IEEE Trans. Geo Sci and Remote sensing*, (May 2012, in-press).

Detecting low earth orbit (LEO) satellites using UK-based atmospheric radars

Jon D. Eastment^{1,2,3}, David A. Hooper^{1,3}, Darcy N. Ladd^{1,2}, and Chris J. Walden^{1,2}

¹ STFC Rutherford Appleton Laboratory, UK

² Chilbolton Facility for Atmospheric and Radio Research, UK

³ NERC MST Radar Facility at Aberystwyth, UK

1. Introduction

A dedicated space surveillance radar network already exists for the purpose of tracking objects in the near-Earth space environment. This is motivated by a number of factors, including the potential for hazardous collisions between operational spacecraft (including satellites) and orbital debris or other spacecraft. There is an ever-increasing number of objects which must be tracked. Consequently, there is considerable interest in how radars that are primarily used for other purposes might contribute to the network. This extended abstract will examine the suitability of two UK-based atmospheric radars for this purpose: the Chilbolton Advanced Meteorological Radar (CAMRa) [Goddard *et al.*, 1994] and the Natural Environment Research Council (NERC) MST Radar at Aberystwyth.

2. The Chilbolton Advanced Meteorological Radar (CAMRa)

CAMRa is a 700 kW peak power, 3 GHz radar system that has been used predominantly for atmospheric research [Goddard *et al.*, 1994]. It has a fully-steerable, azimuth-elevation mount, 25 metre diameter, parabolic dish. This gives it a one-way half-power full-width of 0.28° . The dish can slew at up to 3° s^{-1} in azimuth and 1° s^{-1} in elevation. This allows the radar to continuously track LEO objects, based on their known orbits, as they move across the sky. The dish is typically programmed to begin tracking when the target is 1.0° below the horizon. However, the data acquisition system does not start to record until the target is a few degrees above the horizon. This allows the target to come within the maximum unambiguous range of 2100 km, which is determined by the inter-pulse period of 14 ms. It also reduces the distorting effects of atmospheric refraction for signal paths at very low elevation angles. The receiver signal is sampled at 75 m range gate intervals.

During a recent observational campaign, which was funded by the European Space Agency (ESA), the radar successfully tracked over 40 satellites in LEOs [Eastment *et al.*, 2011]. This was conducted during November/December 2010, April 2011, and May 2011. The missions of these satellites included: communications (IRIDIUM), weather observation (METOP-A, FENGYUN- 3A, FENGYUN-3B), remote-sensing (ADEOS, AQUA, TERRA), Earth-observation (ENVISAT, RADARSAT-1, SPOT-5), and military/intelligence (COSMOS 1346, COSMOS 1782, GEO-1K- 2).

The ease with which a target can be detected is quantified by its radar cross section (RCS). This is the cross-sectional area of a perfectly-reflecting sphere that would give the same radar return signal strength. This does not necessarily bear a direct relationship to the target's physical cross-section. Moreover, for a given target, the RCS can vary as a function of time owing to glints as the aspect angle changes with respect to the radar. CAMRa has been able to detect objects with RCSs as low as 2 m^2 (+3 dBsm) - e.g. CRYOSAT-2, shown in Figure 1 - at ranges of up to 1000 km. The International Space Station (ISS), by contrast, has one of the largest RCSs at 312 m^2 . This

allowed it to be tracked out to the maximum unambiguous range of 2100 km. This also makes it a good test target for the MST Radar - see next section.

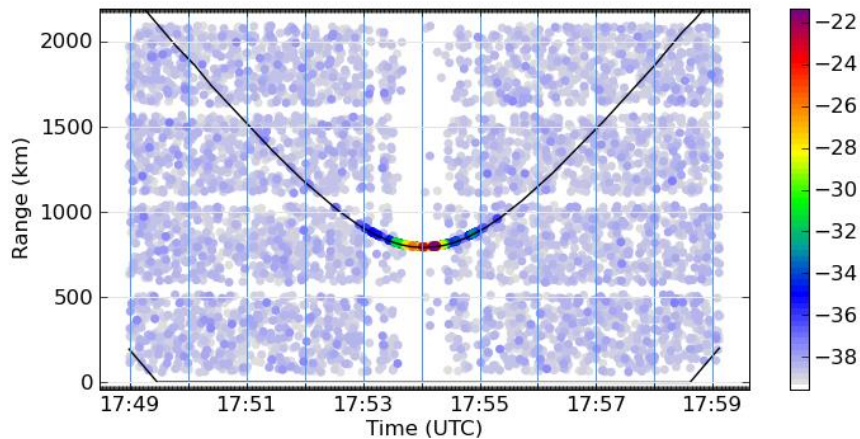


Figure 1: CAMRa signal power (dB), as functions of range and time (UT) on 1st December 2010, whilst tracking CRYOSAT-2.

CAMRa can be used to do more than simply detecting an LEO object. It also has the potential to reveal whether or not an object is tumbling. Reports within the aerospace community indicated that the geodesy satellite GEO-IK-2, which was launched on 1st February 2011, had failed to reach its planned orbit. This was a result of the failure of its final stage rocket to ignite. Moreover, the satellite’s orientation systems malfunctioned on 1st March 2011, which led to it moving out of alignment with the Sun. Owing to the subsequent loss of solar power, the satellite began to tumble. The spectrogram of CAMRa’s co-polar receiver signals in Figure 2 shows evidence of this. The prominent peaks are at frequencies of 0.47 Hz/28.2 revolutions per minute (RPM) and of 0.24 Hz/14.1 RPM. This suggests that the satellite was tumbling at a rate of 14.1 RPM or a sub-multiple of this.

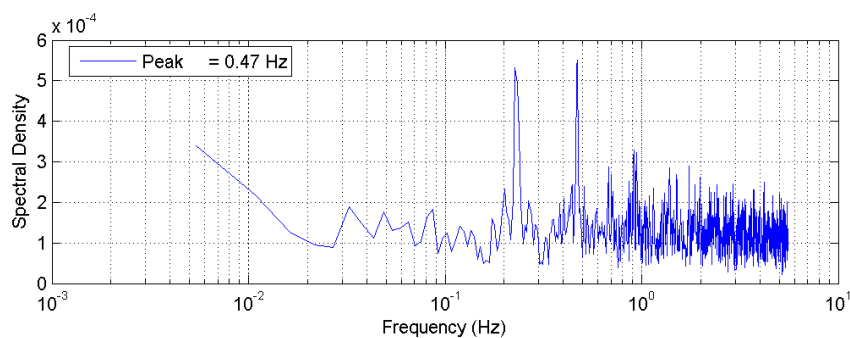


Figure 2: Spectrogram of CAMRa’s co-polar receiver signal for observations made of GEO-IK-2 on 13th April 2011.

3. The NERC MST Radar at Aberystwyth

Although most of the radars used to detect LEO objects operate at UHF and above, the MU Radar in Japan has been used to demonstrate the potential of lower-VHF MST radars [e.g. *Sato et al.*, 1991; *Sato et al.*, 1992]. Initial studies used fixed beam pointing directions, a 7-bit Barker code with 64 μ s sub-pulses, and coherent integration over 25 pulses. The latter corresponded to approximately 1 s.

Owing to the fact that the NERC MST radar still relies on a hardware-based radar control and data acquisition unit, it will not initially be possible to make LEO observations using an optimal

configuration. Moreover, it will be necessary to modify the data acquisition software, to allow it to store the in-phase (I) and quadrature (Q) receiver samples, before a test observation can even be made. At present the I&Q samples are discarded after they have been used to derive the Doppler spectra. Nevertheless, this section demonstrates the steps required for selecting a suitable test target. Attention is focused on a particular orbit of the International Space Station (ISS), which passed over the British Isles at around 10:31 UT on 14th March 2012.

The NERC MST radar is considerably less flexible than both the MU radar and CAMRa in terms of its beam pointing capabilities. There are currently 17 available directions, which cover 5 zenith angles (0.0°, 4.2°, 6.0°, 8.5°, and 12.0°) and 8 azimuth angles (nominally N, NE, E, SE, S, SW, W, and NW, although the actual angles are 17.5° lower than the nominal ones). In fact, the new beam steering components installed during March 2011 allow up to 255 beam pointing directions to be defined - see *“Renovation of the Aberystwyth MST radar: Evaluation”* in these proceedings. Nevertheless, initial tests will concentrate on using existing beam pointing directions, which have proven reliability. Consequently, appropriate test objects must pass within approximately 12.0° of the zenith at the radar site (52.42°N, -4.01°E).

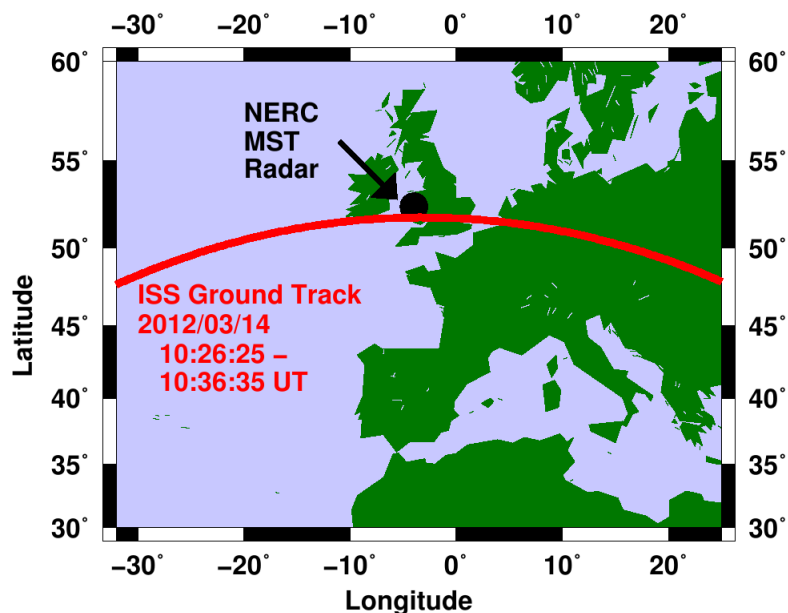


Figure 3: Ground track of the ISS for a particular orbit on 14th March 2012.

The inclination of the ISS’s orbit is 51.6°. On 14th March 2012, the altitude was 378 km at perigee, 402 km at apogee, and 391 km when it passed to the south of the MST radar site around 10:31 UT - see Figure 3. Figure 4 shows the projection of the 17 available beam pointing directions at this altitude to ground level. It can be seen that the ISS passed almost through the centre of the SW12.0 beam, i.e. the one directed 12.0° off-vertical along an azimuth angle of 207.5°.

The hardware-based radar control and data acquisition unit imposes a number of limitations on making LEO observations. Firstly, the maximum available inter-pulse period is 640 μs, which corresponds to a maximum unambiguous range of 96 km. Any reflections from the ISS for the demonstration orbit, i.e. at a slant-range of 400 km, would have been range aliased 4 times over before being detected at an apparent altitude of 16 km. This means that they would have had to compete with atmospheric returns from the lower stratosphere.

The second limitation is that the in-phase and quadrature receiver samples are coherently integrated over a minimum of 81.92 ms. This should not be a problem in terms of isolating the

signal in the time domain. The orbital speed of the ISS is approximately 28,000 km hour⁻¹. The transit time through the radar beam would have been almost 2 s, corresponding to approximately 20 samples. However, the radial component of the velocity would have been in excess of 700 m s⁻¹. The 81.92 ms interval between consecutive samples results in a Nyquist Doppler velocity of just under 20 m s⁻¹. Consequently, the Doppler shift of the signal would have been aliased many times over and of no practical use.

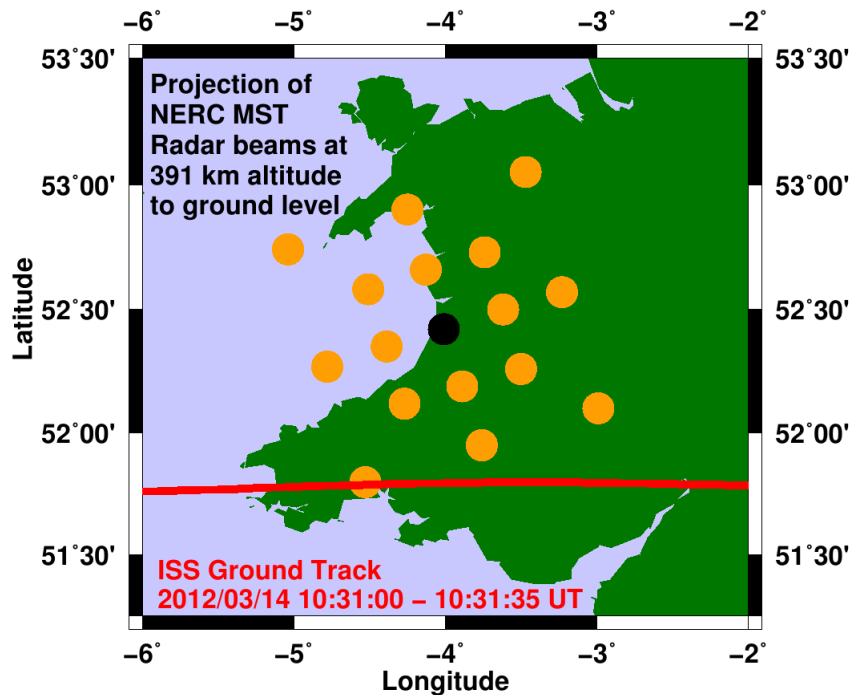


Figure 4: The ground track of the ISS passing almost through the centre of the SW12.0 beam for a particular orbit on 14th March 2012. The size of the dots corresponds to the two-way half-power full-width of the beams (2.1°). The black dot represents the vertical beam.

At the time of writing this abstract (October 2012), the altitude of the ISS's orbit has been boosted by more than 20 km. This means that the exact details shown in this abstract are no longer applicable. The most significant effect will be that if an orbit passes through the SW12.0 beam, it will be range aliased to an apparent altitude of approximately 35 km. This puts it in the range between 21 and 56 km which cannot be sampled by the current hardware-based radar control and data acquisition unit. Consequently a new search for a potential target will have to be made as soon as the software has been modified to allow time series data to be recorded.

References

- Goddard, J., J. Eastment, and M. Thurai, The Chilbolton Advanced Meteorological Radar - a tool for multidisciplinary atmospheric research, *Electron. Commun. Eng. J.*, 6(2), 77–86, doi: 10.1049/ecej:19940205, 1994.
- Sato, T., K.-I. Ikeda, T. Wakayama, and I. Kimura, MU radar observations of space debris, in *ESA Special Publication*, vol. 341, edited by P. M. Bainum, G. L. May, M. Nagatomo, Y. Ohkami, and J. Yang, pp. 273–282, 1992.
- Sato, T., H. Kayama, A. Furusawa, and I. Kimura, MU radar measurements of orbital debris, *J. Spacecr. Rockets*, 28(6), 677–682, doi:10.2514/3.26299, 1991.

Rain Kinetic Energy Measurement with a UHF Wind Profiler: Application to Soil Erosion Survey of a Volcanic Tropical Island

B. Campistron¹ and A. Réchou²

¹ Observatoire Midi Pyrénées, Toulouse University, France.

² Laboratoire de l'Atmosphère et des Cyclones, La Réunion University, France.

1. Introduction

Land degradation by rainfall is strongly dependent on the kinetic energy of raindrops impacting the soil. The approach presented here for the investigation of soil erosion is done with UHF wind profiler data. Based on radar observables and realistic assumptions, we derive the retrieval equations of the rain intensity and of the rain vertical and horizontal kinetic energy flux which are ones of the most pertinent parameters of rainfall erosivity.

The use of radar for obtaining vertical profiles of erosion parameters has a real practical interest when the instrument is at the foot of a nearby mountain as in the case discussed here. This study is based on observations collected by a UHF wind profiler located at La Reunion Island in the Indian Ocean (Fig. 1). This volcanic island, which culminates at an altitude of 3000 m, has a regime of tropical precipitations enhanced by orography. Since its installation in April 2009 the profiler is operated in a continuous survey mode and among other provides measurement of rain rate and rainfall kinetic energy from 400 m above sea level up to the top of the island.



Figure 1: The UHF wind profiler is located at Saint-Denis Airport of La Réunion Island (20°53'33" S, 55°31'44" E).

2. Presentation of the UHF wind profiler

The UHF profiler is a Degréane Horizon PCL1300 working with a 1290 MHz transmitted frequency, a 3.5 kW peak-power and five beams with a 8.5° aperture comprising a vertical beam and 4 oblique ones with a 17° zenithal elevation disposed every 90° in azimuth. It provides during a repetitive cycle of 4 minutes, in clear air and raining conditions, vertical profiles of the reflectivity, the three components of the wind, the Doppler spectral width and skewness.

The cycle is composed of a low and high mode data collection. For the low mode, the data of which are used here, the pulse length, lower gate height, inter-gate range and the vertical coverage are of 300 m, 400 m, 72 m, 5.6 km, respectively. The selection of the relevant peak in the Doppler spectra is made with a 15-minute duration consensus technique based on median filter, thresholds, and vertical and time continuity tests. A particular attention is taken to the detection and correction of bimodal peaks resulting for instance from the concatenation of atmospheric and ground clutter echoes.

3. Methodology

The methodology uses the set of equations presented below. First we assume that on the average the drop size distribution $N(D)$, where D is the diameter, follows a gamma function (Eq. 1) (Ulbrich, JCAM, 1983). Eqs. (2) and (3) give the drop fall speed in still air taking into account the change of density with height (Atlas et al., RGSP, 1973; Foote and du Toit, JAM, 1969). The quadratic form (4) relating μ to Λ permits to reduce Eq. (1) to a two-parameter problem (Chu and Su, JAMC, 2008). The mean vertical velocity $\langle W_f \rangle$ and reflectivity factor $\langle Z \rangle$ are measured by the profiler at the resolution of the pulse volume. Eqs. (5) and (6) give their expression deduced from Eqs. (1) and (2) after integration over the diameter interval supposed to extend from 0 to infinity. With the same procedure the expression of the precipitation rate R is obtained (Eq. 7).

The rain kinetic energy flux crossing an horizontal surface of unit area during a unit time is decomposed here into a vertical kinetic energy flux VKEF function of drop vertical velocity W_f (Eq. 9), and an horizontal kinetic energy flux HKEF related to the drop entrainment by the wind velocity V (Eq. 8). Introducing expression (4) of Λ in Eq. (5) allows us to derive the value of μ from $\langle W_f \rangle$. With this value and Eq. (4) Λ is obtained, and consequently N_0 from Eq. (6) using $\langle Z \rangle$. Then we have all the material to get the value of R , HKEF and VKEF from their respective retrieval equations (7, 8, 9). **In order to obtain rain integrated parameters it is assumed that air vertical velocity is negligible in front of the drop fallspeed.** There is no easy means to insure with only profiler information that this assumption is fulfilled. This weakness of the methodology is partly compensated by a spectral average made here over 3 radar cycles (15 min). On an other hand, only signal with vertical velocity smaller than -2 ms^{-1} and larger than -9 ms^{-1} , reflectivity larger than 5 dBZ, and normalized skewness smaller than -0.1 are considered as rain echoes and retained. The threshold on skewness is very efficient to discard snow echoes. In the equations below ρ and ρ_w are the air and water density respectively at a considered level. ρ_0 is the value of ρ at the ground. Γ is the gamma function. Mksa units are used.

$$N(D) = N_0 D^\mu e^{-\Lambda D} \quad (1) \quad ; \quad W_f(D) = \alpha_1 - \alpha_2 e^{-\alpha_3 D} \quad (2)$$

$$\alpha_1 = 9.65 (\rho_0 / \rho)^{0.4} \quad \alpha_2 = 10.3 (\rho_0 / \rho)^{0.4} \quad \alpha_3 = 600 \quad (3)$$

$$\Lambda = 50.0 \mu^2 + 1200.0 \mu + 3390.0 \quad (4) \quad ; \quad \langle W_f \rangle = \alpha_1 - \alpha_2 (1 + \alpha_3 / \Lambda)^{-(\mu+7)} \quad (5)$$

$$\langle Z \rangle = N_0 \Gamma(\mu + 7) \Lambda^{-(\mu+7)} \quad (6) \quad ; \quad R = N_0 \Gamma(\mu + 4) \pi 6^{-1} (\alpha_1 \Lambda^{-(\mu+4)} - \alpha_2 (\Lambda + \alpha_3)^{-(\mu+4)}) \quad (7)$$

$$\text{HKEF} = \rho_w V^2 R / 2 \quad (8)$$

$$\begin{aligned} \text{VKEF} = & \rho_w N_0 \Gamma(\mu + 4) \pi 12^{-1} [\alpha_1^3 \Lambda^{-(\mu+4)} - \alpha_2^3 (\Lambda + 3 \alpha_3)^{-(\mu+4)} \\ & + 3 \alpha_1 \alpha_2^2 (\Lambda + 2 \alpha_3)^{-(\mu+4)} - 3 \alpha_2 \alpha_1^2 (\Lambda + \alpha_3)^{-(\mu+4)}] \quad (9) \end{aligned}$$

4. Application to a case study

The retrieval technique is applied in what follows to a long lasting (16 hours) precipitation event. Figure 2 presents time-height sections of the observations made by the UHF profiler. Rain echoes correspond to strong reflectivity and spectral width values, and strong negative vertical velocities. Easterly to south-easterly Trades wind prevail at all levels with relative strong intensity in the lower atmosphere. Note that the relative humidity up to 4 km remains larger than 80 % and the 0° C isotherm is above 4.6 km. This radar observation in March is made during the humid season where the strongest precipitations and wind disturbances are observed usually.

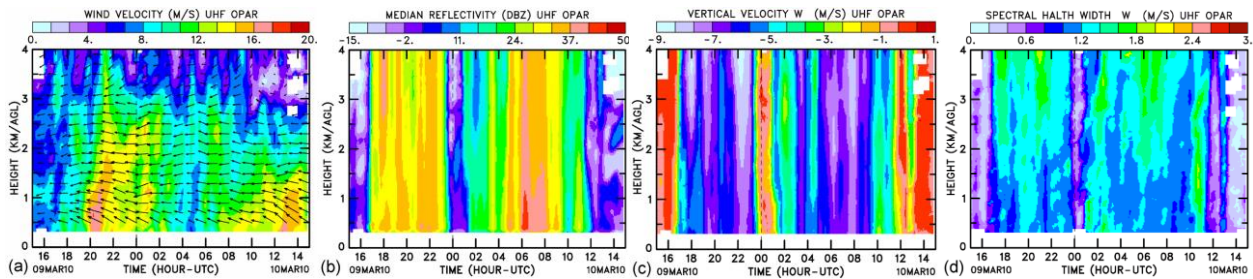


Figure 2: Time-height sections of, (a) wind velocity (V), (b) reflectivity factor (Z), (c) vertical velocity (W) deduced from the 5 beams, and (d) the spectral half width measured by the vertical beam and corrected for beam broadening effect. A 30-minute average is used.

4.1 Rain rate measurement assessment

Radar calibration is the most important step in the data processing. The calibration is based on the comparison between rain rate measured by the profiler and raingauge. The height of the radar data is taken as low as possible considering signal saturation, receiver linearity, and ground clutter. The best level was found around 600 m. A long lasting stratiform precipitations period to avoid the presence of strong vertical air velocities and with high relative humidity to minimize rain modification during its fall was chosen. The radar constant was modified until the best agreement was found between raingauge and radar measurements.

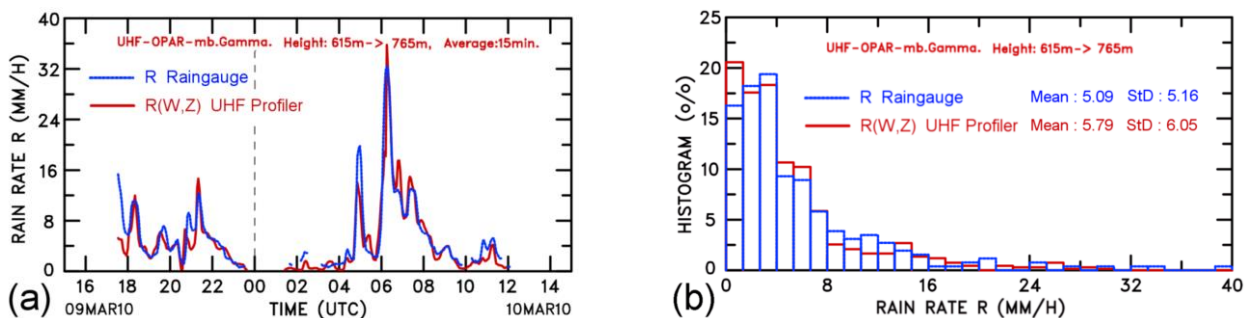


Figure 3: (a): Time series of the rain rate deduced from the UHF profiler data during the considered period between 615 m and 765 m superposed to the rain rate given by a raingauge at sea level. (b): the same data but presented in an histogram.

Figure 3 shows an example of comparison between radar and raingauge during the case under study. The precipitation event comprises stratiform and convective rainfall reaching 40 mmh^{-1} . The time series and histogram of the comparison show a good correspondence between both instruments. The profiler gives an under estimation on rain rate about 10 %. The radar time

series has 15% less data than the rain gauge time series. This loss of radar data might be explained by the effect of the rejection tests on echoes associated with substantial air vertical velocity.

4.2 Characterization of the rain

Figure 4 displays time-height sections of four parameters of the rain deduced from the profilers data which are the rain rate (a) and the three parameters describing the shape of the drop size distribution (DSD) that is to say N_0 (b), μ (c), and Λ (d). At a first glance one can notice that roughly strong rain intensity are associated to low N_0 , μ , and Λ values and that these gamma DSD parameters are well correlated between them.

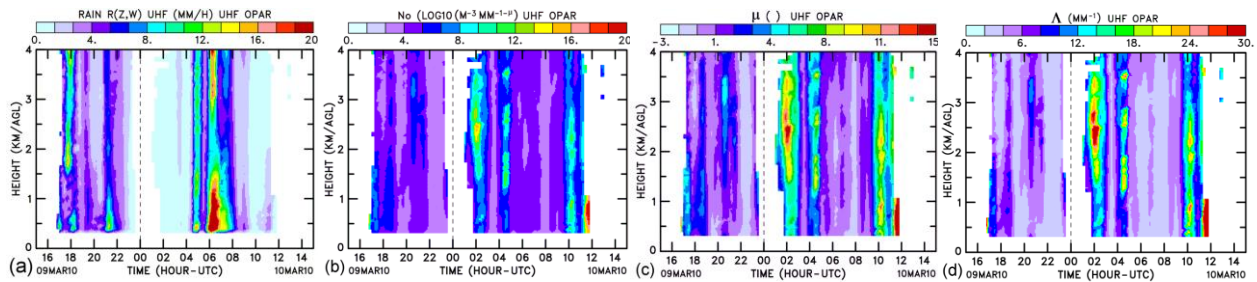


Figure 4: Time-height sections of the precipitation rate and the three shape parameters of the rain drop size distribution deduced from profiler data. An average over 30 minutes is applied.

As explained previously the methodology makes use of an empirical quadratic μ - Λ relationship. Eq. (4) is one of the equations listed by Chu and Su (JAMC, 2008) but in which the coefficients were slightly modified in order that the resulting fit between N_0 and μ follows as close as possible the exponential law $N_0=67340 \exp(3.75\mu)$ found by Ulbrich and Atlas (JAM, 1998). The least square fit in Fig. 5b between these two parameters shows that this requirement is achieved. In fact the strong correlation between μ and N_0 arises, according to Chandrasekhar and Bringi (JAOT, 1987), because N_0 involves units that depend on μ . The histogram of the values of the parameter μ presented in Fig. 5a, strongly peaked around zero with negative values and a mean value of 2, is also close to those given by Ulbrich and Atlas.

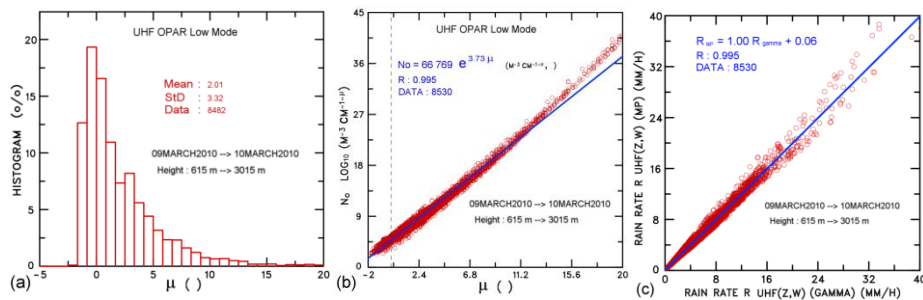


Figure 5: Plot of data used in the study : (a) μ histogram, (b) linear fit between μ and N_0 , (c) linear fit between rain rate computed with a Gamma DSD and rain rate computed with an exponential DSD ($\mu=0$, MP).

Figure 5c presents a plot of the rain rate deduced from the actual gamma methodology versus the rain rate obtained using an exponential distribution ($\mu=0$, Marshall-Palmer law). The least square fit of the data show a perfect agreement between both estimates with a strong correlation coefficient. The same result (not shown) is also obtained for the horizontal or vertical rain kinetic energy flux HKEF and VKEF. Indeed there is a certain data scattering around the fit, but we can suggest that an exponential drop size distribution is appropriate and accurate enough when the goal is to obtain rain integrated quantities from radar data. It is simpler to use than the gamma distribution since it does not involve in particular the selection of a quadratic form between μ and Λ . This conclusion was also reached by Smith (JAM, 2003).

5. Conclusion with rain kinetic energy flux results

The panel displayed in Fig. 6 illustrates some results on the retrieval by the profiler of parameters related to soil erosion. The mean vertical profile of VKEF and HKEF in (b), the rain vertical and horizontal kinetic energy flux respectively, synthesizes the vertical variation of these parameters presented in the time-height sections (a) and (c). Compared to HKEF, VKEF shows on the average a weak evolution with height which can be related to the vertical constancy of the rain characteristics. HKEF decreases rapidly with height following the decrease of wind that we can notice in Fig. 2. For this event the contribution on the erosion process by the rain vertical kinetic energy flux can be considered negligible in front of the horizontal one up to a height of 2 km.

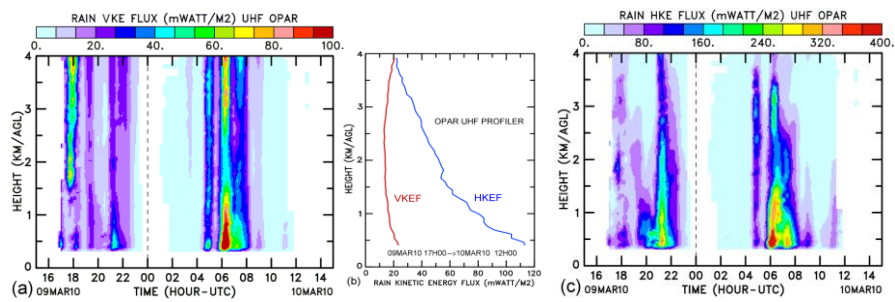


Figure 6: Time-height sections of rain vertical (a) and horizontal (c) kinetic energy flux (VKEF and HKEF); mean vertical profiles of VKEF and HKEF in the same period (b).

The aim of this presentation was to show the potentiality offered by wind profiler radar located at the foot of a mountain to study soil erosion process. The analysis of a case study has shown promising results. The next step of the work is an assessment of the methodology using in situ measurements.

Acknowledgements

We thank H el ene Ferr e and Yann Courcoux for radar data collection and management, and M eteo-France of La R eunion for providing rain time series.

Session 2

HCOPAR: Hainan VHF Coherent Scatter Phased Array Radar - System Description and First Results

Jingye Yan¹, Jürgen Röttger², Sheping Shang¹, Jiankui Shi¹,
Heguang Liu¹, Chi Wang¹, Ji Wu¹

¹ Key Laboratory of Microwave Remote Sensing (MIRSLAB/CAS), National Space Science Center (NSSC), China

² c/o Max-Planck-Institute Solar System Research, Germany

VHF radars have demonstrated to be valuable tools for observing the atmosphere and ionosphere. Several ground based giant radars, such as MUR, EAR and Jicamarca, are successfully operated for observing key parameters of ionospheric irregularities and their relation to space weather. Additionally, a few radars are being constructed or got operational recently in order to provide observations into the future, namely PANSY in the Antarctic and MAARSY in the Arctic. HCOPAR comprises a low-to-mid-latitude complement in this context.

The Hainan VHF Coherent Scatter Phased Array Radar (HCOPAR) is a key component of the Chinese initiative Meridian Space Weather Monitoring Project (in short: Meridian Project). The project is set up as a large-scale ground-based monitoring system composed of 15 stations along the longitude of 120°E and the latitude of 30°N. 95 instruments and systems are now ready after 3 years of construction [1]. Among them is HCOPAR, which is located at the Hainan Sounding Rocket Base (HSRB, 19.31N, 109.08E) of the Chinese Academy of Sciences.

The HCOPAR System

HCOPAR is implemented as active phase array and composed of 72 Yagi antenna elements. The total array has a rectangle shape of 4 by 18 elements. With 0.7 wavelength distance between adjacent elements the radar provides an alias-free scanning field of -30° to +30° in azimuth. The beam width of the antenna array is 5° (W-E) by 21° (N-S) and the squint angle of 27° N matches the orthogonal condition to the E-region field-aligned irregularities. Like some modern radars HCOPAR benefits from the advances of modern digital electronics and software controlled signal generation and processing. A dedicated pre-processor is designed and imbedded in each T/R unit. The pre-processor is composed of high speed ADC, DAC, DSP and FPGA. Each pre-processor receives the synchronous clock signal from the central synchronizer. High performance crystal oscillator is implemented in the synchronizer to keep all the elements work with accurate timing. Basically, HCOPAR is a combination of 72 independent elements. Each element is reconfigurable and works synchronously with software control.

The HCOPAR station is located on Hainan island in southern China and got into operation end of 2010. It operates at the centre frequency 47.0 MHz. The radar is applying a phased array antenna and digital transceiver (T/R) units to reach its full Doppler capability. The main feature of the new radar is the distributed pre-processor which is dedicatedly designed for HCOPAR and enables the internal calibration of the T/R units, as well as the Direct Digital Synthesis (DDS), local digitizers in each T/R unit. The pre-processor is also a network node, which receives commands from the central computer, and uploads digitized data to the computer, thus enabling further

amplified by the transceiver and digitized by the pre-processor at 27 MSPS, so called sub-sampling.

After digital I/Q demodulation and low pass filter, raw data can be either uploaded to one of the 4 sub-processors, or stored at local buffer of the pre-processor. The latter then can be uploaded to the central computer one by one. By this means raw data without information loss are available for each transceiver, thus provide flexibility in radar system diagnostics and future detail analysis. However, a local buffer is not used in normal operation due to limited storage capability. In routine operation, the raw data are uploaded to the sub-processor and combined into single echo with Digital Beam Forming (DBF). This single echo is further combined in the central computer into final radar echo. Final radar echo is stored in the hard disk for future study. Meanwhile, every two minutes a quick image with coherent integration are upload to the Meridian scientific center through internet to help researchers to recognize useful information in the mass data. The radar monitor software also provides a real time interface to senior users. With the monitor software, time-range-intensity map is available for every beam position. Here the time resolution can be as fine as 2.5 ms.

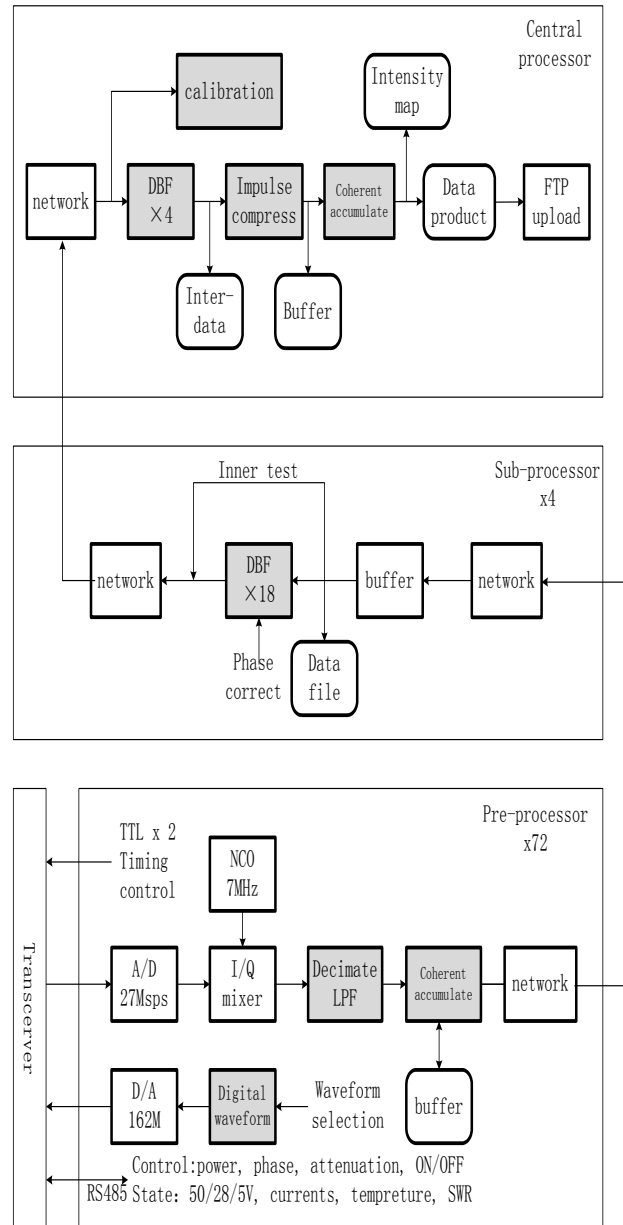


Figure 2: HCOPAR signal flow.

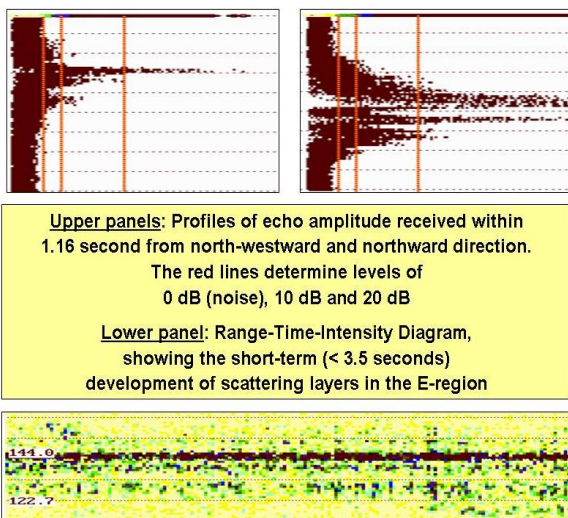


Figure 3: Power profiles and RTI diagram.

Preliminary results

The quality of the raw data has shown to be of good standard. This already allows some initial interpretation in terms of the scattering structure of irregularities. This can be deduced from the variation of signal power as function of beaming angle, which primarily is dominated by the aspect sensitivity and temporal variability of the scatters.

After proper performance of quadrature, linearity etc. was confirmed, the consistency of received scatter echoes was tested, the

characteristics of spatial and temporal appearance of the echoes was initially evaluated. This was done by checking and interpreting power profiles, Doppler spectra and range-time-intensity plots. The variability of power spectra indicates mostly type-2 irregularities as similarly occurring in the Equatorial Electrojet (EEJ).

Initial science topics of HCOPAR:

The **received power** P_r depends on the integral product of the

radar antenna beam pattern $B(\alpha, \beta) \rightarrow B(x,y,z)$,

range gating $R(\alpha, \beta, \underline{r}) \rightarrow R(x,y,z)$, with $\underline{r} = (x,y,z)$.

aspect distribution / sensitivity of irregularities $A(\rho, \sigma) \rightarrow A(x,y,z)$,

spatial irregularity distribution and their cross section $S(x,y,z)$

Then the **received signal power** is: $P_r = \int B(\underline{r}) \cdot R(\underline{r}) \cdot A(\underline{r}) \cdot S(\underline{r}) \underline{dr}$.

From this follows the reflectivity η . i.e. scatter cross section σ .

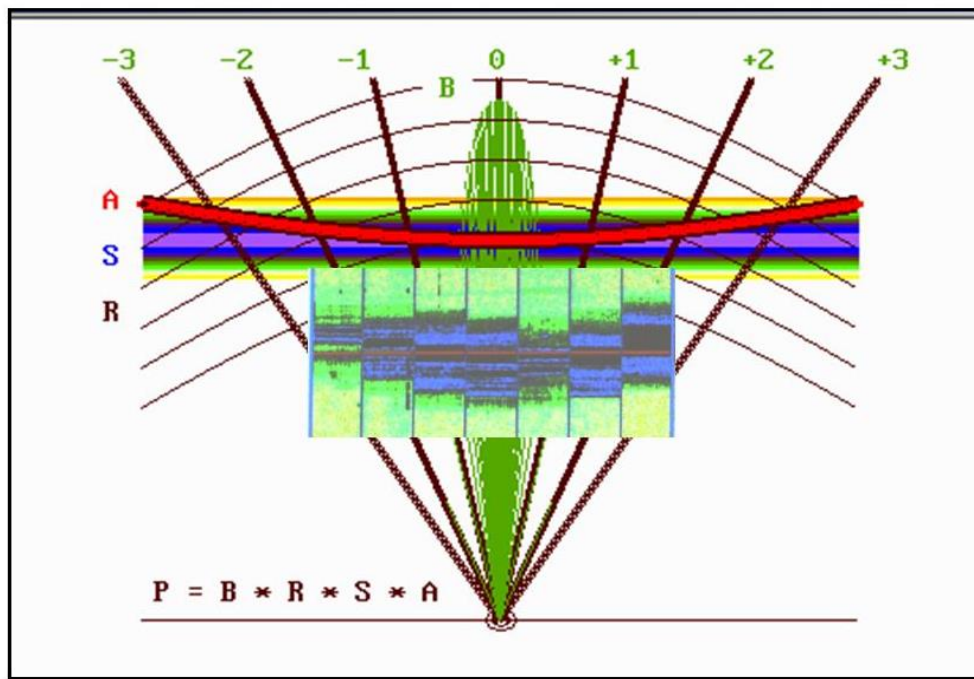


Figure 4: sketches these main components B , R, S, and A. It also shows RTI plots (signal power P) in the seven beam directions -3 to +3, which had been obtained from E-region backscatter. These plots show the dependency of P on range and angle.

Some next steps

- * Adapt pulse scheme and coding for longer codes for further sidelobe reduction, no aliasing and optimized E- and F-region imaging.
- * In-beam angle of arrival measurements to determine best estimate of scattering centre to deduce best estimate of its altitude
- * Design a generalized model to determine S and A, followed by best estimate of velocity distributions.

- * Convert P into reflectivity η / scatter cross section σ
- * Compose the three-dimensional distribution of scatter cross section and the velocity field of extra-equatorial E- and F-region field-aligned irregularities
- * Determine whether the irregularities observed by HCOPAR are equivalent to equatorial (ESF, EEJ) or to mid-latitude (QEP) irregularities or a blend of both.

Conclusion

A new VHF radar system HCOPAR is introduced. The main system components are briefly described proving up-to-the-date techniques, including digital phased array, software radio, hierarchic processing, etc. are applied to the HCOPAR.

Reference

Chi Wang, New Chains of Space Weather Monitoring Stations in China, SPACE WEATHER, VOL. 8, S08001, 5 PP., 2010, doi:10.1029/2010SW000603

The Colorado Software Defined Radar

Cody Vaudrin and Scott Palo

University of Colorado, Department of Aerospace Engineering Sciences
(cody.vaudrin@colorado.edu)

1. Introduction

The Software Defined Radio model of receiver design has enabled the implementation of a highly configurable data acquisition system for radar remote sensing applications. Here, we describe the primary hardware components of the Colorado Software Defined Radar (CoSRad) receiver system. In addition to the hardware, significant work has been done in creating the general purpose computer (GPC) software necessary to implement the traditionally analog radar signal processing tasks such as IQ demodulation, matched filtering and detection. This description deals primarily with the receiver hardware, which at the most abstracted level consists of an 8-channel VHF direct-convert analog-to-digital converter (ADC) and a number of digital-to-analog converters (DAC) providing extensive RF generation capabilities and control signals. The real-valued samples acquired by the receiver are written to GPC storage over a USB 2.0 interface where the traditional radar signal processing tasks are accomplished digitally. With this extended abstract, we concentrate on the hardware before the GPC in the processing chain and leave the GPC signal processing software for description in a future paper.

2. SDR Based Data Acquisition

CoSRad is a software configurable data acquisition system designed to operate within a wide range of data acquisition topologies. A defining characteristic of the Software Defined Radio (SDR) approach to data acquisition is the location of the ADC in the signal chain, which is typically placed at the node of highest possible RF given the ADC specifications. Typically, the input signal will only be subjected to gain and analog preselection filtering before sampling. Transmit waveform structure and processing of the received signals are software defined within the fundamental hardware specifications defined in Table 1. For VHF carrier frequencies with a bandwidth below the receiver's Nyquist frequency ($f_s/2$), traditional analog receiver components such as IF mixers are absent from the high level architecture depicted in Figure 1. When configured for pulsed Doppler operation, the transmit pulse and sampling clock are generated by two Analog Devices AD9954 DDS devices driven by a GPS disciplined oscillator. The transmit pulse is shaped by mixing one DDS output with a pulse envelope generated using an Analog Devices AD5440 DAC. The receiver inputs are sampled with an Analog Devices AD9952 8-channel ADC. After sample rate conversion, the real-valued samples are transferred to a GPC over USB 2.0 where the traditional radar signal processing tasks are preformed.

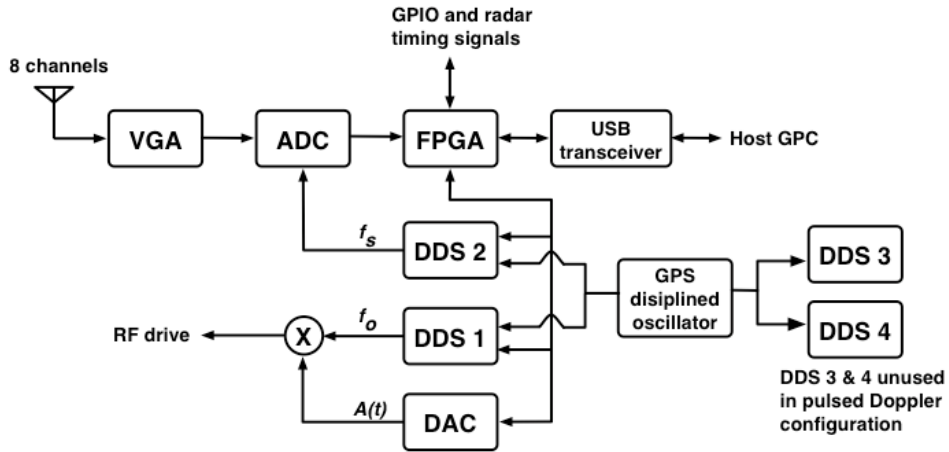


Figure 1: CoSRad hardware block diagram when configured for pulsed Doppler operation. Only gain (VGA) and preselection filtering are applied to the input signals before sampling.

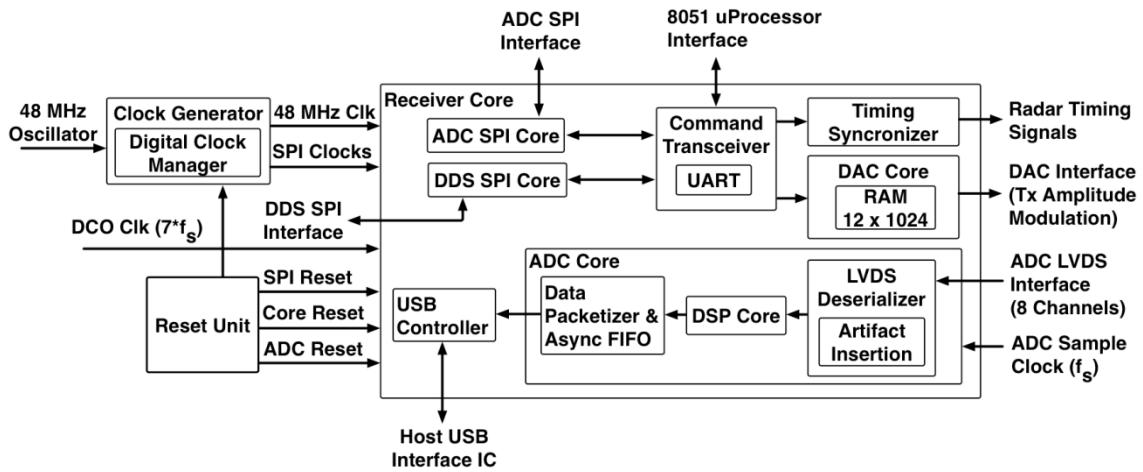


Figure 2: Block diagram of the CoSRad FPGA. The radar timing signals and Tx amplitude modulation are synchronous to the DCO clock ($7f_s$).

Symbol	Description	Value	Unit
f_s	Sampling Frequency Range	5 - 50	MSPS
N_{ch}	Available Number of Channels	8	
f_o	DDS Carrier Frequency Range	0.5 - 200	MHz
B_a	Full Power Analog Bandwidth	0.01 - 325	MHz
B_d	Max Digital Throughput (USB 2.0)	480	Mbps
f_{dac}	DAC Update Rate	20	MHz
V_{in}	ADC Dynamic Range	2	Vpp
ADC_{res}	ADC Resolution	14	bits
PW	Min Transmit Pulse Width	1	μ S
G_{VGA}	VGA gain	-4.5 - 55.5	dB

Table 1: Fundamental Hardware Specifications.

3. CoSRad Configured as a Meteor Wind Radar Receiver

CoSRad is designed as a universal data acquisition and radar controller system, and when configured for VHF pulsed Doppler operation becomes a highly flexible meteor wind radar receiver. For VHF pulsed Doppler applications, the receiver is configured for bandpass sampling the amplified and band limited received signal [1]. See Figure 3 for definitions of the quantities used in the following discussion of Sample Rate Conversion (SRC) [2]. Bandpass sampling intentionally aliases the carrier (f_o) into the Nyquist region ($f_s/2$) of the sampled signal. For the best performance, f_o and f_s are chosen such that $f_s = 4f_o/1 + 4n$ where n is the number of alias folds. This requirement intentionally aliases f_o to $f_s/4 = f_{a1}$. With an uncoded, constant RF pulsed Doppler configuration, f_o is constant which implies the requirement of $FTW_{f_s} = 4FTW_{f_o}/1 + 4n$ where FTW_{f_s} and FTW_{f_o} are the 32 bit frequency tuning words defining the DDS output frequencies (see the AD9954 datasheet). Note that pulse coding and variable f_o pulses are also possible, but not implemented in the basic pulsed Doppler configuration.

After the amplified, band-limited signal is sampled by an ADC channel and received by the FPGA, the samples are passed through the **DSP Core** (see Figure 2) FPGA block where integer multiple SRC further reduces the data rate to a value below that of the USB throughput. CoSRad implements SRC as a two-stage process consisting of low-pass or bandpass filtering using a second-order-section implementation structure followed by a decimation stage. Performing sample rate conversion in the FPGA rather than reducing the sampling rate allows for more flexible subsampling schemes. Fundamentally, SRC reduces the bandwidth of the sampled signal to a value below the USB 2.0 throughput of 60 MB/s and amounts to a data rate on the order of 5 MB/channel (for low-loss bulk USB transfers) when CoSRad is configured for 8 active channels. A wider per-channel bandwidth is possible using fewer channels, but the combined data rate of all channels cannot exceed the maximum USB 2.0 throughput.

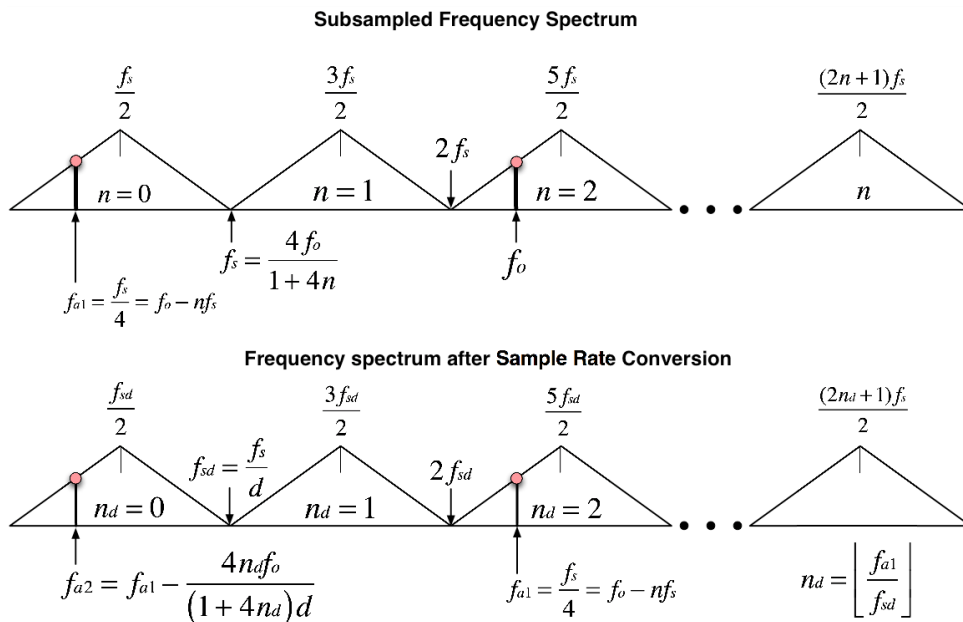


Figure 3: Graphical depiction of sample rate conversion in the CoSRad system. Bandpass sampling shifts the carrier from f_o to f_{a1} when sampled at $4f_o/1 + 4n$ where $n=f_o/f_{a1}$. Programmable integer decimation further transforms f_{a1} to f_{a2} where n_d is the integer decimation factor (i.e. $n_d=3$ implies every 3rd sample is retained for further processing).

CoSRad includes a programmable controller capable of modifying the timing parameters depicted in Figure 4 and Table 2 based on a GPS synchronous oscillator. All timing signals are therefore synchronous to f_s . The inter-pulse period T_{IPP} , pulse width T_{PW} , pulse delay T_{DLY} and for the transmit pulse (f_o), a pulse shaping envelope $A(t)$ are all modified by configuring various FPGA registers and memory locations. In this way, CoSRad functions as a GPS synchronous programmable radar controller. 32 GPS synchronous GPIO signals are also available in most configurations. All time signals have a time resolution of $\Delta t = 1/7f_s$.

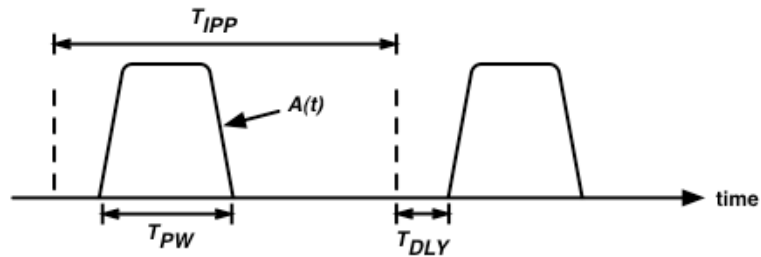


Figure 4: The radar timing signals are synchronous to f_s and configured via a set of FPGA registers controlling the parameters listed. Each timing signal has an independently controlled pulsewidth T_{PW} , interpulse period, T_{IPP} and can be delayed from the internally generated synchronizer pulse, T_{DLY} . The timing and generation of the transmit pulse shaping envelope $A(t)$, is also controlled by a set of programmable registers.

Symbol	Description
T_{IPP}	Inter-pulse period
T_{PW}	Pulsewidth
T_{DLY}	Pulse delay
$A(t)$	Pulse shaping envelope
ΔT	Timing resolution

Table 2: Available timing signals when configured for pulsed Doppler operation.

4. Initial Results

Consider the RTI plot shown in Figure 5. Three regions (a, b, c) containing four echoes are identified. This block of data was chosen to exemplify data produced by the receiver when configured for VHF pulsed Doppler operation. Region c in Figure 5 shows an ‘underdense’ echo where the electron density of the plasma column is sufficiently low to neglect multiple electron scattering effects.

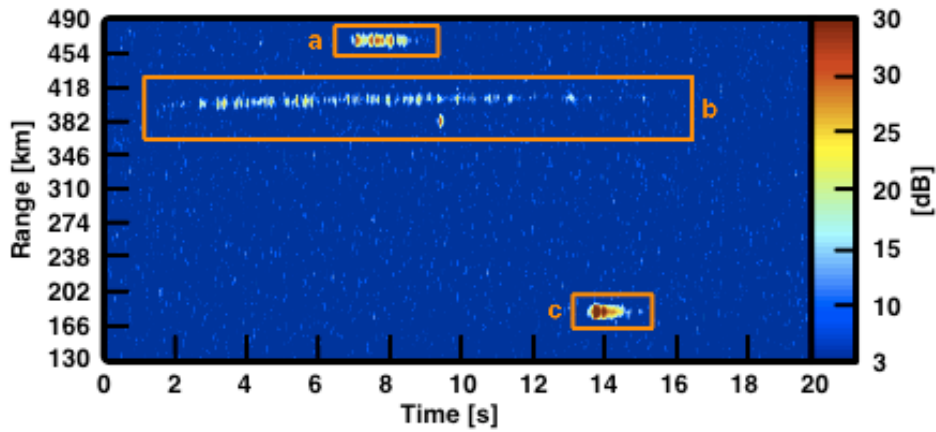


Figure 5: A block of radar pulses observed in Platteville, Colorado in the southern direction at 4:10AM on Aug 16th, 2011 containing four echoes. $f_{sd}=1.037$ MHz, $f_o=30.355$ MHz and $PRF=304.5$ Hz.

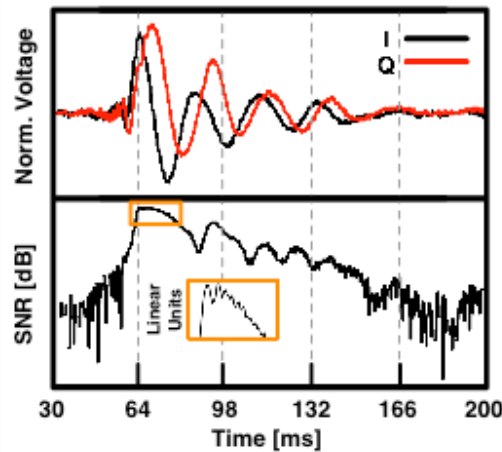


Figure 6: Time series I and Q components at 183 km from region c of Figure 5. Fresnel oscillations are masked on the logarithmic scale, but visible on the linear scale.

SNR and I & Q components at 183 km are shown in Figure 6 which exhibits the canonical exponential rise [3] followed by a series of fresnel oscillations superimposed on a lower-frequency power vacillation. The fresnel oscillations are masked in the logarithmic plot, but are clearly visible when the SNR is plotted on a linear scale. As a consistency check, a meteoric velocity of ~ 33 km/s is calculated using both the post t_o and echo rise-time techniques.

5. Concluding Remarks

We have presented basic hardware details of the Colorado Software Defined Radar (CoSRad) along with pulsed Doppler configuration details and initial measurements taken at an established radar site. The driving design goals of reconfigurability and universality are discussed. The overview presented should provide the reader with a basic understanding of the CoSRad capabilities and limitations, and serve as a starting point for radar configurations based on the CoSRad hardware.

Acknowledgements

This material is based upon work supported by the National Science Foundation under Grant No. ATM-0449985

References

- [1] D. M. Akos, M. Stockmaster, J. B. Y. Tsui, and J. Caschera. Direct bandpass sampling of multiple distinct rf signals. *IEEE Transactions on Communications*, 47(7):983–988, 1999.
- [2] Tim Hentschel. *Sample Rate Conversion in Software Configurable Radios*. Artech House Publishers, 2002.
- [3] D.W.R. McKinley. *Meteor Science and Engineering*. McGraw-Hill, 1961.

Introduction to the Kunming atmospheric radar facility (KARF) and the initial results

Jinsong CHEN^{1,2,3}, Zhenwei ZHAO^{1,2}, Na LI^{1,2}, Jian WU^{1,2}, Jiyao Xu³

¹ China Research Institute of Radio wave Propagation (CRIRP)

² National Key Laboratory of Electromagnetic Environment (LEME)

³ Center for Space Sciences and Applied Research, Chinese Academy of Sciences

Abstract

In the late 2000s China Research Institute of Radio wave Propagation (CRIRP) has further expanded its research program to monitor the Earth's middle and upper atmosphere. In attempt to study the dynamics of the MLT region in lower latitude over China, the Kunming atmospheric radar facility (KARF) consisting of a MF radar, an all-sky meteor radar and a ST Doppler radar with meteor radar capability was installed at Kunming Radio Observatory (25.6° N, 103.8° E), 130 km northeast of Kunming which is the capital city of Yunnan Province, in August 2008 by CRIRP. Since then, continuous observation of winds in the MLT has been underway. KARF gives us opportunity to complement the study of atmosphere oscillations in low-latitude MLT region and the nonlinear interaction between atmospheric waves and ionosphere. The system descriptions will be given first, and then some initial results from the KARF will be shown based on the first year observation also, which include seasonal variations of tides and gravity waves from MF radar as well as the electron density in D region from Aug. 2008 to Jul. 2009.

1. Introduction and system descriptions

The Kunming atmospheric radar facility (KARF), which is constituted of a MF radar, an all-sky meteor radar and a ST Doppler radar with meteor radar capability, was installed at Kunming Radio Observatory (25.6° N, 103.8° E) in August 2008 by CRIRP under the help of engineers from ATRAD company in Australia.

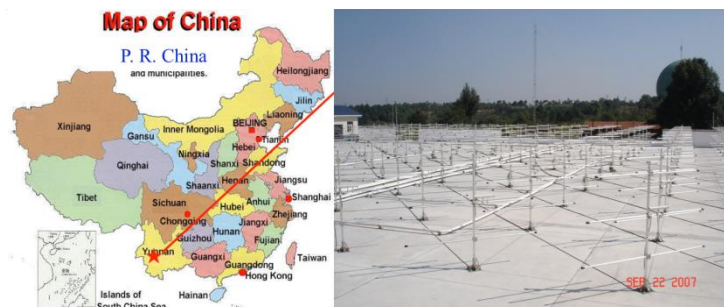


Figure 1: The location of the KARF.

1.1 The Kunming meteor radar

The Kunming Meteor Radar is designed specifically for wind profiling in the Mesosphere Lower Thermosphere (MLT) region (70-110 km) by tracking the drift of trails left by meteoroids as they fall through the atmosphere. It is equipped with a comprehensive data analysis and display suite for routine observations and also provides an ideal platform for developing and evaluating new analysis techniques. The system is designed to support both attended or unattended operation. It can be operated and monitored remotely and data can be automatically analysed and posted to a web site. The meteor radar has many applications, which include: wind, temperature and density profiling; meteor astronomy; rocket launch support; meteor tracking and recording. The KARF consists of two meteor radars with different frequency of 37.5 MHz and 53.1 MHz, which shares the transmitter of the ST radar, that provide an unique chance to observe the meter trail simultaneously using radars with two frequencies.

Radar Configuration	All-Sky Meteor Interferometer
Radar Power	20 kw peak power
Max Duty Cycle	10% (Gaussian monopulse); 15% (Square or coded pulse)
Operating Frequency	37.5 MHz and 53.1 MHz
Antenna Configuration	5 Antenna interferometer plus Transmit antenna (5 x Rx antenna, 1 x Tx Antenna; linearly polarised crossed-dipoles)
Pulse Repetition Frequency	5kHz maximum
Radar Receiver	5 coherent (complex) radar receiver channels
Sampling Range	80-280km
Range Resolution	100-4000m

Table 1: System characteristics of the Kunming meteor radar.

1.2 The Kunming ST radar

The Kunming ST Radar uses Doppler Beam Swinging (DBS) techniques to provide real-time vertical profiles of horizontal wind speed and direction at heights of up to 15 - 20km above ground level. It operates in the low-VHF frequency range, providing significant cost benefits and eliminating data contamination arising from precipitation, birds or insects. The ST radar provides a low-cost alternative to meteorological balloon stations for wind profiling applications. Alternatively, it may be used in conjunction with a meteorological balloon station to reduce the number of costly balloon flights per day. It also has applications in rocket & space launch operations and scientific research.

Radar Configuration	Stratospheric/Tropospheric Radar Dedicated-Doppler Beam Steering Operating mode Solid State STX-II Transmitter modules combined to produce nominal
Radar Power	80 kw peak power
Operating Frequency	53.1 MHz
Antenna Beamwidth	7° (3dB points, one-way)
Antenna Configuration	144 Antenna (12 x 12 square array)
Beamsteering method	Relay Switched, cable phase delays
Radar Receiver	single coherent (complex) radar receiver channels
Sampling Range	1-20km
Range Resolution	100-1200m

Table 2: System characteristics of the Kunming ST radar.

1.3 The Kunming MF radar

The Kunming MF radar has been specifically designed for profiling at heights between 50 and 100 kilometers. The Kunming MF radar power outputs 64kW (peak), and the antenna array consist of 4 antennas and four complex receiver channels are supported. The MF radar has many applications, which include wind profiling; meteor tracking and recording and ionospheric research (D region).

Radar Power	64 kw peak power
Max Duty Cycle	0.5% (Gaussian monopulse)
Operating Frequency	2.138 MHz
Antenna Configuration	4 Cross dipole antennas (For Tx and Rx)
Pulse Repetition Frequency	10-80Hz
Radar Receiver	4 coherent radar receiver channels (I and Q)
Sampling Range	50-100km
Range Resolution	2000m

Table 3: System characteristics of the Kunming ST radar.



Figure 2: The antenna array of the Kunming MF radar.

2. The initial results from the first year observation

2.1 Seasonal Results of Aspect Sensitivity from the Kunming MF radar

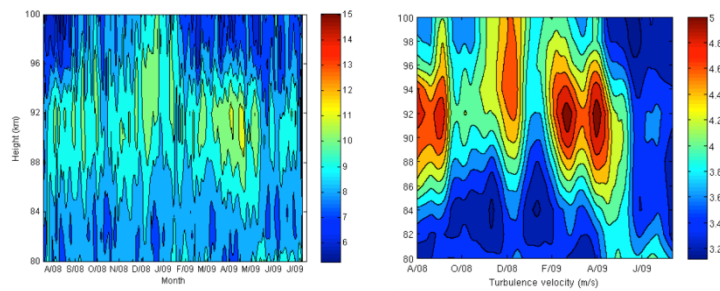


Figure 3: Left: Seasonal results of daily-mean aspect sensitivity in the height range of 80-100 km at Kunming site between August 2008 and July 2009; Right: Weekly-mean contour of turbulence velocity as the function of height (80-100 km) and time from August 2008 to July 2009 measured by the Kunming MF radar.

Figure 3 is an image contour plot of the daily-mean aspect sensitivity calculated by the spatial correlation method. It is shown that the general behaviour is to vary both with height and on a daily basis. The values range from 5 to 15 degrees. Looking down from 80 to 84 km, one can see that while there is no evident seasonal variations, whilst a clear seasonal variations exists at heights above 86 km, which is more evident around the height of 90 km. At the height of 90 km the value of aspect sensitivity is more than 10° during the winter months, which extends up to 100 km, decreasing by several degrees during the summer months, while the peak value about 12° tends to emerge during April and May in 2009. In addition, the contours progress upwards during autumn and downwards during spring at a rate of several kilometres per month. We presented the turbulence velocity, which is derived from the fading time, or mean auto-correlation function half-width, during the same time in figure 3 also. It is evident that the turbulence velocity is correlated highly with the aspect sensitivity in figure 3, and they tend to show almost similar variations in time and height, which indicates that turbulences contribute mainly to the feature of aspect sensitivity rather than waves.

2.2 Seasonal Results of electron density in D region from the Kunming MF radar

Figure 4 show the contour of the electron density (N_e) from Aug. 2008 to Jul. 2009 as well as the zonal wind observed by the Kunming MF radar. N_e peaks at equinoxes, and the minimal happen at solstices. F_{min} from the ionosonde at Kunming Radio Observatory plotted in figure 4 (top c) shows the similar seasonal variation with N_e measured by MF radar. Semiannual Oscillation (SAO) predominant the variation in electron density in D-region, while IRI shows an annual Oscillation (AO) trend determined by the solar zenith angle. Meanwhile Zonal wind presents the similar SAO with N_e in D-region; Westerly wind accords to the increase of N_e , while easterly wind goes with the decrease of N_e . Gravity wave is believed to drive the stratospheric tropical quasi-biennial oscillation (QBO) and the semi-annual oscillation (SAO) both in the stratosphere and mesosphere. Gravity wave is able to induce turbulence and turbulent mixing can change the vertical distribution of chemical species including NO, which lead to the seasonal variation of N_e in D region, as NO is thought the main source for electron in this region.

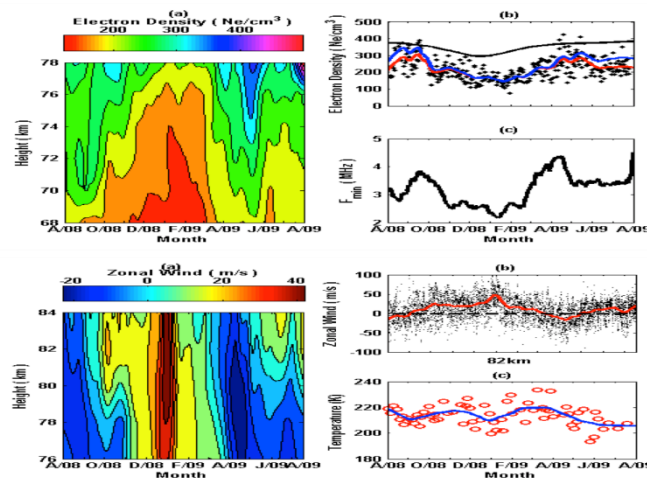


Figure 4: The contours of N_e from Aug. 2008 to Jul. 2009 (top a) and zonal wind (bottom a) observed by the Kunming MF radar; F_{min} from the ionosonde at Kunming Radio Observatory (top c); Temperature near 90 km from SABER observations.

3. Summary

The KARF am able to observe almost the entire height of atmosphere from ground to about 110km, and will give us chances to take up the atmospheric research in low latitude, where we still lack of understanding in many aspects. Meanwhile the KARF will provide the database to study the low-latitude atmosphere combining the data sets from satellite observations and other site observations in the future.

De-noising of atmospheric radar signals using Spectral based sub-space method

VN Sureshbabu¹, VK Anandan¹, Toshitaka TSuda², Jun-ichi Furumoto²

¹ ISTRAC, Indian Space Research Organisation, Bangalore -58, India

² Research Institute for Sustainable Humanosphere (RISH), Kyoto University, JAPAN

Abstract

From the beams synthesized at different pointing directions for wind profiling by Postset Beam Steering (PBS) technique on multi receiver data, the Doppler power spectra are obtained from model based spectral estimation method i.e. Eigenvector (EV). EV, one of the subspace methods, uses eigen-analysis to decompose the signal into two subspaces as signal subspace and noise subspace. Also, the power spectrum produced by sub-space methods like EV has a unique advantage of de-noising atmospheric radar signals from noisy environment. In this article, the advantages of EV are mainly focused for profiler radars. Such advantages are much useful to improve and estimate the spectrum parameters and thereby complete wind profiling about 20 km with temporal resolution less than 1 min.

1. Introduction

Generally atmospheric signals are very weak and contaminated with noise. Retrieving the signal information in the noise background is always an issue. Various techniques and quality checks have been used to extract these signals. In this paper a study has been carried out for de-noising the atmospheric signal using sub-space based method on the data received from middle and upper atmospheric (MU) radar at Shigaraki, Japan. MU radar is a monostatic pulsed phased array radar operates at 46.5 MHz with a peak power of 1 MW. The array is configured as circular array of 475 crossed Yagi elements which are grouped and formed by 25 different receiver channels for observational purpose. Array is also capable of steering the beam electronically using phase shifters in transmit and receive path. The experiment was conducted with full array of transmission (beam width 3.6°) in vertical direction. The data collected is subjected to PBS [2] to synthesize new beams within transmit beam volume by capon method. The EV method has unique advantage of looking the signals (beam) distinctly on to signal sub-space and noise sub-space for a given steered direction. Result shows that in the power spectral distribution, the signals only visible by completely removing noise fluctuations. This approach has shown distinct advantage in identifying the atmospheric signals from a noisy environment. The wind velocity estimated through this approach is compared with other estimation algorithms and shown excellent agreement. Study also reveals that the technique is an excellent tool to identify signals in disturbed condition of the atmosphere and having bi-modal characteristics like occurrence of clear air and precipitation echoes side by side.

Several approaches [1] were presented to overcome the lack of spectral resolution and to identify overlapped echo in the power spectrum. In the case of atmospheric radar signals, the normalized eigenvalues (λ') of auto covariance matrix are sequenced in descending order. The response curve is obtained by taking gradient on the normalized eigenvalues. The valley point is identified such that magnitude of gradient of eigenvalues increases abruptly (10 dB and above) and also the order (p) is minimum. Since sub space methods assume the signal into signal sub space and noise subspace, p numbers of eigenvalues and corresponding eigenvector sets (sinusoids) are assigned into signal sub space and rest of things are assigned into noise subspace. It

is noted that there exists much uncertainty in spectrum parameters if the number of sinusoids are chosen lesser or greater than p . It is observed that number of sinusoids less than p leads to line spectrum and that more than p leads to unwanted multiple peaks within spectrum width. The main importance of EV is revealed through this paper such that atmospheric signals are identified distinctly from a noisy environment. So, EV removes the statistical uncertainties from power spectrum estimations so as to improve the quality of the calculations of spectrum parameters and then wind estimation. Thus, the EV technique may potentially overcome some of the difficulties that standard Fourier based techniques face in low SNR conditions, and also, may improve the temporal resolution of the estimations which is of importance for atmospheric and weather studies.

2. System description and data processing

The system descriptions is given in the companion paper namely *“Extraction of horizontal wind velocities from a multi receiver phased array radar system using post beam steering technique and efficiency of various beamforming methods”*. The data collected from 25 channels are subjected to PBS technique to synthesize new beams at 1.7° tilt angle with 16 equally spaced azimuth positions. The power spectra at different line of sight angles are independently obtained as mentioned in the sections II for 5 overlapping sub bands and the sequence are repeated for three times. In this way, 15 power spectra is obtained from one record itself. The spectra are integrated to improve the SNR. From the average spectrum, zeroth order (total power) and first order (mean velocity) moments [3] are calculated through adaptive moments estimation method [3]. Thus, radial velocities from corresponding line of sight angles are readily obtained. As a result, the horizontal wind components i.e. zonal and meridional velocities are derived by least squares sense.

3. Result analysis and discussion

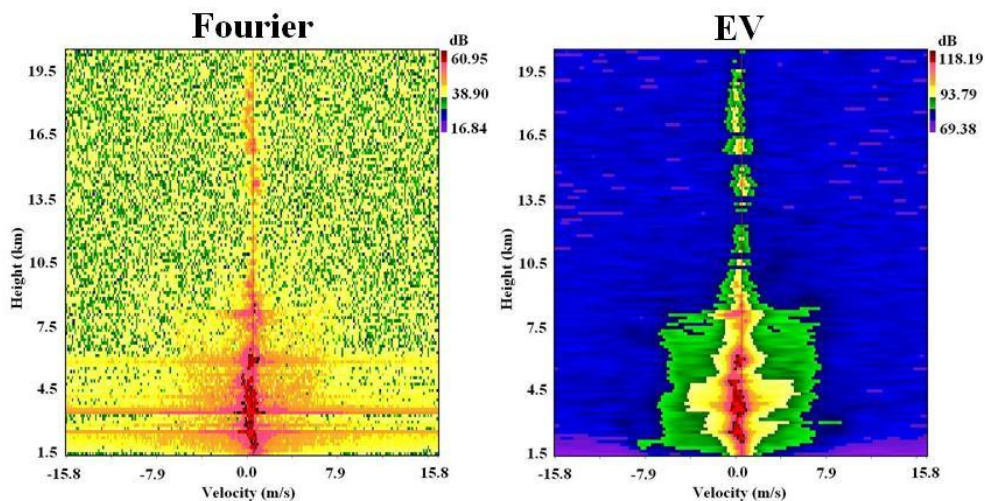


Figure 1: Radial velocity spectra obtained by conventional Fourier and EV based methods. The spectra are obtained from the vertical time series data corresponding to the sub-band 46 MHz. The data (time series) is obtained on Jul 18, 2008, 0803 LT. The figure shows the characteristics of EV such as de-noising, power enhancement in comparison with Fourier method. The dB scale in the figure is arbitrary and has relevance only in comparison of background noise power with respect to signal power.

The power spectrum obtained by Fourier and EV based methods using vertically received time series atmospheric signals are shown in Fig.1. The power spectrum has also been improved by reducing statistical uncertainties (noise) through segmentation and overlapping processes. The enhancement in the quality of the Doppler spectrum has also been observed with incoherent integration of spectra of different sub-bands (figure not shown). The velocity spectrum is obtained by multiplying half of the wavelength with spectral components. As EV assumes a statistical model (unlike Fourier method) to the signals through eigen-analysis, it extremely suppresses the background noise in the power spectrum to improve the quality of the calculations of spectrum parameters. Again, EV overcomes some of the difficulties in obtaining spectrum parameters that standard Fourier based approaches face in low SNR conditions. Particularly the data used in Fig.1 were obtained in a time near convective process and so there exist a number of bands in lower height regions due to higher frequency (noise) spectral components. These bands are seen in the spectra obtained using Fourier based approach. Moreover, Fourier based approach is not appropriate and may introduce much uncertainty in the computation of spectrum parameters in such cases. Also, the bands are unable to eliminate in Fourier based approach. But, EV recognizes only certain signals, whichever seems not to be aliased, for power spectrum estimation by the signal model assumed through eigen-analysis. Hence, EV not only removes the background noise (added to the radar signals) and also the statistical fluctuations (randomness of the radar and noise signals with a variance that decreases as the number of integrations increases) in the estimated spectrum.

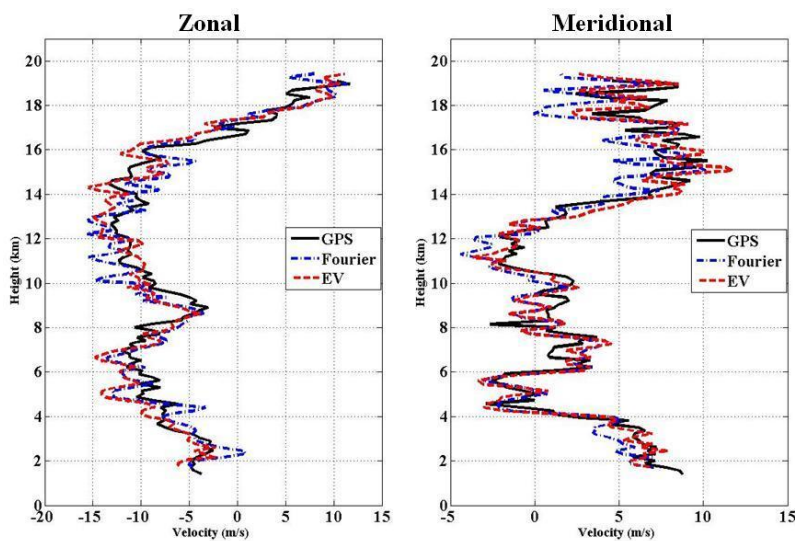


Figure 2: Vertical profile of horizontal velocity derived by PBS technique using Fourier and EV based estimators in comparison with GPS sonde observed wind (black line). GPS sonde wind observation on Jul 18, 2008, 0747-0850 LT and PBS derived winds in near time.

the study reveals that EV has the advantage of (i) identifying atmospheric signal buried in noisy environment (ii) obtaining spectrum parameters (moments) (iii) cleaning the spectrum through denoising process (iv) improving SNR. Thus, the advantage of EV is used to estimate the spectrum parameters from the synthesized beams for PBS wind estimates. For this, the wind estimation is made with 16 equally spaced azimuth positions at the tilt angle of 1.7° . The moments (radial velocities) are obtained in 16 directions and horizontal winds are derived by least square sense.

In general, the Fourier based approach is reliable to estimate spectrum width. A close agreement in spectrum width computation between Fourier and EV is observed (figure not shown). This inferred EV can be better and alternate method for atmospheric radar measurements. In weak SNR height regions, there are deviations in spectrum width calculation between both estimators due to poor performance of Fourier estimator. A better performance in SNR improvements is observed in the case of EV estimator. When compared Fourier approach, there can be better accuracy in the estimation of moments from EV produced spectrum and thereby complete wind profiling. Hence,

The horizontal velocities derived through using both estimators are shown in Fig.2 in comparison with GPS sonde observed winds.

In Fig.2, GPS sonde observation has taken the time duration of about 62 minutes for wind profiling whereas PBS based wind profiles were derived with the temporal resolution of 26 - s. The comparison between both observations methods is made with respect to height and time in Fig.2. The statistical performance of estimators, such as slope value by linear fit, correlation coefficient and Root Mean Square Error (RMSE), in PBS wind estimates is given in Table.1.

Spectral estimation method	Slope		Correlation coefficient		RMSE (m/s)	
	U	V	U	V	U	V
Fourier	0.94	0.86	0.82	0.81	2.98	2.51
EV	1.07	0.93	0.91	0.89	1.81	1.88

Table 1: The performance of spectral estimators in PBS wind estimates (2.0 km -19.0 km) in comparison with GPS sonde observational method. Statistics correspond to the GPS sonde data observed on Jul 16, 2008, 0747-0850 LT and PBS observation (using 5 frame integrations) in near time.

Similarly, the performance of estimators in PBS wind estimates in comparison with DBS observed winds are given in Table.2. Further, the statistics shown in tables 1-2 are in consistent with the results of wind variations reported in previous studies [8].

4. Conclusion

Various processing to improve the Doppler power spectrum is described. EV, one of the subspace methods, has shown as an alternate estimator for Fourier based method to obtain spectrum parameters from the time series atmospheric radar data. The advantages of EV have been used to improve the synthesized spectra (within transmit beamwidth) required for PBS wind estimates. Using the advantages of various signal processing techniques and EV estimator, a high temporal (26 - s) wind estimation by PBS technique is reported in detail at the first time. The obtained results have shown to be reliable and consistent with other wind observational methods. Such high temporal wind estimation with maximum height coverage (about 20 km) can be useful to study the fast changing wind fields during atmospheric convection.

References

- [1] E Boyer., M. Petitdidier., W. Corneil., C. Adnet., P. Larzabal, 2001: Application of model-based spectral analysis to wind-profiler radar observations. *Ann. Geophys.*, 19, 815-824.
- [2] J Rottegr., H Ierkic., 1985: Postset beam steering and interferometer and application of VHF radars to study winds, waves and turbulence in the lower and middle atmosphere. *Radio sci.*, 20(6). 1461-1480.
- [3] V.K Anandan., P Balamuralidhar., P. B Rao., A. R Jain., C. J Pan., 2005: An adaptive moments estimation technique applied to MST radar echoes. *J. Atmos. Oceanic Technol.*, 22, 396–408.

An FPGA-Based Wind Profiler Controller and Signal Processor

Charles Martin, Eric Loew, Chris Burghart, William Brown, Brad Lindseth

National Center for Atmospheric Research, Boulder, Colorado

1. Introduction

In the past decade new capabilities have emerged in digital radar processors, due to the increased capabilities of the Field Programmable Gate Array (FPGA). Because the FPGA is a re-configurable, generic and high-performance computing device, it can serve as the central component in a general-purpose control and signal processor subsystem. This paper summarizes the deployment of a commercial FPGA based digital transceiver as a general-purpose radar controller and signal processor.

2. The Field Programmable Gate Array

The FPGA is simply an integrated circuit with an extremely large number of generic digital logic cells. These cells can be dynamically connected to create building blocks capable of basic digital functions. These components are then combined to produce more sophisticated logic, and so on until complex functionality is realized. The FPGA is well suited to implementing pipelined computations that can be highly parallelized, such as filtering, frequency conversion, and the fast Fourier transform.

The FPGA device has digital I/O connections for bringing signals into and out of the chip. The number of digital I/O lines can number in the hundreds for the larger devices. Processing within the FPGA is driven by numerous clock signals, which gate the digital data through the configured cells. Clock management is one of the more challenging aspects of firmware design, when dealing with mixed frequency applications. This is common for designs that are connecting signals that are derived from IF rates, to computer buses, memories, etc. Fortunately the FPGA development tools provide capabilities for correctly managing the intersection of clock domains.

3. The FPGA Workflow

The FPGA configuration is commonly specified with a hardware specification language such as the VHSIC Hardware Description Language (VHDL). VHDL engineering is much like other software development, following the typical code, compile, test and debug cycle. For FPGA development, the compile step is generally referred to as synthesis, and is highly compute intensive. This aspect considerably slows the development cycle. Simulation allows the firmware design to be tested without using hardware, and is critical to efficient FPGA development.

Approaches that allow for algorithm specification without writing VHDL are becoming common in FPGA applications. For example, signal-processing blocks can be developed, tested and evaluated in Matlab, and incorporated directly into the FPGA firmware.

4. Transceiver Cards

The FPGA provides the embedded computational foundation for a radar controller and signal processor, but it must be integrated with other hardware. A transceiver card is required which can provide transmit, receive and control signal functions. Commercial vendors market products that

provide this general-purpose functionality. The FPGA is typically combined with analog-to-digital and digital-to-analog converters, local memory, digital I/O lines and bus interfaces. The Pentek Model 7142 (Figure 1) was employed for this project. A wide variety of carrier cards are available to host the card in common computer backplanes.

5. The Software-Defined Digital Down Converter (SD3C)

The SD3C is a framework that implements the radar signal processing and control functions. It is built on: (a) firmware running on the Pentek 7142 transceiver card, and (b) software support libraries and applications for the host computer system. These two subsystems interact via the computer bus that the card is attached to.

5.1 SD3C Firmware

Figure 2 presents a high level diagram of the SD3C signal-processing pipeline that is implemented on the FPGA. Building blocks are assembled in a signal processing “pipeline”. These functions are described in Table 1.

5.2 SD3C Host Software

The transceiver card and its firmware provide the hardware component for the SD3C. A software infrastructure implements the high level capability for the host computer to interface with the card. Figure 3 depicts the SD3C system architecture, showing the distinctions between the radar hardware, FPGA firmware, PCIe bus, host software and the network.

Data flow is from right to left. The DRX (“digital transceiver”) and the SD3C Pentek Library are applications and libraries written in C++. The final baseband observations are transmitted to other consumers via a standard publish/subscribe infrastructure. The subscribers are visualization, archive, and derived product processes. Some of these processes may publish results for other downstream subscribers. Segregating the functions using a publish/subscribe model allows the processing to be distributed as needed among multiple hosts on the network (Figure 4).

Experience has proven that separating related functions into independent processes leads to a system which is simpler to construct, more robust, and easier to troubleshoot. It is important that the data distribution scheme allows the connections between two processes to arbitrarily come and go, without negatively impacting either process. The NCAR 449 MHz wind profiler has successfully employed this principle, using the Open Data Distribution Service (OpenDDS) as the data transport mechanism.

6. SD3C Applications

The SD3C is currently employed in three operational radars, whose characteristics are summarized in Table 2. These systems cover a wide range of capabilities. An example observation from the 449 MHz wind profiler is given in Figure 5.

7. Conclusions

FPGA development has traditionally been the domain of specialized digital hardware engineering teams. In contrast, the SD3C project was executed by a very small group of RF system and software engineers, who had to learn the technology “on the fly”. The learning curve was challenging, and required gaining expertise in VHDL concepts and FPGA system design. The development workflow is intricate and time consuming, and the support tools are complicated and often non-intuitive. Debugging and testing can be difficult. However, with reasonable effort these obstacles are surmountable, and the benefits make the investment worthwhile.

Use of FPGA technology transforms many aspects of radar system development into essentially a software activity. This work benefits greatly by employing standard software engineering practices. Designing within a software architecture perspective, using tools such as integrated development environments, source code revision control and bug tracking, and creating embedded documentation all greatly enhance the project productivity.

Block	Function
Timer	Implements a gang of timers for generic timing signal generation.
Control	Interface for reading and writing SD3C configuration and control registers.
Down Converter	Combines an f_s/n down converter, a Kaiser filter and a Gaussian filter.
Pulse Tagging	Prepends an incrementing PRF pulse number, I/Q identifier, format identifier, and channel number to each received pulse.
Coherent Integration	Sums the samples for each range gate, for I and Q, for each channel.

Table 1: The SD3C firmware processing.

	449 MHz wind profiler	W-band cloud radar	K _a -band micro-physics radar
Application	Boundary layer dynamics	Cloud micro-physics	Cloud micro-physics & water vapor retrieval
Gate spacing	150m	37m	75 m
Range	7 km	15 km	75 km
PRF	40 kHz	10 kHz	1 kHz
Peak Power	3 kW	1.5 kW	35 kW

Table 2: Current applications of the SD3C.

The SD3C project has demonstrated that an FPGA solution, based on commercial hardware, brings many benefits to system developments such as those described here. The FPGA is capable of very high signal processing performance, thus mitigating large data bandwidths and host CPU loads. The technology facilitates very flexible applications: the same hardware can be customized to meet quite different requirements simply by loading the application specific firmware. Total system costs are reduced by leveraging the use of a single FPGA card among several systems, and by the consolidation of functions from many discrete hardware components onto a single card.

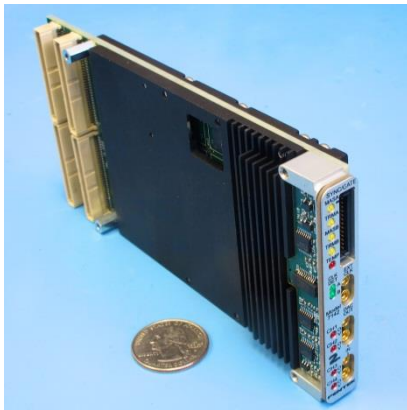


Figure 1: The Pentek 7142 FPGA digital transceiver.

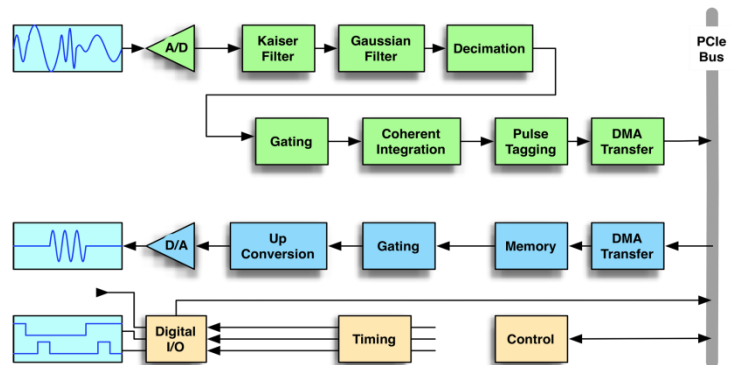


Figure 2: The SD3C FPGA firmware design.

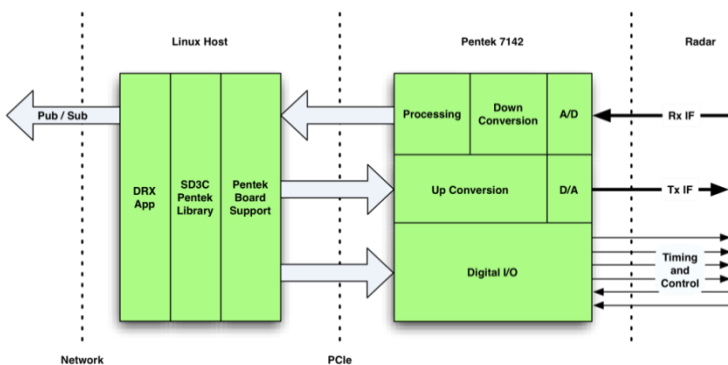


Figure 3: The SD3C firmware/software system architecture.

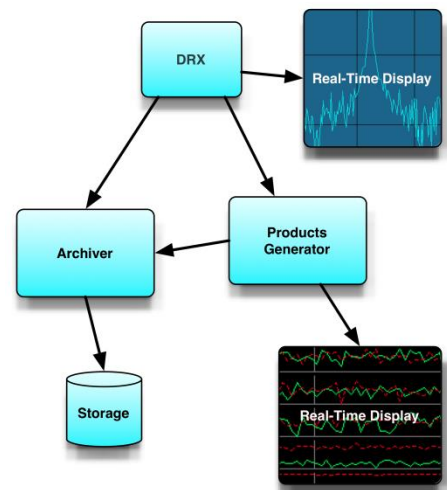


Figure 4: The publish/subscribe architecture isolates software components.

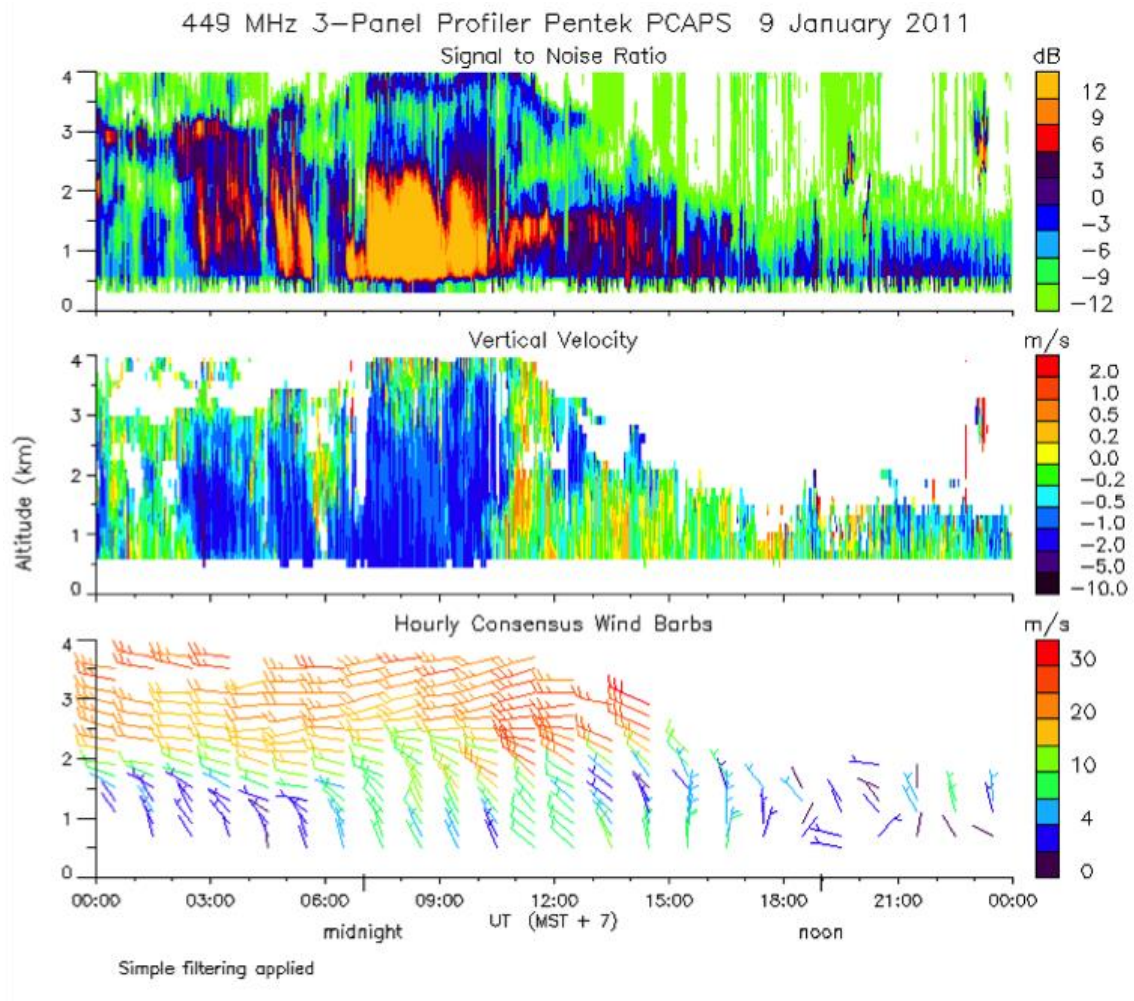


Figure 5: Observations from an SD3C-based 449 MHz spaced antenna wind profiler.

Adaptive suppression of aircraft clutter with the PANSY radar training system

Taishi Hashimoto¹

Koji Nishimura²

Kaoru Sato³

Toru Sato¹

¹Kyoto University

²National Institute of Polar Research

³The University of Tokyo

1. Introduction

1.1 Backgrounds

PANSY (Program of Antarctic Syowa MST/IS Radar) is a project to construct a large atmospheric radar at Antarctic Syowa Station.

PANSY is the first MST radar in the Antarctic region that is the only instrument capable of continuously monitoring three-dimensional structure of the air in high altitude and time resolutions, and thus is expected to substantially progress the polar atmospheric science. PANSY has two antenna arrays, large main array with 1045 Yagi antennas and smaller one towards the direction of the magnetic South Pole for the observations of FAI (Field Aligned Irregularity). Although FAI echoes are of great scientific interests, they can be interferences for the observation of ionospheric incoherent scattering around 100 km, so we must arrange a countermeasure in advance.

Ahead of the construction of PANSY, a training system named "Sumire" had been set up in Shigaraki MU Observatory, Japan. There is busy air traffic around the observatory, and their clutter has been a pending problem in the atmospheric observations of MU radar. Aircraft clutters are similar to FAI echoes in that they are both strong backscattering from rapidly moving objects, but it is less complicated because of its linear movement.

For the aircraft clutter suppression with atmospheric radars, a combination of adaptive beamforming and DOA (Direction Of Arrival) estimation has been suggested [1], which we call 2-constraint NC-DCMP, but the experimental verification has not been performed yet.

1.2 Objectives

The objective of this study is to exploit an algorithm of adaptive clutter rejection against moving objects for atmospheric radars.

In this paper, we show the result of applying 2-constraint NC-DCMP to actual observations. We also introduce another method and compare them in two different systems, Sumire and MU radar.

2. Methods and implementations

2.1 Directionally constrained Minimization of Power

The Directionally Constrained Minimization of Power (DCMP) is one of the adaptive beamforming algorithms for the special case of known desired directions. According to Takao [2], the basic theory of DCMP is written as a non-linear optimization problem

$$\begin{aligned}
& \min \left(P_{\text{out}} = \frac{1}{2} \mathbf{W}^H \mathbf{R}_{xx} \mathbf{W} \right) \\
& \mathbf{W} \\
& \text{subject to } \mathbf{C}^T \mathbf{W}^* = \mathbf{H} \\
& \mathbf{C} = [\mathbf{C}_1 \quad \mathbf{C}_2 \quad \cdots \quad \mathbf{C}_N] \\
& \mathbf{H} = [H_1 \quad H_2 \quad \cdots \quad H_N],
\end{aligned}$$

where $(\cdot)^*$ denotes the complex conjugate, $(\cdot)^T$ for the transposition and $(\cdot)^H$ for the adjoint (conjugate transpose) matrix. Here, N is the number of constraints. Assuming M receivers, $\mathbf{R}_{xx} \equiv \mathbf{X}\mathbf{X}^H$ is the covariance matrix of the received signals $\mathbf{X} = [X_1 \quad X_2 \quad \cdots \quad X_M]^T$. \mathbf{W} is the optimal weight vector for combined outputs Y , i.e. $Y = \mathbf{W}^H \mathbf{X}$. \mathbf{C}_j ($j = 1, \dots, N$) is called as the directional constraint, which is a function of the geometric location of each receiver \mathbf{L}_i ($i = 1, \dots, M$) and the desired direction (zenith, azimuth) (θ_j, ϕ_j) .

Using array manifold function $\mathbf{A}(\theta, \phi)$, C_{ij} can be written as

$$\begin{aligned}
C_{ij} &= A_i(\theta_j, \phi_j) = \exp\left(\frac{2\pi i}{\lambda} \mathbf{L}_i \mathbf{V}_j\right) \\
\mathbf{V}_j &= [\sin \theta_j \cos \phi_j \quad \sin \theta_j \sin \phi_j \quad \cos \theta_j]^T.
\end{aligned}$$

H_j is called as the constraint response against each corresponding \mathbf{C}_j .

H_j takes from 0 to 1, which determines the null depth or the peak height of the beam pattern toward the specific direction defined by \mathbf{C}_j .

1.1 Norm Constrained DCMP

The Norm Constrained DCMP (NC-DCMP) has an additional constraint about the magnitude of the norm of \mathbf{W} in DCMP,

$$\mathbf{W}^H \mathbf{W} \leq U.$$

Here, U is the norm constraint to preserve the shape of the main lobe even when only an incorrect steering vector is available.

In NC-DCMP algorithm, one can determine U from the permissive loss of gain in signal-to-noise ratio (SNR). The relationship between the SNR loss G_{SNR} and the norm constraint U is [3],

$$G_{\text{SNR}} = \frac{\left(1 + \alpha \sqrt{U/(M-1)}\right)^2}{1 + U},$$

where α takes from -1 to 1, which represents the phase rotational relation between each channel. $\alpha = 1$ means in-phase, which is obtained by the ideal beamforming method without clutter rejection availability.

$\alpha = -1$ means opposite-phase, which is the worst case suppressing the desired signals.

$\alpha = 0$ is the intermediate of these two cases, and we used this for deciding the norm constraint U in later sections.

Figure 1 is an example plotting of equation above at each $\alpha = -1, 0, 1$ for $M = 25$, which corresponds to the number of channels of the MU radar.

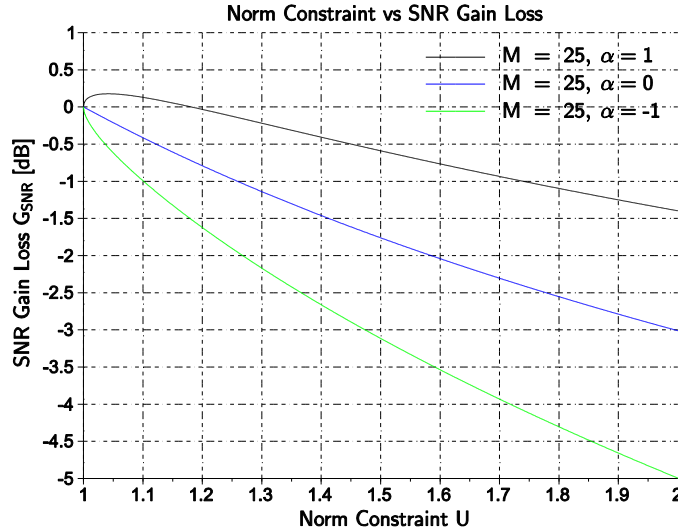


Figure 1: Relationship between norm constraint U and SNR gain loss G_{SNR} in the 25 channels radar system assuming the MU radar.

1.2 Algorithms for aircraft clutter suppression with atmospheric radars

For aircraft clutter rejection, there are two different approaches, 2-constraint or 2-step NC-DCMP. Both methods use the information about desired and undesired directions. In 2-constraint NC-DCMP, one assigns two directional constraints at a time. For atmospheric radars, the desired direction is the beam direction itself, while undesired directions, which are the directions of arrival of the clutters, are estimated by some sort of DOA estimating methods like MUSIC [4]. On the contrary, 2-step NC-DCMP uses each constraint sequentially. The procedure of 2-step NC-DCMP is as follows,

1. Estimates the direction of arrival of the clutter.
2. Performs 1-constraint NC-DCMP with the desired direction set toward the clutter. This means reproducing the clutter signals.
3. Subtracts the reproduced clutter signals from the original received signals.
4. Performs 1-constraint NC-DCMP again with the desired direction set toward the beam direction.

2. Applying to actual observations

2.1 Experimental settings and methods

Sumire has 4 channels shown in figure 2.

The main channel consists of 19 Yagi antennas and their outputs are combined into one, while the sub array has three elements and each has its own channel. Also the antenna positions of MU radar is shown in figure 3 MU radar has 25 channels, and each channel is a combination of output signals of 19 Yagi elements.

The observational parameters are set as the same with standard observations. The only difference between two systems is the sampling interval, which is 64 ms for Sumire and 128 ms for MU radar. Table 1 is the digest of the radar system setting in standard observations.

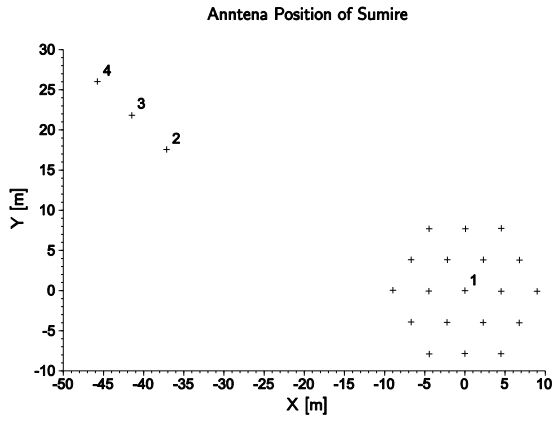


Figure 2: The antenna position of Sumire.

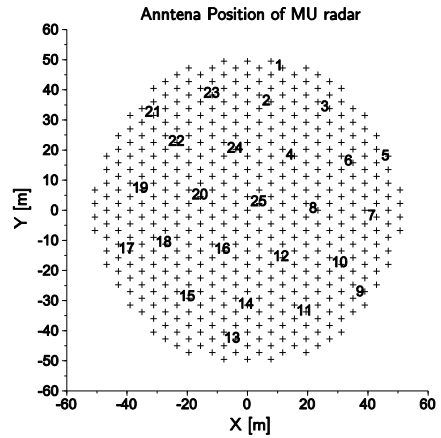


Figure 3: The antenna position of the MU radar.

Sampling Interval	64 ms for Sumire 128 ms for the MU radar
Range resolution	150 m
No. of Time samples	128
No. of range sample	128

Table 1: Radar system settings.

3.2 Results

Figures 4 and 5 are the comparison of results obtained by each combining methods, non-adaptive beamforming and 1-constraint, 2-constraint or 2-step NC-DCMP in two systems, Sumire and MU radar. As figure 4 shows, 2-step NC-DCMP works the best among all methods for Sumire. The aircraft clutters are suppressed by 23 dB in average, and the performance is improved by 5 dB against the 1-constraint NC-DCMP. However, 2-constraint NC-DCMP does not work for the negative frequencies. On the other hand, for MU radar, 1-constraint NC-DCMP works well as shown by figure 6. Aircraft clutters are suppressed by 38 dB, but 2-step and 2-constraint NC-DCMP show no advantage. Figure 5 and 7 are the results obtained by the best method for each system. Strong clutters at zero Doppler velocities are from the ground.

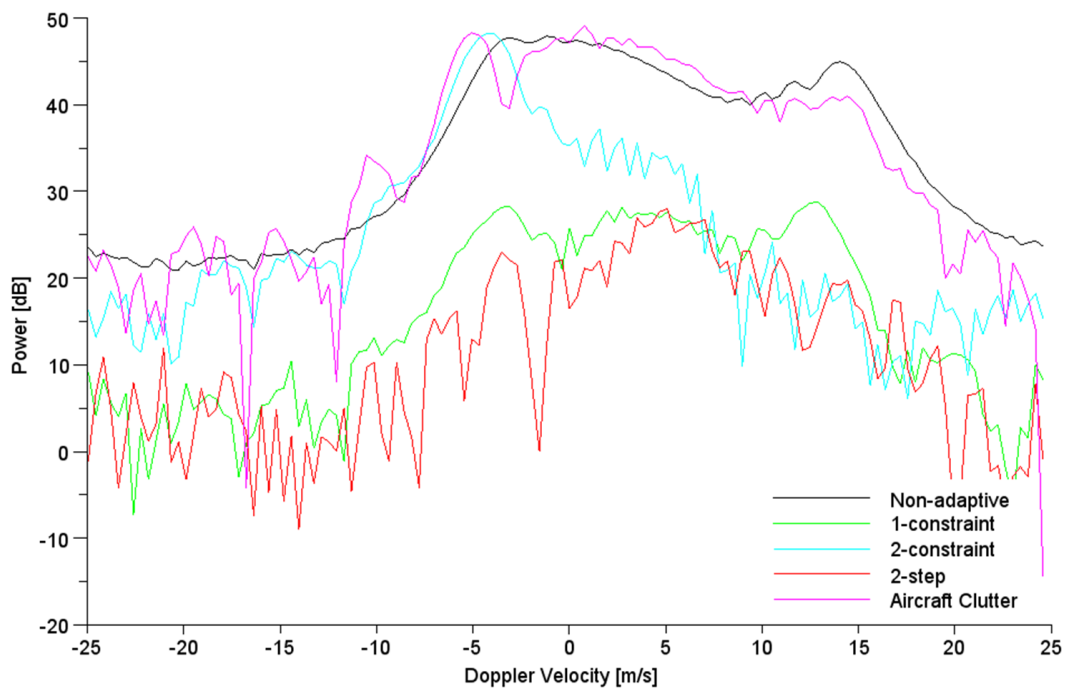


Figure 4: Spectra with aircraft clutters combined by various methods in Sumire.

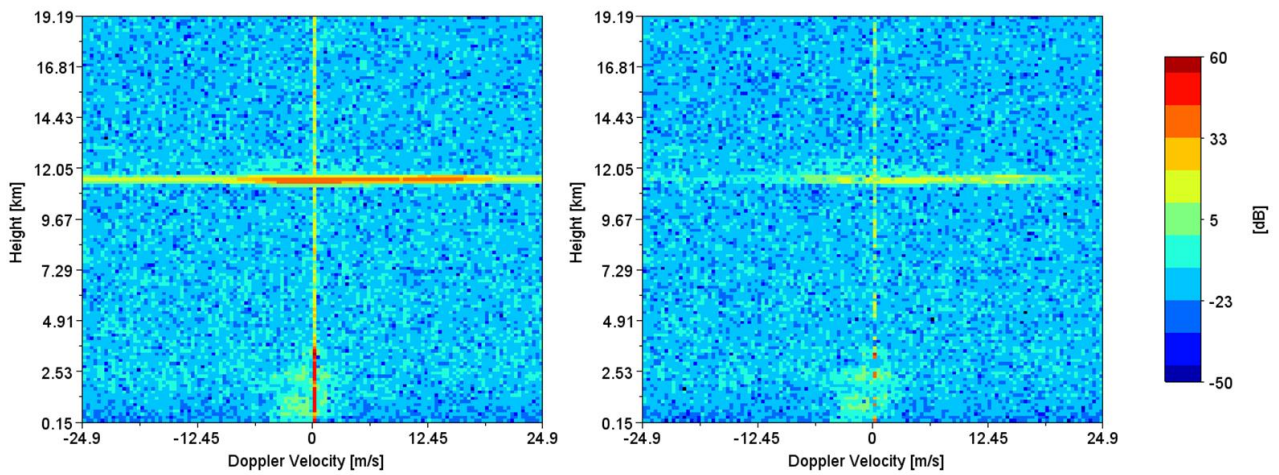


Figure 5: Doppler height patterns combined by the beamforming and NC-DCMP in Sumire.

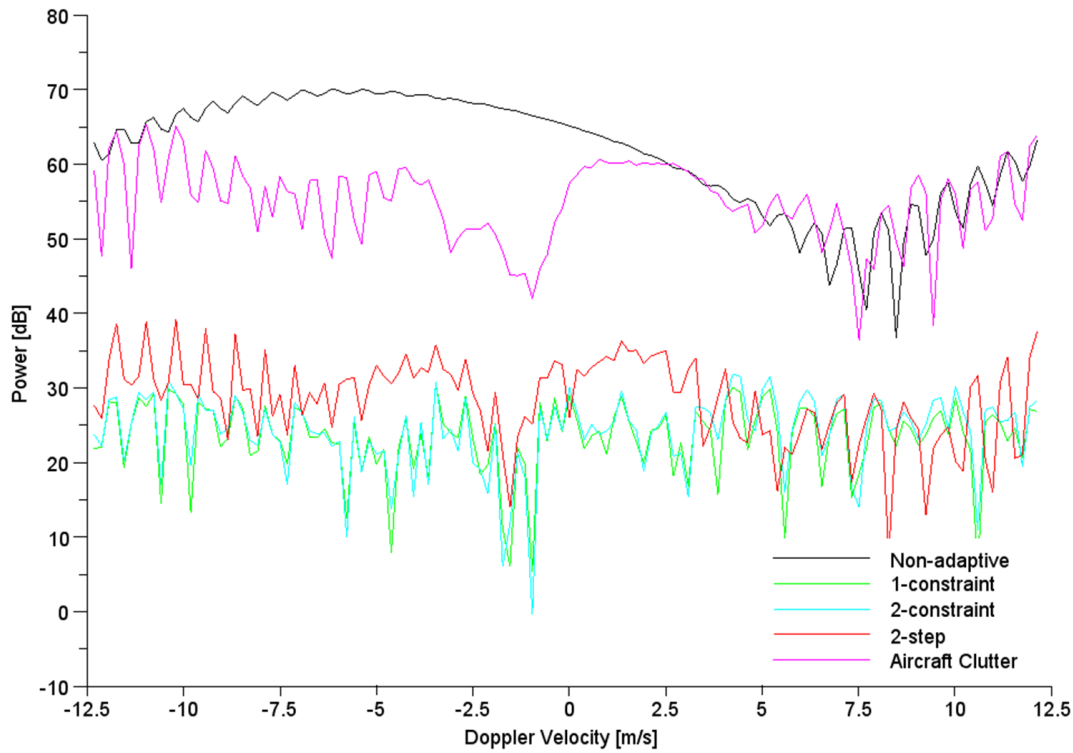


Figure 6: Spectra with aircraft clutters combined by various methods in the MU radar.

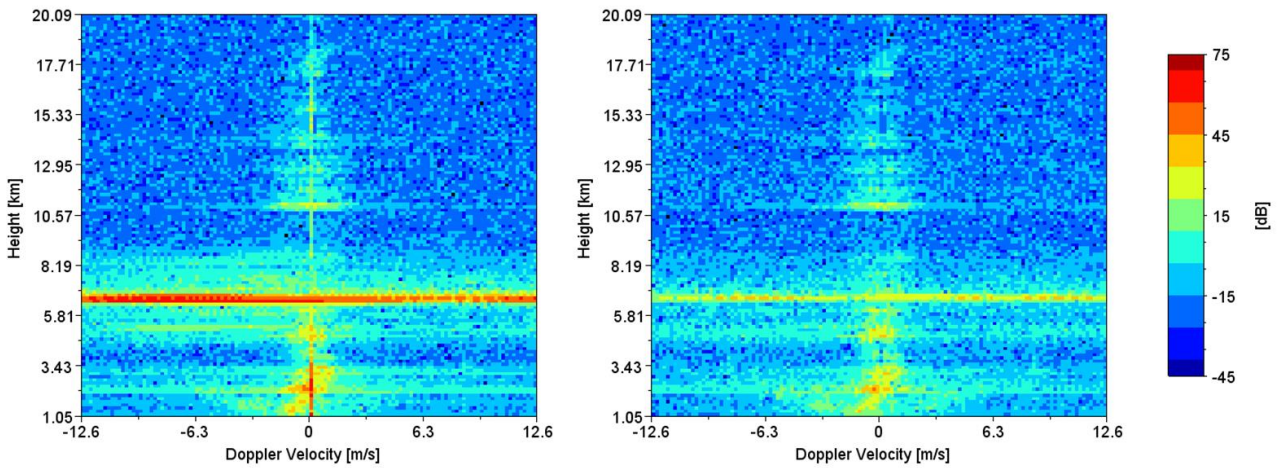


Figure 7: Doppler height patterns combined by the beamforming and NC-DCMP in the MU radar.

3.3 Considerations

Here, we give detailed considerations about the results obtained in the previous section.

The reason of why 2-constraint NC-DCMP failed for Sumire is thought to be the lack of degree of freedom of the antenna array. As figure 2 shows, Sumire has rather linear layout and the array freedom may be lost at the diagonal direction to the baseline. 2-step NC-DCMP have easier condition than 2-constraint NC-DCMP, because it works as 1-constraint NC-DCMP in each step, and thus it should work more efficiently in small systems like Sumire. As seen in figure 5, some ground

clutters are left to be suppressed for Sumire. These are also caused by the lack of degree of freedom.

On the contrary to the above, in large systems like MU radar, 1-constraint NC-DCMP worked the best, because of their greater degrees of freedom. Also this result is considered to show that 2-constraint or 2-step NC-DCMP require more accurate DOA estimation of clutter signals in large systems to meet their sharp beam shape. The reason why 2-constraint NC-DCMP shows better performance than 2-step NC-DCMP, which is opposite to the result for Sumire, is thought that even if the second directional constraint toward the wrong direction wasted the array degree of freedom, there would be still enough margin.

3. Conclusions

Adaptive clutter suppression algorithms with NC-DCMP and DOA estimations are examined with actual observations in two different systems, Sumire, the training system of PANSY radar, and MU radar. In small systems like Sumire, 2-step NC-DCMP works well and improved the performance by 5 dB against the ordinary 1-constraint NC-DCMP. On the other hand, in large systems like MU radar, 1-constraint NC-DCMP shows the best performance, because there are enough margins in the degree of freedom of the array. Also errors in DOA estimation are thought to cause more fatal inaccuracy on additional directional constraint in 2-constraint NC-DCMP, or on subtracting clutter signals in 2-step NC-DCMP.

On the basis of the discussions above, our future work is to improve the accuracy of DOA estimation and take the linear movement of the aircraft into account, i.e. introducing some sort of prediction filters.

References

- [1] Vijaykumar, A. Gupta, Adaptive clutter rejection by angle of arrival tracking using unscented filters for atmospheric radars, Proc. 11th Intl. Workshop on Technical and Scientific Aspects of MST Radar, 2006.
- [2] K. Takao, M. Fujita and T. Nishi, An adaptive antenna array under directional constraint, IEEE trans., Antennas and Propag., vol.21, pp.662-669, 1976.
- [3] K. Kamio, K. Nishimura, T. Sato, Adaptive sidelobe control for clutter rejection of atmospheric radars, Ann. Geophys., Vol. 22, 4005-4012, 2004.
- [4] R. Schmidt, Multiple emitter location and signal parameter estimation, IEEE trans., Antennas and Propag., Vol.34, pp. 276-280, 1986.

Renovation of the Aberystwyth MST radar: Evaluation

David A. Hooper¹, John Bradford¹, Les Dean², Jon D. Eastment¹, Marco Hess³, Eric Hibbett³,
John Jacobs⁴, and Richard Mayo³

¹ STFC Rutherford Appleton Laboratory, UK

² Aberystwyth University, UK

³ ATRAD, Australia

⁴ John Jacobs Consulting, UK

1. Introduction

During March 2011, the Natural Environment Research Council (NERC) MST Radar at Aberystwyth underwent its first major renovation in a 22 year lifetime. This principally consisted of a replacement of the Doppler Beam Swinging (DBS) phasing units. The design and installation of the new components was undertaken by the company ATRAD. As can be seen from the central panel of Figure 1, the renovation led to a remarkable 28% increase in the overall availability of horizontal wind data relative to pre-renovation levels. The quality of the data also appears to have improved. This extended abstract focuses on how geophysical considerations were used in order to evaluate the changes in radar performance.

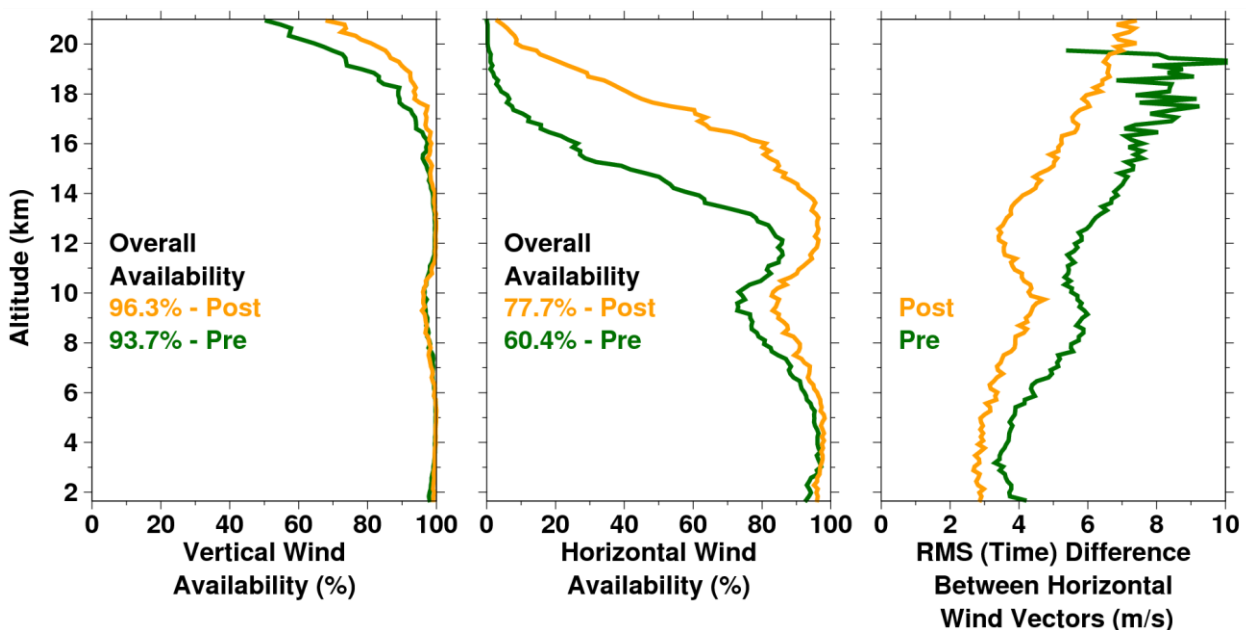


Figure 1: Statistical measures of radar performance for 18 days each of (green lines) pre-renovation observations (10th - 27th February 2011) and of (orange lines) post-renovation observations (18th March - 4th April 2011).

2. History of radar operations

For the first few years following its construction in 1989/1990, the radar was operated on a part-time basis. It would typically alternate between periods of use and non-use for up to a few

days at a time. From 1992, special observations were made at six hourly intervals on behalf of the Met Office. If the radar was not already in use, it would be powered up specifically for this purpose. The frequency of special observations was increased to three hourly in late 1994.

The radar was operated continuously for the first two and a half months of 1997. Although it reverted to part-time operations for most of the rest of that year, it has been operated on a quasi-continuous basis ever since October 1997. By 2005, the useful altitude coverage for wind-profiling purposes was noticeably lower than it had been in the first years of operation. The situation became progressively worse until the time of the renovation in 2011. During these 22 years of operation, the radar's hardware had remained virtually unchanged.

A detailed inspection of the entire system was carried out during late 2008. This suggested that the poor state of the electro-mechanical relays, which are used in the DBS phasing units, was the primary reason for the reduced performance. The beam pointing direction is changed every 24 s, which results in approximately 1 million switching operations per year. The relays are therefore subject to continual but slow degradation, particularly through contact erosion. Examples of this can be seen in *Eastment et al.* [2010]. The original relays were repeatedly reconditioned rather than being replaced. Although this was initially effective, in some cases the erosion had become so bad that the relays had to be removed from active service.

Over the past decade the majority of observations have been made using a standard cycle of 12, principally st-mode, dwells. This takes approximately 5 minutes to complete and uses 6 of the 17 available beam pointing directions: NE6.0, Vertical, SW6.0, Vertical, SE6.0, Vertical, NW6.0, Vertical, W4.2, Vertical, m-mode Vertical, Vertical. The names represent the nominal azimuths and the zenith angles. The actual azimuth angle is 17.5° less than the nominal value, e.g. NE implies 27.5° .

In order to be able to validate the performance of the renovated radar, a special cycle of 24 dwells was used for just over 2 weeks prior to the renovation and for 6 weeks afterwards. This took approximately 10 minutes to complete and used all 17 available beam pointing directions: NE12.0, NE6.0, Vertical, SW6.0, SW12.0, Vertical, SE12.0, SE6.0, Vertical, NW6.0, NW12.0, Vertical, W8.5, W4.2, Vertical, E4.2, E8.5, Vertical, N8.5, N4.2, Vertical, S4.2, S8.5, m-mode Vertical.

3. Evaluating the performance of the renovated radar

It can be seen from the previous section that the validation cycle comprises of scans along each of the available azimuths at 5 consecutive zenith angles, including 0.0° . In this context, azimuth angles separated by 180° are considered to be equal and the difference is attributed to a change in the sign of the zenith angle. This sequence allowed an immediate check to be made of beam pointing direction self-consistency from an inspection of the Doppler shift profiles. As expected (but not shown here), consecutive profiles for each azimuth were qualitatively similar, albeit with the signs and magnitudes of the Doppler shifts changing as a function of the zenith angle. A quantitative measure of this self-consistency was also immediately available for the observations made at 6.0° off-vertical, i.e. the primary zenith angle used for wind-profiling purposes. The differences between the horizontal wind components derived from opposing beam pointing directions are used by the signal processing for quality control purposes [*Hooper et al.*, 2008]. The post-renovation values were similar to those for the pre-renovation period.

It was possible to demonstrate the consistency between pre- and post-renovation beam pointing directions using the spectral noise power. For each direction there is a distinct diurnal pattern, which follows the variations in lower-VHF cosmic emissions along a circle of constant declination [*Campistron et al.*, 2001]. This pattern is repeated once each sidereal day and so is

seen approximately 4 minutes earlier on consecutive solar days. Figure 2 relates to observations made by the NE6.0 beam (declination $+57.65^\circ$). These include an off-centre transit by Cassiopeia-A (declination $+58.80^\circ$) at around 13:00 UT for the pre-renovation period and at around 11:30 UT for the post-renovation period. The radar beam has a one-way half-power half-width of 1.5° . It is noted that the amplitude of the transit feature is approximately 1 dB greater for the post-renovation period. There are also noticeable offsets between the two sets of lines at other times of the day. Although these differences are smaller than those between the patterns for different beam pointing directions, they suggest a slight change in the beam shape and/or pointing direction. It is likely that at least some of the original relays were no longer functioning. This would have caused the off-vertical beam pointing directions to be closer to the vertical than expected. This, in turn, would have led to horizontal wind speeds being slightly underestimated. However, as will be seen shortly, this appears to have been compensated, to some extent, by another effect. Surprisingly, the Met Office model-comparison statistics - see *"The usefulness of model-comparison statistics for wind-profiling radar operators"* in these proceedings - suggest a negligible change in wind speed bias as a result of the renovation.

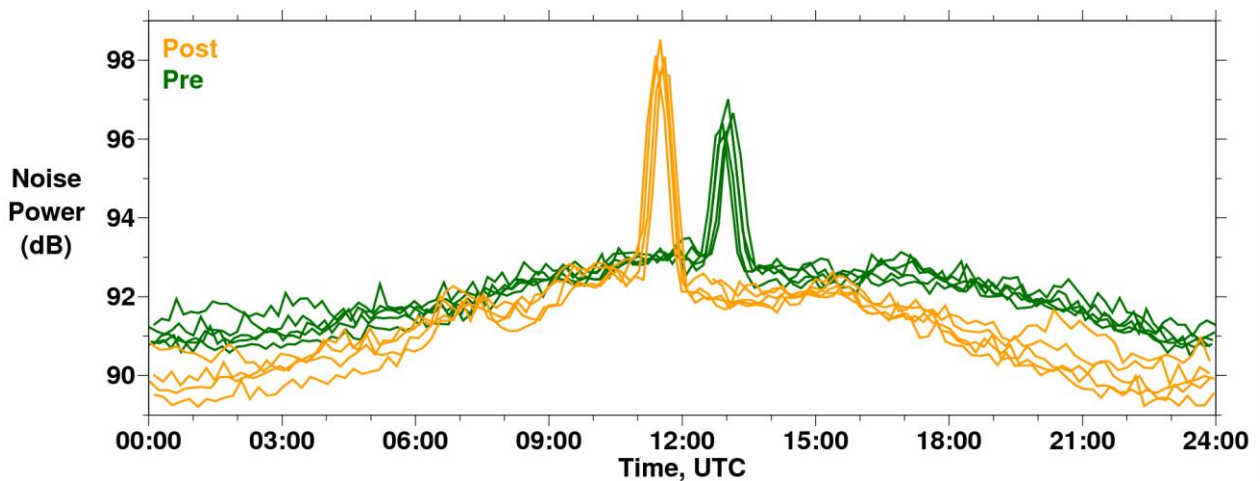


Figure 2: NE6.0 beam noise power, averaged over all range gates, for 5 consecutive days of (green lines) pre-renovation observations (23rd - 27th February 2011) and of (orange lines) post-renovation observations (17th - 21st March 2011).

None of the relays is activated in order to make observations in the Vertical direction. At least some of the relays must be activated for all other beam pointing directions. It can be seen from Figure 1 that the renovation led to a 28% increase in the overall availability of horizontal winds, relative to pre-renovation levels, but to only a 3% increase for vertical winds. This suggests that the original relays were attenuating signals, but primarily only when they were activated. There is further evidence for this in Figure 3, which shows two different measures of aspect sensitivity. The 6° off-vertical beam signal power decrease, relative to the Vertical beam, is expected [Hooper and Thomas, 1995] to be often (but not exclusively) close to 0 dB for tropospheric altitudes (lower left-hand panel). Although this is clearly the case for the post-renovation observations, it was rarely so during the pre-renovation period. The aspect sensitivity is expected to be generally larger for lower-stratospheric altitudes (top-left panel), but here too the pre-renovation distribution is significantly offset from the post-renovation one. These differences are consistent with the original relays causing 4 - 6 dB more attenuation for the 6° off-vertical beams than for the Vertical beam.

Aspect sensitivity causes the magnitude of the effective pointing zenith angle, θ_{eff} , for off-vertical beams to be slightly smaller than the nominal angle. This leads to the horizontal wind speed being slightly underestimated. However, a compensation factor can be applied through consideration of the θ_s parameter [Hocking *et al.*, 1986], which is determined from the ratio of signal powers observed at two zenith angles. This is routinely applied for observations made by the Aberystwyth MST radar using observations made at 4.2° and 6.0° off-vertical [Hooper and Thomas, 1995]. The right-hand panels of Figure 3 suggest that the wind speeds were being over-compensated by approximately 6% prior to the renovation. However, as mentioned previously, this effect appears to have been balanced by a slight reduction in off-vertical beam zenith angles. The root mean square (RMS) of the magnitude of the differences between adjacent horizontal wind vectors in time gives a combined measure of natural variability of the wind and of the random measurement errors [e.g. Hooper *et al.*, 2008]. The profiles shown in the right-hand panel of Figure 1 suggest that the random errors might indeed be smaller post-renovation.

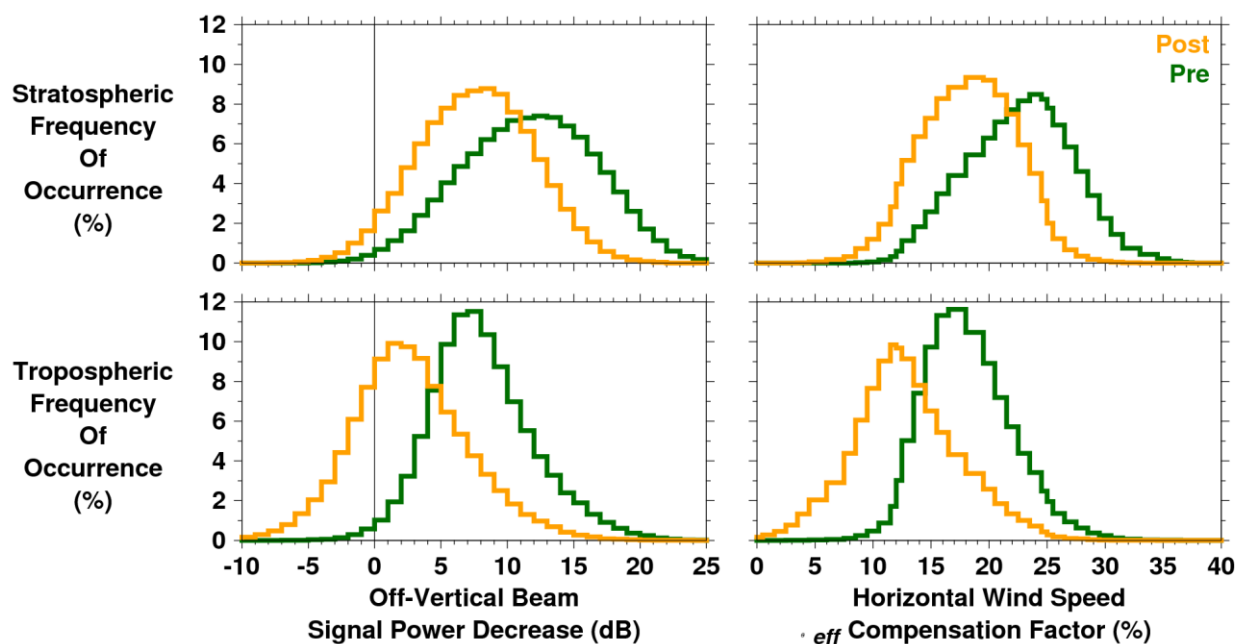


Figure 3: Two different measures of aspect sensitivity based on 18 days each of (green lines) pre-renovation observations (10th - 27th February 2011) and of (orange lines) post-renovation observations (18th March - 4th April 2011).

4. Further work

It will be necessary to extend the RMS horizontal wind vector difference analysis over longer periods and pre- and post-renovation periods in order to encounter a wider range of atmospheric conditions. This will increase the confidence that the reduction in values does not represent a smaller range of natural variability during the post-renovation period. Moreover, the aspect sensitivity analysis needs to be extended over the entire observation archive in order to determine at what point the degradation of the original relays started to affect the quality of the data.

References

- Campistron, B., G. Despaux, M. Lothon, V. Klaus, Y. Pointin, and M. Mauprivez, A partial 45 MHz sky temperature map obtained from the observations of five ST radars, *Ann. Geophys.*, 19(8), 863–871, 2001.
- Eastment, J. D., W. J. Bradford, D. A. Hooper, Z. A. K. Olewicz, O. T. Davies, and L. Dean, The effects of almost 20 years of operation on the performance of the Aberystwyth MST radar, in *Proceedings of the Twelfth International Workshop on Technical and Scientific Aspects of MST Radar*, edited by N. Swarnalingam and W. K. Hocking, pp. 119–122, Canadian Association of Physicists, Ottawa, Ontario, Canada, ISBN:978-0-9867285-0-1, 2010.
- Hocking, W. K., R. Rüster, and P. Czechowsky, Absolute reflectivities and aspect sensitivities of u VHF radio wave scatterers measured with the SOUSY radar, *J. Atmos. Terr. Phys.*, 48(2), 131–144, 1986.
- Hooper, D., and L. Thomas, Aspect sensitivity of VHF scatterers in the troposphere and stratosphere from comparisons of powers in off-vertical beams, *J. Atmos. Terr. Phys.*, 57(6), 655–663, doi:10.1016/0021-9169(94)00056-T, 1995.
- Hooper, D. A., J. Nash, T. Oakley, and M. Turp, Validation of a new signal processing scheme for the MST radar at Aberystwyth, *Ann. Geophys.*, 26(11), 3253–3268, doi:10.5194/angeo-26-3253-2008, 2008.

Extraction of horizontal wind velocities from a multi receiver phased array radar system using post beam steering technique and efficiency of various beamforming methods

VK Anandan¹, VN Sureshababu¹, Toshitaka TSuda², Jun-ichi Furumoto²

¹ ISTRAC, Indian Space Research Organisation, Bangalore -58, India

² Research Institute for Sustainable Humanosphere (RISH), Kyoto University, JAPAN

Abstract

Postset Beam Steering (PBS) technique has been used to extract horizontal winds from the data collected from multi receiver phased array atmospheric radar (Middle and Upper (MU) atmospheric radar). PBS includes various signal processing algorithms such as beamforming, spectral estimation, moments estimation and etc. Capon beamformer is used for beam synthesizing in the desired direction within the radar beam width. Using the synthesized beam, the power spectrum is obtained through various power spectral estimation methods such as Fourier (non-parametric), Multiple Signal Classification (MUSIC) and Eigenvector (EV) methods. A study has been carried out to analyze the performances of the spectral estimators for better moments computation and thus wind estimations. Results suggest that EV based spectral estimation is a best approach (among three) for complete wind profiling up to the maximum height about 20 km with a temporal resolution about 1.3 min. The analyzed results are in good agreement with other wind observational methods in contiguous time.

1. Introduction

In this article, a comparative study has been carried out using spectral based techniques on data received from middle and upper atmospheric (MU) radar at Shigaraki, Japan. MU radar, mono static pulsed phased array radar, operates at 46.5 MHz with a peak power of 1 MW. The antenna array is also capable of steering the beam electronically using phase shifters in transmit and receive path. The experiment was conducted with full array of transmission (beam width 3.6°) in vertical direction. Signals received from spatially separated antennas are made to interfere constructively by phasing the received signals within the transmit beam width. This technique is used to synthesize the beams in the desired directions and so called as Post Beam Steering Technique (PBS) [3]. As these measurements typically involve reception of signals by minimum three spatially separated arrays, the vertically received signals are steered along the desired line of sight angle by introducing systematic phase shifts in the received signals themselves. The beam steering can be optimized by weighting vectors through beamforming approach like Capon method [2], [5]-[6]. Then the weighted steered signals are combined linearly to produce a two-way beam pattern in the desired line of sight angle within the transmit beam volume. The power spectrum in the desired AOA is obtained by various spectral estimation methods, such as Periodogram (Fourier), MUSIC [1], [5] and EV, from the synthesized beam (time series signal) in a given direction.

As the power spectrum is obtained by various power spectral estimation methods, a comparative study has been carried out to analyze the performances of the spectral estimators for better moments computation [4] and thus wind estimations. Results suggest that EV based spectral estimation is a best approach (among three) for complete wind profiling up to the

maximum height about 20 km with a temporal resolution about 1.3 min. The obtained results are compared with other wind observational methods like DBS and GPS sonde in contiguous time.

2. System description and data processing

MU radar located in Shigaraki, Japan ($34.85^{\circ}\text{N}, 136.10^{\circ}\text{E}$) has a large circular antenna array of 110 m in diameter with 475 crossed Yagi elements, the peak transmission power of 1 MW, and the bandwidth of 3.5 MHz. This frequency band is divided into five overlapping sub bands with the interval of 0.25 MHz and the bandwidth of 1.65 MHz. These sub bands are alternatively switched by pulse-to-pulse manner for obtaining phase information about targets. For receiving, the antenna array can be separated to 25 sub-arrays (channels) that have independent signal processing and storage units for spatial interferometry. The observation is conducted with full array of transmission (beam width 3.6°) in vertical direction for PBS technique. A $1\ \mu\text{s}$ transmitted pulse is used for 150 m range resolution. The sampling time including all coherent integrations is set to be 0.1024 s and each record of 256 time series points are obtained for 25 channels. The data collected from 25 channels are subjected to PBS technique to synthesize new beams at 1.7° tilt angle with 32 equally spaced azimuth positions. The power spectra at different line of sight angles are independently obtained as mentioned in the sections II for 5 overlapping sub bands and the sequence are repeated for three times. In this way, 15 power spectra are obtained from one record itself. All the fifteen (5x3) spectra are integrated to improve the SNR. From the average spectrum, zeroth order (total power) and first order (mean velocity) moments are calculated through adaptive moments estimation method [4]. Thus, radial velocities from corresponding line of sight angles are readily obtained. As a result, the horizontal wind components i.e. zonal and meridional velocities are derived by least squares sense.

3. Results

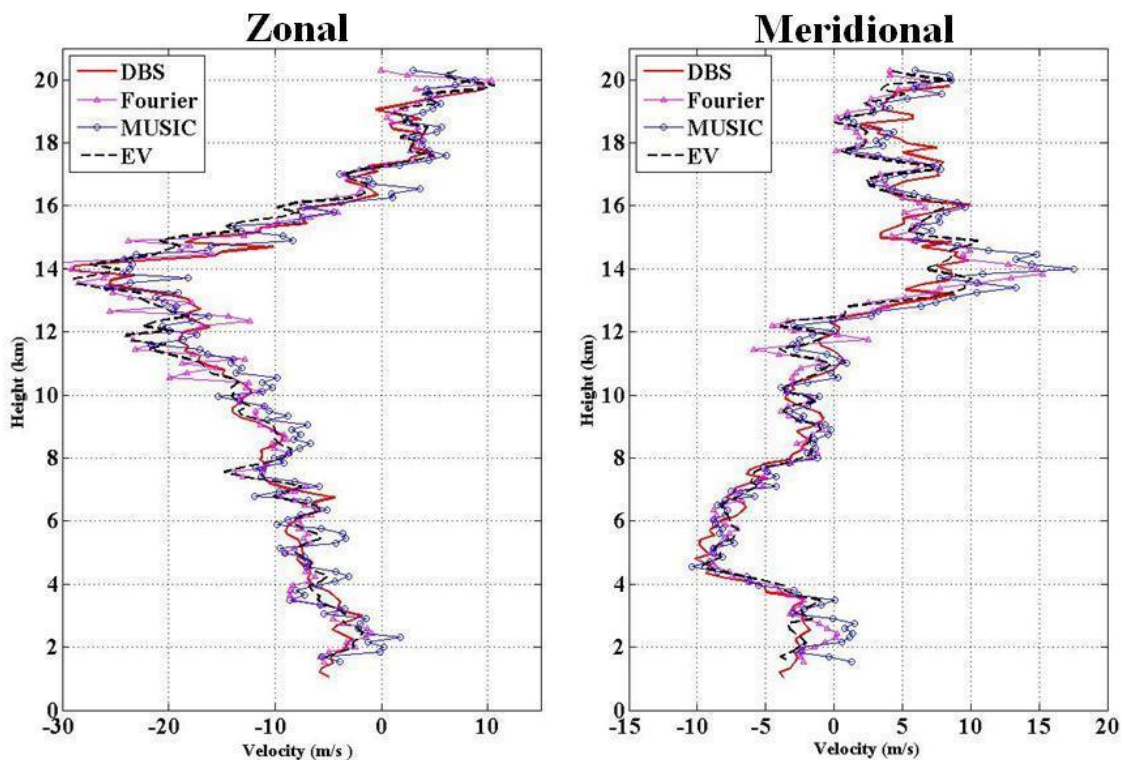


Figure shows the vertical profile of horizontal winds derived using PBS technique and compared with DBS derived winds (red thick line) in near time. The profiles corresponds to DBS wind observation on Jul 18, 2008, 0413 LT and PBS observation at 0401 LT

In this section, the horizontal wind components derived by PBS technique (1.7° tilt angle with 16 beam configuration) using Capon beamforming method have been compared with DBS and GPS sonde estimated winds in near time. As the moments are obtained through frequency domain, performances of various spectral estimation methods, in deriving atmospheric winds are quantitatively analyzed. The comparison of performances of spectral estimators in deriving winds is given in Fig.1. It is observed that PBS derived winds are shown in comparison with standard DBS derived winds up to a height about 20 km. In DBS observational method, tilt angle was 10°. Fig.1 reveals that horizontal wind velocities can be derived reliably by tilting the beam at 1.7° itself say within transmit beam width. Earlier study has reported [7] wind profiling from 6 to 15 km with a temporal resolution of 10 min using Imaging Doppler Interferometry (IDI) technique and about 10 km height with a temporal resolution of 5 min by Coherent Radar Imaging (CRI) using Capon's method [6] in time domain analysis. In simulation study, it has been realized that subspace methods improve SNR for atmospheric signals compared to Fourier based method. Particularly MUSIC improves SNR of the signal compared to other two spectral estimators. In the case of atmospheric signal, the power spectral distribution is of Gaussian shaped. But, the power spectrum produced by MUSIC is sharply peaked (line/pseudo spectrum) at the frequencies of the sinusoidal components of the signal. Though it is an advantage by de-noising the noise fluctuations in atmospheric signals through eigen-decomposition, the retrieval of spectrum width by MUSIC is not reliably observed to be same as Fourier based method. The spectrum width derived by Fourier based method can be reliable and so it has been considered as a reference in this paper. The impact of error in spectrum width retrieval by MUSIC has led to uncertainty in the measurement of radial Doppler frequency and thus horizontal winds. So, there are derivations in winds estimated by MUSIC in comparison with standard DBS observed winds. Hence, MUSIC could not be considered as a best spectral estimation method for wind estimation on atmospheric radar data. It is clearly noticed in Fig.1. In addition, Fourier based spectral estimation methods are more suitable for atmospheric radar signals. But, identifying atmospheric signal in low SNR regions is difficult and may not be reliable. Hence, there are deviations in wind estimation in comparison with standard DBS observed winds in mostly low SNR regions.

When MUSIC is weighted by eigenvalue, EV is derived as mentioned in the previous section. EV not only improves SNR, as in the case of MUSIC, it produces Gaussian shaped power spectrum, which almost resembles with Fourier based spectrum. EV does not find the problem faced by MUSIC in the computation of spectrum parameters. Also appreciable spectrum width has been observed rather than sharp peak. Again, the wind profile obtained using EV has very close agreement with DBS observed winds in various low SNR regions and so the possibility of complete and high temporal wind profiling is reported for the first time. Through this study, it is also revealed that EV has the advantage of (i) identifying atmospheric signal buried in noisy environment (ii) obtaining spectrum parameters (moments) (iii) cleaning the spectrum through de-noising process (iv) improving SNR (v) high temporal (about 1.3 minutes) wind profiling and (vi) maximum height coverage (about 20 kms) for profilers. However, there are small deviations in wind derived by EV compared to DBS winds. These deviations are attributed with bias in different observational methods, different tilt angle usages in the comparison, time of observations, atmospheric condition and quality of the data. The statistical analyses, such as slope value by linear fit, correlation coefficient and Root Mean Square Error (RMSE), on the performance of spectral estimators in PBS wind estimates with DBS wind estimates are given in Table 1.

Spectral estimation method	Slope		Correlation coefficient		RMSE (m/s)	
	U	V	U	V	U	V
Fourier	0.95	0.84	0.78	0.74	2.9	3.68
MUSIC	0.9	0.82	0.71	0.7	3.2	4.01
EV	1.03	0.89	0.87	0.81	1.81	2.34

Table 1: The performance of spectral estimators in PBS wind estimates (1.5 km -19.5 km) in comparison with DBS observational method. Statistics correspond to the MU radar data observed on Jul 18, 2008, 0413 LT and PBS observation at 0401 LT.

In the Table 1, DBS observed winds have been considered as mean winds. The performance of EV (for longer data sets) has been observed to be better than other two spectral estimators in different date and time. These results suggest that EV could be a best approach for PBS based wind estimation method. The best performance of EV is also observed in comparison with GPS sonde observed winds.

4. Conclusion

PBS technique has been used to derive horizontal winds using MU radar data. A detailed study has been investigated to encompass the best spectral estimator suitable for PBS wind estimates. In this study, the best performance and accuracy of EV in wind estimation have been revealed to identify and trace the atmospheric signals in noisy environment, which help the complete wind profiling up to the maximum height and is an alternate method to Fourier based spectral estimation. The winds derived using EV spectral estimator are in very good agreements with standard DBS and GPS sonde observed winds in near time. The systematic improvements done for PBS based wind observation have revealed the complete wind profiling up to the maximum height about 20 km with a temporal resolution about 1.3 minutes. Statistical analyses have also shown the consistency and reliability of EV in deriving the winds. The study has brought out the advantage of wind profiling using PBS for high temporal resolution compared to DBS based wind estimation with almost same height coverage. Such high temporal estimation can be reliably used to study the fast changing non-homogeneous wind fields during disturbed atmospheric condition.

References

- [1] E Boyer., M. Petitdidier., W. Corneil., C. Adnet., P. Larzabal, 2001: Application of model-based spectral analysis to wind-profiler radar observations. *Ann. Geophys.*, 19, 815-824.
- [2] M.Y Chen., T.Y. Yu, Y.H. Chu, W.O.J. Brown., S. A. Cohn., 2007: Application of Capon technique to mitigate bird contamination on a spaced antenna wind profiler. *Radio Sci.*, 42, 1-12.
- [3] J Rottegr., H Ierkic., 1985: Postset beam steering and interferometer and application of VHF radars to study winds, waves and turbulence in the lower and middle atmosphere. *Radio sci.*, 20(6). 1461-1480.
- [4] V.K Anandan., P Balamuralidhar., P. B Rao., A. R Jain., C. J Pan., 2005: An adaptive moments estimation technique applied to MST radar echoes. *J. Atmos. Oceanic Technol.*, 22, 396-408.

- [5] H Krim., M Viberg., 1996: Two decades of array signal processing research, *IEEE signal processing magazine*, 87-94.
- [6] R.D Palmer., S Gopalam., T Yu., S Fukao., 1998: Coherent radar imaging using Capon's method. *Radio Sci.*, 33, 1585–1598.
- [7] R.D Palmer., X Huang., S Fukao., M Yamamoto., T Nakamura., 1995: High resolution wind profiling using combined spatial and frequency domain interferometry. *Radio Sci.*, 30, 1665-1679.

Good Resolution at High Effective Power without Traditional Pulse-Coding

W.K. Hocking¹, A. Hocking², D.G. Hocking³ and M. Garbanzo-Salas¹

¹ University of Western Ontario, 1151 Richmond St., London, Ontario, Canada N6A 3K7

² Mardoc Inc., 18 Pitcarrie Cres., London, Ont. Canada, N6G4N4

³ The Myrans Group, 33 Strasbourg Ramble, Port Kennedy, WA, Australia, 6172

Abstract

Pulse coding using phase-flipping between successive sub-elements is currently the most common procedure used to produce fine height resolution with high power. However, new developments with radar processor design have permitted better approaches to data-recording and analysis. Using several multi-core CPUs, we have been able to achieve speeds of up to 40GHz from a standard commercial motherboard, allowing data to be digitized and processed without the need for any type of hardware except for a transmitter (and associated drivers), a receiver and a digitizer. No Digital Signal Processor chips are needed, allowing great flexibility with analysis algorithms. As a result of these advances, we have been able to re-address the modes of optimal pulse compression, and these are discussed in this paper.

1. Introduction

Most previous radars have been limited by digitization speeds, and systems have been designed so that the received radio-frequency signal (RF) is beaten down to an intermediate frequency (IF), and then further beaten down to baseband, through a series of mixers. Mixers introduce additional harmonics, requiring extra filtering, and increase receiver noise levels, but this has been necessary to permit slower digitization rates. Normally in-phase and quadrature components are separately sampled at a digitization frequency of 1 MHz or less.

With the advent of multi-CPU computers, and the possibility to apply threads to allow different CPU's to process different pulses, it is now relatively easy to sample the data at the radio-frequency of the radiowaves, and yet still be able to process the data in real-time. This capability allows alternative strategies such as chirped pulses, and even pulse shape variations from pulse to pulse.

2. A New radar Design

We have built a new radar which can sample at speeds of several tens of MHz, and then process all the data and produce real and imaginary components in real time without the need for any hardware except a wave-form generator and a digitizer. By also recording the transmitted pulse, real-time deconvolution with the transmitted pulse can be performed. This permits optimal resolution, and by interleaving pulses of different frequency, can even be used to remove range-ambiguity effects in high PRF systems. A deconvolution procedure was applied in earlier years by Rottger and Schmidt (1979), but that required special post-acquisition processing – our new system is the first that we are aware of that does deconvolution in real-time. The key aspects of our new procedure are discussed below.

1. The RF waveform is digitized for each receiver, and also for the transmitter. The clock speed in our case was 12.5 MHz, but values between 10 and 150 MHz were available. Our choice

of 12.5 MHz results in a frequency-aliased signal, since the original RF was 46.6 MHz, but because our receiver filter has a -30dB bandwidth of 4 MHz, we know that the bulk of the recorded signal is actually within +/-2MHz of 46.6 MHz. The digitizer produces spectra between -6.25 and 6.25 MHz, and so the aliased RF is received at +/- 3.4 MHz, in each case with a bandwidth of +/-2 MHz. These aliased frequencies can easily be de-aliased.

2. Only the real component is recorded - no In-phase or Quad components are produced at this time. This reduces digitization time and storage.

3. Each pulse is Fourier transformed using a C++ code running on multiple co-processors, with each new pulse being allocated to a new CPU. Programming is done using threads to track the progress of each FFT. The FFT is performed using a Singleton Mixed Radix FFT allowing factorization down to primes less than 23.

4. The spectra are de-aliased and then shifted to baseband. Single side-band procedures are used to recover the i/p and quad components.

5. A limited, user-specified bandwidth of data is selected for storage. Bandwidth allocation depends on the desired pulse resolution.

6. A complex division of the receiver FFTs by the Transmitter FFT results in an efficient deconvolution. Typical effective computer speeds of 30-40 GHZ are achieved, permitting real-time analysis. User-specified filters may be applied. These are supplied in Fortran software and can be of any chosen form (Hanning, Hamming, Butterworth, etc.)

7. The resultant spectrum is inverse-Fourier transformed to produce a deconvolved height-series of points.

8. Generally 20-25 seconds of data are recorded on the digitizer card while the computer analyses the previous data block in parallel, reducing down-time to a minimum.

9. Data are extracted from this height profile at user-specified range-gates, and collated into storage files for standard subsequent analysis.

10. The real-time deconvolution produces optimal signal-to-noise. Long pulses with a swept-frequency carrier are used - typically a pulse with a length of 2 -4 km is used, but during the duration of the pulse, the frequency is swept by 2 or 3 MHz or more. Hence the pulse contains a sufficient range of frequencies so that upon deconvolution the system may achieve a resolution of 30-50 metres.

11. Subsequent analysis is standard (determination of time-series spectra, winds, interferometry, etc.)

3. Advantages of the new Method

Pulse coding procedures record one point per pulse-element, and the sampling must be locked to the inter-element spacing (e.g. Farley, 1985 and references there-in). The new deconvolution procedure requires no such locking, and points are sampled approximately at 5-15m steps (depending on clock frequency), giving a much higher data rate and consequently better signal-to-noise. In our case the steps are 12m. Use of software filters allows greater flexibility in filtering processes.

Pulse coding can be subject to the existence of serious sidelobes - sidelobes with a deconvolution procedure are quite minimal.

Deconvolution also reduces the need for high frequency stability of the oscillator, since variations in frequency occur simultaneously in the receiver and the transmitter signal. Stability only needs to be good within the length of the IPP - a stability of 1 part in 10^6 over one IPP is adequate. RF digitization permits software correction of any receiver non-linearities.

The ability to choose all filters in software allows optimal reduction of noise, since RF filters as narrow as a few kHz or as wide as several MHz can be chosen. A flow-chart summarizing the system can be seen in fig. 1.

4. A Test System

A prototype system was built and tested at the Santa Cruz campus of the University of Costa Rica. The site was chosen due to the availability of a wide frequency bandwidth allocation.

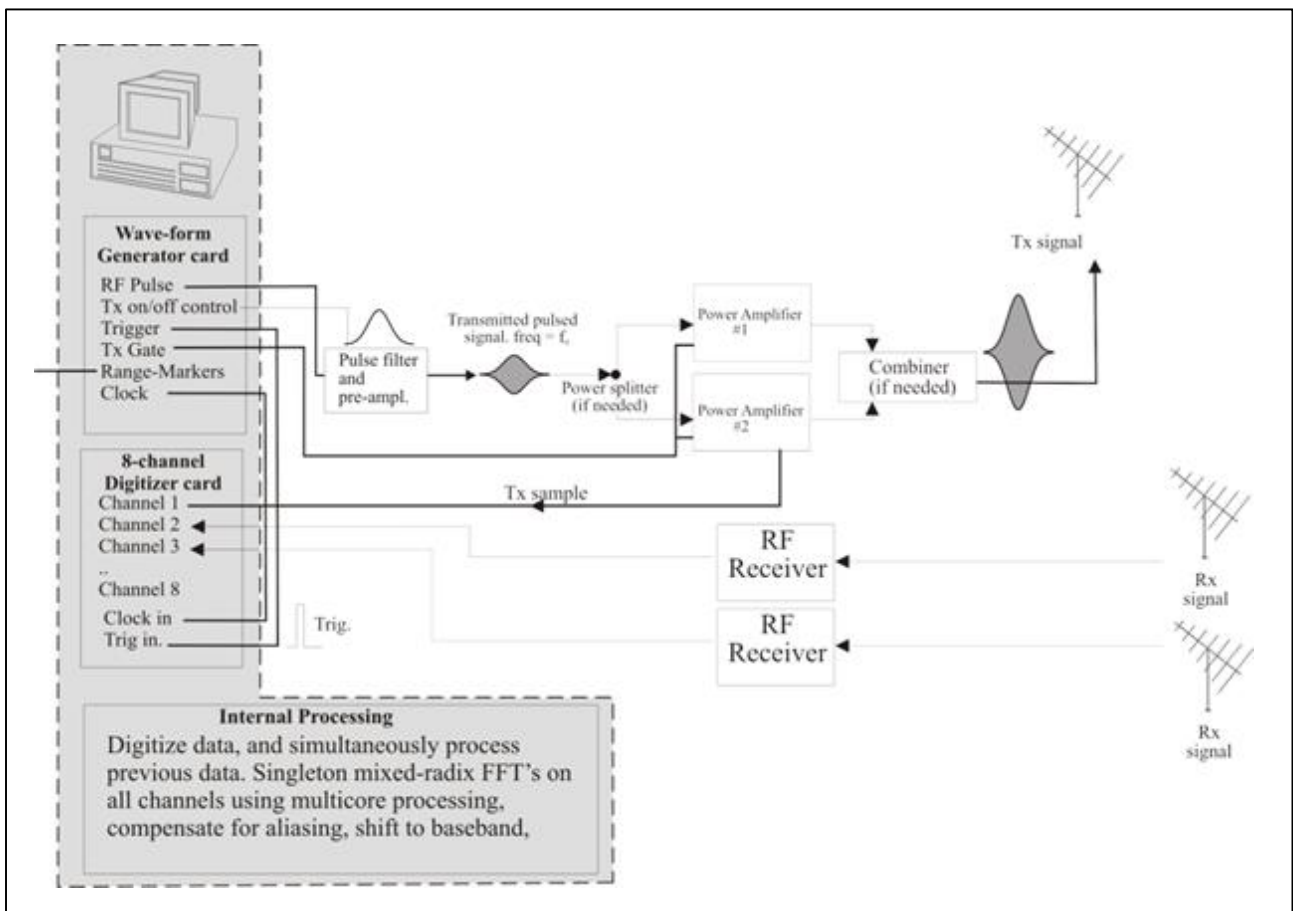


Figure 1: Flow chart showing the new transmitter-control and digitization hardware.

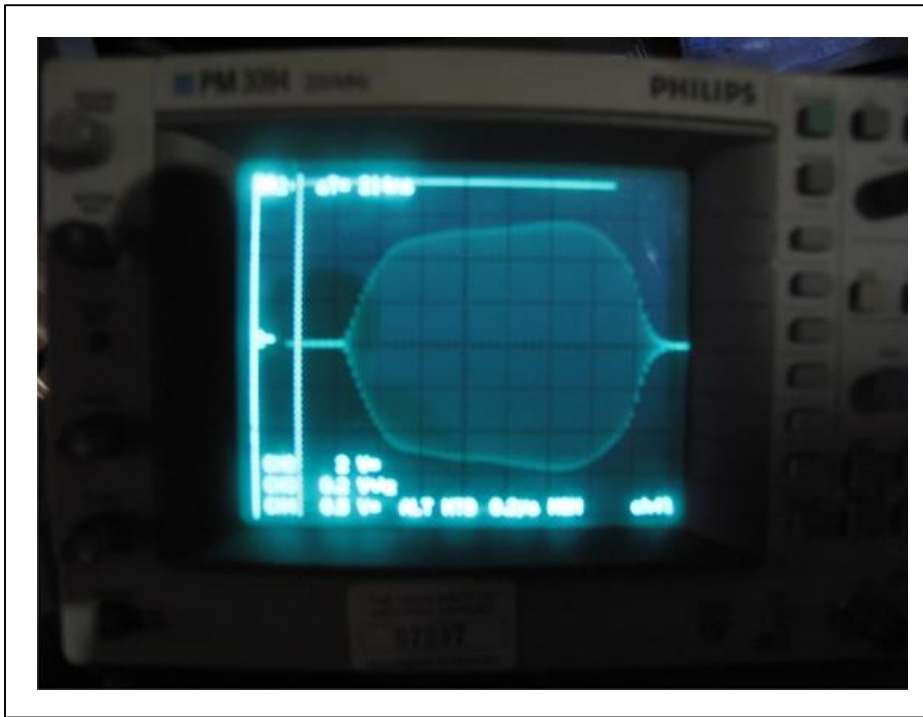


Figure 2: The transmitted pulse produced by the wave-form generator and pulse-amplifier.



Figure 3: Transmitter array used in the experiment.

The transmitted pulse of the system is shown in fig. 2, and fig. 3 shows the transmit antennas. Transmission was from a group of 9 antennas, and reception was achieved using 3 closely spaced groups of 4 antennas. These antennas could be used for interferometry, or combined to make a single antenna array. In the experiment discussed here, we received on the 12 receiver antennas as a single array. Fig. 4 shows the polar diagram of the combined transmit-receive system. The two-way half-power beam half-width was 7.5° . Fig. 5 shows the VSWR of the antennas, and demonstrates a band-width of about 3.8 MHz for a VSWR less than 2.0. A VSWR of 2.0 means that 89% of the power sent to the transmitter antennas is actually transmitted, and 11% is reflected back to the transmitter.

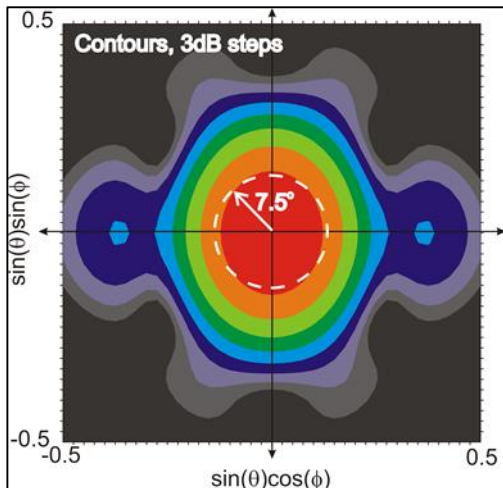


Figure 4: The two-way polar diagram of the radar.

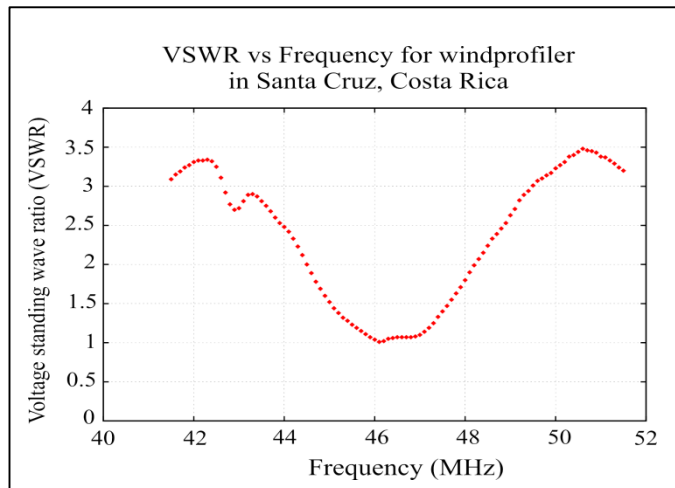


Figure 5: VSWR of the antennas as a function of frequency.

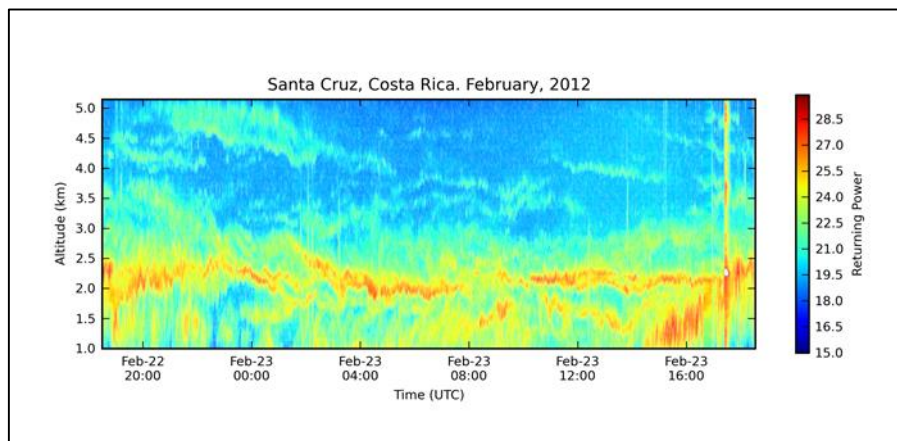


Figure 6: Height-time plots of received power (dB), showing a resolution of about 60m.

5. Results

The results of an experiment using a 1 km pulse with a frequency-sweep of 2.5 MHz are shown in fig 6. This corresponds to a resolution of about 60m, sufficient to see Kelvin-Helmholtz instabilities (e.g. 04:00 at 2.25 km) and other small-scale structures. Other examples exist, but fig.6 is representative of current capabilities.

References

- Farley, D., "On-line data processing techniques for MST radars", *Radio Sci.*, 20, 1177–1184, 1985.
- Rottger, J., and G. Schmidt, "High-resolution VHF radar soundings of the troposphere and Stratosphere", *IEEE Trans. Geosci. Electron.*, GE-17, 182–189, 1979.

The NCAR 449 MHz Modular Wind Profiler – Prototype and Future Plans

Stephen A. Cohn¹, William O. J. Brown¹, Bradley J. Lindseth¹, and Charlie Martin¹

¹ NCAR / EOL, PO Box 3000, Boulder, CO 90307, USA. Email: cohn@ucar.edu

ABSTRACT

NCAR / EOL have made progress towards development of a modular, 449-MHz wind profiler system for application to a broad range of lower atmospheric observation needs. The facility, deployed as part of NCAR's Integrated Sounding System, will provide new flexibility and capability to the research community. The new wind profiler consist of modular antenna panels and distributed TX and RX electronics, which will ultimately be configured either as a single 449 MHz full troposphere radar or as networks of lower atmosphere radars. A low side-lobe antenna design and advanced signal processing methods are being used, bringing new capabilities to NCAR's user community.

a. INTRODUCTION

The Earth Observing Laboratory (EOL) of the National Center for Atmospheric Research (NCAR) is developing a new wind profiler designed to be more flexible and easy to deploy than existing wind profilers. EOL currently deploys 915 MHz Radian/Vaisala LAP 3000 type wind profilers as part of its Integrated Sounding Systems (ISS) [1], a suite of instruments deployed to support researchers at a wide variety of meteorological research field projects around the world. The new wind profiler is more capable and flexible than the traditional 915 MHz wind profiler because of its modularity and use of advanced electronic components and design features [2,3].

b. 449 MHz MODULAR WIND PROFILER

The new wind profiler operates at 449 MHz in order to probe higher into the atmosphere than traditional 915 MHz wind profilers. Key features of the prototype wind profiler system are its modularity and antenna design. The system consists of antenna modules, each of which transmits and uses an independent receiver and data acquisition system. The antenna modules are hexagonal in shape to produce a radiation pattern with very low sidelobes (*D. Law, pers. communication*). Varying the number of modules creates radars of different size and capabilities, depending on the goals of each experiment or deployment. We currently have a three-module wind profiler capable of probing the full boundary layer. Adding more modules enables the radar to probe higher into the atmosphere. A seven-module system is currently being constructed, which is expected to produce a wind profiler capable of probing to the mid-troposphere, or capable of being split into two 3-module boundary layer profilers.

The wind profiler uses the multiple antenna modules to measure winds with spaced antenna techniques. These techniques, used on the NCAR MAPR (Multiple Antenna Profiler) [5], enable rapid wind measurements to be made on time scales as short as 1 to 5 minutes.

PROTOTYPE DEPLOYMENT

The three-module prototype system, shown in figure 1, was deployed to the PCAPS (Persistent Cold Pool Study) [6] in Salt Lake City, Utah, from Nov 2010 through Feb 2011.



Figure 1: Prototype 3-antenna 449 MHz wind profiler Salt Lake City, UT for PCAPS, Nov 2010.

During this first deployment changes were constantly being made to test or improve the equipment, so the data collected is not optimized. However the initial results are very promising. The prototype was operated close to a standard 915 MHz Doppler Beam Swinging (DBS) profiler, allowing a direct comparison of their performance.

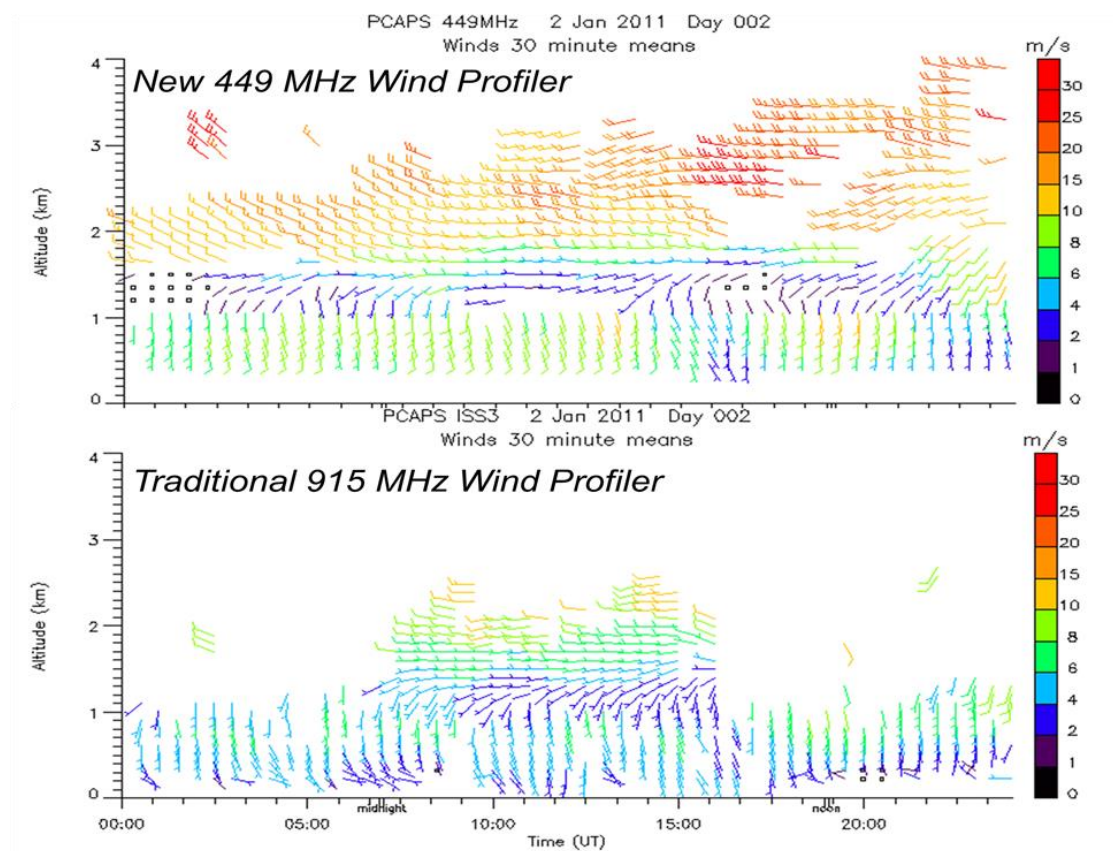


Figure 2: Comparison of winds from a traditional 915 MHz and a new 449 MHz wind profiler over 24 hours, 2 January 2011 at the PCAPS campaign.

Fig. 2 shows an example of wind observations over one day from the two wind profilers. The spaced-antenna technique requires a higher signal-to-noise ratio than DBS to measure winds. The radar parameters of the 449-MHz system, including its larger transmit power and longer wavelength, allowed the 449 MHz profiler to probe higher into the atmosphere. Over approximately two months of operation at PCAPS, the system probed an average of about 500 meters higher than the 915 MHz wind profiler. This was especially important for PCAPS because the interface region above the cold pool (the region of high directional shear in Fig. 2) is a target of the study. It will also be beneficial to many future projects where observing winds above the boundary layer is also important.

c. SUMMARY AND FUTURE PLANS



Figure 3: Prototype 7 antenna module 449-MHz wind profiler, under construction.

A prototype three antenna 449 MHz modular wind profiler has been constructed and successfully deployed. The new profiler compares very favorably to co-located traditional 915 MHz wind profilers, generally probing higher into the atmosphere. The system is being expanded to 7 antenna modules, and is expected to be capable of reaching mid-troposphere altitudes. The 7 antenna system, shown in figure 3, should be built in the coming months, with testing during the first half of 2013. Future plans also include the development of a trailer or truck mounted mobile version for rapid deployment. Other planned additions include Radio Acoustic Sounding System

(RASS) capability for boundary layer profiling of virtual temperature, Range Imaging (RIM; [7]) to improve the system's altitude resolution, and the development of a shipboard system.

In the longer term, the proposed system will include expansion to 19 antenna modules, which should be capable of probing up to the tropopause region. Alternately these modules could be deployed as two 7-module profilers capable of probing to the mid-troposphere; or reconfigured as a network of six 3-module boundary layer profilers.

ACKNOWLEDGMENTS

The authors are grateful for the efforts of Jim Jordan, Warner Ecklund, Terry Hock, Dan Law and EOL technical staff, as well as the advice of others at NCAR, NOAA and partner institutions. This work is supported by EOL and NCAR. NCAR, EOL and PCAPS are funded by the U.S. National Science Foundation.

REFERENCES

- [1] Parsons, D. B., and Co-Authors, 1994: The Integrated Sounding System – Description and preliminary observations from Toga-COARE, *Bull. Amer. Meteor. Soc.*, **75**, 553-567.
- [2] Lindseth, B.J., J. R. Jordan, D. Law, T. Hock, S. A. Cohn and Z. Popovic, 2012: "A New Portable 449 MHz Spaced Antenna Wind Profiler Radar." *IEEE Trans. on Geoscience and Remote Sensing*, DOI: 10.1109/TGRS.2012.2184837
- [3] Brown, W.O.J., S.A. Cohn, P.B. Chilson, and R. D. Palmer, 2007: A 449MHz modular wind profiler development study. *33rd International Conference on Radar Meteorology (AMS)*, Cairns, Australia. Paper P13B.3. Proceeding available at <http://ams.confex.com/ams/pdfpapers/123735.pdf>
- [4] Cohn, S. A., W. O. J. Brown, J. Jordan, P. B. Chilson, D. Law, 2009: "A Deployable Modular Profiling Network (MPN) for Lower Atmospheric Applications", *8th ISTP*, Delft, The Netherlands, Oct, 2009. Proceedings S06–P05 available at <http://cerberus.rivm.nl/ISTP/data/1660292.pdf>
- [5] Cohn, S. A., W. O. J. Brown, C. L. Martin, M. S. Susedik, G. Maclean, and D. B. Parsons, 2001: Clear air boundary layer spaced antenna wind measurements with the Multiple Antenna Profiler (MAPR), *Annales Geophysicae*, **19**, 845-854.
- [6] Lareau, N.P., E. Crosman, C.D. Whiteman, J.D. Horel, S.W. Hoch, W.O.J. Brown, T.W. Horst, 2012: The Persistent Cold-Air Pool Study, Submitted to *BAMS*. Also <http://pcaps.utah.edu/>
- [7] Palmer, R., T.-Y. Yu, and P. Chilson, 1999: Range imaging using frequency diversity, *Radio Sci.*, **34**, 6, doi:10.1029/1999RS900089

An inter-comparison of wind velocities in different observation approaches and signal processing techniques using multi receiver phased array MU radar system

Shridhar Kumar¹, VN Sureshababu¹, VK Anandan¹, Toshitaka Tsuda², Jun-ichi Furumoto²

¹ ISTRAC, Indian Space Research Organisation, Bangalore -58 (anandanvk@hotmail.com)

² Research Institute for Sustainable Humanosphere (RISH), Kyoto University, Uji, JAPAN

Abstract

Application of ST/MST radars to observe back ground air motion and deriving horizontal winds has been well established. Doppler beam swinging (DBS) is the most popular technique. Multi-receiver data analysis broadly divided in spaced antenna (SA), imaging Doppler interferometry (IDI) and Post-set beam steering (PBS) technique. In this paper a detailed study has been presented on horizontal winds derived with SA and PBS technique on the observation conducted with middle and upper atmospheric (MU) radar at Shigaraki, Japan. Analysis is carried out on 6 hrs of observation, various statistical parameters on winds derived from SA and PBS has been determined to confirm the robustness and reliability of both techniques in deriving horizontal winds.

1. INTRODUCTION

Wind profilers are Doppler radars capable of measuring the component of winds in the every few minutes over troposphere and lower stratosphere. Doppler Beam Swinging (DBS), Spaced Antenna (SA), Post-set Beam Steering (PBS) technique etc. are most commonly used technique to estimates of horizontal winds. Various comparative studies between different technique and other observational methods have been reported in the literature. The comparison between DBS and SA observations with MU had shown systematic difference between SA and DBS observation in tropopause region [5]. The study [4] concluded that the performance of SA and DBS wind estimates are same for VHF profilers and that of DBS estimates are better than SA estimates for UHF profilers.

The remainder of this paper focuses, on the comparative study of SA and PBS derived wind to quantitatively analyze the accuracy and precession of both measurements. This is the first time that, a detailed comparative study between SA and PBS derived wind up to 20 km has been presented . The comparison between SA and PBS derived wind is interesting in sense of that in both techniques wind has been estimated using only vertical observation for the same instant of time. Using the winds derived by PBS and SA, the statistical performance of both measurements has been discussed for the duration of 0001– 0659 LT on Jul 16, 2008. Inter comparative study of results shows a very good comparison of all statistical parameters, which shows the robustness and reliability of both techniques.

2. DATA ANALYSIS AND WIND ESTIMATION TECHNIQUES

MU radar located at Shigaraki, Japan is pulsed phased array radar, operates at 46.5 MHz with a peak power of 1 MW. The array consists of 475 crossed Yagi elements which are rearranged into 25 receiver channels. The observation parameters are 3.6° of beam width, 64 coherent integration, 320μs inter pulse period, 256 numbers of samples and 0.1024 sec sampling time

interval. The time series vertical data is collected for all 25 channels with height resolution of 150 m and time resolution of 1.3 min. For a given single record, transmission is carried out fifteen times in sequence.

The wind measurement by PBS technique is described as follows. The vertical data collected from 25 channels are used to synthesize multiple beams within the transmitting beam width using Capon beamforming methods [3] at a certain off-zenith angle of 1.5° and equally separated 32 different azimuth angles. From a synthesized beam, Doppler power spectrum is obtained by Eigenvector (EV) method [2], which is one of the spectral based sub-space methods. Further, 15 power spectra are integrated to improve the SNR. From the average power spectra, first moments are calculated through adaptive moments estimation method [5]. Thus, radial velocity at a desired direction is readily obtained. The same process is repeated for obtaining radial velocity in other desired directions. As a result, the horizontal winds are derived by least squares sense from the angular distribution of radial velocities.

In general, SA technique uses three non-collinear spaced receiving antennas to measure the horizontal wind. Thus, the channel of MU radar has been rearranged into three groups named ANT1, ANT2 and ANT3. Each group consists of eight channels. The phase center of each group is calculated in terms of wavelength λ . The phase center of these group forms an equilateral triangle. Likewise, grouping has been done with four different spatial distributions named Orientation 1, Orientation 2, Orientation 3 and Orientation 4. A horizontal wind has been estimated for each orientation using FCA [1] and is averaged. The spatial averaging has advantage in term of better height coverage up to 20 km.

Orientation 1: ANT1 consist of channels D1, D2, D3, D4, E1, E2, E3 &E4 with phase center $(-3.4857\lambda, -2.8875\lambda)$. ANT2 consist of channels F1, F2, F3, F4, A1, A2, A3 &A4 with phase center $(-0.7579\lambda, 4.4625\lambda)$. ANT3 consist of channels B1, B2, B3, B4, C1, C2, C3 &C4 with phase center $(4.2435\lambda, -1.5750\lambda)$.

Orientation 2: ANT1 consist of channels C3, C4, D1, D2, D3, D4, E1, &E2 with phase center $(-1.8994\lambda, -4.0688\lambda)$. ANT2 consist of channels E3, E4, F1, F2, F3, F4, A1 & A2 with phase center $(-2.5765\lambda, 3.6750\lambda)$. ANT3 consist of channels C1, C2, B1, B2, B3, B4, A3 &A4 with phase center $(4.4709\lambda, 0.3938\lambda)$.

Orientation 3: ANT1 consist of channels D3, D4, E1, E2, E3, E4, F1 & F2 with phase center $(-4.4709\lambda, -0.3938\lambda)$. ANT2 consist of channels F3, F4, A1, A2, A3, A4, B1 & B2 with phase center $(1.8944\lambda, 4.0687\lambda)$. ANT3 consist of channels B3, B4, C1, C2, C3, C4, D1 & D2 with phase center $(2.5765\lambda, -3.675\lambda)$.

Orientation 4: ANT1 consist of channels E1, E2, E3, E4, F1, F2, F3 & F4 with phase center $(-4.2435\lambda, 1.5750\lambda)$. ANT2 consist of channels A1, A2, A3, A4, B1, B2, B3 & B4 with phase center $(3.4857\lambda, 2.8875\lambda)$. ANT3 consist of channels C1, C2, C3, C4, D1, D2, D3 & D4 with phase center $(0.7579\lambda, -4.4625\lambda)$.

3. RESULT AND DISCUSSION

The horizontal components of wind derived by SA technique with and PBS have been compared to the same obtained from standard DBS (off-zenith angle of 10^0) at contiguous time and GPS sonde observation and shown a good agreement with DBS and GPS sonde observed winds up to the height of 20 km (not shown in Fig. 1).

Standard deviation (SD) analysis has been performed for each our of duration on PBS and SA wind estimate and is averaged over all over all height in the range of 1.05 km -20,1 km. The obtained SD is given in Table1.

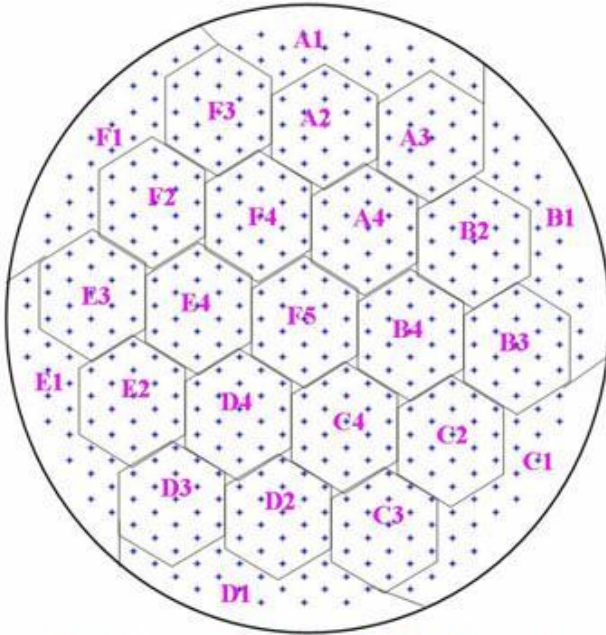


Fig.1 Array configuration of MU radar system.

Time of observation (on Jul 16, 2008)	SD (m/s)			
	Zonal		Meridional	
	PBS	SA	PBS	SA
0101 - 0159 LT	1.33	1.13	1.17	1.20
0201 - 0258 LT	1.30	1.05	1.11	1.21
0300 - 0359 LT	1.13	0.99	0.99	1.12
0400 - 0459 LT	1.07	0.89	1.06	1.05
0500 - 0559 LT	1.25	0.96	0.99	0.96
0600 - 0659 LT	1.30	1.05	1.00	1.03

Table 1: SD for each hour of observation during wind estimates.

Correlation analysis has been performed on PBS and SA wind estimate for each hour and 6 hour of duration is shown in Fig. 2. Various statistical parameters like obtained slope (s), correlation (r) and RMSE (e) is being derived. The statistics of correlation analysis at the interval of each 60 min observation are given in the Table 2.

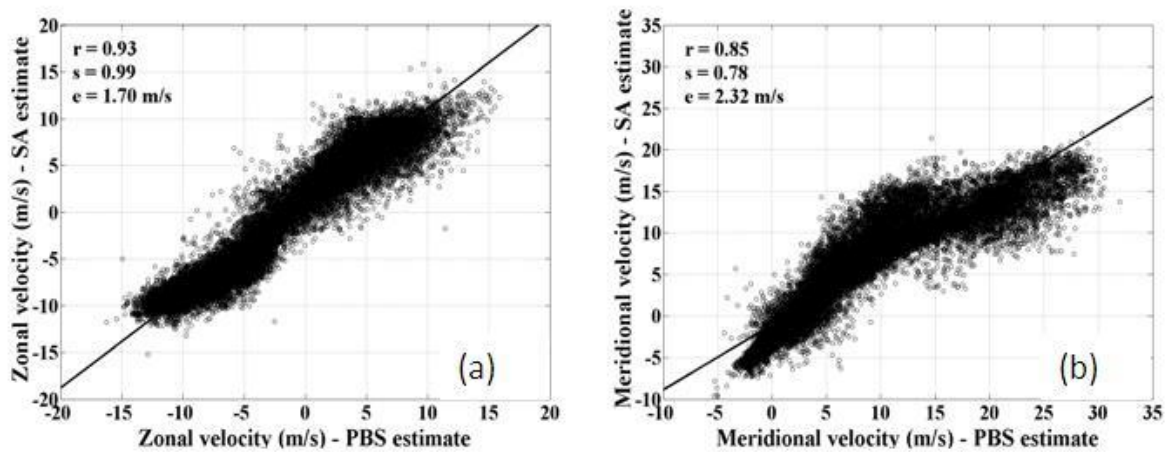


Fig. 2 Scatter plots of PBS and SA derived horizontal wind velocities from the height range 1.05-19.8 km during the observation on 0101LT - 0659 LT on Jul 16, 2008 (a) Zonal (b) Meridional.

Time of observation (on Jul 16, 2008)	Slope (s)		Correlation coefficient (r)		RMSE in m/s (e)	
	Zonal	Meridional	Zonal	Meridional	Zonal	Meridional
0101 - 0159 LT	1.04	0.76	0.92	0.84	1.80	2.44
0201 - 0258 LT	0.99	0.79	0.92	0.84	1.84	2.41
0300 - 0359 LT	0.93	0.80	0.93	0.88	1.65	2.13
0400 - 0459 LT	0.97	0.75	0.94	0.84	1.50	2.30
0500 - 0559 LT	0.99	0.78	0.93	0.85	1.67	2.26
0600 - 0659 LT	0.99	0.80	0.93	0.84	1.63	2.30

Table 2: Statistical factors for each hour of observation during wind estimates.

4. CONCLUSION

The statistical analyses on robustness and reliability of PBS and SA techniques in deriving horizontal winds are investigated using the same data set with same instant of time obtained from MU radar. Comparison with GPS sonde and DBS has shown very good agreement up to the height of 20 km. SD averaged over a height range of 1.05–20.1 km and is comparable to a related work. The SA and PBS velocity estimates show high correlation (0.93 for zonal and 0.85 for meridional wind). This quantitative and qualitative analysis concluded that PBS is equivalently as good as SA in wind measurements for multi channel wind profiler radar.

Acknowledgement

Study was conducted by using the MU radar under a support of the Asia-Africa Science Platform Program (AA-SP) of JSPS, Japan and Indian Space Research Organisation (ISRO), India.

References:

- [1] B. H. Briggs The analysis of spaced sensor records by correlation techniques, in *Handbook for MAP*, Vol.13, pp.166-166, 1984.
- [2] G. Bienvana and L. Kopp, "Optimality of high resolution array processing using the eigen system approach," *IEEE Trans. Acoustic, Speech, Signal processing*, vol. 34, pp. 1234-1248, 1983.
- [3] J. Capon, "High resolution frequency-wave number spectrum analysis," *Proc. IEEE*, vol. 57, pp.1408-1418, 1969.
- [4] P. T. May, "Spaced antenna versus Doppler radars: A comparison of techniques revisited". *Radio Science*, Vol. 25, pp. 1111-1119, 1990.
- [5] Van Baelen, T. Tsuda, A.D. Richmond, S. K. Averys, S. Kato, S. Fukao, and M. Yamamoto, "Comparison of VHF Doppler beam swinging and spaced antenna observations with the MU radar: First results" *Radio Science*, Vol. 25, pp. 629-640, 1990.
- [6] V. K. Anandan, P. Balamuralidhar, P. B. Rao, A. R. Jain, and C. J. Pan, "An adaptive moments estimation technique applied to MST radar echoes," *J. Atmos. Oceanic Technol.*, vol. 22, pp. 396–408, 2005

Improved performance in Horizontal wind estimation from a multi receiver phased array atmospheric radar system using Spaced Antenna Drift Technique and signal processing approaches

Shridhar Kumar¹, VK Anandan¹, Toshitaka Tsuda², Jun-ichi Furumoto²

¹ ISTRAC, Indian Space Research Organisation, Bangalore -58 (anandanvk@hotmail.com)

² Research Institute for Sustainable Humanosphere, Kyoto University, Uji, JAPAN

Abstract

Middle and Upper atmospheric (MU) radar at Shigaraki, Japan is an excellent system to carry out observation using spaced antenna (SA) technique. In general, SA based wind estimation could not give the good height coverage due to smaller aperture being used to receive signals which lead to poor signal-to-noise ratio (SNR). The receiver channels are divided into three equal segments to form the baselines suitable for deriving horizontal winds using SA technique. The complete analysis is repeated with 4 different spatial distributions of array. In each case, the wind velocity is estimated and is averaged to obtain mean horizontal winds. The results are compared with the wind velocity estimated using Doppler Beam Swinging (DBS) technique GPS sonde. It is observed that the new approach adopted using spatially distributed array grouping has yielded higher height coverage up to 20 kms and in good agreement with DBS and GPS sonde observations.

1. Introduction

The SA method is multi receiver alternatives to DBS. A standard SA experiment uses a single array for transmission but receives the returned signals with three spatially separated antennas along non-collinear baselines. Assume that the three receivers exist at the vertices of a right angle triangle with the sides along the x and y axes. By calculating the cross-correlation functions, one can obtain the delay times along x and y axes. By knowing time delay and receiver separation, apparent velocities can be estimated [4]. Due to random changes in the atmospheric motion, apparent velocities will be large. To resolve this difficulty, the full correlation analysis (FCA) [1] & [2] is used is to derive horizontal winds.

In this paper, a study has been carried out to derive the horizontal wind components from the observations of MU radar in multi channel receiver mode. The receiver channels are divided in to three equal segments to form an equilateral triangle group. Horizontal wind vector components are estimated for four different orientations with different spatial distribution. Average wind is calculated from the winds estimated by orientations. As the grouping has been done with different spatial orientation and each orientation different spatial structure is created by antenna grouping. Also, a simulation study has been made for each antenna segments in group to observe the beam pattern in X and Y plane. The beamwidth (3dB width of beam) and sidelobe (first sidelobe near the mainlobe) for each antenna group is estimated for understanding the asymmetry of beam formed and its possible influence in wind observation.

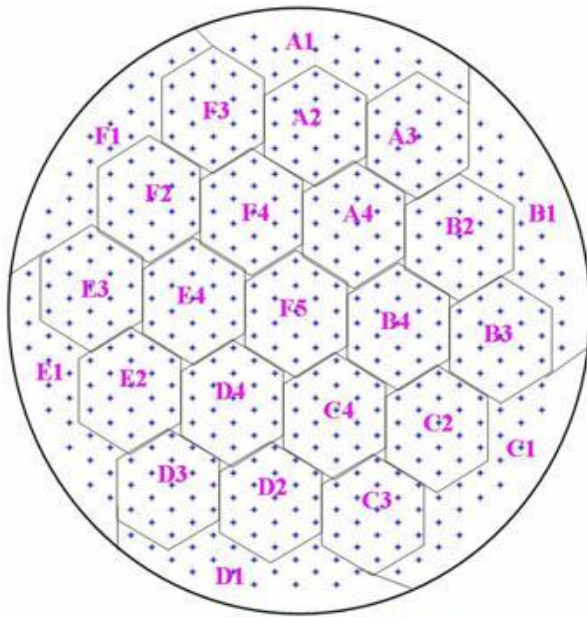


Fig.1 Array configuration of MU radar system.

2. System description and data analysis

MU radar is pulsed phased array radar operates at 46.5 MHz with a peak power of 1 MW. The array pattern is circular with 475 crossed Yagi elements and rearranged into 25 different receiver channels. The array pattern of MU radar is shown in Fig.1. Transmission is done only along vertical direction with five different frequencies (46.00 MHz, 46.25 MHz, 46.50 MHz, 46.75 MHz and 47.00 MHz) switched over pulse to pulse and repeated three times in sequence for a single record. The observations has parameters are 3.6° of half power beam width, 64 coherent integration, $320\mu\text{s}$ inter pulse period, 256 numbers of samples for each frequency and 0.1024 sec sampling time interval. The time

series data along vertical direction is collected for all 25 channels with height resolution of 150 m and time resolution of 1.3 min. Channels are divided into three segments named ANT1, ANT2 and ANT3 during the data analysis. Each segment consists of 8-channels. For each segments, phase center is calculated in terms of wavelength λ . Each segment acts like a separate antenna. The phase centers of corresponding segments lie exactly at the vertices of an equilateral triangle. Likewise, grouping has been done with four different orientations. The obtained sidelobe and beamwidth from simulation study of beampattern in X and Y plane is different for each antenna in each orientation. The horizontal wind velocity components are estimated for all spatial orientations using FCA and average horizontal winds is obtained. This approach has significant advantage in terms of better height coverage up to 20 km.

Grouping of CHANNEL with Different orientation

Orientation 1: ANT1 consist of channels D1, D2, D3, D4, E1, E2, E3 & E4 with phase center $(-3.4857\lambda, -2.8875\lambda)$. ANT2 consist of channels F1, F2, F3, F4, A1, A2, A3 & A4 with phase center $(-0.7579\lambda, 4.4625\lambda)$. ANT3 consist of channels B1, B2, B3, B4, C1, C2, C3 & C4 with phase center $(4.2435\lambda, -1.5750\lambda)$.

Orientation 2: ANT1 consist of channels C3, C4, D1, D2, D3, D4, E1, & E2 with phase center $(-1.8994\lambda, -4.0688\lambda)$. ANT2 consist of channels E3, E4, F1, F2, F3, F4, A1 & A2 with phase center $(-2.5765\lambda, 3.6750\lambda)$. ANT3 consist of channels C1, C2, B1, B2, B3, B4, A3 & A4 with phase center $(4.4709\lambda, 0.3938\lambda)$.

Orientation 3: ANT1 consist of channels D3, D4, E1, E2, E3, E4, F1 & F2 with phase center $(-4.4709\lambda, -0.3938\lambda)$. ANT2 consist of channels F3, F4, A1, A2, A3, A4, B1 & B2 with phase center $(1.8944\lambda, 4.0687\lambda)$. ANT3 consist of channels B3, B4, C1, C2, C3, C4, D1 & D2 with phase center $(2.5765\lambda, -3.675\lambda)$.

Orientation 4: ANT1 consist of channels E1, E2, E3, E4, F1, F2, F3 & F4 with phase center $(-4.2435\lambda, 1.5750\lambda)$. ANT2 consist of channels A1, A2, A3, A4, B1, B2, B3 & B4 with phase center $(3.4857\lambda, 2.8875\lambda)$. ANT3 consist of channels C1, C2, C3, C4, D1, D2, D3 & D4 with phase center $(0.7579\lambda, -4.4625\lambda)$.

3. Result and discussion

The horizontal components of winds derived by SA technique with four different orientation and average wind have been compared with the same obtained from standard DBS (tilt angle of 10°) and shown in Fig. 2. It is observed that average horizontal winds obtained by SA show a good agreement with DBS observed winds up to the height of 20 km.

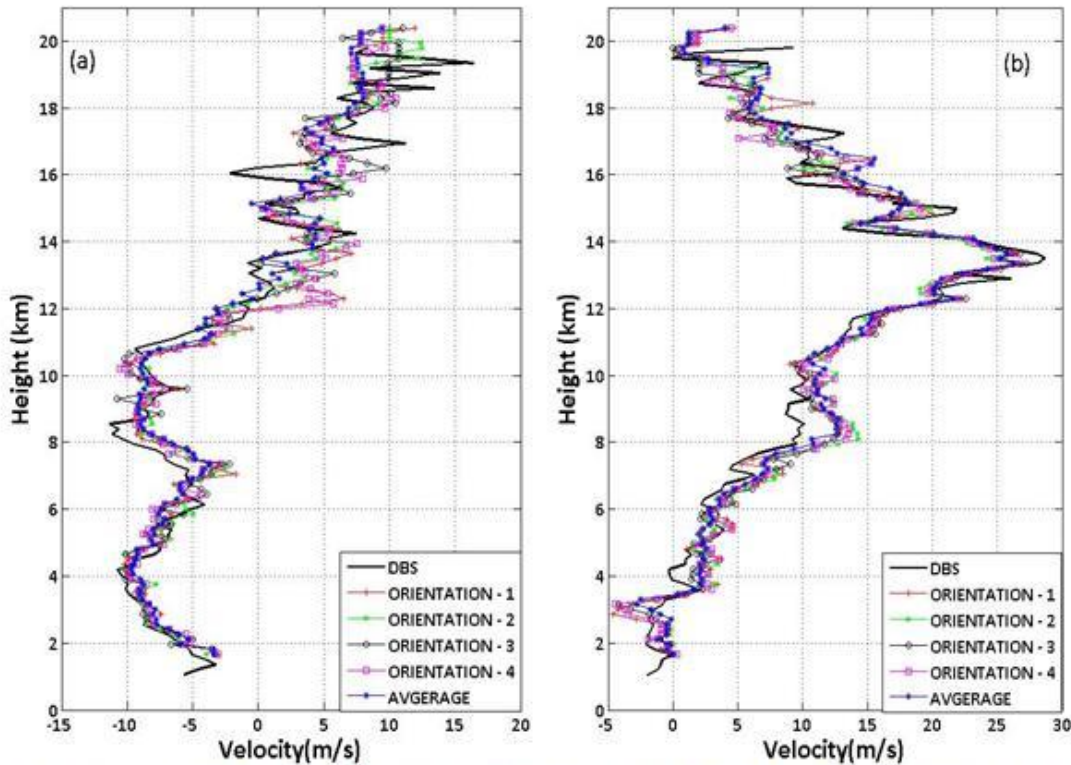


Fig. 2 Vertical profile of SA derived wind (Jul 16, 2008, LT 0347 LT) and compared with DBS derived wind (Jul 16, 2008, LT 0338 LT) (a) Zonal (b) Meridional.

The SA derived average winds show very good agreement up to the height of 20 km with GPS sonde and is presented in Fig.3. To validate the consistency of the approach carried out to estimate horizontal wind, the standard deviation (SD) has been estimated for half an hour data around the GPS sonde observation and shown in Fig.4. In Fig. 4, the segment numbers from 1 to 6 correspond to the height intervals 1.05-4.05, 4.05-7.05, 7.05-10.05, 10.05-13.05, 13.05-16.05 and 16.0-19.05 km respectively. The averaged value of SD for zonal component of wind at all the heights for orientation1, orientation2, orientation3, orientation4, and average are 1.61 , 1.60 , 1.79 , 1.76 and 1.35 ms^{-1} respectively. Similarly, the averaged value of SD for meridional component of wind at all the heights for orientation 1, orientation 2, orientation 3, orientation 4, and average are 2.14 , 2.20 , 1.75 , 1.91 and 1.46 ms^{-1} respectively. For both zonal and meridional winds, average velocity has less SD compared to all other orientation group. The obtained SD values are comparable to a related work [3].

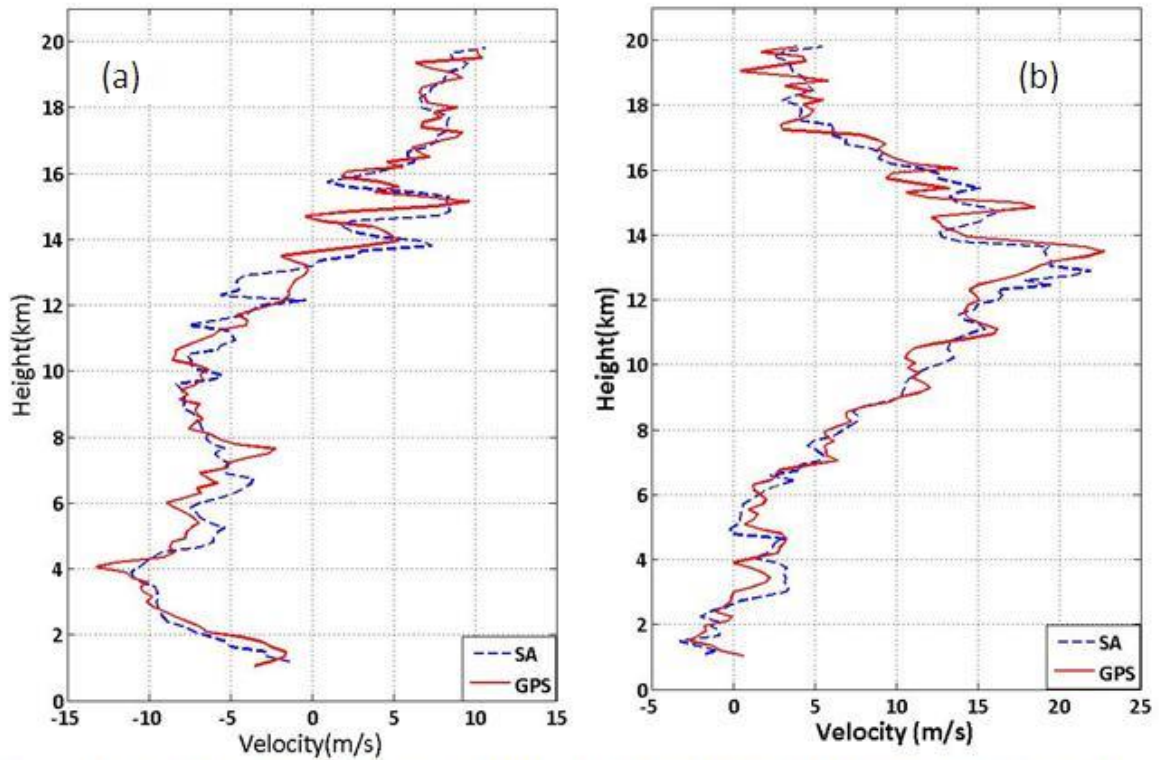


Fig. 3 Vertical profile of Average horizontal velocity derived using SA technique and compared with GPS sonde (Jul 16, 2008, 0701 LT) observed winds (a) Zonal (b) Meridional.

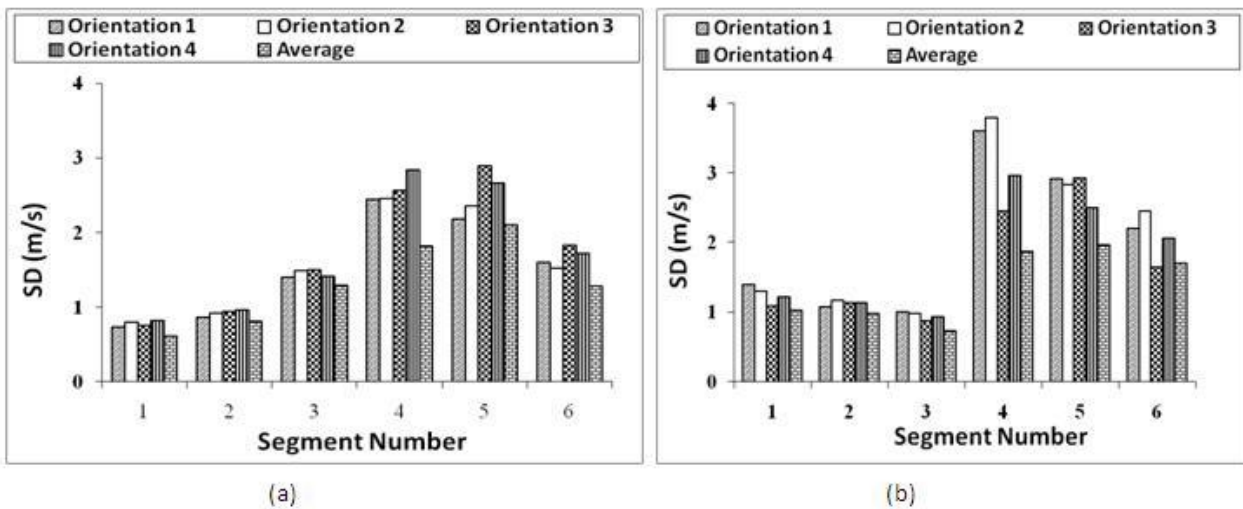


Fig. 4 SD differences in wind velocities between the GPS sonde and the SA observations (a) Zonal (b) Meridional.

4. Conclusion

An improved performance in wind estimation with very high temporal resolution and greater height coverage using SA technique is demonstrated. The wind estimated by new approach has been compared with DBS and GPS sonde observed winds. Comparison has shown very good agreement in estimated winds up to the height of 20 km. The standard deviation of difference of GPS sonde and SA derived wind velocity observation shows that average winds have minimum

standard deviation. This is the first time that height coverage of 20 km with high temporal resolution (1.3 min) wind observation is reported using SA technique.

Acknowledgement

Study was conducted by using the MU radar under a support of the Asia-Africa Science Platform Program (AA-SP) of JSPS, Japan and Indian Space Research Organisation (ISRO), India.

References

- [1] B. H. Briggs The analysis of spaced sensor records by correlation techniques, in *Handbook for MAP*, Vol.13, pp.166-166, 1984.
- [2] D. A. Holdsworth Signal analysis with applications to atmospheric radars, PhD thesis, University of Adelaide, S.Australia, 1995.
- [3] H. Luce, S. Fukao, M. Yamamoto, C. Sidi and F. Dalaudier Validation of Winds Measured by MU Radar with GPS Radiosondes during the MUTSI Campaign, *Journal of Atmospheric and Oceanic Technology*, Vol.8, pp. 817- 829, 2001.
- [4] S. N. Mitra "A radio method of measuring winds in the ionosphere, *Proceedings of the institute of electrical engineers*, Vol. 96, pp.441-446, 1949.

Performance analysis of optimum tilt angle with necessary beam configuration to minimize error in measurement of horizontal wind velocities derived by Post Beam Steering technique

VN Sureshbabu¹, VK Anandan¹, Toshitaka Tsuda², Jun-ichi Furumoto²

¹ ISTRAC, Indian Space Research Organisation, Bangalore -58 (anandanvk@hotmail.com)

² Research Institute for Sustainable Humanosphere (RISH), Kyoto University, Uji, JAPAN

Abstract

Software beam synthesis by Post set Beam Steering (PBS) technique is used to derive the horizontal wind velocities from multi receiver phased array radar data. In order to improve the efficiency of beam synthesis, Capon beamforming method is used to synthesize time series signals in the desired line of sight angle within the radar transmit beam volume (3.6° beam width). This paper describes beam synthesizing in optimum directions to reduce the error in the measurement of horizontal wind velocities using PBS technique. For this purpose, beams are synthesized at various tilt angles with multi beam configuration. The statistical comparisons of performance of various tilt angles and beam configurations are being studied using the data collected from multi receiver phased array radar system (MU radar, Shigaraki, Japan). The analyzed results shows that beam synthesize at the tilt angle from 1.5° to 2.0° using 16 beam configuration minimize the error in horizontal wind estimation by PBS technique.

1. Introduction

In the present work, PBS [1] technique is used as software beam steering for wind profiling using multi receiver data. Signals received from spatially separated antennas are made to interfere constructively by phasing the received signals within the transmit beam width. This technique is used to synthesize the beams in the desired directions and so called as Post Beam Steering Technique. As these measurements typically involve reception of signals by minimum three spatially separated arrays, the vertically received signals are steered along the desired line of sight angle by introducing systematic phase shifts in the received signals themselves. The beam steering can be optimized by weighting vectors through beamforming approach like Capon method [4]. Then the weighted steered signals are combined linearly to produce a two-way beam pattern in the desired line of sight angle within the transmit beam volume. Also, it is reported that the biasing effect of aspect sensitivity and the effect of interfering signals can be removed by robustness of Capon beam former [4], [6].

This paper mainly focuses on beam synthesize in spatial domain along effective directions [2]-[3] within the transmit beam volume to minimize the error in wind estimation using PBS technique. For this, two-way beam patterns are synthesized in different tilt angles using multi beam configuration. The horizontal wind profiles obtained by PBS for different tilt angles are compared with those derived from DBS observed winds in near time. In order to justify the optimum tilt angle for which Standard Deviation (SD) in winds over the time is minimal, the consistency in deriving wind velocity is shown for different tilt angles. The same

kind of analysis is done to prove the number of useful beams (at optimum tilt angle) required to minimize the error in wind measurements. The analyses are carried out in clear air condition due to very small magnitude of vertical velocity.

2. System description and data processing

The system descriptions is given in the companion paper namely “*Extraction of horizontal wind velocities from a multi receiver phased array radar system using post beam steering technique and efficiency of various beamforming methods*”. The data collected from 25 channels are subjected to PBS technique to synthesize new beams at 1.5° tilt angle with 16 equally spaced azimuth positions. The power spectra at different line of sight angles are independently obtained as mentioned in the sections II for 5 overlapping sub bands and the sequence are repeated for three times. In this way, 15 power spectra is obtained from one record itself. The spectra are integrated to improve the SNR. From the average spectrum, zeroth order (total power) and first order (mean velocity) moments are calculated through adaptive moments estimation method [5]. Thus, radial velocities from corresponding line of sight angles are readily obtained. As a result, the horizontal wind components i.e. zonal and meridional velocities are derived by least squares sense.

3. Result analysis and discussion

In this section, the horizontal wind velocities are obtained using Capon beamforming method for different tilt angles say 0.5°, 1.0°, 1.5°, 2.0° and 2.5° with 32 equally separated azimuth angles. The reason for 32 beam configuration is to be discussed later. In general, the horizontal wind components for 3- beam configuration by PBS can be calculated in a simple way as below

$$\text{Zonal wind component } U = \frac{V_{RE} - W \cos(\theta)}{\sin(\theta)} \quad (\text{or}) \quad -\frac{V_{RW} - W \cos(\theta)}{\sin(\theta)}$$

$$\text{Meridional wind component } V = \frac{V_{RN} - W \cos(\theta)}{\sin(\theta)} \quad (\text{or}) \quad -\frac{V_{RS} - W \cos(\theta)}{\sin(\theta)}$$

It is familiar that any measurement has its own uncertainty. A small uncertainty in the measurement of radial velocity in a weak SNR region introduces the error in PBS estimated winds as listed below.

Uncertainty in radial velocity (m/s) along North/East	Tilt angle (deg)	Error in wind component (m/s) i.e. meridional/zonal
0.2	0.5	11.46
	1.0	5.73
	1.5	3.82
	2.0	2.86
	2.5	2.29

Table 1: Uncertainty in radial measurement Vs error in wind components.

In the above table, the magnitude of vertical velocity (W) is considered to be 0.1 m/s. From the table, it is obvious that possibility of error in wind measurement is more for 0.5° and 1.0° tilt angles. The details given in the above table is for 3-beam configuration with negligible value of vertical velocity (clear air). It is evident that the uncertainty in wind velocity

measurement can be reduced by tilting the beam for large off-zenith angle. But, the receive beam should be essentially within the transmit beam for better SNR. Thus, tilting the beam at large off-zenith angle has limitation. Also, the possibility of error in winds can come due to poor SNR along different azimuth angle at a given tilt angle. This error can be reduced by using more number of beams in azimuth plane for deriving the winds using least square sense.

The horizontal wind velocities derived from different tilt angles are shown in Fig.1 and compared to DBS observations at contiguous times. It is noted that DBS observation for wind estimation is conducted for the tilt angle of 10° with 4 equally spaced azimuth angles. The standard DBS observed winds are considered as mean winds. From the Fig.1, it is clear that the horizontal winds derived by PBS for the tilt angles 1.5° and 2.0° using Capon beamforming method are in good agreement with DBS observed winds. In Fig.1, the error in the winds due to uncertainty in radial measurement is seen more for tilt angles 0.5° and 1.0° even though 32 beams are used. The influence of uncertainty (Table.1) is observed only for the tilt angles 0.5° and 1.0° in weak SNR regions. However, the performances of tilt angles (0.5° - 2.0°) in wind estimation are in consistent with standard DBS observed winds in good SNR regions in which infinitesimal uncertainty has no much influence in wind measurements. As the beam synthesized at the tilt angle 2.5° lies outside the transmit beam width ($\pm 1.8^\circ$), the possibility of wind profiling could not be observed due to poor SNR. Though the uncertainty in wind estimation is less for the tilt angle 2.5° , possibility of detecting atmospheric parameters is observed to be very less. Hence, wind profiling by PBS technique at the tilt angle 2.5° and above cannot be useful (Fig.1). In clear air condition, horizontal wind velocity is expected to be uniform over several kilometers. In this work, the comparative study is carried out in clear air condition only. Thus, the PBS retrieval should agree with DBS retrieval. However, small variations are noticed in wind estimation by both retrieval methods. These variations are attributed with small fluctuations in wind itself, estimation technique, bias and SNR. Nevertheless, trends in wind estimation by both retrievals are similar. This is clearly observed in Fig.1. Further, the existence of optimum tilt angles have been justified for long data sets of profiler data in different date and time. A similar analysis has been carried out to find the required number of beams to improve PBS based wind estimation. For this, beam patterns are synthesized for 4, 8, 16 and 32 equally spaced azimuth angles with fixed tilt angle of 1.5° . The consistency in statistical performance of horizontal wind estimation is reliably observed by 16 beam configuration onwards. But, there is little gained in wind estimation by increasing the number of beams beyond 16.

4. Conclusion

A detailed analysis on the effect of tilt angles as well as number of necessary oblique beams on horizontal wind estimation derived by PBS was discussed. The statistical performance of different tilt angles and beam configurations are analyzed in clear air condition. From the analyzed results, wind estimations for the tilt angles 1.5° - 2.0° have better agreement with DBS observed winds. The consistency in deriving horizontal wind velocities over the time interval is reliably observed for the tilt angles of 1.5° - 2.0° . Thus, the tilt angle from 1.5° to 2.0° is expected to be an optimum tilt angle for wind estimation by PBS. This optimum tilt angle is justified only for PBS based wind observation in which radar transmit beam width is of 3.6° ($\pm 1.8^\circ$ about zenith). Also, the error in zonal and meridional wind velocities is observed less from 8 beam configuration onwards. Based on the error analysis and statistical performances, 16 beam configurations are expected as an optimum

beam configuration for complete wind profiling. Thus, it is reported that beam synthesizing in optimum tilt angle with 16 beam configuration minimizes the error in PBS based wind estimation and enhances wind profiling up to the height of about 20 km. The results obtained in this fashion are in good agreement with standard DBS observed winds.

References

- [1] J. Rottger, H.M. Ierkic, "Postset beam steering and interferometer applications of VHF radar to study wind, waves, and turbulence in the lower and middle atmosphere", *Radio Sci.*, vol. 20, no. 6, pp. 1461-1480, Jul.1985.
- [2] I.Srinivasa Rao, V.K. Anandan, P. Narasimha reddy, "Evaluation of DBS wind measurement technique in different beam configuration for a VHF wind profiler", *J. Atmos. Oceanic Technol.*, vol. 25, pp. 2304-2312, Dec. 2008.
- [3] V.K. Anandan, I. Srinivasa Rao, P. Narasimha reddy, "A study on optimum tilt angle for wind estimation using indian MST radar", *J. Atmos. Oceanic Technol.*, vol. 25, pp. 1579-1589, Sep. 2008.
- [4] H. Krim, M. Viberg, "Two decades of array signal processing research : the parametric approach", *IEEE signal processing magazine*, vol. 13, no. 4, pp. 67-94, Jul. 1996.
- [5] V.K. Anandan, P. Balamuralidhar, P. B. Rao, A. R. Jain, C. J. Pan, "An adaptive moments estimation technique applied to MST radar echoes", *J. Atmos.Oceanic Technol.*, vol. 22, pp. 396-408, Apr. 2005.
- [6] R.D. Palmer, S. Gopalam, T. Yu, S. Fukao, "Coherent radar imaging using Capon's method", *Radio Sci.*, vol. 33, no. 6, pp. 1585-1598, 1998.

Session 4

Predicting the occurrence of visual Noctilucent Clouds

John Rowlands¹, Kerry A. Day¹, David A. Hooper², and Nicholas J. Mitchell¹

¹ University of Bath

² STFC Rutherford Appleton Laboratory

1. Introduction

Noctilucent clouds (NLCs) form as a result of exceptionally cold (< 150 K) mesopause temperatures at upper-middle and high latitudes during the mid-summer months. They are composed of ice crystals with sizes in excess of ~ 20 nm. In the northern hemisphere, they can often be seen during the twilight hours of June and July at latitudes poleward of $\sim 50^\circ\text{N}$ - see Figure 1 for examples. Records of their appearance at geographically-diverse locations are available thanks to the efforts of a mainly-amateur observing community. Smaller, sub-visible ice crystals play a role in the occurrence of strong Mesosphere Summer Echoes (MSEs), which can be observed by radars operating at frequencies of between 10s and 100s of MHz [Rapp and Lübken, 2004].

The mesopause temperature increases with decreasing latitude and it is relatively close to the frost point at upper-middle northern latitudes, i.e. $50^\circ - 55^\circ$ N. Moreover, the characteristics of both NLCs and MSEs are highly variable at these latitudes. The fundamental aim of this work is to determine whether fluctuations in the mesopause temperature are responsible for the variations in NLC and MSE characteristics. A secondary aim is to determine whether daytime MSE observations can be used to predict whether NLCs are likely to be seen on the following night. This is motivated by the interests of the amateur observers and of the general public, who would like to know in advance which nights are likely to offer the best NLCs.



Figure 1: NLCs photographed by John Rowlands from Anglesey, 53.42° N, (left) on the morning of 2nd July 2011 and (right) on the morning of 3rd July 2011.

2. Observations

NLC data from a single observer (Rowlands) are considered here. The observation site (53.42° N, -4.45° E) on Anglesey in North Wales - see Figure 2 - is characterised by low levels of light pollution and flat terrain in all directions. Visual observations were made on a nightly

basis during June and July of each year since 2009. Periods for which low-level cloud obscured the sky are represented by vertical orange bands in Figure 3. For the 2010 season, no NLC observations were made after 17th July (day 198) and so the subsequent period has been blanked in the same fashion.

NLCs are typically seen between NW and NE, where they remain illuminated for a considerable period after the Sun has set from the lower atmosphere. Some studies [e.g. *Dalin et al., 2011*] have considered the brightness of NLCs as the primary variable of interest. Here we consider the maximum elevation angle, which ranges between 2° and 180° , i.e. NLCs were seen from the northern to the southern horizon. The inner orange arc in Figure 2 represents a great circle distance of $2.5^\circ/280$ km from the observation site, which corresponds to the median elevation angle of 15° . This assumes an NLC altitude of 82 km. The outer arc represents a great circle distance of $3.6^\circ/400$ km, which corresponds to an elevation angle of 10° . Owing to the large spread in elevation angles, and to the fact that they are more-clustered at the lower end of the range, log₁₀ values are used: 0.5 corresponds to 3.1° , 1.0 to 10.0° , 1.5 to 31.6° , 2.0 to 100.0° , and 2.26 to 180.0° .

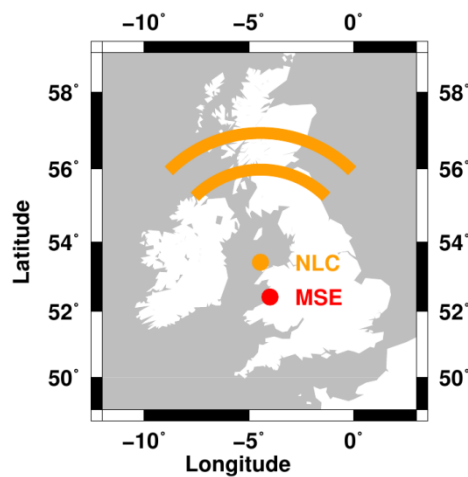


Figure 2: Locations of the Aberystwyth MST Radar (red dot) and of the NLC observation site (orange dot). The inner orange arc represents the potential locations of NLCs with an elevation angle of 15° and the outer arc an elevation angle of 10° .

The Natural Environment Research Council (NERC) MST Radar at Aberystwyth (52.42°N , -4.01°E) - see Figure 2 - has been making a single Vertical beam observation of the mesosphere once every 5 minutes since April 2005. MSEs are commonly observed during June and July of each year. These are similar in nature to the PMSEs observed at polar latitudes, although their daily integrated durations - see Figure 3 - are considerably shorter [*Bremer et al., 2006*]. This is assumed to be the result of the facts that the mesopause is not subject to continuous daylight at these latitudes and that its temperature is relatively close to the frost point.

Daily temperature data are taken from the University of Bath's (SKYiMET) meteor radar at Esrange in Northern Sweden (67.89°N , 21.08°E). Clearly there is a large (> 2000 km), principally-meridional separation between this and the other two sites, which are only 115 km apart. Consequently, the measured temperatures are expected to be significantly lower than those for the latitudes of interest. Nevertheless, it is known that planetary waves - such as the wavenumber 1, westward-propagating, (W1) 5-day wave, whose period actually

varies between 4 and 7 days - plays a significant role in modulating the temperature of the upper mesosphere. The power spectrum of Kiruna data for 2011, shown in Figure 4, contains significant activity within this range (although this alone does not prove the existence of planetary wave activity). Modulations in NLC occurrence/brightness and in MSE occurrence at polar latitudes have been linked to such wave activity [e.g. *Kirkwood et al.*, 2001]. The zonal separation of 25° between the meteor radar and the other two sites implies a phase difference of just 8 hours in the context of a W1 planetary wave with a period of 5 days.

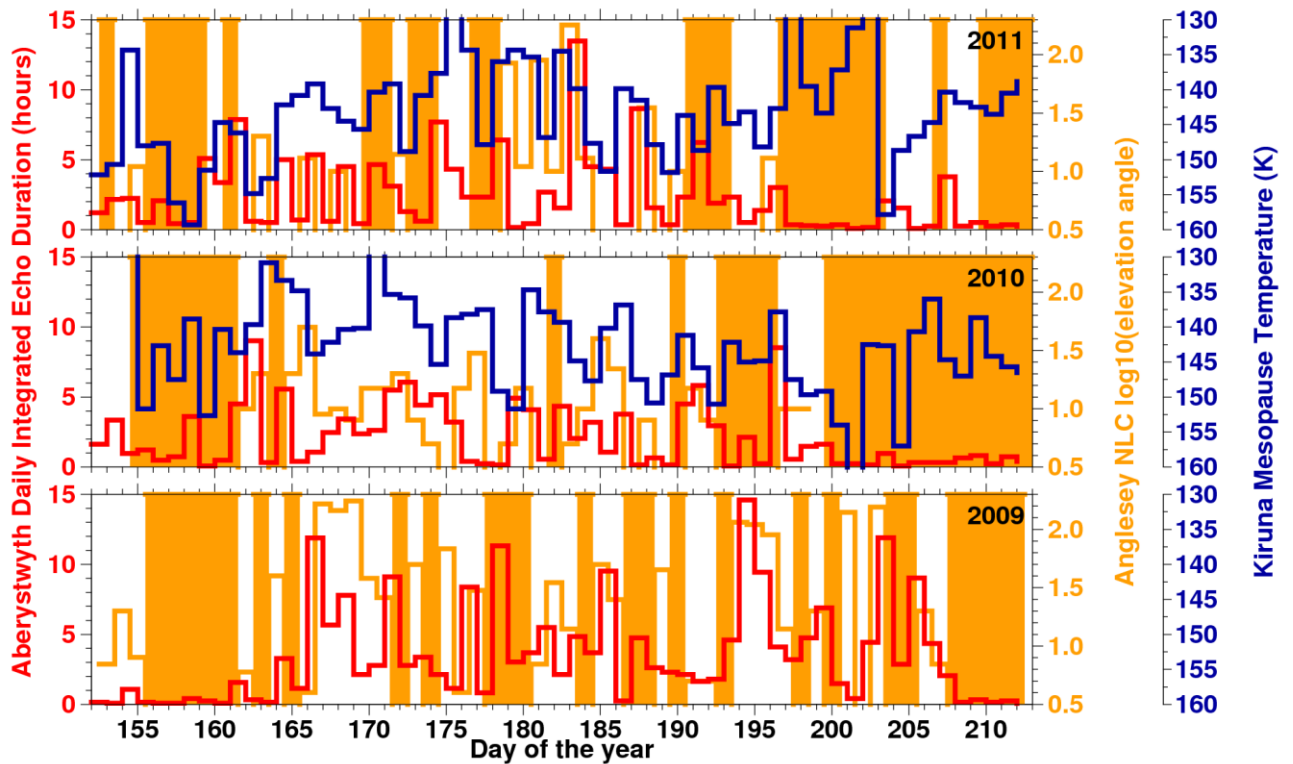


Figure 3: Time series of daily integrated echo duration (red), \log_{10} (NLC elevation angle) (orange), and temperature (blue). Note the inverted temperature axis. Orange bands represent periods when no NLC observations could be made. Tick marks represent 00:00 UT for days in the range between 1st June and 31st July.

3. Results and Further Work

The correlation coefficient of -0.48 between \log_{10} (NLC elevation angle) and temperature suggests that the Kiruna measurements have value in trying to understand the NLCs observed from the British Isles. Admittedly, this is based on a relatively small set of samples. The correlation coefficients between echo duration and temperature (-0.18) and between echo duration and \log_{10} (NLC elevation angle) (0.26) are not so good. Nevertheless, it can be seen from Figure 3 that the relatively rare echoes with durations in excess of 10 hours are associated with large NLC elevation angles, either on the previous or on the following night. This analysis is currently being extended with more-geographically-localised mesopause temperature data from the MLS instrument on-board the Aura satellite.

4. Public Engagement through NLC studies

During 2010, BBC Radio 4's "Material World" science programme aimed to promote the popular understanding of science using a contest format known as "So You Want To Be A Scientist?". John Rowlands' NLC project was one of four proposals selected from over 1300 entries. Nicholas Mitchell acted as John's mentor.

Through this radio production, the subject of NLCs was brought to the attention of an enormous popular audience. An "audio slide show", featuring images of NLCs set to a narrative sound-track, generated over 1 million unique hits within the first few hours of its release. It remained the most-viewed item on the BBC website for the greater part of a week. Several British newspapers and magazines subsequently published features on NLCs. Moreover, the Japanese broadcaster NHK made an entire programme on the subject. This featured interviews with both John and Nicholas. The possible influence of human activities on the remote mesosphere was of particular interest to the BBC audience. The ease with which anyone including those living under heavily light-polluted skies can observe NLCs was another attraction.

John has been systematically observing, and photographing, NLCs since 2008. This was initially motivated by the lead-up to solar minimum and the possibility that there might be corresponding increases in NLC occurrence and extent. John is also keen to improve the scientific-usability of the NLC observations that are submitted to amateur observation websites, which do not filter for the reliability of the submitted data. He has set up Facebook pages for the 2011, 2012, and 2013 seasons - see e.g. <http://www.facebook.com/NoctilucentClouds2013>. The nocturnal observing schedule is extremely demanding and leads to the loss of approximately 120 hours of sleep each summer! Consequently John hopes to set up a series of automatic cameras. One is planned for the Falkland Islands in attempt to improve the detection of NLCs in the southern hemisphere. This will be carried out with the kind assistance of IRF-Kiruna and the British Antarctic Survey.

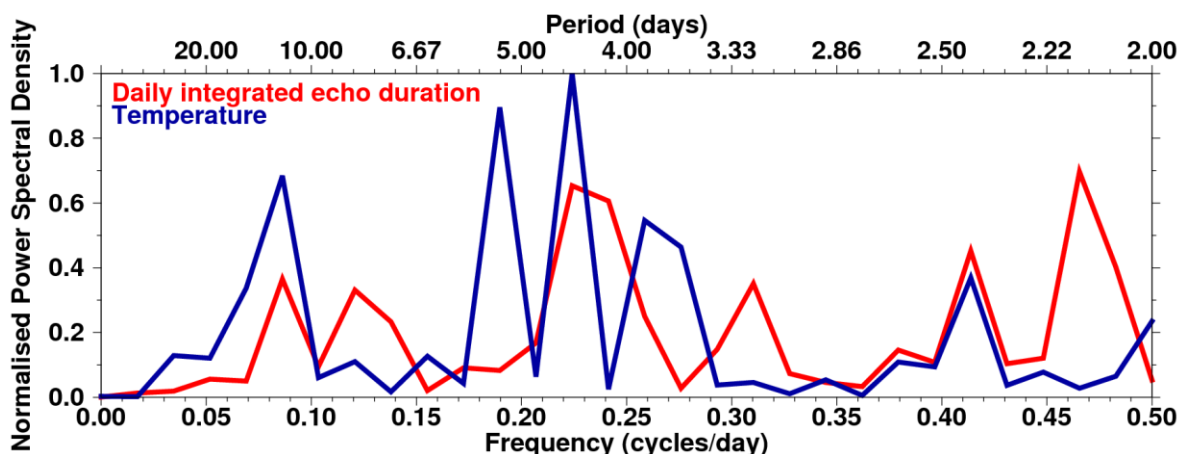


Figure 4: Power spectra for the period 4th June - 31st July 2011. The lowest frequency components have been removed by subtracting a 15 day running mean from the samples in the time domain. Power spectral densities have been normalised so that the total powers are equal for the temperature (blue) and radar echo (red) data.

References

- Bremer, J., P. Hoffmann, J. Hoffner, R. Latteck, W. Singer, M. Zecha, and O. Zeller, Long-term changes of mesospheric summer echoes at polar and middle latitudes, *J. Atmos. Sol.-Terr. Phys.*, 68, 1940–1951, doi:10.1016/j.jastp.2006.02.012, 2006.
- Dalin, P., et al., A comparison between ground-based observations of noctilucent clouds and aura satellite data, *J. Atmos. Sol.-Terr. Phys.*, 73, 2097–2109, doi:10.1016/j.jastp.2011.01.020, 2011.
- Kirkwood, S., V. Barabash, B. U. E. Brändström, A. Moström, K. Stebel, N. Mitchell, and a o o W. Hocking, Noctilucent clouds, PMSE and 5-day planetary waves: A case study, *Geophys. Res. Lett.*, 29(10), 1411, doi:10.1029/2001GL014022, 2001.
- Rapp, M., and F.-J. Lübken, Polar mesosphere summer echoes (PMSE): review of observations u and current understanding, *Atmos. Chem. and Phys.*, 4, 2601–2633, 2004.

Session 5

Vertical flow in atmospheric boundary layer observed by a lower troposphere radar under clear air condition

Tomoyuki Nakajo¹, Kenji Sasaki¹, Yuki Ogura¹, Yoichiro Saito¹, Hiroyuki Hashiguchi², Manabu D. Yamanaka³, Shoichiro Fukao¹

¹ Department of Electrical, Electronics and Computer Engineering, Fukui University of Technology, Fukui, Japan

² Research Institute for Sustainable Humanosphere, Kyoto University, Uji, Japan

³ Research Institute for Global Change, Japan Agency for Marine-Earth Science and Technology, Japan

Abstracts

Statistical data analysis of lower troposphere (LTR) radar at Shigaraki MU observatory in Japan was done in this study for investigating the vertical flow in atmospheric boundary layer (ABL). As the results, it is confirmed that the main origin of echoes observed by LTR is atmospheric turbulence and is not small targets as insects. We also found that the downward flow with the speed of a few 10 cm/s was dominant in daytime ABL, however, the cause of downward flow has been remained as a problem to be solved. It is expected that a new LTR observation with range imaging technique will be useful in order to reveal the detailed aspect of vertical flow.

1. Introduction

The atmospheric boundary layer (ABL) is one of most important atmospheric layers in terms of having a direct influence on our life, the detailed motion of atmosphere. It has been well known that turbulences with various spatial scales from a few cm to a few hundred meters dominate in ABL by an effect of friction between ground and atmosphere. Therefore, it is very important to measure the characteristics and actual detailed motion of the turbulences from the viewpoint of weather forecasting and prediction of air pollutants diffusion. However, they have not been fully investigated because of its immense complexity.

2. Lower Troposphere Radar and purpose of this study

One of powerful tools for exploring ABL is Lower Troposphere Radar (LTR). LTR can observe wind velocity in 3D from a few hundred meters to about ten km in altitude with the range resolution of a few hundred meters and the temporal resolution of a few minutes. In Japan, Kyoto University had developed a LTR using L band radio wave (Hashiguchi et al., 1995). The LTR has compact aperture area (16 m²) and adopts phased-array system which enables measurement of wind velocity in 3D by sweeping beam direction. Based on the achievements, network of LTR named as "WINDAS" (WInd profiler Network and Data Acquisition System) has been worked since 2000 by Japan Meteorological Agency for improvement of accuracy of weather forecast (Ishihara and Goda., 2000). However, only the horizontal component of wind velocity is used for weather forecast, the actual aspect of vertical component which directly influence the evolution of clouds has not been investigated. In this study, we re-analyzed LTR data obtained continuously in 2000 at Shigaraki MU observatory in Japan for investigating the actual aspect of vertical flow in ABL.

3. Data analyses and results

As the first stage, we selected the data obtained in daytime under clear air condition because air motion is expected to be simple relatively. Fig.1 shows a result of data analysis showing an example of evolution of ABL observed by LTR on May 4 in 2000. The strong upward flow in the morning (~8:30) and the following growth and fading after 14:00 of ABL are the reasonable features that are expected as the effect of sunshine. However, we can clearly recognize that downward flow dominates in ABL from 11:00 to 14:00 despite the top of ABL moves upward. In addition, we can also see the strong upward flow from 15:30 to 16:30 despite the top of ABL moves downward. These observed features of vertical flow are unexpected features.

In order to investigate whether the observed features of vertical flow is usual, we calculated the averaged image of ABL under clear air condition in each season. For selection of data under clear air condition, we selected the days where hours of sunshine per day are longer than 4.8 hours. The hours of sunshine per day was calculated by using the data of sunshine rate supplied by AMeDAS system operated by Japan Meteorological Agency. As the result, 46, 41, 39 and 24 days were selected in spring (Mar-May), summer (Jun-Aug), fall (Sep-Nov), and winter (Dec-Feb), respectively. We calculated the averaged images of wind velocity, echo power and spectral width by using the data obtained in the selected days in each season. Fig.2 shows the resulting averaged image of ABL in the case of summer. We can recognize the evolution of ABL similar to Fig.1. Especially, the downward flow dominates in daytime ABL, which is commonly observed in the results of all seasons (The results in other seasons are omitted due to limitations of space).

4. Discussions

The results of data analysis indicate the dominant downward flow in daytime ABL is almost always observed by LTR under clear air condition. Angevine (1997) reported similar results and concluded the downward flow was caused by the effect of small targets such as insects. However, the evolution of daytime ABL based on the data of echo intensity and spectral width in this study shows reasonable features despite the dominant downward flow is observed. Therefore, we consider that the observed echo intensity and spectral width include the information of atmosphere in ABL ; the observed echoes come from atmosphere.

We show another example that the dominant downward flow concerning with atmosphere was observed. Fig. 3 shows an example of comparison LTR data with radiosonde data at Shigaraki MU observatory at about 11:45 on August 15 in 2001. In the day, the dominant downward flow was observed in daytime ABL by LTR. In the rightmost panel of Fig.3, the downward flow is observed from 1 to 2 km in altitude. The second panel from the left indicates turbulence structure constant and mixing ratio where the dependences of both physical quantities are in good agreement. In addition, the altitude (~2 km) with the strongest echo intensity has a good agreement with the altitude with strong turbulence of a refractive index (the leftmost panel). In addition, the values of spectral width are larger in the area where potential temperature is almost constant. Therefore, we conclude the origin of echoes in Fig.3 was atmospheric turbulence, not insects.

Based on the above discussions, we conclude that the echoes observed by LTR come from atmosphere in almost cases. Table 1 shows some parameters of ABL obtained by data of echo intensity and spectral width. The ascent rate in the table shows the upward speed of top of ABL. The value of each parameter is at a maximum in summer, which also indicates that the main origin of observed echoes is atmosphere.

A cause of dominant downward flow is unknown in this study. In the present LTR observation, time constant is 10 minutes ; wind velocity obtained by LTR is the result of spatial average with the horizontal spatial resolution of a few km. Therefore, true vertical flow may not be measured correctly. About this point, a new LTR with range imaging technique (Yamamoto, 2012) will be useful in the future study. In July of 2012, such new LTR was installed at Awara campus in Fukui University of Technology. We will study the detailed features of vertical air motion by using the new LTR.

5. Summary

We re-analyzed LTR data obtained continuously in 2000 at Shigaraki MU observatory in Japan for investigating vertical flow in ABL which is very important for weather forecast. As the results, we found that downward flow dominates in the daytime ABL under clear air condition in all season. The reason that downward flow dominates is not clear in this study, however, we showed that observed echoes by LTR come from atmosphere (not insects) in almost all cases and it is possible to measure some parameters of daytime ABL. For the future, a new LTR observation with range imaging technique and short time constant (a few seconds) is expected to reveal true vertical flow in ABL.

References

- Angevine, W. M., Errors in Mean Vertical Velocities Measured by Boundary Layer Wind Profilers, *Journal of Atmospheric and Oceanic Technology*,14, 565-569, 1997.
- Hashiguchi, H., M.D.Yamanaka, T. Tsuda, M.Yamamoto, T.Nakamura, T.Adachi, S.Fukao, Diurnal Variations of the Planetary Boundary Layer Observed with An L-band Clear-Air DopplerRadar, *Boundary-Layer-Meteorology*, 74, 419-424, 1995.
- Ishihara, M. and H. Goda, Operational 1.3GHz wind profiler network of Japan Meteorological Agency, *Proceeding of the MST and COST76 Workshop*, 538-540, 2000.
- Yamamoto, M. K., New observations by wind profiling radars, in *Doppler Radar Observations - Weather Radar, Wind Profiler, Ionospheric Radar, and Other Advanced Applications*, J. Bech and J. L. Chau ed.,247-270, InTech, Rijeka, Croatia, 2012.

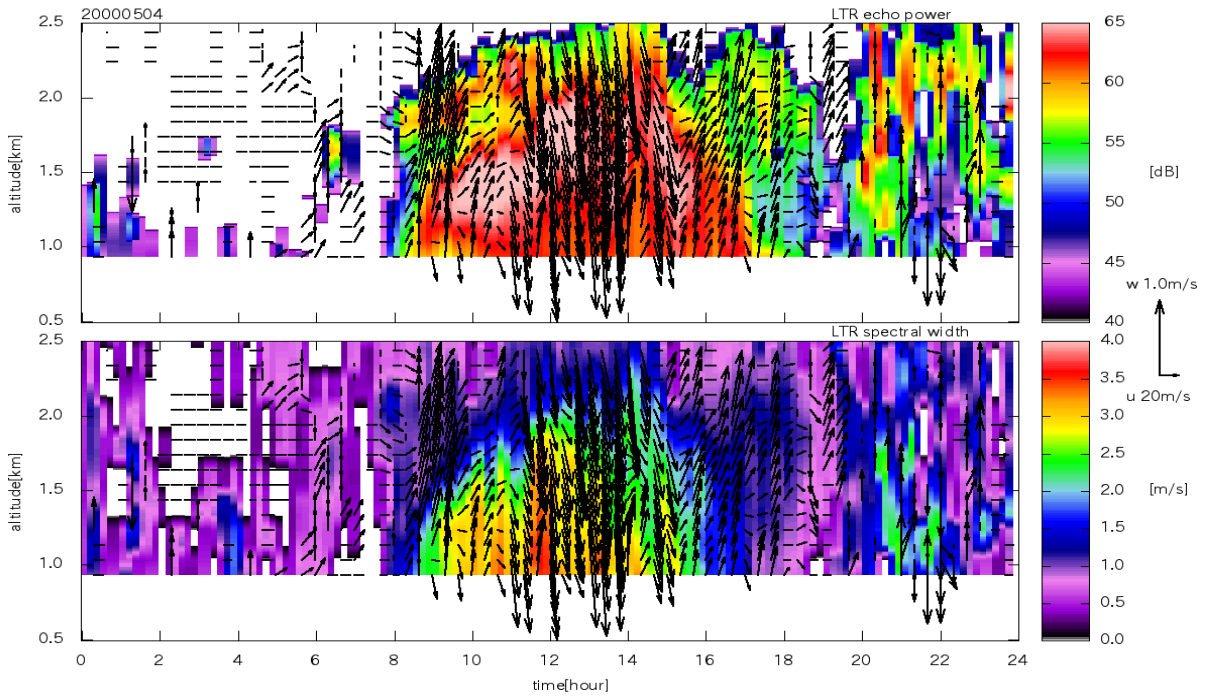


Figure 1: An example of observation of ABL by LTR at Shigaraki MU observatory on May 4 in 2000. The color contours indicate relative echo intensity in the upper panel and spectral width in the lower panel. The arrows indicate wind velocities where horizontal components are westerly velocity (u) and vertical components are vertical velocity (w).

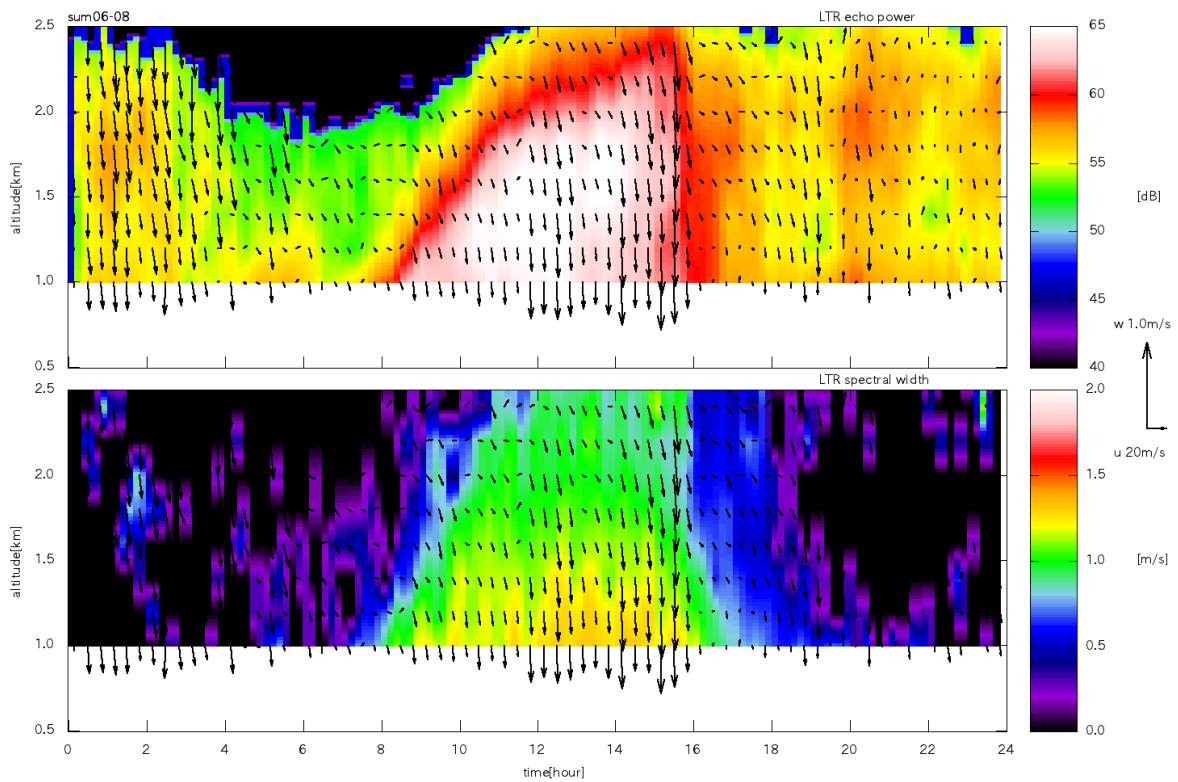


Figure 2: Averaged image of ABL in summer based on LTR data obtained at Shigaraki MU observatory. The format is same as Fig.1.

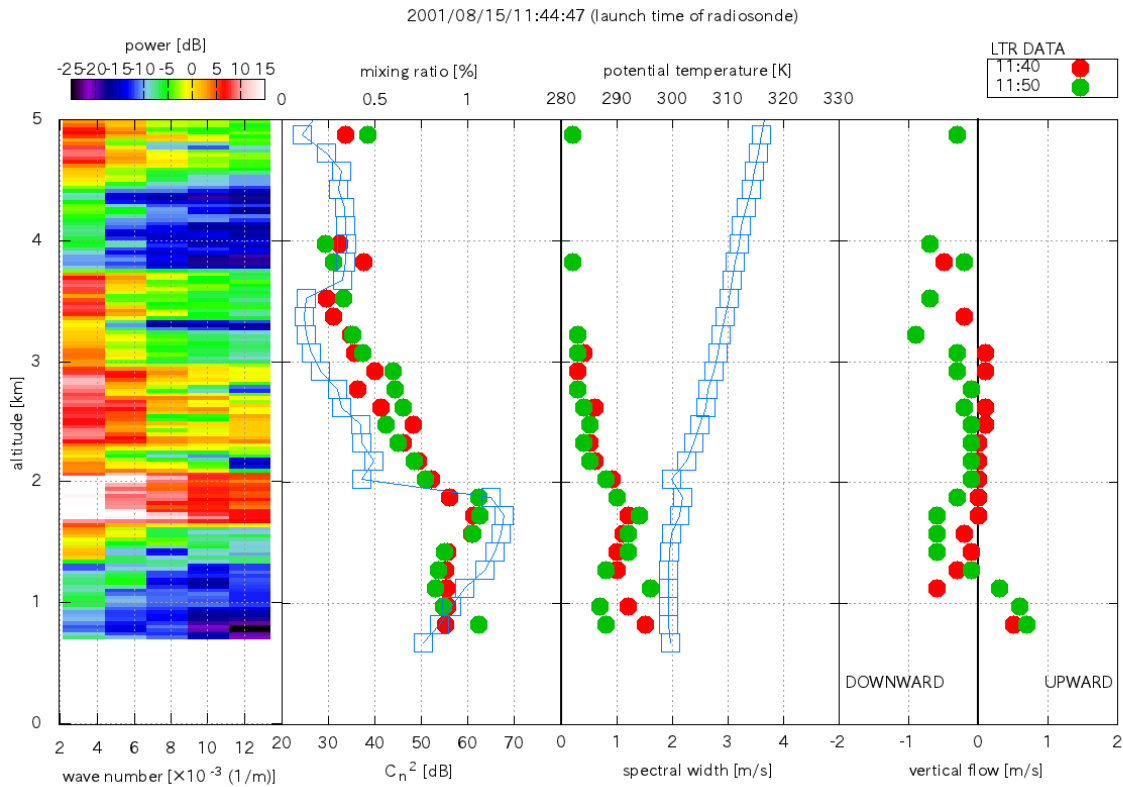


Figure 3: An example of comparison LTR data with radiosonde data at Shigaraki MU observatory on August 15 in 2001. The leftmost panel indicates the spectrum of wave number of refractive index measured by radiosonde. In other panels, the circles and squares are physical quantities measured by LTR and radiosonde respectively. The second panel from the left indicates turbulence structure constant and mixing ratio. The third panel from the left indicates spectral width and potential temperature. The rightmost panel indicates vertical components of wind velocity.

parameters	Spring	Summer	Fall	Winter
Maximum altitude	2.0km	2.5km	1.8km	1.5km
Ascent rate	0.05m/s	0.08m/s	0.08m/s	0.05m/s
Maximum echo relative intensity	65dB	70dB	57dB	50dB

Table 1: Resulting parameters of daytime ABL under clear air condition parameters.

Measurement of vertical air velocity and hydrometeors in stratiform precipitation by the Equatorial Atmosphere Radar and polarization lidar

Masayuki K. Yamamoto¹, Tomoaki Mega¹, Yasukuni Shibata², Makoto Abo², Hiroyuki Hashiguchi¹, Toyoshi Shimomai³, Yoshiaki Shibagaki⁴, Mamoru Yamamoto¹, Manabu D. Yamanaka^{5,6,7}, Shoichiro Fukao^{1,8}, Timbul Manik⁹

¹ Research Institute for Sustainable Humanosphere, Kyoto University, Japan

² Faculty of System Design, Tokyo Metropolitan University, Japan

³ Interdisciplinary Faculty of Science and Engineering, Shimane University, Japan

⁴ Faculty of Information and Communication Engineering, Osaka Electro-Communication University, Japan

⁵ Japan Agency for Marine-Earth Science and Technology, Japan

⁶ SATREPS-MCCOE Promotion Office, Indonesia

⁷ Graduate School of Science, Kobe University, Japan

⁸ Fukui University of Technology, Japan

⁹ National Institute of Aeronautics and Space (LAPAN), Indonesia

Abstract

Results from simultaneous measurements of vertical air velocity (W), particle fall velocity, and hydrometeor sphericity in stratiform precipitation are reported for the first time. Cases of stratiform precipitation on 8 (case A) and 16 December 2008 (case B) observed at Sumatra, Indonesia (0.2°S, 100.32°E) are described. A 47-MHz wind profiling radar measured W and reflectivity-weighted particle fall velocity relative to the air (V_Z) simultaneously. Upward W above ~6.0 km altitude in the case B ($> 0.2 \text{ m s}^{-1}$) was greater than the case A ($< 0.1 \text{ m s}^{-1}$). V_Z at 300 m above the 0°C altitude in the case B (1.8 m s^{-1}) was greater than the case A (1.3 m s^{-1}). The thickness of melting layer (ML) in the case B (900 m) was greater than the case A (300 m). Because the large-sized aggregates contribute to produce greater V_Z and thicker ML, it is likely that entangled growth of dendritic crystals under the presence of significant upward W and enhanced aggregation occurrence by the well-developed dendritic crystals produced large-sized aggregates. Lidar measured an increase of linear depolarization ratio (δ) and lidar dark band in the ML. Volume δ of raindrops was 0.08-0.10 in the case B and close to zero in the case A. Stronger multiple scattering in the case B is likely a cause that produced the greater δ . In the case B, a dip of δ was measured at the bottom of ML. The decrease of hydrometeor nonsphericity at the final stage of melting explains the dip. More details of the study are described by Mega et al. (2012).

1. Introduction

Though vertical air velocity (W) in stratiform precipitation is small compared to fall velocity of ice crystals, upward air motion above the 0°C altitude plays a crucial role in maintaining supersaturation by condensing vapor, which is deposited onto ice particles (Houze, 1993). Wind profiling radars operated near 50 MHz frequency (i.e., 6 m wavelength; hereafter 50-MHz wind profiling radars) have been proved to be useful for measuring W in stratiform precipitation region, because their low frequency enables them to detect clear-air echoes and precipitation echoes separately (e.g., Wakasugi et al., 1996). Though frequencies used by wind profiling radars (i.e., less than 2-3 GHz) are lower than those of weather radars, they have sufficient sensitivity to measure particle fall velocity relative to the ground (hereafter V_{Z+air}) using echoes scattered by

hydrometeors. Further, W measured by wind profiling radars contributes to measure reflectivity-weighted particle fall velocity relative to the air (V_Z) correctly, because V_Z can be retrieved by subtracting W from V_{Z+air} . Lidars which detect echoes scattered by hydrometeors are also a promising tool to measure microphysical properties of precipitation. Especially, linear depolarization ratio (δ) measured by lidars has been proved to be useful for differentiating the phase, shape, and orientation of hydrometeors (Sassen, 1991). Though measurements using a wind profiling radar and lidar have been used to study wind and turbulence features in and around non-precipitating clouds (e.g., Yamamoto et al., 2009), measurement results in precipitating conditions have not been reported. W , V_Z , and δ profiles in stratiform precipitation were measured simultaneously at the Equatorial Atmosphere Observatory at Kototabang, West Sumatra Indonesia (0.2°S, 100.32°E, 865 m height above the mean sea level (MSL)) on 8 and 16 December 2008. Using the measurement results of a 47-MHz wind profiling radar referred to as the Equatorial Atmosphere Radar (hereafter EAR; Fukao et al., 2003) and 532-nm polarization lidar (hereafter lidar), characteristics of W , V_Z , and δ in the stratiform precipitation were investigated.

2. Data

EAR has an antenna array with a diameter of 110 m and total peak output power of 100 kW. During the period described in the study, the radar beam was fixed to the vertical incidence in order to intensively measure W and V_{Z+air} . V_Z was computed using the relation $V_Z = V_{Z+air} - W$. Because time for data sampling (i.e., time for transmitting and receiving signals) was 131 s and time for transferring observed data to the hard disk drive was 9 s, the time interval of each record was 140 s. The vertical resolution was 150 m.

The laser used in this study was radiated to the vertical incidence with an output power of 200 mJ, pulse repetition frequency of 10 Hz, beam diameter of 10 cm, and half laser beam divergence of 0.1 mrad. The telescope receiver was aligned with the laser axis and consisted of Makustov-Cassegrain telescope with 11 cm diameter. The receiver field of view (FOV) was 0.5 mrad. Altitude profiles of lidar return at the direction perpendicular to the laser polarization (P_{\perp}) and at that parallel to the laser polarization (P_{\parallel}) were collected with 1-min and 30-m intervals. Volume δ was defined as the ratio of P_{\perp} to P_{\parallel} (i.e., $\delta = P_{\perp}/P_{\parallel}$). Backscattered intensity (P) was calculated as the sum of P_{\perp} and P_{\parallel} .

During the intensive observation period of the EAR and lidar in 2008 (i.e., from 6 to 23 December 2008), the lidar returns were detected up to the melting layer (ML) in the stratiform precipitation on 8 and 16 December 2008. Therefore the two cases on 8 December (case A) and 16 December (case B) were intensively studied. The case A can be characterized as weak rainfall because raindrops evaporated until they reach to the ground. The case B can be characterized as moderated rainfall because rainfall intensity was 2-5 mm h⁻¹ (Tokay and Short, 1996).

3. Result

Figure 1a and 2a show altitude profiles of W for the case A and B, respectively. Upward W above 6 km MSL in the case B (> 0.2 m s⁻¹) was greater than that in the case A (< 0.1 m s⁻¹). This indicates that the processes that produce upward W (i.e., latent heat release resulting from deposition growth, gravity waves, old cells which have origin in the convective region, and latent heat release resulting from riming) were more active in the case B. Figure 1b and 2b show altitude profiles of V_Z for the case A and B, respectively. Because V_Z for the case B was greater than that for the case A and V_Z is weighted by reflectivity proportional to the 6th power of equivalent diameter of hydrometeors, it is concluded that raindrop size for the case B is greater than the case A.

The ML altitude estimated from the large V_z change in altitude was 4.6-4.9 km MSL (i.e., 300-m thickness) for the case A and 4.0-4.9 km MSL (i.e., 900-m thickness) for the case B. The lidar dark band, a decrease in lidar returns in ML (Sassen and Chen, 1995), also existed where the large V_z changes were observed (Figures 1c and 2c). Because only large-sized aggregates determine the thickness of melting layer (Willis and Heymsfield, 1989), the difference in ML thickness also indicates the presence of larger-sized snowflakes in the case B than in the case A. In the case B, the increase of V_z was seen even in the altitude range 4.9-6.2 km MSL, where upward W was not observed. In the case B, V_z was $\sim 1.4 \text{ m s}^{-1}$ around 6.2 km MSL and $\sim 1.8 \text{ m s}^{-1}$ around 5.1 km MSL (Figure 2b). Aggregation is the most plausible cause that produced the greater increase in V_z in the altitude range 4.9-6.2 km MSL in the case B, because it occurs even in the absence of upward W (necessary condition for riming occurrence), and occurrence frequency of aggregation becomes much greater at temperature above $\sim -5^\circ\text{C}$ (i.e. below 6.0 km MSL). The greater δ in ML in the case B also indicates the increase in snowflake nonsphericity caused by aggregation (Figure 1d and Figure 2d). Therefore aggregation is a plausible cause that produced the thicker ML in the case B. For occurrence of aggregation, entangled arm growth of snowflakes between -10 and -16°C (i.e., 6.7-7.7 km MSL) is necessary. A greater W at 6.7-7.7 km MSL in the case B provided more preferable condition for entangled arm growth of dendritic crystals than that in the case A (Figures 1a and b).

Though volume δ for raindrops in the case A (below 4.5 km; Figure 1d) was close to 0, volume δ for raindrops in the case B (below 4.0 km; Figure 2d) was 0.08-0.10. Multiple scattering which occurs under the presence of large-sized raindrops (Tatarov and Kolev, 2001) explains the increase in volume δ in the case B. It is noted that δ dip was observed around 4.0 km MSL in the case B (Figure 2d). The large-sized aggregate disrupts into small-sized particles at the final stage of melting, and the disrupted small-sized particles display round, plate, or lenslike shapes (Fujiyoshi, 1986; Knight, 1979). The decrease of nonsphericity at the final stage of melting explains the δ dip at the bottom of ML.

4. Summary

Using the measurement results of a 47-MHz wind profiling radar (EAR) and 532-nm polarization lidar (hereafter lidar), characteristics of W , V_z , and δ in the stratiform precipitation for the cases on 8 and 16 December 2008 at Equatorial Atmosphere Observatory at Kototabang, West Sumatra Indonesia were described. Observations to collect more stratiform precipitation cases are planned.

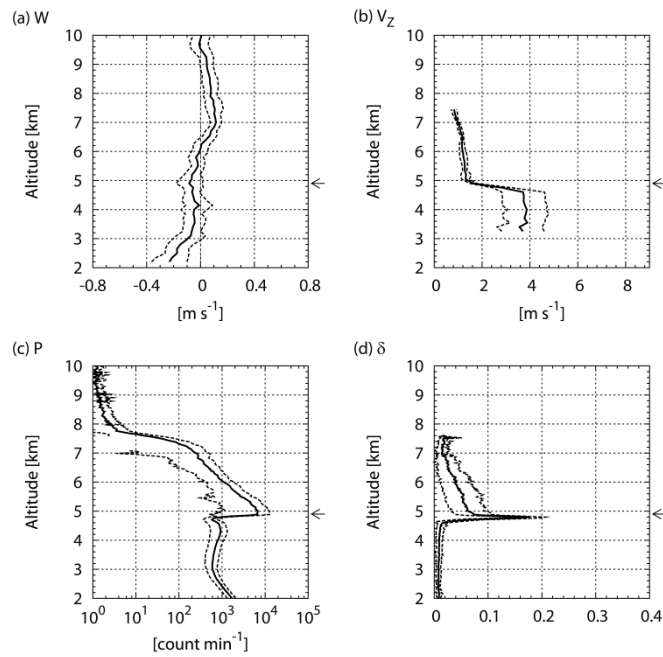


Figure 1: Altitude profile of (a) W , (b) V_z , (c) P , and (d) δ averaged from 0330 to 0450 LST on 16 December 2008. Positive W values indicate that wind velocity is upward, and positive V_z values indicate that hydrometeors fall toward the ground. Arrows at the right of each panel show the altitude of 0°C estimated by the radiosonde soundings. The thick curves show the average values, and the dotted curves on the both sides of the averaged values show disturbance determined by the standard deviation (Mega et al., 2012).

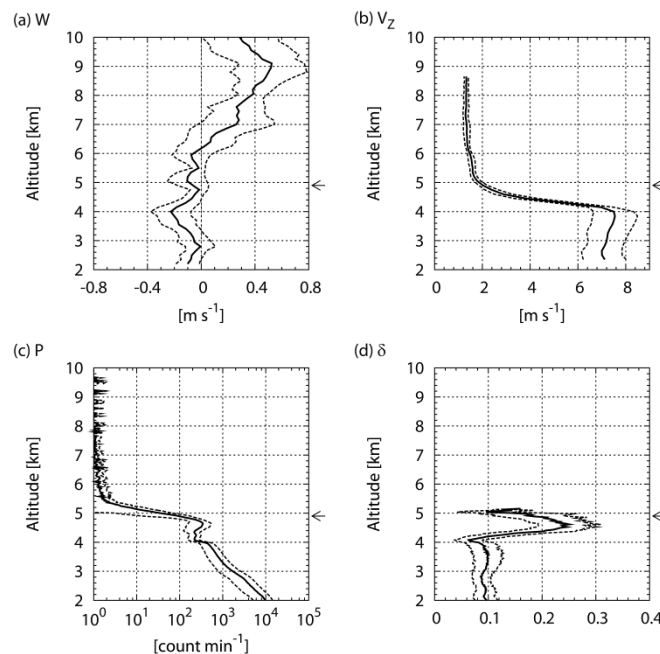


Figure 2: Same as Figure 1, expect the averaging period is from 2014 to 2141 LST on 16 December 2008 (Mega et al., 2012).

Acknowledgements

The study was supported by Hydrometeorological Array for Isv-Monsoon Automonitoring (HARIMAU) project of the Japan EOS Promotion Program (JEPP) funded by the Ministry of Education, Culture, Sports, Science, and Technology (MEXT) of Japan, Science and Technology Research Partnership for Sustainable Development (SATREPS) funded by Japan Science and Technology Agency (JST) and Japan International Cooperation Agency (JICA), Grant-in-Aid for Scientific Research (B) (19403008, 22403009 and 23340142) funded by Japan Society for the Promotion of Science (JSPS), and Grant-in-Aid for Young Scientists (B) (19740293) funded by MEXT, and the research grant for Exploratory Research on Sustainable Humanosphere Science from RISH.

References

- Fujiyoshi, Y. (1986), Melting snowflakes. *J. Atmos. Sci.*, *43*(3), 307-311.
- Fukao, S., H. Hashiguchi, M. Yamamoto, T. Tsuda, T. Nakamura, M. K. Yamamoto, T. Sato, M. Hagio, and Y. Yabugaki (2003), Equatorial Atmosphere Radar (EAR): System description and first results, *Radio Sci.*, *38*(3), 1053.
- Houze, R. A., Jr. (1993), Nimbostratus, in *Cloud dynamics*, pp. 196-220, Academic, San Diego, Calif.
- Knight, C. A., (1979), Observations of the morphology of melting snow, *J. Atmos. Sci.*, *36*(6), 1123-1130.
- Mega, T., M. K. Yamamoto, M. Abo, Y. Shibata, H. Hashiguchi, N. Nishi, T. Shimomai, Y. Shibagaki, M. Yamamoto, M. D. Yamanaka, S. Fukao, and Timbul Manik (2012), First simultaneous measurement of vertical air velocity, particle fall velocity, and hydrometeor sphericity in stratiform precipitation: Results from 47-MHz wind profiling radar and 532-nm polarization lidar observations, *Radio Sci.*, *47*, RS3002, doi:10.1029/2011RS004823.
- Sassen, K. (1991), The polarization lidar technique for cloud research: A review and current assessment, *Bull. Amer. Meteorol. Soc.*, *72*(12), 1848-1866.
- Sassen, K., and T. Chen (1995), The lidar dark band: An oddity of the radar bright band analogy, *Geophys. Res. Lett.*, *22*(24), 3505-3508, doi:10.1029/95GL03367.
- Tatarov, B. and I. Kolev (2001), Experimental determination of the multiple-scattering effect on the lidar-signal polarization characteristics during liquid- and solid-phase precipitation, *Appl. Phys. B*, *73*(3), 261-268.
- Tokay, A., and D. A. Short (1996), Evidence from tropical raindrop spectra of the origin of rain from stratiform versus convective clouds, *J. Appl. Meteorol.*, *35*(3), 355-371.
- Wakasugi, K., A. Mizutani, M. Matsuo, S. Fukao, and S. Kato (1986), A direct method for deriving drop-size distribution and vertical air velocities from VHF Doppler radar spectra, *J. Atmos. Oceanic Technol.*, *3*(4), 623-629.
- Willis, P. T., and A. J. Heymsfield (1989), Structure of the melting layer in mesoscale convective system stratiform precipitation, *J. Atmos. Sci.*, *46*(13), 2008-2025.
- Yamamoto, M. K., M. Abo, T. Kishi, N. Nishi, T. H. Seto, H. Hashiguchi, M. Yamamoto, and S. Fukao (2009), Vertical air motion in midlevel shallow-layer clouds observed by 47-MHz wind profiler and 532-nm Mie lidar: Initial results, *Radio Sci.*, *44*, RS4014.

Incorporation of O-QNet windprofiler data into numerical forecast models

W.K. Hocking¹, P. Taylor² and A. Hocking³

¹ University of Western Ontario, 1151 Richmond St., London, Ontario, Canada N6A 3K7

² York University, 4700 Keele St., Toronto Ont., Canada, M3J 1P3

³ Mardoc Inc., 18 Pitcarnie Cres., London, Ont. Canada, N6G4N4

Abstract

The process of incorporating Canadian profiler data into numerical forecast models is described. The sequence involved a series of successive comparisons and integrations, and to date tests have been performed using the Canadian Environment Canada GEM model and the UK Meteorological Office model. After many months of testing, the UK Met office has now begun assimilating the data into the model. Environment Canada is still performing further tests. Here, we describe the steps taken toward this integration.

1. Introduction

The first O-QNet (Ontario-Quebec Windprofiler NETwork) profiler began operation in November 2005, and by 24 July 2011, the ninth profiler was completed in Aumond, Quebec. The distribution of sites is shown in fig. 1. This includes profilers funded under two grants from the Canadian Foundation for Innovation – one for the profiler at McGill University in Quebec (led by I. Zawadzki and F. Fabry), and another led by P. Taylor and W. Hocking for establishment of 9 additional profilers. The profilers use Doppler methods above 1.5 km, and Spaced Antenna methods between 400m and typically 2 km, with joint methods utilized in the overlap region.

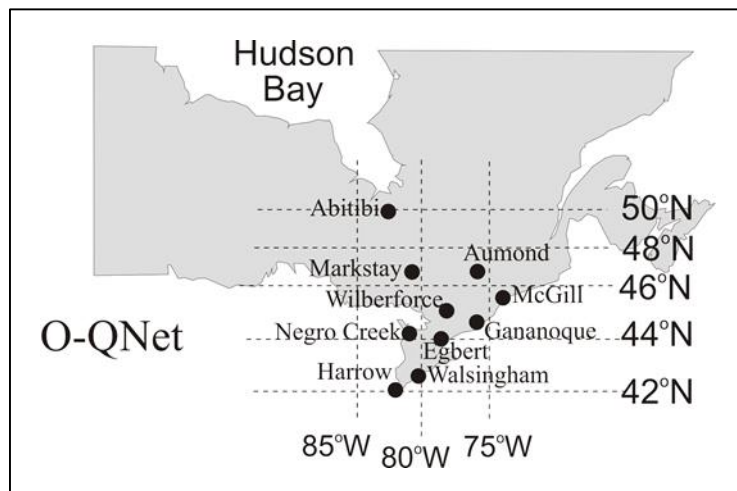


Figure 1: Distribution of the radars in the O-QNet.

The radar at Abitibi is still under construction. The radars at McGill, Walsingham, Harrow, Negro Creek, Egbert and Wilberforce had all been completed by January 2010. Subsequently the radar at Markstay began operation in October 2010, the one at Gananoque in February, 2011, and the one at Aumond in July 2011. The radars at Aumond and McGill are in Quebec, the others in

Ontario. Comparisons between the Canadian GEM model began in late 2009 and early 2010. Comparisons with EWINPROF began in November 2011.

2. Methodology

Radar data are sent hourly to sites at Environment Canada in Dorval, Quebec, Canada, and to an EWINPROF receiver site in England. Data from the radar were passed through a modified Weber-Wuertz outlier-rejection algorithm (Weber and Wuertz, 1991), then sent by bufr format to the designated sites.

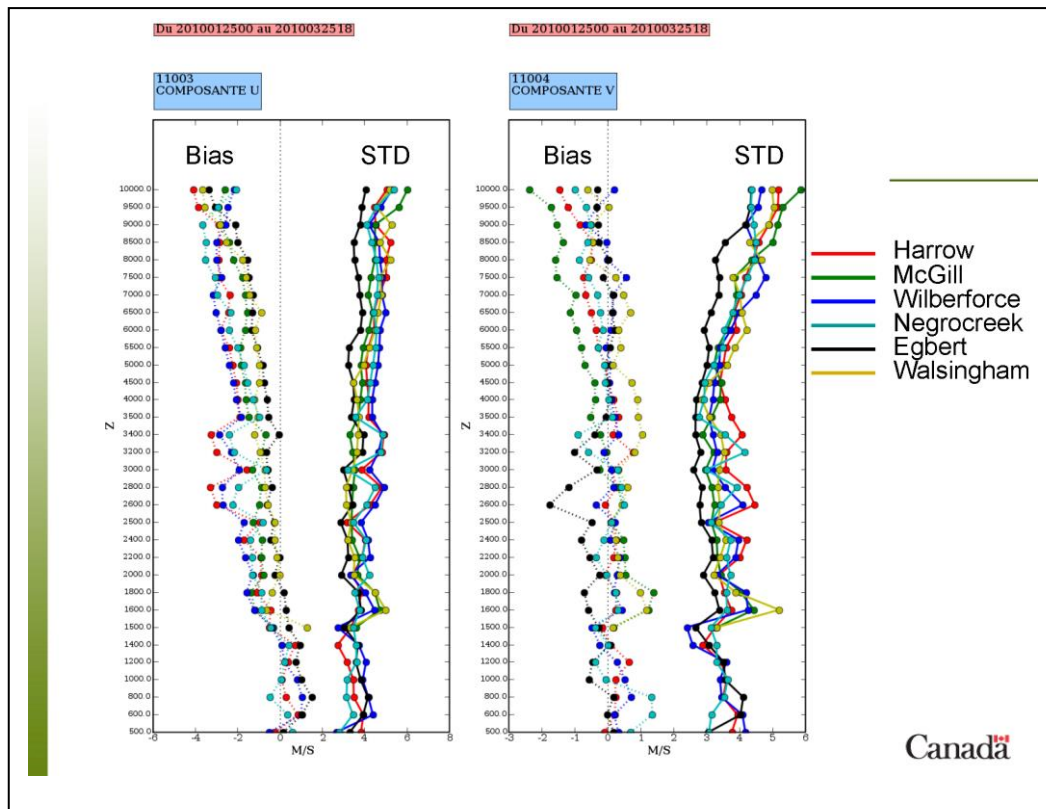


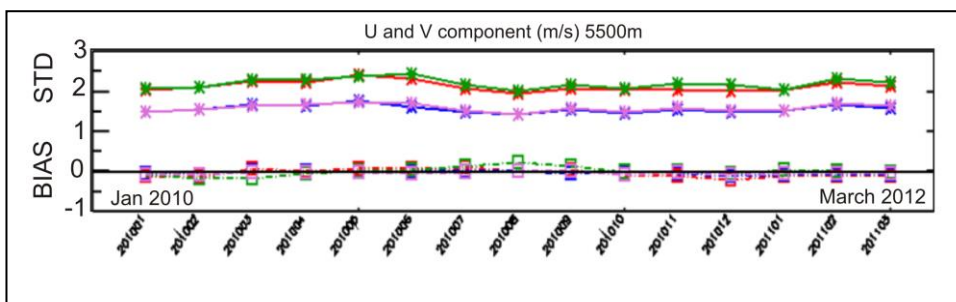
Figure 2: An early comparison of model and profiler data (Jan 2010). The comparisons make the agreement look worse than it really was, for reasons discussed in the text. Scales on the abscissa are from -6 to 8 m/s on the left and from -3 to 6 m/s on the right. Heights cover 500m to 10 km.

Fig.2 shows some very early comparisons. Both mean biases and standard deviations are shown for eastward (u) and northward (v) components. Several points are evident. A bulge in the biases at around 3 km altitude is evident in both components, and also to a lesser extent at 1800m. An increase in biases and standard deviations with increasing height is also evident, and a negative general bias is evident. All radars showed similar behaviour. Subsequent investigations showed several errors, as will be outlined in the next few paragraphs.

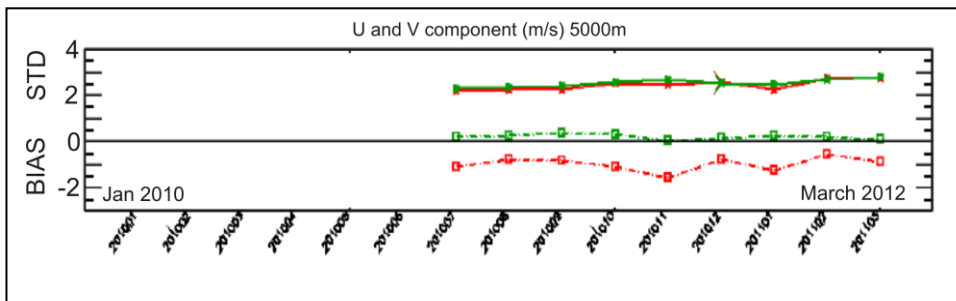
The first error is now described. Bufr files have various forms of storage, and the one used here used the height above sea-level. However, 1000m is added to the height as part of the format. The software used at Environment Canada did not correct for this height-offset, and the bulges seen in fig. 2 arose at heights where the mean wind shear was large, so that a 1000m offset led to enhanced differences between the model and the measurements. Corrections in the bufr-reading software led to removal of this bulge.

The “model” values are not just numerical simulations, but include input from a variety of accepted observation methods, such as commercial aircraft, balloons, and ground-based measurements. In general, it is expected that standard deviations should be less than 5 m/s, and preferably less than 3.5 m/s. Biases are expected to be of the order of 1 m/s or less in order for the profiler data to be accepted. Larger errors are generally attributed to the profilers. Our standard deviations were of the order of 4-5 m/s, which was considered marginal. The negative bias was a concern. We will discuss these points shortly.

Further studies suggested a second error. The effective beam direction was less than the assumed value. The nominal direction was 10.6 degrees, but due to anisotropy of the scatterers, the effective pointing direction was closer to 10.0°. A longer term plan is to compensate for scatterer anisotropy using direct measurements of θ_s , but as an interim measure we chose to use height-independent climatological values. This removed the bias on all beams. Use of corrected heights (as discussed above) reduced the standard deviations.



(a)



(b)

Figure 3: Comparisons of profiler data to models for (a) the NOAA network and (b) the O-QNet. The data covers all of 2010 and 3 months of 2011 for the NOAA profilers, and July 2010 to March 2011 for the O-QNet. Data were averaged over all profilers in each network.

Fig. 3 shows later comparisons, at a fixed height of ~5 km. Fig. 3(a) shows the NOAA network compared to the GEM model predictions, while (b) shows the O-QNet results. In fig. 3(a), the biases are close to zero, as indicated by the broken lines. The solid lines show pairs of results for the standard deviations. The upper ones (green and red) are normally denoted “O-P”, while the lower ones are “O-A”, for “Observation vs. Analysis”. Only the upper ones should be considered – the lower ones use the windprofiler data from the NOAA network as input to the analysis, then compare with the results with the profiler, so are not truly independent. The O-QNet comparisons were performed without using their data as input, so are best compared to the upper curves in 3(a). The O-QNet data suggest a bias in the northward winds of about 1 m/s (lower curve), and

good agreement in the zonal component. Standard deviations for the O-QNet are of the order of 2.5-3 m/s, whilst for the NOAA network they are 2-2.5 m/s.

Fig 4 shows comparisons between the O-QNet data and EWINPROF, which will be considered in the next section.

3. Discussion

O-QNet biases and standard deviations seem larger than for the NOAA network, but extenuating circumstances exist. It should be noted that winds in Canada tend to be stronger than in the USA. Maximum winds speeds of 60 and 70 m/s are common in the jet stream, for example, while in the southern USA, 30-40 m/s is a more common maximum (except for hurricanes). Hence although some of the increased standard deviation at upper levels can be attributed to decreasing signal-to-noise of the profiler, larger winds are invariably associated with greater variability. The jet stream is a known source of gravity waves, so even greater variability is expected there.

In addition, there is only 1 radiosonde near the O-QNet area, so the models have little in the way of accurate boundary conditions. Only AMDAR aircraft data can be used, and these are weighted to lower values by pilot desires to avoid strong winds and turbulence to improve passenger safety.

For all these reasons, higher standard deviations for the O-QNet are a reasonable expectation. With regard to the biases, look again at Fig. 4. The vertical profiles show wind speeds relative to the UK Met Office model. The filled circles show the mean biases of the wind-speeds for these profiles. Then, using measured offsets between the profiler winds and the EC-GEM model, the locations of the mean GEM values have been plotted as green squares in fig. 4. The offset of the green squares from zero represents the difference between the EC and UK models. Hence this offset represents a difference between the two models, using the profiler data as a reference. Clearly the two models have a difference of over 1 m/s – yet each made use of all available boundary-conditions and measured data. If the models cannot agree to better than 1 m/s, it is clearly unreasonable to assume that the profiler data should. So we conclude that biases of up to 1 m/s should be acceptable, and that the procedure of using the models as the “undisputed reference” is too extreme.

4. Conclusions

Following all these tests, the UK Met office has accepted the O-QNet data for assimilation into their models. All sites in the O-QNet are deemed acceptable, though over different height ranges. Data from all radars are accepted from 3 to 7 km altitude. Data from Egbert, Gananoque, Aumond, McGill and Negro Creek have been accepted down to 500m, and data from Egbert, Gananoque, Harrow, Negro Creek, Walsingham and Wilberforce have been accepted to upper heights of 9 and 10 km. Another site in Eureka (80N) has been accepted between 500m and 9 km. Environment Canada is continuing its tests further.

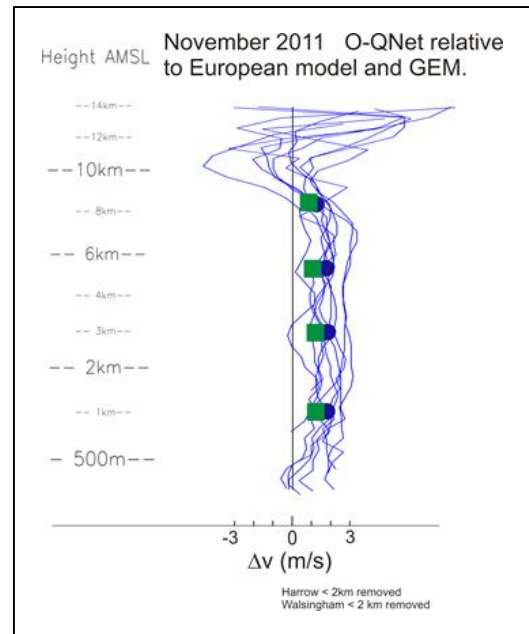


Figure 4: O-QNet data compared to both the GEM and UK Met Office models.

Acknowledgements

Drs. Frederic Fabry and I. Zawadzki own and operate the McGill radar. The O-QNet was built by Mardoc Inc. Funding came from the Canadian Foundation for Innovation and the Ontario Innovation Trust. Figs. 2 and 3 were prepared through Judy. St. James through software written at Environment Canada. Data for fig. 4 were provided through the staff at Ewinprof.

References

- Hocking, W.K., et al., "A New 40-55 MHz Windprofiler Network in Ontario and Quebec, Canada – The O-Qnet", Proc. of the Eleventh International Workshop on Technical and Scientific Aspects of MST Radar, Gadanki, India, Dec 11-15, 2006, ed. V.K. Anandan, pp 377-380, publ. Macmillan India Inc., 2007.
- Hocking, W. K. et al., "Progress report on the O-QNET, a new Canadian windprofiler network", Proc. of the 12th Int. Workshop on Technical and Scientific Aspects of MST Radar, London, Ont., Canada, May 17-23, 2009, eds. N. Swarnalingam and W. Hocking, 179-182, 2010.
- Weber, B.L. and D.B. Wuertz, "Quality control algorithm for profiler measurements of winds and temperatures", NOAA Technical Memorandum, ERLWPL-212:32, 1991.

The usefulness of model-comparison statistics for wind-profiling radar operators

David A. Hooper^{1,2}, David M. Edwards³, Gemma Holmes³, Kevin Linklater³, Tim Oakley³,
Colin Parrett³, and Myles Turp³

¹ STFC Rutherford Appleton Laboratory, UK

² NERC MST Radar Facility at Aberystwyth, UK

³ Met Office, UK

1. Introduction

Wind-profiler radar data are commonly assimilated by meteorological organisations for the purposes of numerical weather prediction (NWP). Within Europe, radars of different types are operated by a variety of organisations. Nevertheless, they effectively form a single network through the coordination of the EUMETNET Composite Observing System (EUCOS) E-WINPROF programme. This grew out of the CWINDE demonstration network, which was set up under COST-76 [Dibbern *et al.*, 2003b]. The data are submitted to a central hub before being distributed to the various meteorological organisations across Europe. The quality of the data is evaluated through statistical comparisons against NWP model wind fields [e.g. Dibbern *et al.*, 2003a]. The (UK) Met Office carry out comparisons against their Unified Model (UM), Météo France against their ARPEGE model, and Deutscher Wetterdienst against their COSMO model. These statistics are fed back to the radar operators on a monthly basis in graphical form.

The aim this extended abstract is to demonstrate how the model-comparison statistics can be of use to the radar operators. It is focused entirely on the Natural Environment Research Council's (NERC's) MST Radar at Aberystwyth. Although this has always been operated primarily on behalf of the UK's research community, the Met Office took an early interest in its potential to contribute to their upper air measurement network. This long association has benefitted both parties. The involvement of the research community has ensured that the characteristics of the radar observations have been studied in great detail. The involvement of the Met Office has provided a mechanism for quantifying data quality. Consequently, this abstract will focus on the model-comparison statistics provided by the Met Office rather than those provided by Météo France or Deutscher Wetterdienst. An introduction to these statistics is given in Section 2. Section 3 gives a case study of how the statistics were used to validate a new signal processing scheme. Section 4 looks at how they were used to identify a range gating error. Section 5 looks at the effects of renovating the Aberystwyth radar and demonstrates the limits of what can be inferred from these monthly statistics. Finally, Section 6 looks at how daily statistics, derived from comparisons against the Deutscher Wetterdienst model, are starting to be used to identify highly-localised problems.

2. Met Office monthly statistics

Figure 1 shows three different Met Office (global) model-comparison statistics for February 2012. The root mean square (RMS) differences between radar and model wind components give a combined indication of the systematic, random, and representativeness errors [Dibbern *et al.*, 2003a]. It is emphasised that NWP models are not perfect and so these differences should not be attributed solely to errors in the radar data. In particular the models have a limited (albeit increasing) ability to accurately represent smaller-scale features. For example, they parameterise

gravity waves rather than modelling their effects explicitly. Nevertheless, inertia-gravity waves are commonly observed in the lower-stratosphere above Aberystwyth [e.g. *Vaughan and Worthington, 2007*]. They give rise to wind perturbations with magnitudes of a few m s^{-1} . This is an example of a representative-ness error. Therefore, in order to distinguish between the model and wind-profiler contributions to such statistics, the Met Office do not consider each wind-profiler in isolation.

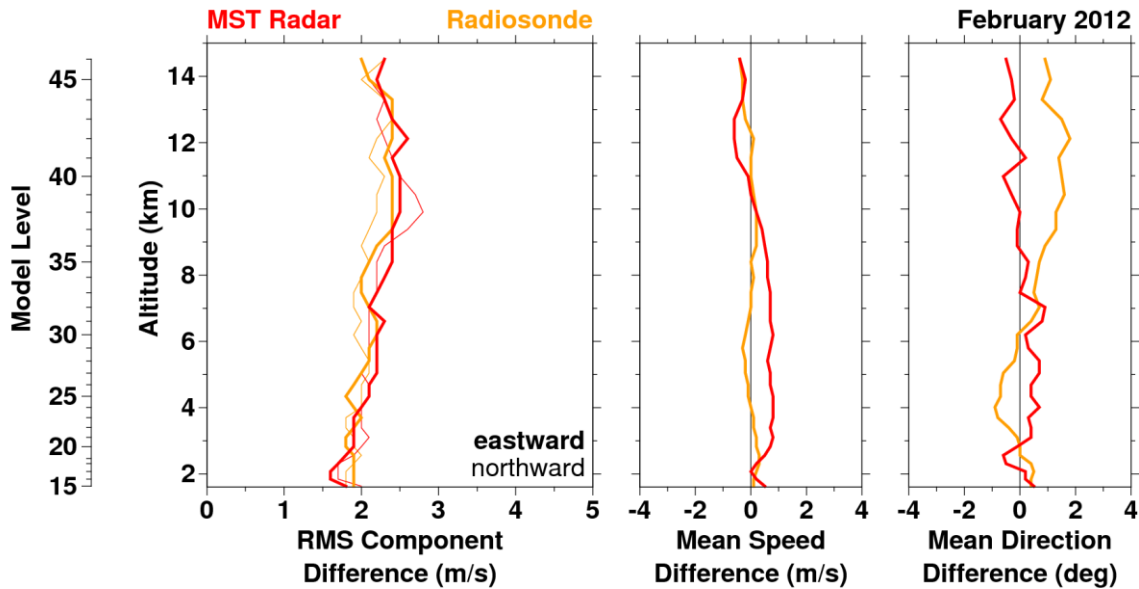


Figure 1: Met Office model-comparison statistics for February 2012. The orange lines relate to the composite data from all radiosonde sites in the British Isles. The red lines relate to the NERC MST Radar at Aberystwyth. In the left hand panel, eastward wind component data are represented by thick lines and northward wind component data by thin lines.

The ideal source of data for evaluating wind-profiler data quality would be radiosondes launched from a nearby location. Temporal and spatial separations will both be expected to give rise to natural variations. Radiosondes are still regarded as the standard instrument for measuring winds. However, as can be seen in Figure 2, the nearest primary radiosonde sites (large orange dots) are 200 km away from the Aberystwyth radar (52.42°N , -4.01°E). Indeed, the fact that the radar conveniently fills a gap in the pre-existing upper-air observation network is one of the reasons that the data are of interest to the Met Office. Similarly, three out of the Met Office’s five Boundary-Layer Wind-Profilers (small blue dots) are located within gaps in the network (the other two are located at test sites). Consequently, for routine evaluation of UK-based wind-profiler data quality, the Met Office also calculate model-comparison statistics for the composite data from all radiosonde sites across the British Isles. This reduces the impact of natural variations associated with any one radiosonde site. Similar analyses are carried out for wind-profilers in other countries, albeit using different groups of radiosondes.

As an aside, atmospheric measurements made by commercial aircraft also contribute to the upper air network through the Aircraft Meteorological Data Relay (AMDAR) programme. The locations of the airports used by contributing aircraft are indicated by the black crosses in Figure 2. During extreme wind events at near-surface levels, radiosondes cannot be launched and aircraft cannot take-off or land for safety reasons. However, wind-profiling radars can continue to operate as long as there is no disruption to their electricity supplies. *Parton et al. [2010]* has shown that

that this leads to a systematic absence of such (admittedly-rare) events from the radiosonde record.

If two sources of measurements have similar model-comparison statistics, it can be inferred that their measurement errors are comparable [Dibbern *et al.*, 2003a]. Therefore the differences between the wind-profiler and radiosonde values are more-significant than the absolute values for either instrument in isolation. The pattern seen in Figure 1, of similar RMS component differences for both the radar and radiosonde data, is typical for the Aberystwyth radar. Similar conclusions regarding the data quality [e.g. Thomas *et al.*, 1997; Hooper *et al.*, 2008] have been reached from directly comparing winds measured by the radar and those measured by radiosondes launched from Aberporth (small orange dot on Figure 2). The latter is just 45 km to the south-west of the Aberystwyth radar. However, it is not part of the Met Office's primary observation network and so radiosondes are not launched from there as frequently as from the other sites.

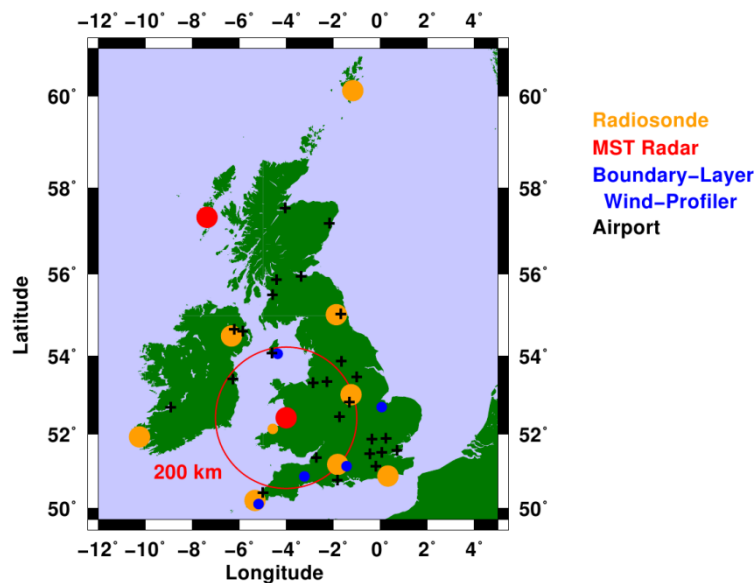


Figure 2: Map of measurement sites within the Met Office's upper-air network for the British Isles. The large orange dots show the locations of the primary radiosonde launch sites. The small orange dot represents the Aberporth launch site. The red dots show the locations of the South Uist and Aberystwyth MST radars. The red circle has a radius of 200 km and is centred on the Aberystwyth MST radar. The small blue dots show the locations of the boundary-layer wind-profilers. The black crosses show the locations of airports associated with the AMDAR programme.

The typical cycle time for the Aberystwyth radar is approximately 5 minutes. Consequently, each half-hourly wind-profile sent to the E-WINPROF hub represents an average of up to 6 individual wind profiles. Although such averaging reduces the magnitude of the random measurement error, it has no effect on systematic errors. These show up in the mean differences between the measured and model winds (i.e. measured - model) - or rather, in the separations between the radar and radiosonde model-comparison values. As can be seen in Figure 1, the biases are small. It is typical for the radar wind speed to show a slight positive bias (with respect to the radiosonde data) at tropospheric altitudes and a slight negative bias at lower-stratospheric altitudes. The altitude of the tropopause above Aberystwyth is most-commonly between 10 and 12 km [Hooper *et al.*, 2008]. The difference between the biases is thought to be related to the aspect sensitivity of the radar returns. This causes the effective zenith angle, for off-vertical radar beams, to be slightly smaller than the nominal angle. The effect, which leads to an underestimate

of the wind speed, tends to be largest at lower-stratospheric altitudes. The signal processing scheme applies a compensation for this [Thomas *et al.*, 1997; Hooper *et al.*, 2008]. The mean direction differences suggests a bias in the radar-derived wind direction of no more than 1°.

3. Evaluating a new signal processing scheme

The original Aberystwyth radar signal processing scheme, which is referred to as version-0 or v0, was gradually developed over the period 1990 - 2000. The development benefitted from the Met Office's early efforts to evaluate the usefulness of the wind-profile data. Nevertheless, the scheme relied on a number of not-entirely-accurate simplifying assumptions. Although these were of use in the early years of radar operation, when computing power was relatively limited, they were no longer necessary a decade later. This prompted the development of a new scheme [Hooper *et al.*, 2008]. It had reached version-3, or v3, before it began real-time operations in January 2006. It was run in parallel with the v0 scheme for a full year. During this time, wind-profiles from both schemes were sent to the E-WINPROF hub. However, data from only one scheme (initially v0) were operationally assimilated.

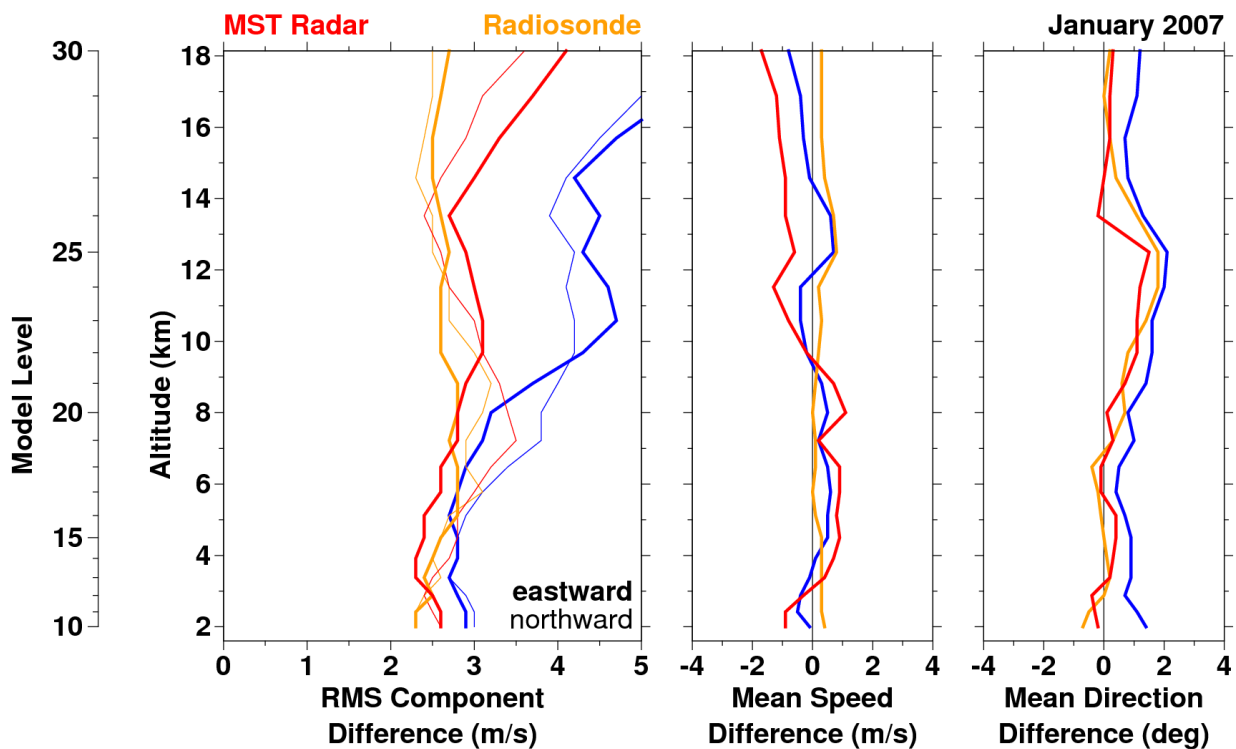


Figure 3: As for Figure 1, but for January 2007. Also shown in blue are model-comparison statistics for winds derived from the version-0 MST radar signal processing scheme.

Figure 3 shows the model-comparison statistics for January 2007. The v0 mean direction difference had always shown a small positive bias. This was reduced slightly by the v3 scheme. However, the magnitude of its mean speed difference shows a slightly larger bias than the v0 scheme. Ultimately, it is the RMS component differences which differentiate the two schemes. For the duration of the evaluation period, the v3 scheme consistently outperformed the v0 scheme. This is particularly noticeable at altitudes above 8 km. This led to the Met Office switching over to the v3 data stream for operational purposes in August 2006. Use of the v0 scheme was discontinued in February 2007.

Attention is drawn to the fact that Figure 3 shows data up to an altitude of slightly greater than 18 km, whereas all other examples of Met Office monthly model-comparison statistics only extend to 15 km. It should be noted that the even the v3 data quality, in this example, decreases noticeably at the highest altitudes. This is a consequence of the decreasing radar return signal power with increasing altitude, which results in fewer signals passing quality control tests. During March 2011, the radar underwent its first major renovation in a 22 year lifetime - see "*Renovation of the Aberystwyth MST radar: Evaluation*" in these proceedings for more details. This led to a significant increase in altitude cover. However, the performance was slowly decreasing before then, which led the Met Office to discontinue their consideration of data above 15 km in late January 2009. Also note that the number of NWP model levels increased in late 2009.

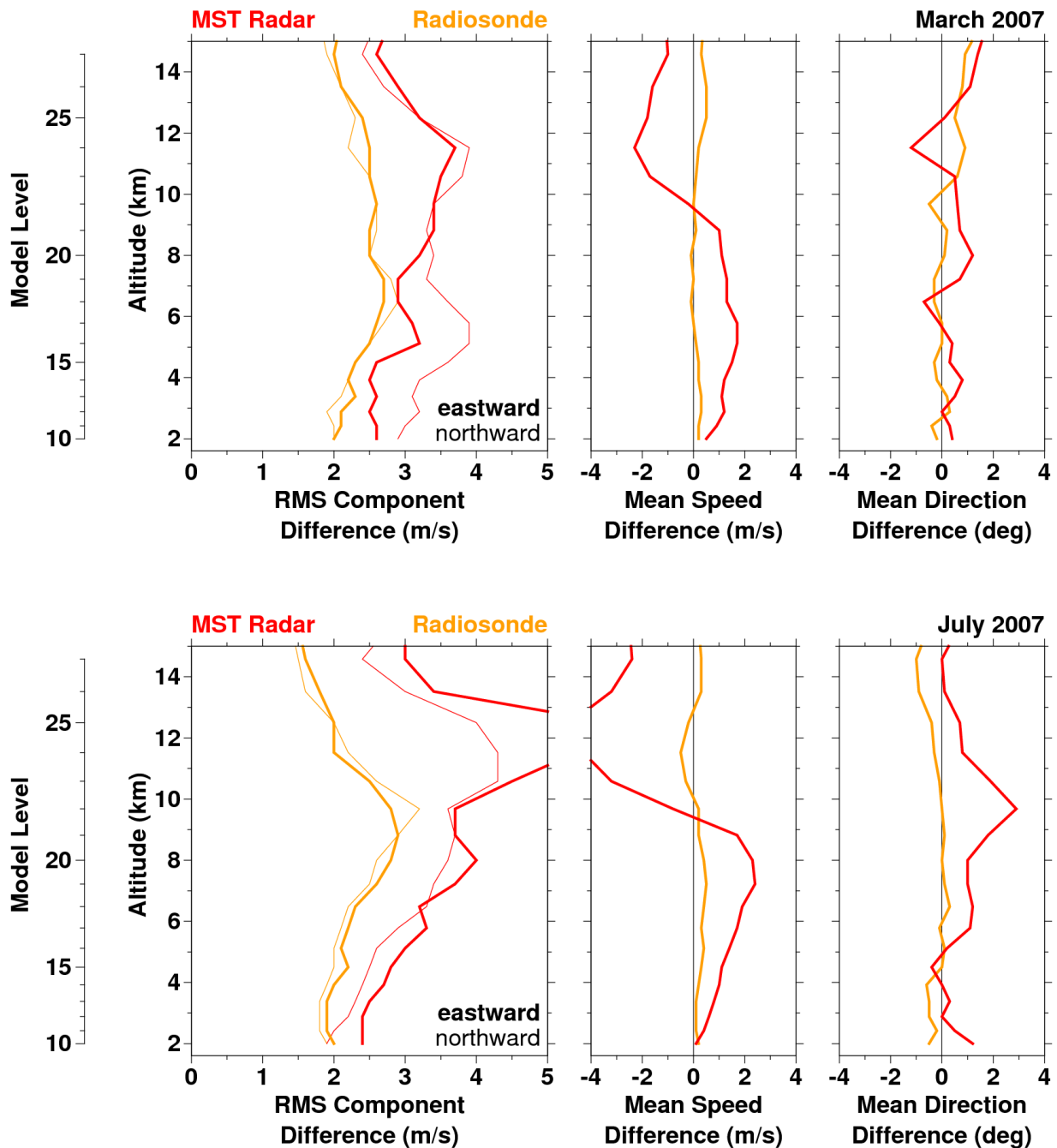


Figure 4: As for Figure 1, but for (upper panels) March 2007 and (lower panels) and July 2007.

4. Diagnosis of a range gating error

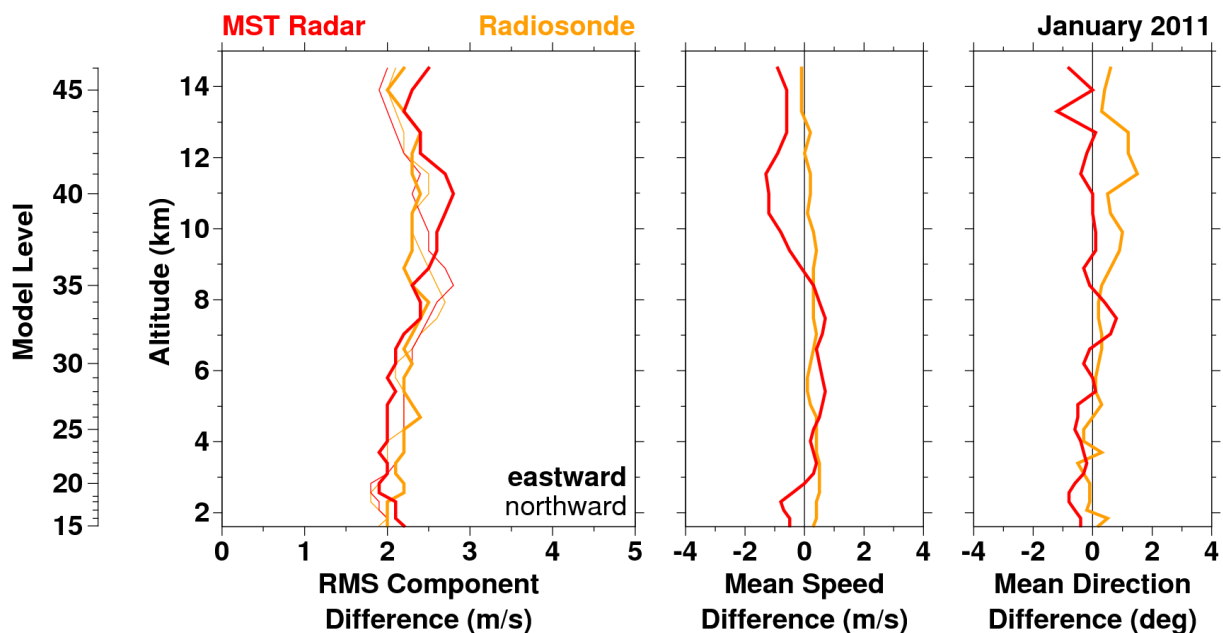
A new radar control and data acquisition PC was installed in February 2007. Although the software for the new Linux-based PC was a modified version of that used for the old WindowsNT-based PC, it introduced a range gating error [Hooper *et al.*, 2010]. Winds were reported 4 gates lower, corresponding to an altitude difference of 597 m, than they should have been.

The Met Office model-comparison statistics for March 2007, i.e. the first full month following the change, gave an immediate indication that there was a problem - see upper panels of Figure 4. This was surprising since the radar wind data showed no change in self-consistency, i.e. in terms of changes with time and altitude. Although the statistics did not reveal the cause of the problem, it is easy to see its signature in the mean speed difference profiles. This is particularly true for months such as July 2007 (lower panels of Figure 4), when jet stream activity predominated. Wind speeds can be as large as 90 m s^{-1} within the peak of the jet, which typically occurs in the altitude range 10 - 12 km above Aberystwyth, but are seldom more than a few tens of m s^{-1} elsewhere. Moreover, the speed reduces more-rapidly as a function of altitude above the peak than below it.

The MST radar wind speed difference values show a large negative bias at altitudes of between 10 and 12 km, i.e. where the jet peak should be located but where much-lower wind speeds are reported. A smaller positive bias is found at altitudes of between 8 and 10 km, i.e. below the peak of the jet but where it is reported to be.

5. Evaluating the effects of renovating the Aberystwyth radar

As mentioned above in Section 3, the Aberystwyth radar underwent its first major renovation in a 22 year lifetime during March 2011. This principally consisted of a replacement of the beam steering components. It is clear that the poor condition of the original components led to a reduction in the useful altitude coverage for wind-profiling purposes. It also appears that other aspects of the radar's performance were affected. These would be expected to have had a negative impact on the wind data quality. An analysis of limited periods of pre and post renovation data suggests that the random measurement errors, for single cycle data, were reduced as a result of the renovation.



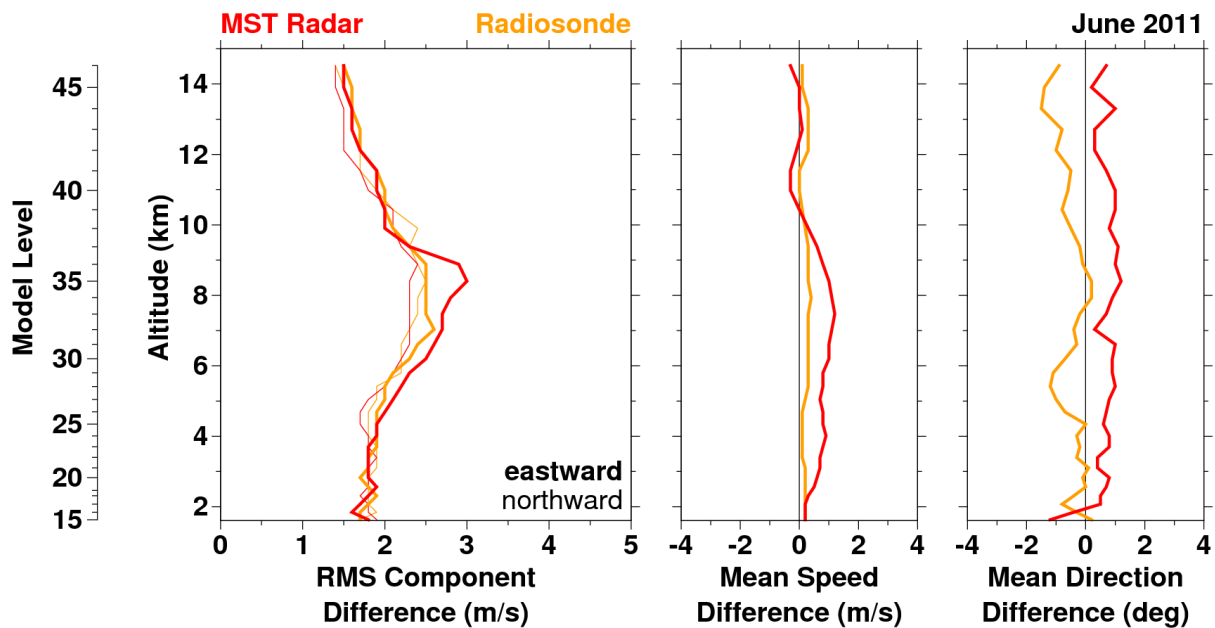


Figure 5: As for Figure 1, but for (upper panels) January 2011 and (lower panels) June 2011.

Nevertheless, the Met Office’s RMS component differences for a pre-renovation month and a post-renovation month - upper and lower panels, respectively, in Figure 5 - do not suggest a significant change in the 30 minute averaged data quality. This was surprising. Between February and May 2011, inclusive, a special observation format was used for the specific purpose of evaluating the effects of the renovation. The approximately 10 minute duration of the cycles was double that for standard observations. This meant that the 30 minute average wind- profiles sent to the E-WINPROF hub were based on, at most, 3 individual measurements rather than the usual 6. For this reason, data from January and June 2011, when standard observations were being made, have been used to represent the pre- and post-renovation conditions. The characteristics seen in Figure 5 are typical of the months to either side.

An analysis of the special observation format data suggests that the radar’s beam shape and/or its zenith angle, for off-vertical beams, would have been affected by the state of the pre-renovation beam steering components. If the zenith angles were affected, they would be expected to be slightly smaller than their nominal angles. This would lead to the horizontal wind speeds being underestimated. This is separate to the effects of radar return aspect sensitivity, described in Section 2, which also tend to cause an underestimate of the horizontal wind speeds. Nevertheless, the analysis of the special observation format data suggests that the aspect sensitivity compensation factor was actually over-correcting the horizontal wind speeds. The mean speed differences shown in Figure 5 suggest that the net result of these influences was to actually slightly underestimate the wind speed. The values for the post-renovation period consistently (i.e. for the months to either side) show a positive bias relative to those of the pre-renovation period. However, the differences are only of the order to 1 m s^{-1} . There is also a slight positive bias in wind direction, but again this is small - approximately 1° .

6. EUCOS statistics

The changes in Met Office monthly model-comparison statistics as a result of the renovation are considerably smaller than those resulting from the improved signal processing scheme or from the range gating error. Although the small shifts in speed and direction biases appear to be

genuine, the changes in the RMS component differences, relative to the radiosonde values for January and June 2011, are comparable to the variability seen from month to month. This is despite the fact that the analysis of the special observation format radar data (in isolation) suggests a reduction in random measurement error (for single cycle data). This suggests a limit to the magnitude of changes which can be inferred from the Met Office’s monthly model-comparison statistics.

Since January 2011, the Met Office have been distributing an additional measure of monthly data quality. These are provided by EUCOS from comparisons against the Deutscher Wetterdienst model, but in the form of just 3 parameter values which cover all altitudes. These values are expected to fall within target limits, which have been defined by EUCOS.

The “Quality” parameter is similar to the Met Office’s RMS component difference. It represents the RMS difference between the measured and model wind vectors. The target is that this value should not exceed 5.0 m s^{-1} . As can be seen from Figure 6, winds from the Aberystwyth MST Radar mostly fall below this threshold, indicating that the data are typically of an acceptable quality. Owing to the fact that these new model-comparison statistics only started to be distributed 2 months prior to the March 2011 renovation, it is not possible to say with confidence whether the data quality has improved. However, it is noted the value of the “quality” parameter slightly exceeded the threshold for both of the pre-renovation months.

The “Timeliness” parameter refers to the number of wind-profile messages within 30 minutes of the end of the averaging period. The target is for a minimum of 90%. This is virtually-always achieved for the Aberystwyth radar. The exception was during March and April 2011, i.e. when the special, 10 minute long cycle format was being used as part in order to evaluate the effects of the radar renovation. The signal processing chain has been optimised for the standard 5 minute long cycle format. Consequently, it is not surprise that this was less effective, in terms of timeliness, when the cycle time was doubled.

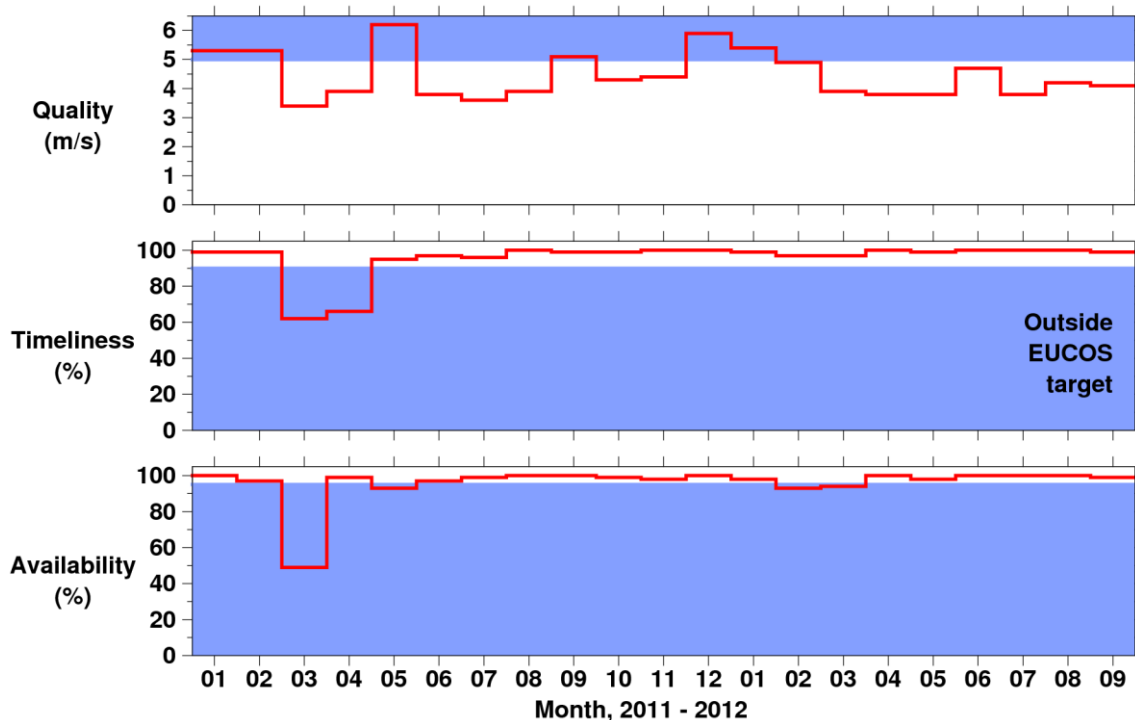


Figure 6: Monthly EUCOS model-comparison statistics for the Aberystwyth MST Radar for January 2011 - March 2012. Values in the blue regions are outside of the EUCOS targets.

The “Availability” parameter refers to the percentage of wind-profile messages received relative to the maximum number possible. The target is for a minimum of 95%. The only month for which this was missed by a significant margin was March 2011, i.e. when the radar was out of action for half the month as a result of the renovation.

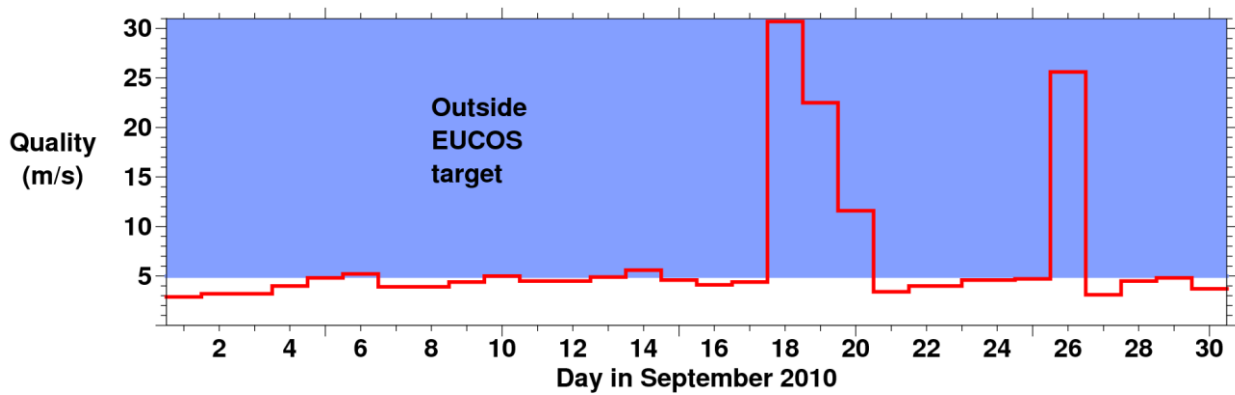


Figure 7: Daily EUCOS “Quality” parameter for the Aberystwyth MST Radar during September 2010.

EUCOS model-comparison statistics can be generated for any time interval and the Met Office have access to the daily data. Although these are not distributed on a routine basis, the Met Office are starting to make use of them in order to identify transitory but significant problems with the data quality. The Aberystwyth radar beam steering unit became stuck in an off-vertical direction at 16:00 UT on 18th September 2010, a Saturday, and was not fixed until the following Monday morning (20th) at 11:00 UT. During this period, the winds were still passing self-consistency checks, since their variations as functions of time and altitude were within realistic limits. Consequently they were flagged as being reliable. As can be seen in Figure 7, this malfunction leads to the daily values of the “Quality” parameter of between 10 and 30 m s⁻¹, which are considerably in excess of the 5.0 m s⁻¹ target.

It is not clear what caused the large value on 26th September 2010 in the above example. Nevertheless, in other cases, similarly-large daily values have been traced to erroneous wind vectors that are confined to just one or two range gates and to only a single 30 minute averaging period. Figure 8 shows one such example, from 4th February 2012. The v3 signal processing scheme is typically highly-effective at removing outlying data points, so it is not yet clear how this wind vector managed to be flagged as reliable. The point of showing this is to demonstrate how the daily EUCOS statistics can be used to identify highly-localised problems with the signal processing scheme.

7. Conclusions

This abstract has demonstrated the usefulness of monthly model-comparison statistics for identifying significant changes in data quality. The two examples shown relate to a change in signal processing scheme and a long-term instrument problem. However, the statistics cannot be used for identifying more-subtle changes. Nevertheless, daily model-comparison statistics appear to have the potential for identifying highly-localised problems with signal processing.

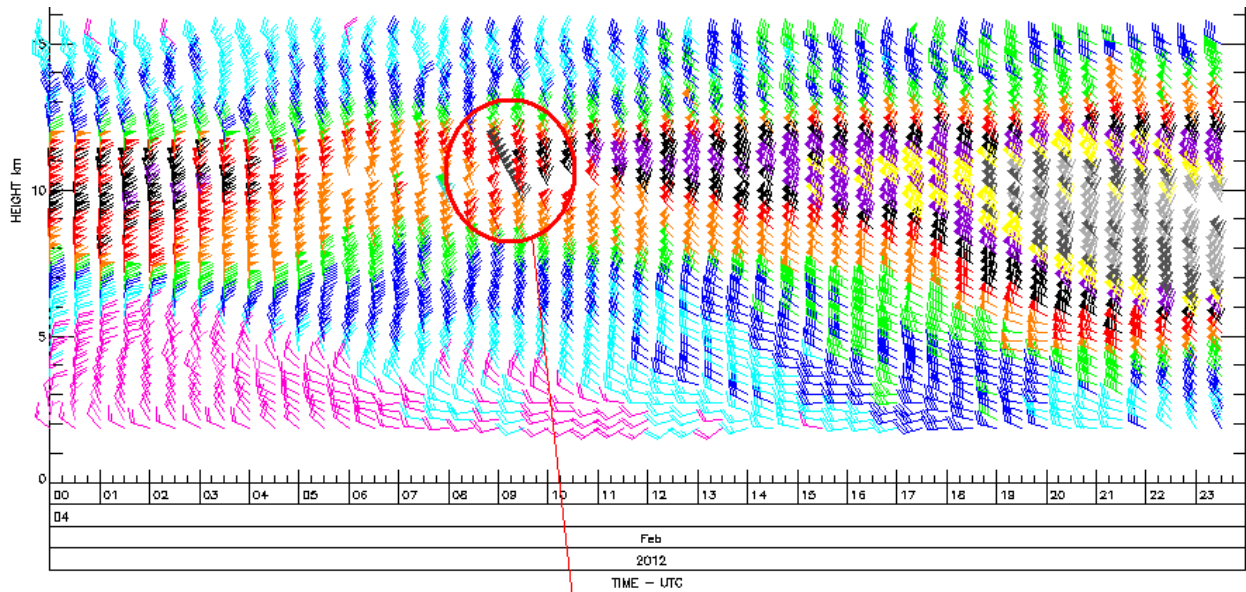


Figure 8: Horizontal winds measured by the Aberystwyth MST radar on 4th February 2012. The red circle highlights the outlying data point.

References

- Dibbern, J., D. Engelbart, U. Goersdorf, N. Latham, V. Lehmann, J. Nash, T. Oakley, H. Richner, and H. Steinhagen, Operational aspects, in *EUR 20614 - COST Action 76 - Development of VHF/UHF wind-profilers and vertical sounders for use in European observing systems - Final report*, edited by J. Dibbern, W. Monna, J. Nash, and G. Peters, pp. 133–224, European Commission, Luxembourg, 2003a.
- Dibbern, J., W. Monna, J. Nash, and G. Peters (Eds.), *EUR 20614 - COST Action 76 - Development of VHF/UHF wind profilers and vertical sounders for use in European observing systems - Final report*, European Commission, 2003b.
- Hooper, D. A., J. Nash, T. Oakley, and M. Turp, Validation of a new signal processing scheme for the MST radar at Aberystwyth, *Ann. Geophys.*, 26(11), 3253–3268, doi:10.5194/angeo-26-3253-2008, 2008.
- Hooper, D. A., O. T. Davies, J. Nash, T. Oakley, and M. Turp, The diagnosis of a range gating problem suffered by the Aberystwyth MST radar, in *Proceedings of the Twelfth International Workshop on Technical and Scientific Aspects of MST Radar*, edited by N. Swarnalingam and W. K. Hocking, pp. 123–126, Canadian Association of Physicists, Ottawa, Ontario, Canada, ISBN:978-0-9867285-0-1, 2010.
- Parton, G., A. Dore, and G. Vaughan, A climatology of mid-tropospheric mesoscale strong wind events as observed by the MST radar, Aberystwyth, *Meteorol. Apps.*, 17, 340–354, doi: 10.1002/met.203, 2010.
- Thomas, L., I. Astin, and R. M. Worthington, A statistical study of underestimates of wind speeds by VHF radar, *Ann. Geophys.*, 15, 805–812, doi:10.1007/s00585-997-0805-8, 1997.
- Vaughan, G., and R. M. Worthington, Inertia-gravity waves observed by the UK MST radar, *Q. J. R. Meteorol. Soc.*, 133(S2), 179–188, doi:10.1002/qj.142, 2007.

Monitoring and data assimilation of Wind Profiler

Catherine Gaffard¹, David Simonin¹, Colin Parrett², Richard Marriott², Myles Turp², Dirk Klugmann²

¹ UK Met office PO Box 243 Earley Gate Reading Berks RG6 6BB, UK

² UK Met Office FitzRoy Road, Exeter, Devon EX1 3PB, UK

1. Introduction

OB_BG Wind component Zieg 2012 08

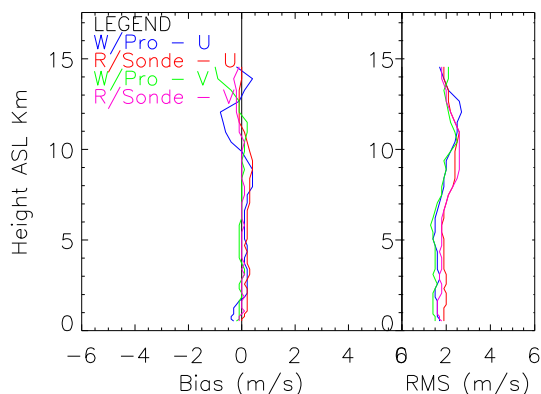


Figure 1: Example of observation – background comparison statistics for Ziegendorf wind profiler and for all radiosondes in Germany for a month (August 2012).

The UK Met office receives wind profiles from around 100 wind profilers located worldwide, mainly in Europe, Japan, United States and Canada. These data are monitored against our numerical global model. If the wind quality is stable and meets some criteria, the data are used in conjunction with all other observations during the assimilation cycle to produce the initial conditions for the model run.

Within the last couples of years several Met services like NRL, ECMWF, UK Met Office have developed forecast sensitivity to observation (FSO) tools which estimate the reduction of forecast error associated with individual observations. At the Met office, this tool has been recently developed for the global model by Andrew Lorenc and Richard Marriott and is run to correspond with parallel suites

containing significant changes to the UM and /or data assimilation. It allows comparison of the impact of different observing systems (Lorenc and Marriott 2012) for different versions of the model. For the first time, the impact of each wind profiler can easily be examined in the global model.

In this paper, we first present how the wind profiler data compare with the global model, then we show preliminary results on the impact of wind profiler estimated using the FSO tool. We also present some results of a wind profiler data denial experiment done using the 1.5km now casting model (UKVNDP) for which the FSO tool has not been yet developed.

2. Wind profiler monitoring

All wind profiler winds available on the GTS or send to CWINDE hub and received in the UK Met Office data base within the cut off time for data assimilation are monitored against the model first guess wind field (background): short term forecast. In general, the quality of wind is comparable to the radiosonde wind. See figure 1. An automatic blacklisting of either the full profiler or just some level is in place based on monthly statistic. When the profiler is accepted for assimilation a background check will reject the value in real time. This process is relatively efficient to reject gross error, but some erroneous wind can be assimilated. Figure 2 shows an example of winds with gross error due to external contamination; the red vectors are rejected but in that example a significant number of erroneous winds are assimilated. Such problem can be completely undetected (see Figure3) when only looking at monthly statistic.

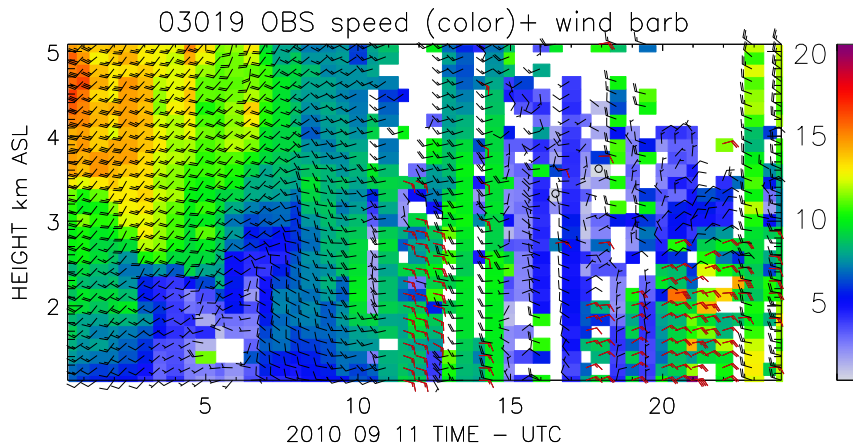


Figure 2: Example of winds from South Uist wind profiler (low mode), red barbs are winds rejected by the data assimilation quality control.

3. FSO impact on the global model preliminary results

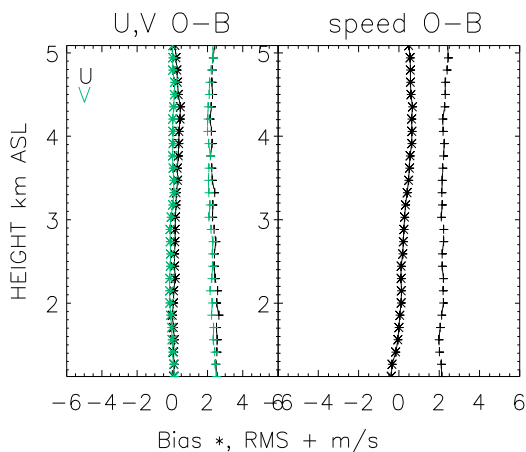


Figure 3: Comparison of wind data from the 22/08/12 until the 29/09/12 data against the background from the global model including data with gross error as shown in figure 2.

The method used at the UK Met Office to compute observation impacts is very similar to the one described by Langland (2004). The main difference from most results found in the literature is that the computation of the forecast error metric used in this study includes moisture. A full description of the method is in the process of being published in the QJRMS (Lorenc and Marriott 2012). For completeness we outline the method in the annexe.

Using the chain rule of derivatives (adjoint techniques), values of forecast error sensitivity to observations (usually at a forecast length of 24h) can be computed for each assimilated observation simultaneously. The values represent the change in forecast error for a unit observation innovation. Multiplying the sensitivity by the observation innovation gives

an estimate of the forecast error difference due to the observation. This is an estimate of the observation's impact in the full system, i.e. assimilation + forecast model. The innovation is the difference between the equivalent model observation computed from the forecast valid at the analysis time issued from the previous analysis and the observation use in the current analysis cycle. The forecast error is computed using an energy norm which includes elastic and potential energy, thermal energy, the latent thermal energy of condensation and kinetic energy (Lorenc and Marriott 2012). The forecast error can be computed on any domain. In this study the domain is the full globe for model levels up to 150 hPa.

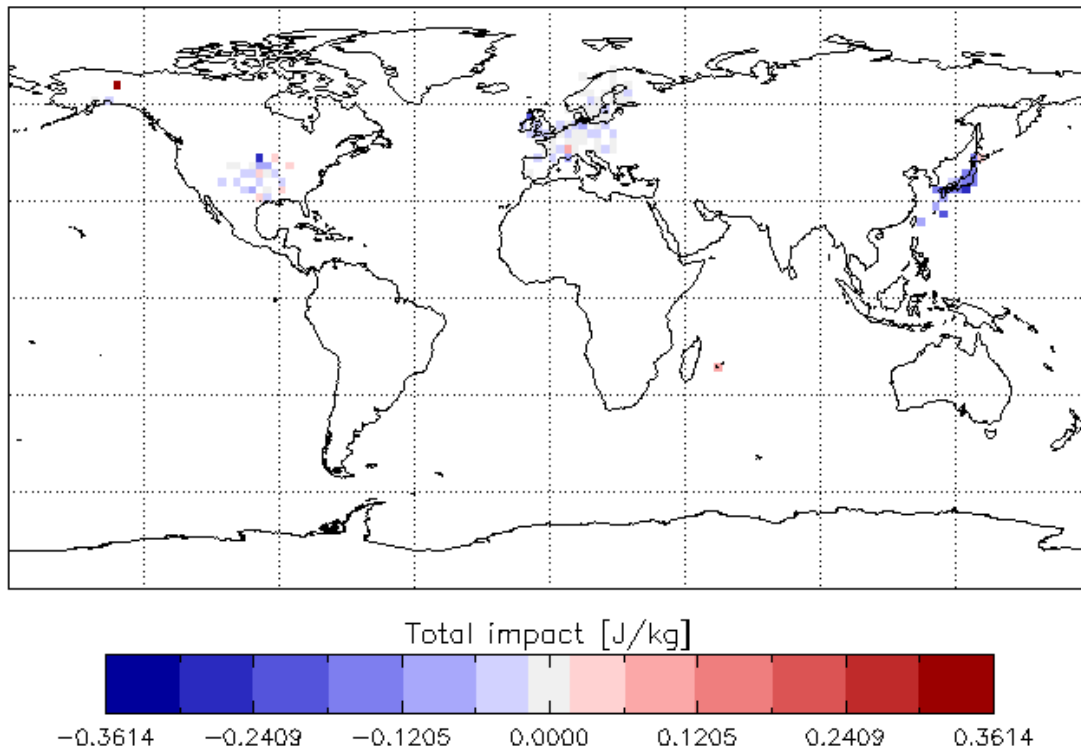


Figure 4: Values for 24-hour forecast impact associated with the use of wind profiler within areas of 2.5 by 2.5 degrees. If in that grid box two profilers are present, their impacts are combined. (In Europe wind profiler are together with VAD wind from weather radar). Negative values indicate beneficial forecast impacts (corresponding to a reduction in forecast error). Impacts were accumulated over the full period (22/08/2010-29/09/2012).

This tool has been developed for the operational global model which uses a 4D-Var assimilation scheme (Rawlins et al 2007). The FSO tool was run over a period of approximately one month from the 22/08/2010 until the 29/09/2010 using a reduced-resolution version of the UM that was operational at the Met Office between 16 March and 20 July 2011. The full forecast model was run at N512 resolution (approx. 25km in the horizontal and the adjoint model at N216 (approx. 60km in the horizontal. The 4D-Var assimilation scheme uses a 6 hour window and was run at N216 resolution in both the forward and adjoint runs. The wind profilers which are suitable for data assimilation are quality controlled using a background check (if the innovation is too large the observation is rejected).

Figure 4 shows FSO-estimated values of the difference in 24h forecast error associated with the use of wind profiler observations within areas of 2.5 by 2.5 degrees. If in that area two profilers are present, their impacts are combined. N.B. the field shows estimated values of forecast error impact attributed to observations in those locations, not the change in forecast error itself. The error difference measured by the FSO tool was accumulated over the full period for each of the wind profilers and weather radars assimilated in the UK Met Office global model. The impact is quite variable but most of the wind profilers have a beneficial impact (negative value corresponding to a reduction in forecast error). The strongest beneficial impact comes from the Japanese network whilst a few wind profilers have a detrimental impact. The profiler in the middle of Alaska is clearly giving a detrimental impact. A few wind profilers in the US are also measured as

having a detrimental impact. In Europe, impacts are mostly neutral/beneficial except for over Switzerland.

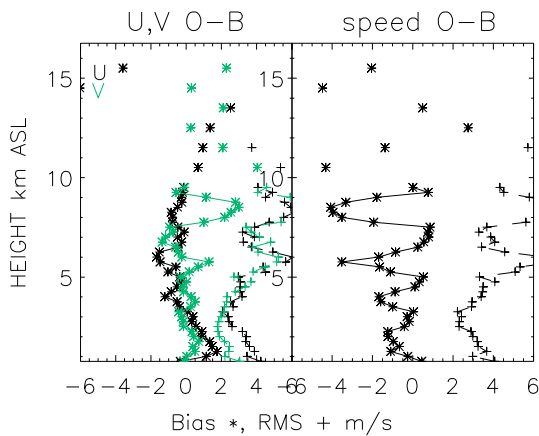


Figure 5: Comparison of wind data from 70197 (CENA2 Alaska) against the background from the global model for the whole period.

The detrimental impact of the wind profiler located in Alaska is probably due to the quality of the data. The comparison of the wind against the first guess (Figure 5) reveals strong bias and a large root mean square deviation. This wind profiler is now blacklisted by the Met Office and is in need of maintenance. (It stopped sending data in 2012.) Some of the other wind profilers from the NOAA network are also giving slightly detrimental impacts; the origin of these detrimental impacts has not yet been studied. The wind profiler in Switzerland at Payerne is located in the vicinity of very complex terrain not well represented by the global model and it is not surprising that such detailed information might have a detrimental effect on the global model.

WP RS UK/ 100822_qu18-100929_qu12

WP RS Ger/ 100822_qu18-100929_qu12

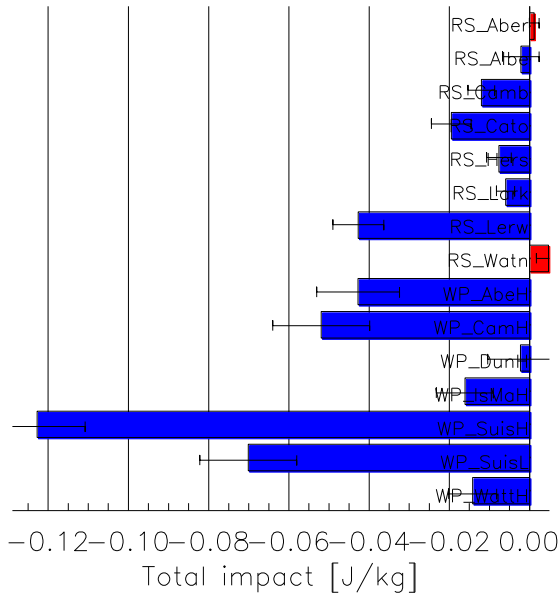


Figure 6: Total impact for wind profilers (starts with WP) and radiosonde (starts with RS) over UK cumulated over the full period. The impact includes all observations reported by radiosondes: wind, temperature and humidity data.

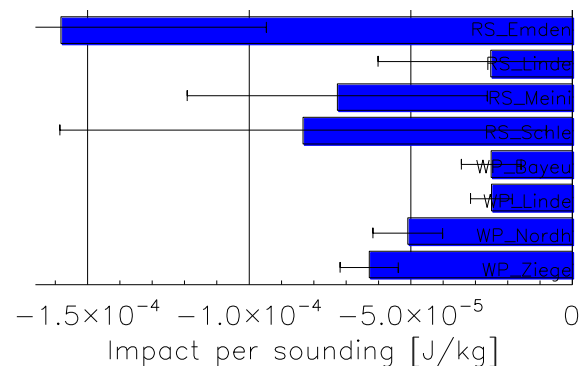


Figure 7: Impact per sounding for wind profilers (starts with WP) and radiosonde (starts with RS) over Germany cumulated over the full period. The impact includes all observations reported by radiosondes: wind, temperature and humidity data.

In the UK, the total wind profiler impact, which is the sum of all individual impacts (in time and height) for the period, is larger than for radiosonde (see Figure 6) by a factor ~ 3 when comparing the South Uist wind profiler and Lerwick radiosonde, which are both located in Scotland, and for the wind profiler and the radiosonde both at Camborne (Cornwall).

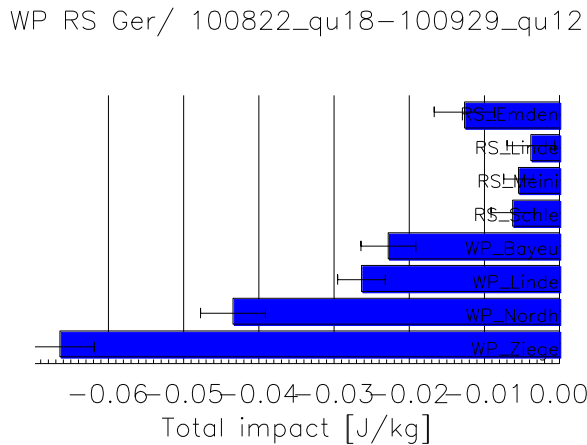


Figure 8: Total impact for wind profilers (starts with WP) and radiosonde (starts with RS) over Germany cumulated over the full period. The impact includes all observations reported by radiosondes: wind, temperature and humidity data.

However, it is possible that errors in the impacts of individual observations might be correlated (in height and in time). The total impact might then be exaggerated. This needs more investigation. At Lindenberg in Germany, the mean wind profiler impact per sounding is as large as the mean impact per radiosonde sounding (Figures 7) even though radiosonde observations include temperature and humidity readings as well as winds. Part of the reason for this could be that the Lindenberg wind profiler is located at a manned observatory (GRUAN station) and is very well maintained. When accumulated over the full period, the wind profiler impact is larger than the radiosonde impact by a factor ~ 7 due to the higher frequency at which wind profiler soundings are performed. The variance of the Lindenberg radiosonde impacts is large meaning that there may be error in our estimation of this mean impact. This result should therefore be confirmed over a larger period of time. As already mentioned, it is

possible that errors in the impacts of individual observations might be correlated. The total impact might then be exaggerated. This needs more investigation. However, as the Lindenberg wind profiler and radiosonde are collocated, their impact estimates should each suffer from similar error-correlations at least for the impact per sounding.

When comparing the total impact of Lindenberg with Ziegendorf or South Uist, the impact is relatively small (Figure 6 and 8). This is not surprising as, at Lindenberg, the atmosphere is already well described in the model due to assimilation of the radiosonde four times a day. The same applies for Camborne where both wind profiler and radiosonde are assimilated (with less extent as only 2 radiosondes per day are launched). There is a tendency to measure larger impacts for wind profilers and radiosondes located close to the sea, e.g. Lerwick, South Uist, Eimden, Ziegendorf.

4. Data denial experiment on high resolution model

UKVNDP is a high resolution (1.5km grid spacing) convective scale model on a limited domain (South of UK) with a time step of 50s. In UKVNDP the assimilation process is done every hour using a 3D-Var scheme with forecasts up to 6 (or 12) hours. The aim of this model is to provide accurate NWP based now casting. This model uses all available observations; it recently assimilates the radial winds from the weather radar.

A data denial experiment where the wind profilers were removed was performed on one case study. The control assimilates wind profiler data for a 24h period, the experiment don't. For the analysis the fit to the wind profiler data has been largely reduced (Figure 9). This improvement ($\sim 0.5\text{m/s}$ on U and $\sim 1\text{m/s}$ on V at 1km) is still present at the 2 hour forecast in particular in the first 2km where most of the wind profiler observations are (Figure10). At T+5 (not shown) the improvement is marginal.

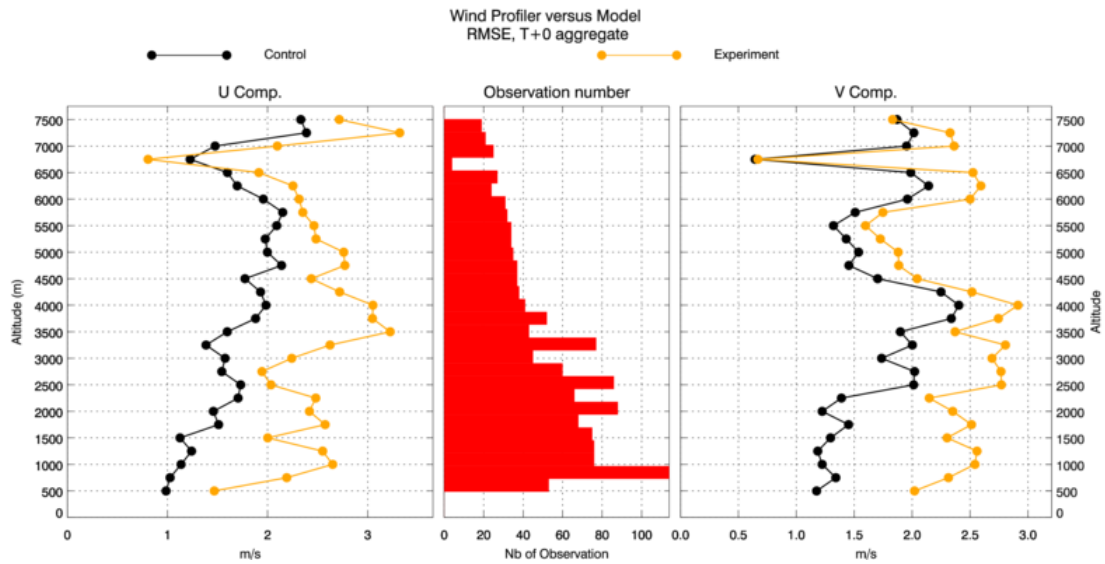


Figure 9: Fit to wind profiler observations for all analysis (T+0) (RMS for Each component). The control is the assimilation with wind profilers; the experiment is without wind profilers.

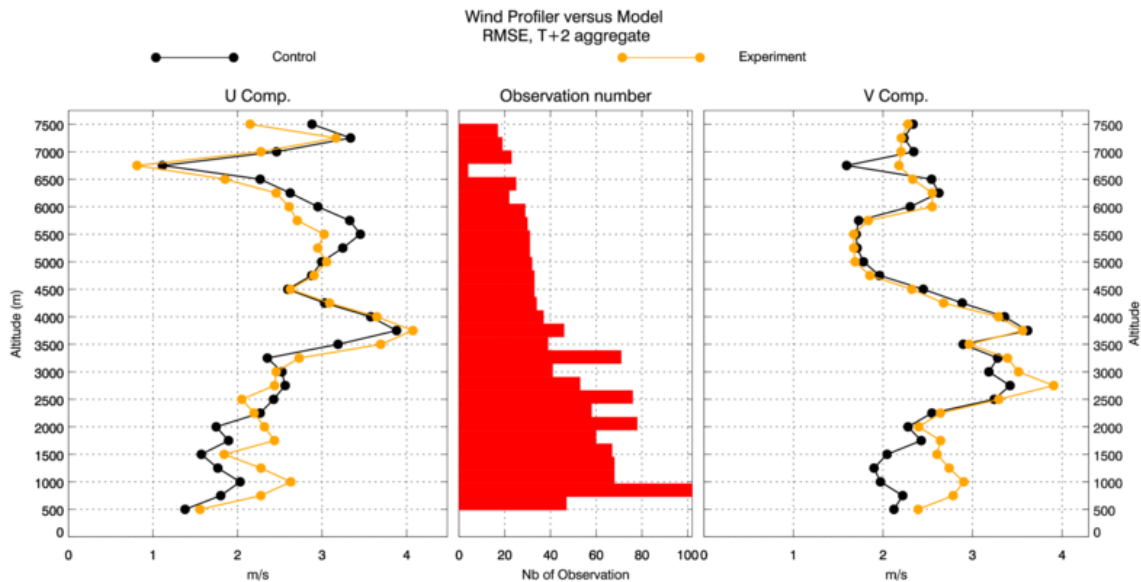


Figure 10: Fit to wind profiler observations for all 2h forecast (T+2) (RMS for Each component). The control is the assimilation with wind profilers; the experiment is without wind profilers.

The use of wind profilers not only improves the wind, but increases the fraction skill score for the rain detection at 3h forecast (Figure 11). The fraction skill score as defined in (Roberts 2008) smoothes at different scale the detected rain and compare it with the radar image smoothed as well on the same scale. Within a defined neighbourhood (sample radius), the pixel at the centre is attributed a value which is the proportion of pixel with rain (model grid size with rain rate above 1mm/h), the exact location does not matter, these fractions for the model and for the radar image are then compared together to produce the FSS for a defined sample radius.

5. Conclusion

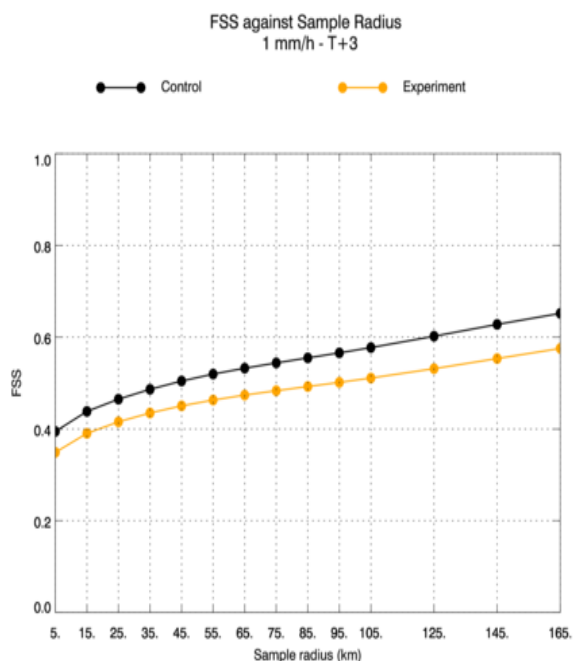


Figure 11: Fraction skill score for rain average for all the a T+3h forecast for different sample radius.

accumulated over time. Correlation of errors may cause the beneficial or detrimental impact of observations to be exaggerated. However, these preliminary results tend to indicate that wind profilers could be giving large impacts where they are well maintained and placed in strategic locations. An extended period should be studied to confirm these findings in particular over different seasons.

On one case study we found that wind profiler data could also improve our now casting system, however more situations should be studied to see how useful wind profiler can be in high resolution NWP.

Annexe

The method used at the UK Met Office to compute observation impacts is very similar to the one described by Langland (2004). The main difference from most results found in the literature is that the computation of the forecast error metric used in this study includes moisture. A full

description of the method is in the process of being published in the QJRMS (Lorenc and Marriott 2012). For completeness we repeat here the basic steps of the method.

For each assimilation cycle the forecast error for a forecast \mathbf{fa} valid at time t , issued from an analysis at $t-L$, and for a forecast \mathbf{fb} also valid at time t but issued from the previous analysis at $t-L-\delta t$, are computed by subtraction of the analysis \mathbf{xt} , valid at time t , from the two forecasts. δt is the length of the 4D-Var data assimilation time window (6h in for the global model) and L is the length of the forecasts on which we are measuring the impact - typically 24h. Scalar values for the overall forecast error, e_{fa} and e_{fb} , are computed using an energy norm (inner product of the difference of the forecast and analysis state vectors with itself, the inner product being defined by a matrix \mathbf{C} which combines the vector components of elastic potential energy, thermal energy, the latent thermal energy of condensation, and kinetic energy). The forecast error difference $\Delta e = e_{fa} - e_{fb}$ (should be a decrease) is due to the use of observations in the analysis at $t-L$.

$$e_{fa} = (\mathbf{fa} - \mathbf{xt})^T \mathbf{C}(\mathbf{fa} - \mathbf{xt})$$

$$e_{fb} = (\mathbf{fb} - \mathbf{xt})^T \mathbf{C}(\mathbf{fb} - \mathbf{xt})$$

and

$$\Delta e = \Delta e_{fa} - \Delta e_{fb} = (\mathbf{fa} - \mathbf{xt})^T \mathbf{C}(\mathbf{fa} - \mathbf{xt}) - (\mathbf{fb} - \mathbf{xt})^T \mathbf{C}(\mathbf{fb} - \mathbf{xt})$$

and by the difference of two squares

$$\Delta e = \Delta \mathbf{xf}^T \mathbf{C}((\mathbf{fa} - \mathbf{xt}) + (\mathbf{fb} - \mathbf{xt}))$$

where $\Delta \mathbf{xf}$ is the change in the forecast due to the assimilation of observation in the analysis at $t-L$. What we want is to be able to attribute this error reduction to each of the observations used in that analysis. For this we need to express the reduction of error as the inner product between the innovation vector for the analysis at $t-L$ and some vector of sensitivities which we assume to be independent of the observations.

Holding the sum of the forecast errors constant, the gradient of the forecast impact with respect to the change in forecast due to observations can be written as

$$\frac{\partial \Delta e}{\partial \Delta \mathbf{f}} = \mathbf{C}((\mathbf{fa} - \mathbf{xt}) + (\mathbf{fb} - \mathbf{xt}))$$

If the forecast length is not too long we can assume that applying a linear version of the forecast model to analysis increments will give, to a reasonable approximation, the difference between the two nonlinear forecasts. This is the largest approximation used in the FSO method.

$$(\mathbf{fa} - \mathbf{fb}) \cong \mathbf{M}_{t-L \rightarrow t}(\mathbf{xa} - \mathbf{xb})$$

where \mathbf{M} is the linear version of the model, \mathbf{xa} is the analysis at $t-L$ and \mathbf{xb} is the background state used to produce analysis \mathbf{xa} . Using the chain rule we get

$$\frac{\partial \Delta e}{\partial \Delta \mathbf{xa}} = (\mathbf{M}_{t-L \rightarrow t})^T \frac{\partial \Delta e}{\partial \Delta \mathbf{f}}$$

where $\Delta \mathbf{xa}$ is the analysis increment rather than the analysis itself. We can now express forecast impact as a function analysis increments.

$$\Delta e = \Delta \mathbf{xa}^T \frac{\partial \Delta e}{\partial \Delta \mathbf{xa}} = (\mathbf{xa} - \mathbf{xb})^T (\mathbf{M}_{t-L \rightarrow t})^T \mathbf{C}((\mathbf{fa} - \mathbf{xt}) + (\mathbf{fb} - \mathbf{xt}))$$

The analysis increment can now be written as a function of the innovation by using

$$\Delta \mathbf{xa} = \mathbf{BH}^T [\mathbf{HBH}^T + \mathbf{R}]^{-1} (\mathbf{y} - \mathbf{Hxb})$$

or

$$\Delta \mathbf{xa} = \mathbf{K}(\mathbf{y} - \mathbf{Hxb})$$

By using the adjoint of the assimilation scheme, \mathbf{K}^T , we can express Δe as a scalar product of the innovation vector and the vector of corresponding sensitivities.

$$\Delta e = (\mathbf{y} - \mathbf{Hxb})^T \mathbf{K}^T \frac{\partial \Delta e}{\partial \Delta \mathbf{xa}}$$

$$\frac{\partial \Delta e}{\partial \Delta \mathbf{y}} = \mathbf{K}^T \frac{\partial \Delta e}{\partial \Delta \mathbf{xa}}$$

We now have the contribution (i.e. the impact) of each of the observations to the reduction of 24-hour forecast error. Because of the influence of random errors in verifying analyses, random observation errors and the fact that data assimilation is a statistical process which can only use observations to improve forecasts on average, impacts need to be averaged to give reliable results (Lorenc and Marriott 2012). At the Met Office the forecast error is computed from simplified model states. The adjoint forecast model used is that of the simplified perturbation forecast model. The reason for using this rather than a tangent linear of the full model is explained in Lorenc (2003). The actual numerical computation of the observation sensitivity vector is quite complex and computationally demanding. Observation impacts are currently calculated on a per study basis but may be produced operationally in future. In the results shown, the forecast error is computed over the full globe.

References

- Langland, R. H. and Baker, N. L. 2004. Estimation of observation impact using the NRL atmospheric variational data assimilation adjoint system. *Tellus* 56A, 189-201.
- Lorenc AC 2003. Modelling of error covariances by four-dimensional variational data assimilation. *Q. J. R. Meteorol. Soc.* 129: 3167-3182.
- Lorenc A. C and Marriott R.T 2012 Observation Impacts in the Met Office Global NWP System, submitted to QJRMS
- Rawlins F, Ballard SP, Bovis KJ, Clayton AM, Li D, Inverarity GW, Lorenc AC, Payne TJ. 2007. The Met Office global 4-dimensional data assimilation system. *Q. J. R. Meteorol. Soc.* 133: 347-362.
- Roberts NM. 2008. Assessing the spatial and temporal variation in the skill of precipitation forecasts from an NWP model. *Meteorological Applications* 15: 163–169

A study of Indian Summer Monsoon clouds during drought and normal monsoon years using data Cloud Profiling Radar on CloudSat

M Muhsin¹ and Kusuma G Rao¹

¹ Atmospheric Science Programme, Indian Space Research Organization Hq, Bangalore, India, aspmuhsin@gmail.com

Abstract

The 94-GHz Cloud Profiling Radar onboard CloudSat was designed to provide global information on the vertical structure of clouds. It was launched during April 2006, as part of the A-Train of Earth science satellites. Here an attempt is made to investigate the characteristics of the Monsoon Cloud System of Indian summer monsoon region using data from Cloud Profiling Radar during a drought year (2009) and a normal monsoon year (2007). As per Indian Meteorological Department (IMD) report, the average rainfall over Indian region during June-September 2009 was less by 23% than Long Period Average (LPA). The year 2009 was a severe drought year and 2007 was a normal monsoon year. Relative percentages of occurrence of different types clouds have been examined for the summer monsoon months (June-September) for the years 2007 and 2009. It is inferred that the percentages of spatial occurrence of the clouds are relatively large during the year 2007 than the year 2009, especially in the case of Deep Convective (DC) clouds.

1. Introduction

In tropical countries, especially in India, the economy of the country essentially is dependent on agriculture which in turn depends mostly on the seasonal rains, called South West Monsoon (SWM) and North East Monsoon (NEM). The country receives more than 80 % of the annual rainfall during a short span of four months (June to September) of the southwest monsoon season which is also known as Indian Summer Monsoon (ISM). The variations of monsoon in terms of onset, withdrawal and amount of rainfall will make deep impact on agriculture, power generation and the ecosystem in the country. The clouds during monsoon occur at a wide range of sizes starting from isolated cumulus clouds to large cluster of clouds and further develop into mesoscale organization. Deep Convective (Cumulonimbus, Cb) clouds play a major role in summer monsoon. Depending upon the occurrence of Deep Convective (DC) clouds, the respective year is going to be determined as drought or good monsoon year. The present study is to investigate the behavior of different clouds during drought and normal summer monsoon year using CloudSat data. As per Indian Meteorological Department (IMD) report, the average rainfall over Indian region during June-September in the year 2009 was 23% less than Long Period Average (LPA). The year 2009 was a severe drought year. During June-September 2007 the average rainfall over Indian region was 5% more than Long Period Average, so this year was a normal monsoon year.

2. Data and Methodology

For the present study we used two-years of CloudSat observations over the Indian monsoon region (10 S to 35 N; 50 E to 100 E). CloudSat, launched on 28 April 2006, is orbiting information with other NASA spacecraft in the A-Train [Stephens et al., 2002]. The Cloud Profiling Radar (CPR) on CloudSat is a 94-GHz nadir-looking radar which measures the energy backscattered by clouds and precipitation within a 1.3 km across-track by 1.7 km along-track radar footprint. Each CloudSat

profile is generated over a 160 millisecond interval which corresponds to a 1.1 km along track distance and repeats the ground track every 16 days. CloudSat is very much helpful to study the vertical structure of clouds since it gives the profile of the required data. Data used for the analysis are 2B-GEOPRF, 2B-CLDCLASS and 2B-CWC-RO data products of CloudSat for the present study. In 2B-CLDCLASS data product, the clouds are classified into cumulus (Cu), stratocumulus (Sc), stratus (St), altocumulus (Ac), altostratus (As), nimbostratus (Ns), High Clouds (cirrus and cirrostratus), and Deep Convective (DC) clouds (i.e., Cumulonimbus) based on the International Satellite Cloud Climatology Project (ISCCP) (Rossow and Schiffer 1999) approach. To get the relative percentage of occurrence of different cloud type, we have gridded the study region at $1^\circ \times 1^\circ$ degree resolution and then classified the clouds from 2B-CLDCLASS and counted the number of bins passing through each grid for each cloud classification. Then normalize the total count of four months with the grid maximum count of the region. We use the Contoured Frequency by Altitude Diagram (CFAD), developed by Yuter and Houze, to investigate the vertical structure of reflectivity, Liquid Water content (LWC), Ice Water Content (IWC), Ice Effective Radius (IER) and Liquid Effective Radius (LER) of different cloud types during summer monsoon (JJAS) months of 2007 and 2009.

3. Results and Discussion

Since DC clouds play a major role in summer monsoon, this study gives an emphasis on DC clouds. Figures 1(a) and 1(b) show the distribution of relative percentage of occurrence of DC clouds over the Indian monsoon region during 2007 and 2009, which are normal monsoon and drought years respectively. In 2007, DC distribution is spread over the entire BOB region and also in the Arabian Sea region (Fig 1a), whereas in 2009, it is highly concentrated in the north east of Bay of Bengal (BOB) (Fig 1b). Altostratus (As) clouds also shows significant deficiency during drought year than the normal monsoon year (figure not shown). During 2009 the distribution of As clouds are mostly spread over the BoB, whereas during 2007 it is spread all over the BoB, Indian Ocean, Arabian sea and southern peninsular of India. Low clouds (Sc, Cu, Ns) are distributed largely over the Tibetan Plateau and is not showing much variation over Tibetan Plateau during these two years. Stratocumulus also distributed over northern Arabian Sea but the occurrence of clouds over here is less during drought year than normal monsoon.

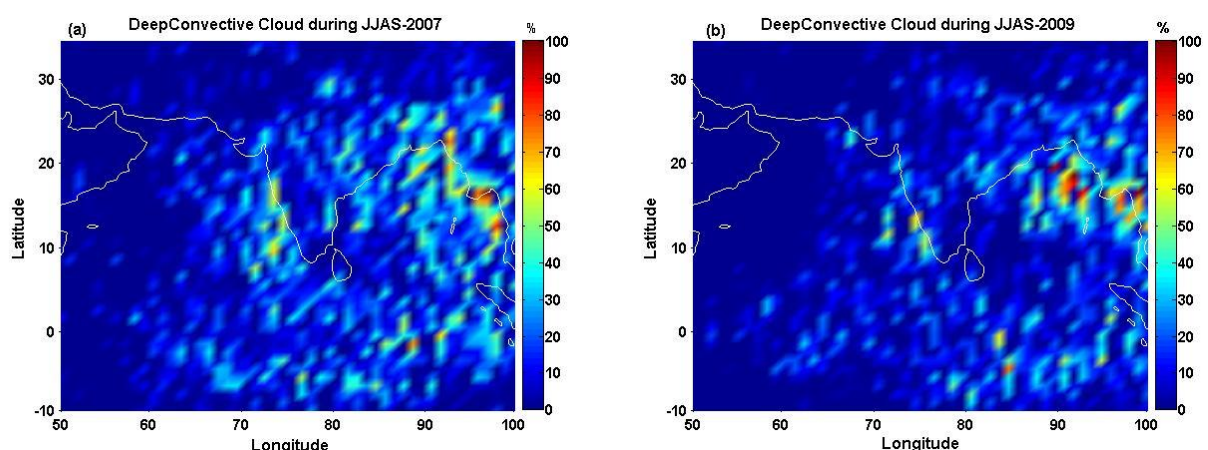


Figure 1: Distribution of relative percentage of occurrence of DC clouds over the Indian monsoon region in (a) 2007 and (b) 2009, which is a normal monsoon and drought years respectively.

Figure 2(a) and 2(b) shows Contoured Frequency by Altitude Diagrams (CFADs) for the observed reflectivity during 2007 and 2009 respectively. It is found that there is a significant difference in reflectivity between -15dBZ and 20 dBZ when compared with 2007 and 2009. So we can say that the occurrence of cloud those have reflectivity between -15dBZ and 20 dBZ are more in 2007 than 2009. Also we found that the cloud occurring in altitude between 10km to 14km is dominant during both year and it should be cirrus clouds.

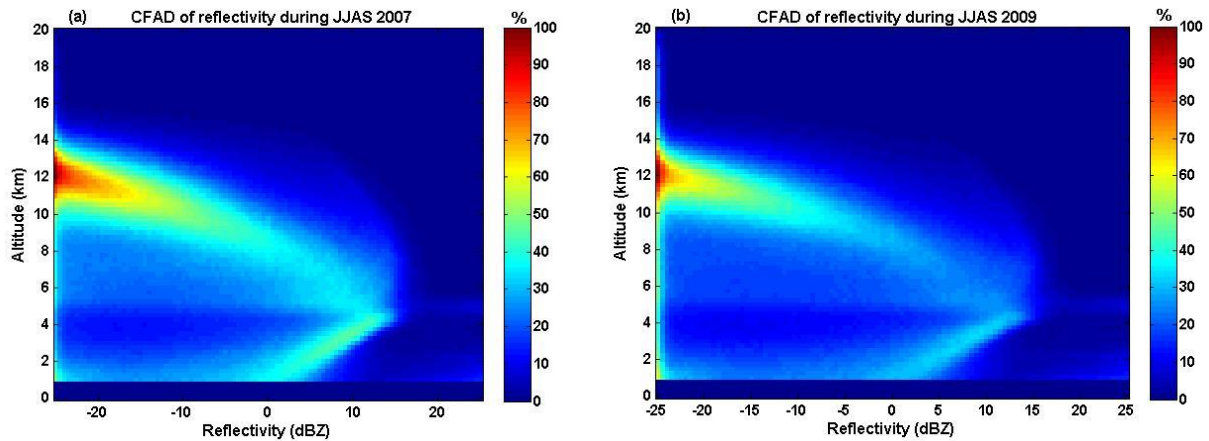


Figure 2: Contoured frequency by altitude diagrams (CFADs) for CPR measured reflectivity during (a) 2007 and (b) 2009 over Indian Summer Monsoon region.

Figures 3(a) and 3(b) show the CFADs of reflectivity for the DC clouds over the Indian monsoon region during JJAS months of 2007 and 2009. From these plots, we could find that the occurrence of DC clouds is less by 27% less during 2009 than during 2007. CFAD of all other cloud types have been plotted. The occurrences of Ns and As clouds are much less, by 35% and 25% respectively during 2009 in comparison with the occurrences during 2007. We could find out that the occurrences of other cloud types are also less during drought year except Stratocumulus (Sc) clouds which is almost the same in both the years. CFAD of IWC, LWC, IER and LER also have been plotted to present a histogram of ice and liquid properties at each altitude (figures not shown).

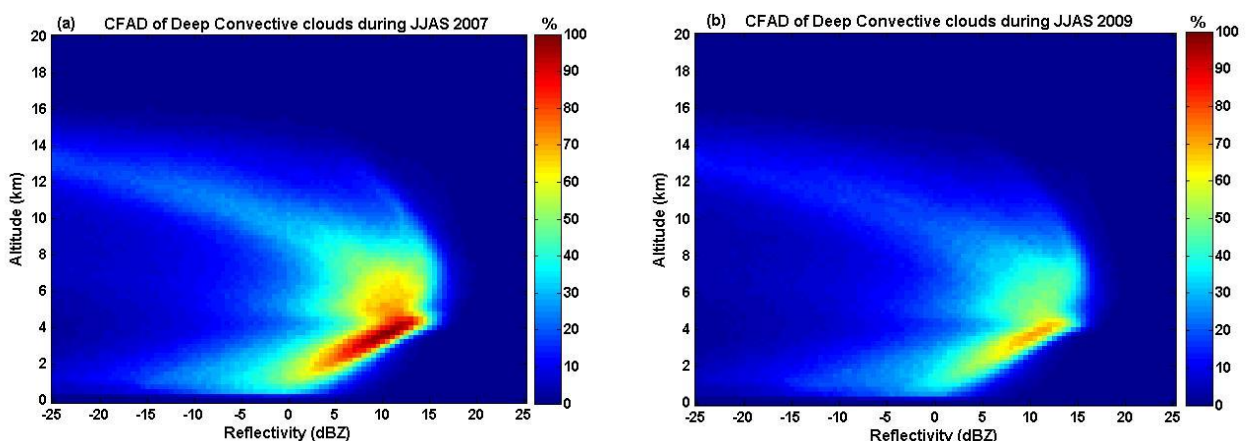


Figure 3: Contoured Frequency by Altitude Diagrams (CFADs) of reflectivity for the DC clouds over Indian monsoon region during (a) 2007 and (b) 2009.

It revealed that maximum IWC occurring at about 8 km altitude and the peak ice water content is about 0.5 g/m^3 at an altitude of 8 km. The LWC is occurring up to 8 km and the peak LWC is about 0.5 g/m^3 at almost all altitude. IER radius decreases with altitude and it is varying $\sim 180 \text{ }\mu\text{m}$ to $20 \text{ }\mu\text{m}$ when it reaches an altitude of 16 km from surface. LER changes from $5 \text{ }\mu\text{m}$ to $20 \text{ }\mu\text{m}$ in almost all altitude but in the altitude of 3-5 km LER changes from $5 \text{ }\mu\text{m}$ to $15 \text{ }\mu\text{m}$.

4. Summary

A study of different types of clouds during the summer monsoon months of 2007 and 2009, which are normal monsoon and drought years respectively, revealed that the distributions of relative percentage of occurrence of clouds are varying during the two years. Especially the distributions of Deep Convective (DC) clouds and Altostratus (As) clouds are varying largely between these two years. In 2007, DC distribution is spread over the entire BOB region and also in Arabian Sea region, where as in 2009, it is highly concentrated in the north east of Bay of Bengal (BOB). During 2009 the distribution of As clouds are mostly spread over the BoB, whereas during 2007 it is spread all over the BoB, Indian Ocean, Arabian sea and southern peninsular of India. Contoured Frequency by Altitude Diagram (CFAD) of reflectivity for the DC clouds shows that the occurrence of Ns, DC and As clouds are less by 35%, 27% and 25% respectively during 2009 than 2007. The distribution of other clouds such as Altocumulus, Altostratus and Nimbostratus clouds also showed interannual variability in their occurrence. CFAD of Ice Water Content (IWC), Liquid Water Content (LWC), Ice Effective Radius (IER) and Liquid effective Radius (LER) are also plotted to present a histogram of ice and liquid properties at each altitude. The characteristics of different types of clouds in terms of IWC, LWC, IER, LER, etc need to be further investigated.

Acknowledgement

The authors are greatly thankful to CloudSat team and the data products were obtained from the CloudSat website <http://www.cloudsat.cira.colostate.edu>.

Reference

- Rossow, W. B., and R. A. Schiffer, 1999: Advances in understanding clouds from ISCCP. *Bull. Amer. Meteor. Soc.*, **80**, 2261-2286.
- Stephens, G. L., et al. (2002), The CloudSat mission and the A-Train: A new dimension of space-based observations of clouds and precipitation, *Bull. Am. Meteorol. Soc.*, 83, 1771– 1790, doi: 10.1175/BAMS-83-12-1771.
- Yuter SE, Houze RA. Three-dimensional kinematic and microphysical evolution of Florida cumulonimbus. Part II: frequency distributions of vertical velocity, reflectivity, and differential reflectivity. *Mon Wea Rev* 1995; 123(7): 1941-63.

Shrinking of Tropical Tropopause Layer during Organized Deep Convection of Indian Summer Monsoon over the Bay of Bengal with JASMINE Measurements

Kusuma G Rao^{1,2}, Nelli-Narendra Reddy^{1,2} and Paquita Zuidema³

¹ Atmospheric Science Programme, Indian Space Research Organization, Antariksh Bhavan, New BEL Road, Bangalore, 560 094, India, kusuma_rao@yahoo.com

² Space Physics Laboratory, Vikram Sarabhai Space Center, Trivandrum, 695022, India

³ Rosenstiel School of Marine and Atmospheric Science University of Miami, Miami, USA

1. Introduction

The Tropical Tropopause Layer (TTL) was traditionally recognized as a sharp boundary demarcating the troposphere from the stratosphere. *Gettelman and Forster* [2002] defined TTL as extending between the Lapse Rate Minimum Altitude (LRMA) to the Cold Point Tropopause Altitude (CPTA) based on theoretical considerations and on the proposition that the level of minimum potential temperature is a good marker for the maximum influence of convection on the temperature profile. *Gettleman et al.*, [2002] indicated that for a small fraction of the time, convection penetrates above the cold point in isolation. Stability of the TTL regulates the transports from the troposphere to the stratosphere. Thus it is interesting to study TTL variations including its stability as a function of convection in comparison with those associated with clear sky conditions.

The present study used data during the two small-scale surveys made for the two 6 days periods, May 10-15, 1999 (Star1 period) and May 21-26, 1999 (Star2 period) from the Joint Air Sea Monsoon Interaction Experiment (JASMINE-99) conducted by *Webster et al.*, [2002] in the Bay of Bengal region with the NOAA Research ship Brown at the location [10 N, 89 E]. The data set analysed here include the surface parameters, the rain rate, the cloud parameters and the upper air data of wind, temperature and humidity.

2. Synoptic conditions

The weather conditions that prevailed during the period of analysis are described in terms of cloudiness based on METEOSAT IR brightness temperatures (IRBRT), the rainfall, the gustiness, the near surface wind speed and humidity and the SST, etc., around the ship location [10 N, 89 E] in the Bay of Bengal. Time-latitude plots of METEOSAT IRBRT (figure 1) and 3 hourly spatial imageries (figure not shown) reveal that absolute clear sky conditions prevailed during Star1 period around the ship location during 10 to 15 May

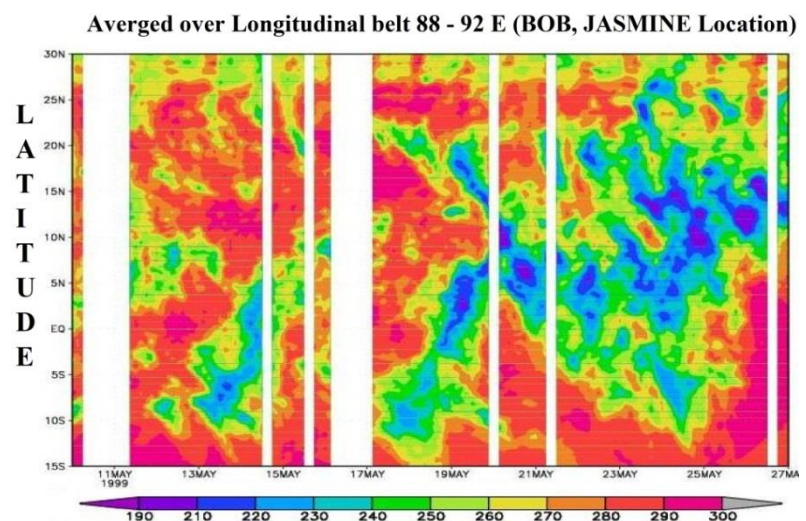


Figure 1: Time - Latitude variation of METEOSAT IR Brightness temperature averaged over longitudinal belt of 88 – 92 E during 10 - 27 May, 1999.

1999 except during 09 GMT – 21 GMT of 11 May and 06 GMT – 12 GMT of 12 May. During Star2 period of 21-26 May, very deep clouds prevailed with IRBRTs as low as 210 K extending spatially over 600 – 700 km in space and in time scales of days. During Star1 period, the wind speeds at 17.7 m height are relatively low and decreasing with time in contrast to the Star2 period with wind speeds increasing and crossing $\sim 12 \text{ m s}^{-1}$. A few heavy rain events occurred during Star2 period on 23 and 25 May, 1999. Thus Star1 and Star2 periods are noticed to be associated with contrasting variations in several parameters. Hereafter, Star1 period characterized by nearly clear sky conditions, low wind speed ($0\text{-}6 \text{ m s}^{-1}$), less humidity, relatively warmer SST is referred here as “Undisturbed” period, whereas the contrasting Star2 period, characterized as highly humid and convective associated with large wind speeds ($0\text{-}12 \text{ m s}^{-1}$) and relatively cooler SSTs is referred here as “Disturbed” period.

3. Results

Contrasting variations in CPT Temperatures (CPTT) and the corresponding CPTA between the Disturbed (May 10-16) and the Undisturbed periods (May 21-26) are shown in figure 2. CPTT being in ranges [185.5-191.5 K] and [187.0-192.3 K] during Disturbed and Undisturbed periods clearly indicate that relatively lower CPTT values occurred on days of deep convection during Disturbed period with the coldest temperature of 185.5 K prevailing on 25 May 1999.

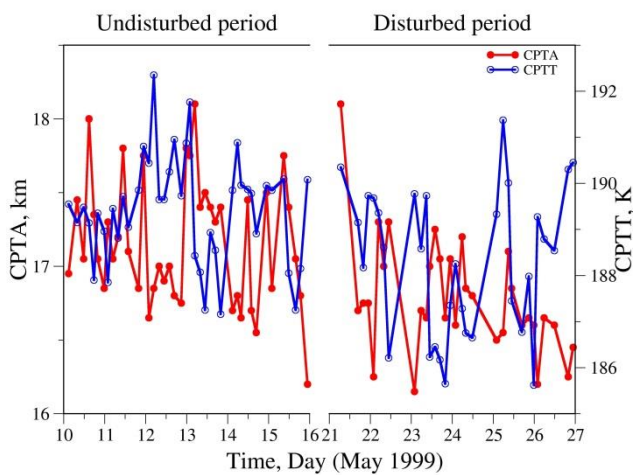


Figure 2: Contrasting variations in CPTT and CPTA between Undisturbed and Disturbed periods.

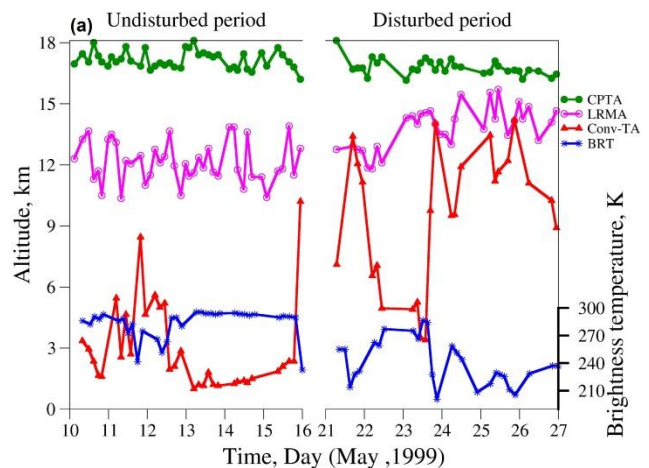


Figure 3: Various tropopause altitudes during the undisturbed and disturbed periods.

Most of the data points in figure 2 correspond to Warmer (Colder) CPTTs at relatively lower (higher) altitudes consistent with normal temperature lapse rate as expected. Interesting noteworthy observation, in figure 2, is that the CPTT is cooling at relatively lower heights on days 13, 24 and 25 unlike in normal cases of cooling at higher heights governed by lapse rate decrease. *Mehta et al.*, [2010] identified similar unlike normal cases in radiosonde data over the tropical land station Gadanki. In order to understand the impact of convection on CPT cooling for unlike normal cases, various tropopause altitudes, namely, CPTA, LRMA and Convective Tropopause Altitude (Conv-TA) and IRBRT have been plotted in figure 3 for one to one comparisons on daily basis for Disturbed and Undisturbed periods. During Undisturbed days, middle level cumulus clouds

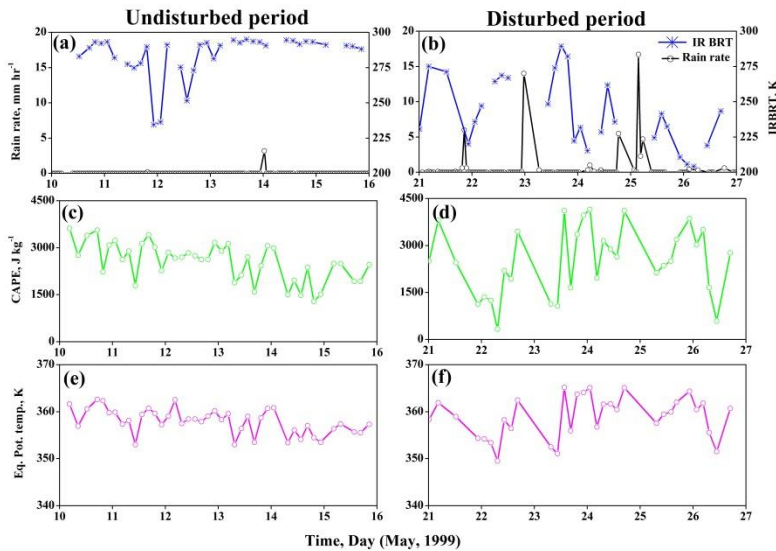


Figure 4: Variations in (a - b) IRBRT and Rain Rate, (c - d) CAPE and (e - f) Equivalent Potential Temperature during Undisturbed and Disturbed periods.

prevailed on 11 and 12 May 1999. During the disturbed periods, cloud top temperatures and the cloud top altitudes indicate that most of the data points are associated with deep cumulus clouds with IRBRTs < 240 K. Sometimes, very deep convection prevailed with IRBRTs < 210 K. IRBRT is at 200 K on 25 May during when heavy rain of 16 mm hr^{-1} occurred (figure 4). Lapse rate minimum altitudes show significant variations between Disturbed and Undisturbed periods with maximum in LRMA on 25 May 1999. Both LRMA and Conv-TA are relatively higher during the disturbed period in comparison with their variations during the Undisturbed period. The striking result to note from figure 3 is that,

LRMA is increasing hand in hand with Conv-TA on days of occurrence of deep cumulus clouds. The inference is that the transition in stability regime from convectively dominated regime to radiatively controlled regime occurs at relatively higher levels during the time of occurrence of deep cloud systems. Thus TTL Thickness, defined here as CPTA-LRMA, reduced significantly during convectively Disturbed period when compared with its values during the Undisturbed period. The statistics for Disturbed and Undisturbed periods on CPTT, CPTA, LRMA, TTL thickness and Potential temperature at LRMA are given in table 1. Average and standard deviations given in the first two rows indicate that CPTT is cooler by 1.1 K on an average during Disturbed period at a lower height of 16.8 km when compared with the undisturbed period. Rows 2 to 4 indicate that, on an average, TTL shrunk by 2.9 km, CPTA lowered by 0.4 km and LRMA increased by 1.7 km during the Disturbed period in comparison with the Undisturbed period. Potential temperature at LRMA is higher by 4.1 K during the Disturbed period when compared with that during the Undisturbed period. Our major interest here is to explore possible links between the Tropopause layer variations and the surface layer processes during the Disturbed convective conditions. Figures 4(a-f) describe one to one variations with time in IRBRT, Rainfall, CAPE and surface equivalent potential temperature for Undisturbed (left panel) and Disturbed (Right panel) conditions. First of all one can note that, quite often both CAPE and surface equivalent potential temperature reached very high values during the Disturbed period when compared their values during the Undisturbed period. CAPE builds up and equivalent potential temperature shoots up at instants before the intense rain events on 23, 24 and 25 May 1999 and drops down to lowest values with the occurrence of the events. This is consistent with the findings of *Bhat et al.*, [2001] with similar measurements for Bay of Bengal. With these consistency noted in CAPE and the prevailing weather during the study period, we explored the correlation between CPTT and CAPE, CPTT and surface equivalent potential temperature. The variations in CPT temperatures with CAPE and equivalent potential temperature combined for Undisturbed and Disturbed periods showed that cooler CPT is associated with higher CAPE and higher surface equivalent potential temperature values, especially during the Disturbed period.

What causes “CPT cooler at lower heights” during Disturbed conditions?

A comparison in temperature variations with height averaged over Disturbed (thick line) and Undisturbed periods (dotted line) is shown in figure 5(a); the variations with height of the corresponding differences in the average temperatures is shown in figure 5(c) (thick line). Figure 5(b) describes comparisons in temperature lapse rate variations with height during Disturbed (Continuous line) and Undisturbed periods (dotted line); the variations with height of the

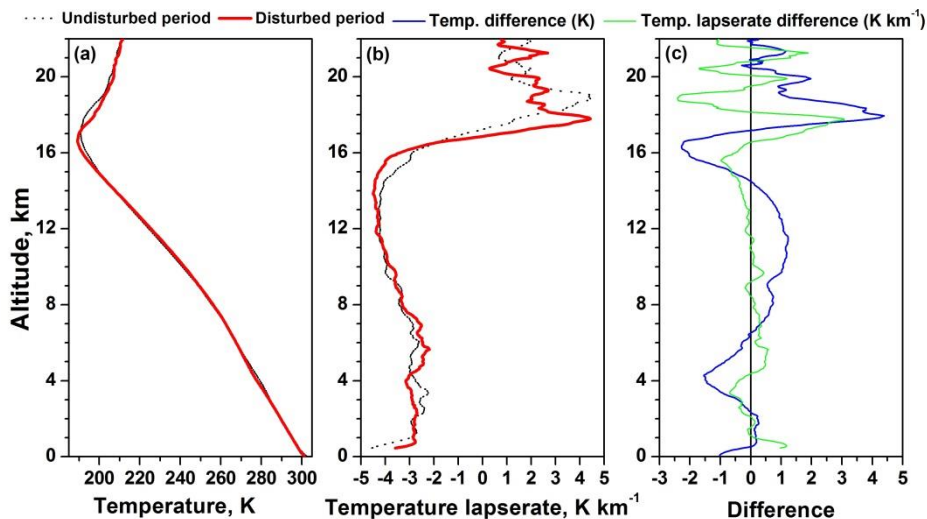


Figure 5: Mean profiles of (a) Temperature, (b) Temperature lapse rate, Undisturbed and Disturbed periods (c) Temperature, Temperature lapse rate difference between Undisturbed and Disturbed periods.

5 (c); whereas, the maximum warming of 4.0 K occurred above the TTL at 17.95 km with respect to the Undisturbed period. The temperature lapse rates being higher negative during the Disturbed period in the region 11.65 km to 16.55 km (figure 5(b)) with maximum at 15.6 km (Figure 5(c)), indicates that a higher cooling rate of 1 K km^{-1} prevailed during the Disturbed period. The cooling of CPT at lower heights noted with higher lapse rate below the tropopause is consistent with the findings of *Jain et al.*, [2006]. This clearly substantiates why CPT is cooler during the Disturbed conditions. Equally striking result is the lower stratospheric warming observed above the TTL in the height region, 16.6 km to 18.1 km with maximum warming at 17.75 km with positive lapse rate of 3.1 K km^{-1} .

The major inference here is that the CPT is significantly cooler at relatively lower altitudes during Disturbed convective conditions when compared with Undisturbed clear sky conditions. Thus it is surprising to note that the cooling observed at lower heights is unlike the case governed by normal lapse rate cooling. During the disturbed conditions, a handful of points are found to be associated with surface equivalent potential temperature, $\theta_e \geq 364 \text{ K}$ as shown in figure 4(f). This is much higher compared to the threshold of $\theta_e \geq 345$ arrived at by *Neelin and Held*, [1987], *Folkens and Braun.*, [2003], who showed that parcels crossing this threshold first attain positive CAPE and may participate in convection. First of all, it is to be noted that the threshold arrived at here on θ_e is 364 K. Hence, this high value of θ_e may be forcing the surface parcels to participate in very deep convection and thus the parcels can raise above the LNB by ‘Overshooting’. Overshooting air parcels become progressively colder with height than the environment. If the overshooting parcels mix with ambient air of higher potential temperature, they will cool these levels and finally reach equilibrium above the LNB. This may be one of the mechanisms which could explain the CPT cooling at relatively lower altitudes during the conditions of deep convection.

Acknowledgements

This work is done under CAWSES-India programme under the theme of Atmospheric coupling processes. We acknowledge the support from Indian Space Research Organization (ISRO).

References

- Gottelman, A. and de Forster, P. M., (2002), A climatology of the tropical tropopause layer, *J. Meteor. Soc.*, Vol. 80, pp. 911-924.
- Mehta, S. K., M. Venkat Ratnam, and B. V. Krishna Murthy (2010), Variability of the tropical tropopause over Indian monsoon region, *J. Geophys. Res.*, 115, D14120, doi:10.1029/2009JD012655.
- Neelin, J. D., and I. M. Held (1987), Modelling tropical convergence based on the moist static energy budget, *Mon. Weather Rev.*, 115, 3–12.
- Folkins, Ian, Christopher Braun, (2003), Tropical Rainfall and Boundary Layer Moist Entropy. *J. Climate*, **16**, 1807–1820.
- Gottelman, A., Salby, M. L., and Sassi, F., (2002), The distribution and influence of convection in the tropical tropopause region, *J. Geophys. Res.*, 107 (D10).
- Webster, P. J., E. F. Bradley, C. W. Fairall, J. S. Godfrey, P. Hacker, R. A. Hopuze jr., R. Lukas, Y. Serra, J. M. Hummon, T. D. M. Lawrence, C. A. Russel, M. N. Ryan, K. sahami, Zuidema, P. (2002), The Joint Air-Sea Monsoon Interaction Experiment (JASMINE) Pilot Study, *Bull. Amer. Met. Soc.*, 83, 1603-1630.

Session 6

The Wave-Driven Circulation and Variability of the Wintertime Arctic Middle Atmosphere

Richard L. Collins¹, Amal Chandran¹, V. Lynn Harvey², Michael Gerding³, Gerd Baumgarten³, Franz-Josef Lübken³, Kohei Mizutani⁴, Anja Strømme⁵, Rolando R. Garcia⁶, Daniel R. Marsh⁶, Brentha Thurairajah⁷

¹ Geophysical Institute, University of Alaska Fairbanks, 903 Koyukuk Drive, Fairbanks, AK 99775, USA

² Laboratory for Atmospheric and Space Physics, University of Colorado, 1234 Innovation Drive, Boulder, CO 80303, USA

³ Leibniz-Institute of Atmospheric Physics, at the University of Rostock, Schloßstr. 6, 18225 Kühlungsborn, Germany

⁴ Applied Electromagnetic Research Institute, National Institute of Information and Communications Technology, 4-2-1 Nukui-kita, Koganei, Tokyo 184-879, Japan

⁵ Center for Geospace Studies, SRI International, 333 Ravenswood Ave, Menlo Park, CA 94025, USA

⁶ Earth System, Laboratory, National Center for Atmospheric Research, 3450 Mitchell Lane, Boulder, CO 80301, USA

⁷ Bradley Department of Electrical and Computer Engineering, Virginia Polytechnic Institute and State University, Blacksburg, VA 24061, USA

1. Introduction

The structure of the wintertime circulation of the Antarctic middle atmosphere is generally stable and the polar vortex robust, while the wintertime circulation of the Arctic middle atmosphere is unstable and the vortex is smaller and often disrupted due to stronger forcing by planetary-waves in the northern hemisphere. In recent years the wintertime Arctic middle atmosphere has been routinely disrupted by Sudden Stratospheric Warming events (SSWs, Manney et al., 2005; 2009). During strong SSWs (e.g., 2004, 2006, 2009) the Arctic polar vortex broke down and the formation of polar stratospheric clouds and subsequent ozone depletion was suppressed. In contrast in the winters of 2004-2005 and 2010-2011, there was weak planetary-wave activity, the Arctic vortex remained robust, polar stratospheric clouds were widespread, and there was significant ozone depletion (Rex et al., 2006; Manney et al., 2011). The evolution of the stratosphere and mesosphere during these disturbed winters is not only determined by the planetary-wave activity. Smaller-scale gravity waves also determine the structure of the stratosphere. High stratopause temperatures during the polar winter have been recognized as a gravity wave-driven climatological feature since the late 1980s (Hitchman et al., 1989). Thus the wintertime Arctic middle atmosphere serves as a natural laboratory for understanding wave-mean flow interactions.

Here we present recent observational and model studies that we have conducted to investigate the contribution of waves in the middle atmosphere. We highlight the variations in wave activity and its contribution to the wintertime circulation. We introduce a new study that addresses questions raised by the work to date.

2. Observations of the Circulation and Wave Activity in Recent Arctic Winters

We conducted Rayleigh ongoing lidar measurements at Chatanika, Alaska (65°N, 147°W) that

yielded measurements of the nightly temperature profile over the 40-80 km altitude region and the relative density fluctuations at 15 min resolution over the 40-50 km altitude region. In the three winters of 2002-2003, 2003-2004, 2004-2005 Thurairajah and colleagues calculated the potential energy density of the gravity wave fluctuations (with periods of 30 min to 4 h) to characterize the gravity wave activity (Thurairajah et al., 2010a).. Thurairajah and colleagues found that in each of the three winters, the gravity wave activity and temperature structure of the stratosphere and mesosphere were consistent. In 2004– 2005, when no stratospheric warming events occurred, the gravity wave activity was highest (5.7 J/kg) and the stratopause temperatures were higher than expected. In 2002–2003, when there were several stratospheric warming events, the gravity wave activity was lower (2.1 J/kg) and the stratopause temperatures were also lower than expected. In 2003–2004, when one of the most prolonged midwinter stratospheric warming events occurred, the gravity wave activity was lowest (1.1 J/kg) of all three winters, the stratosphere was coldest, and the stratopause was displaced vertically to ~70 km. These lidar observations provide direct evidence of the suppression of gravity wave activity during an elevated stratopause event. Thurairajah and colleagues found that the day-to-day gravity wave activity was positively correlated with the weakest winds in the lower stratosphere. This finding was consistent with both the work of Wilson et al. (1991) who found positive correlation between wave activity and stratospheric winds, and the work of Dunkerton and Butchart (1984) who showed that weak winds associated with the Aleutian anticyclone would block the upward propagation of orographic gravity waves.

We extended the Chatanika-based Rayleigh lidar study during the International Polar Year (IPY) to include observations at Kangarlussuaq, Greenland (67°N, 51°W) and Kühlungsborn, Germany (54°N, 147°E). Lidar observations were conducted during the winters of 2007-2008 and 2008-2009. Major stratospheric warmings with displacement of the vortex and splitting of the vortex occurred in 2007-2008 and 2008-2009, respectively. These multi-site observations yielded measurements of the nightly temperature profiles over the 40-80 km altitude region and gravity wave activity (with periods of 1 h to 4 h) in the 40-50 km altitude region (Thurairajah et al., 2010b). The lidar data from each site was processed identically to ensure consistency in the measurements of gravity wave activity. Thurairajah and colleagues had shown that subtle differences in the data manipulation yielded factors of 1.7 in the reported potential energy densities (Thurairajah et al., 2010a). During January and February 2008, they found a lower average potential energy density (1.6 J/kg) at Chatanika than at Kühlungsborn (2.6 J/kg) and Kangerlussuaq (4.7 J/kg). They attributed this lower wave activity at Chatanika to the blocking of gravity waves by the lower winds in the Aleutian anticyclone, while the higher value at Kangerlussuaq (where the winds are similar in strength to those at Kühlungsborn) reflected stronger sources of gravity waves. During February and March 2009, they found similar gravity wave activity at both Chatanika and Kühlungsborn (1.1 J/kg) and attributed the lower average potential energy density to the seasonal decrease of the winds. At Chatanika they found that the 2004 warming had a stronger influence on the gravity wave activity with lower values in January and February 2004 (0.8 J/kg) than in 2008 (1.6 J/kg) and 2009 (1.9 J/kg).

3. Model Study of the Arctic Wintertime Circulation

Initially Thurairajah and colleagues (Thurairajah et al., 2010a) had interpreted their observations in terms of the study of Siskind and colleagues (Siskind et al., 2007). Their interpretation was that the reversal of the horizontal winds blocked orographic gravity waves from propagating into the middle atmosphere and breaking, thus allowing the atmosphere to relax to a radiative equilibrium. To better understand the role of the gravity wave in influencing the mean

flow during stratospheric warming and elevated stratopause events we employed the Whole Atmosphere Community Climate Model (WACCM). Chandran and colleagues found that SSW followed by an elevated stratopause is a climatologically robust phenomenon in free-running WACCM (Chandran et al., 2011). The simulations closely resembles recently observed events in the Arctic. Chandran and colleagues initially compared dynamically undisturbed and disturbed years using two model winters. Chandran and colleagues further analyzed elevated stratopause events in four WACCM simulations of the 1953-2005 period (Chandran et al., 2012). They characterized planetary wave forcing by calculating the Eliassen-Palm flux divergence of the resolved waves and the zonal mean gravity wave forcing by calculating the unresolved forcing in the model. They found that intense planetary wave activity during an SSW drives the reversal of the zonal mean wind in the stratosphere. This reversal alters the penetration of eastward propagating, non-orographic gravity waves into the mesosphere. They found 68 elevated stratopause events in 212 winters. The composites of winters with elevated stratopauses (68 winters) and major SSWs (54 winters) show the reversal of the circulation persists for about a week longer for elevated stratopause events than for major SSW events. Chandran and colleagues distinguished the role of planetary waves and gravity waves in the mesosphere-lower thermosphere (MLT, ~80-100 km). While significant planetary wave forcing is found in the mesopause region during ~90% of elevated stratopause events, significant gravity wave forcing is found in the MLT region during all elevated stratopause events. Thus the simulations indicate that the formation of an elevated stratopause is due primarily to the adiabatic heating from non-orographic gravity wave driven downwelling following the reestablishment of the westerly stratospheric jet.

4. Conclusions and Further Work

Our lidar observations have shown significant interannual variability in the wintertime gravity wave activity in the lower mesosphere (40-50 km). This variability is driven by systematic changes in the mean winds associated with SSWs. Consistent analysis of lidar measurements from multiple sites shows that while the levels of gravity wave activity are modulated by lower stratospheric winds, the magnitude of the wave activity at different sites also reflects differences in wave sources. Persistently lower wave activity is found over Alaska during the presence of the low winds associated with the Aleutian anticyclone. While for given wind conditions, higher wave activity is found over Greenland than over Germany and Alaska. However, understanding of the modulation of gravity wave activity is limited by the number of years where gravity wave observations have been made at each site with significantly disturbed dynamic conditions. The wind reversals associated with the SSWs in February 2008 were not as strong or long-lived as those in February 2009. The wind reversals in February 2009 were not as strong or long-lived as those in January-February 2004 when the gravity wave activity was most suppressed. We are currently coordinating observations at Andoya (69°N, 16°E), Chatanika, Kangarlussuaq, and Kühlungsborn to extend our set of observations over the winters of 2011-2012, 2012-2013, 2013-2014. There was a significant minor SSW in 2011-2012. Initial analysis of the gravity wave measurements shows a relatively low level of the gravity wave activity at Chatanika. Furthermore the capabilities of the Rayleigh lidar at Chatanika have been extended by incorporating a larger telescope and more powerful laser (Irving 2012). These extensions of the lidar system will allow measurements of gravity waves at higher resolution and enable investigation of higher frequency gravity waves. Furthermore, the extension will allow measurements over a larger altitude range and thus enable investigation of the vertical propagation and evolution of the waves.

WACCM has revealed the role of planetary waves and non-orographic gravity waves in the formation of SSWs and the elevated stratopause. Recent simulations by Tan et al. (2011) have shown that the inclusion of a spectrum of lower frequency gravity waves in WACCM results in wave forcing of the stratosphere that resolves outstanding discrepancies in model simulations of the Antarctic wintertime circulation (where the stratospheric vortex is colder and more robust than observed and the mesosphere is warmer than observed). We will conduct further analysis of the role of these waves in WACCM to determine the significance of these waves in the circulation.

5. Acknowledgements

The authors acknowledge support from the United States National Science Foundation (under grants ARC 0632387, ARC 1107498), the Mecklenburg- Vorpommern Ministry of Education, Science and Culture and the German Federal Ministry of Education and Research (as part of the Leibniz School for Gravity Waves and Turbulence in the Atmosphere and Ocean).

6. References

- Chandran, A., et al., 2011: A case study of an elevated stratopause generated in the Whole Atmosphere Community Climate Model, *Geophys. Res. Lett.*, 38, L08804, doi:10.1029/2010GL046566.
- Chandran, A., et al., 2012: A Climatology of Elevated Stratopause Events in the Whole Atmosphere Community Climate Model, *J. Geophys. Res.*, submitted.
- Dunkerton, T. J., and N. Butchart, 1984: Propagation and selective transmission in internal gravity waves in a sudden warming, *J. Atmos. Sci.*, 41, 1443-1460.
- Hitchman, M. H., et al., 1989: The separated polar winter stratopause: A gravity wave-driven climatological feature, *J. Atmos. Sci.*, 46, 410-422.
- Irving, B. K., 2012: Rayleigh lidar studies of mesospheric inversion layers at Poker Flat Research Range, Chatanika, Alaska, MS Thesis, University of Alaska Fairbanks, July 2012.
- Manney, G. L., et al., 2005: The remarkable 2003-2004 winter and other recent winters in the Arctic stratosphere since the late 1990s, *J. Geophys. Res.*, 110, D04107, doi:10.1029/2004JD005367.
- Manney, G. L., et al., 2009: Aura Microwave Limb Sounder observations of dynamics and transport during the record-breaking 2009 Arctic stratospheric major warming, *Geophys. Res. Lett.*, 36, L12815, doi:10.1029/2009GL038586.
- Manney, G. L. et al., 2011: Unprecedented Arctic ozone loss in 2011, *Nature*, 478, 469-475., doi:10.1038/nature10556.
- Rex, M., et al., 2006: Arctic winter 2005: Implications for stratospheric ozone loss and climate change, *Geophys. Res. Lett.*, 33, L23808, doi:10.1029/2006GL026731.
- Siskind, D. E., et al., 2007: On recent interannual variability of the Arctic winter mesosphere: Implications for tracer descent, *Geophys. Res. Lett.*, 34, L09806, doi:10.1029/2007GL029293.
- Tan, B et al., 2011: Studying 'cold pole' problem in WACCM and comparisons to lidar temperature morphology, Abstract SA31B-1973, presented at 2011 Fall Meeting, AGU, San Francisco, CA, 5-9 December.

- Thurairajah, B., et al., 2010a: Rayleigh lidar observations of reduced gravity wave activity during the formation of an elevated stratopause in 2004 at Chatanika, Alaska (65°N, 147°W), *J. Geophys. Res.*, 115, D13109, doi:10.1029/2009JD013036.
- Thurairajah, B., et al., 2010b: Gravity Wave Activity in the Arctic Stratosphere and Mesosphere during the 2007-2008 and 2008-2009 Stratospheric Sudden Warming Events, *J. Geophys. Res.*, 115, D00N06, doi:10.1029/2010JD014125.
- Wilson, R. et al.,: 1991: Gravity waves in the middle atmosphere observed by Rayleigh lidar 2. *Climatology, J. Geophys. Res.*, 96, 5169-5183.

Comparison of mesospheric gravity wave momentum fluxes derived by MF Doppler radar and meteor radar measurements at 69°N

Manja Placke¹, Peter Hoffmann¹, Markus Rapp^{1,2}, Werner Singer¹, and Ralph Latteck¹

¹ Leibniz Institute of Atmospheric Physics at the Rostock University, Kühlungsborn, Germany

² Now at Deutsches Zentrum für Luft- und Raumfahrt (DLR), Institut für Physik der Atmosphäre, Oberpfaffenhofen, Germany

1. Introduction

Gravity waves propagate through the whole atmosphere and transport energy and momentum far away from their source regions. With increasing altitude gravity wave amplitudes grow exponentially due to the air density decrease which can lead to wave breaking in the upper mesosphere and lower thermosphere (MLT) region between about 80 and 100 km. Thereby the waves impose their momentum onto the mean flow and induce a force which may even cause a wind reversal at mesospheric heights. Thus gravity waves have a significant influence on global atmospheric circulation patterns and the momentum flux is an essential parameter to study the dynamics of the middle atmosphere.

The present study shows a comparison of gravity wave momentum fluxes derived from different radar instruments and analysis methods: With the Saura MF radar on Andøya (69°N, 16°E) narrow beam wind measurements can be performed in the upper mesosphere between about 60 and 100 km. Gravity wave momentum fluxes can be determined from radial velocity variations of coplanar beams when running the radar in the Doppler Beam Steering (DBS) mode by using the method from *Vincent and Reid* (1983). With the co-located Andenes all-sky interferometric (SKiYMET) meteor radar winds are measured from reflections at ionization trails of ablating meteoroids from about 80 to 100 km height. A simultaneous determination of momentum fluxes and also wind variances is possible by applying a regression method proposed by Hocking (2005). The annual variations of the horizontal winds and momentum fluxes of these two independent instruments will be investigated giving insight into the coupling processes between gravity waves and the background circulation.

2. Observation and data analysis

In this study two different radar instruments are taken into account using different methods for momentum flux determination. On the one hand the narrow-beam Saura MF radar is used operating on a frequency of 3.17 MHz. It uses a Mills-Cross antenna consisting of 29 crossed dipoles. The arm length of the antenna array is about 1 km long which makes this radar a very extensive, complex, costly, but also world-wide unique radar system (*Singer et al.*, 2008). Atmospheric dynamics such as radial winds, winds, momentum fluxes, internal gravity waves, tides, and planetary waves can be determined in the upper mesosphere from about 60 to 100 km height by successive transmission of two coplanar tilted radar beams in different spatial directions (Doppler Beam Steering (DBS) mode). On the other hand the Andenes all-sky interferometric (SKiYMET) meteor radar (32.55 MHz operation frequency) is used which consists of one crossed 3-elements Yagi antenna for an almost all-sky transmission and five crossed 2-elements Yagi antennas for signal reception. The receiver antennas are arranged as an interferometer with a maximum distance of only about 41 m between each other. Thus in contrast to the MF radar the

meteor radar is relatively simple and cost-efficient and is a world-wide distributed radar making comparisons between atmospheric properties of different parts of the world possible. By an interferometric analysis of the radar echoes which are reflected at wind-drifted meteor ionization trails of ablating meteoroids the radial wind velocities and hence the mesospheric wind field as well as gravity wave activity and momentum fluxes can be determined between about 80 and 100 km.

To determine gravity wave momentum fluxes for the MF radar the dual-beam method after *Vincent and Reid (1983)* has been applied using the determined radial velocities in zonal direction (West and East) and meridional direction (North and South) from the coplanar tilted radar beams. From the radial velocity variations the vertical flux of zonal and meridional momentum are then calculated. Meteor radar momentum fluxes can be determined by applying the regression method from *Hocking (2005)* which is a generalization of the dual-beam method. Covering almost the whole sky the meteor radar measures radial velocities from many meteor positions and thus makes a statistical momentum flux determination possible. Therefore a minimizing problem is solved under the assumption that gravity waves cause wind fluctuations which are visible in radial wind deviations from the mean when a homogeneous (horizontal) background wind field is assumed. This method allows a simultaneous calculation of atmospheric wind variances and momentum fluxes.

For a reliable momentum flux investigation different outlier rejections are applied to both radar instruments and analysis methods, respectively. The measured radial velocities of the MF radar are selected after the following successively applied outlier criteria: only measurements with a signal-to-noise ratio greater than five are taken into account, radial velocities greater than 15 m/s (corresponding to a horizontal wind speed of greater than about 125 m/s) are neglected, individual radial wind values are neglected which exceed the three-times standard deviation within a 6-h time interval, and in a last check only those radial wind values of opposite radar beams are taken into account which have opposite signs or where one value or both values lie close to zero irrespective of their signs. The influence of the individual criteria has been proven before for a case study (not shown here). For the meteor radar only meteors with unambiguously determined positions are investigated, the minimum needed number of meteors per 3 km evaluation height gate and 2 h evaluation time interval is 30, only meteor observations between 10° and 50° zenith angle are regarded, the maximum distance between radar and meteor is limited to 400 km and the radial drift velocity is limited between ± 200 m/s. Under these selection criteria the calculation of momentum fluxes leads to reasonable results which will be discussed in the following.

3. Results

The understanding of the coupling processes between gravity waves and the background circulation is a very important topic. In this study the annual variation of horizontal momentum fluxes and winds has been investigated for the year 2011. The time resolution of the MF radar (radial) wind analysis is 4 min. Meteor radar momentum fluxes base on 2 h calculations. For both radar systems winds and momentum fluxes have been calculated as averages over 20 days and are determined for every 10 days. The covered vertical ranges extend from 70 – 100 km for the MF radar with a resolution of 1 km and 80.5 – 98.5 km for the meteor radar with 3 km vertical resolution, respectively.

The results for the MF radar are displayed in Figure 1. The zonal wind shows the typical known mesospheric structure with eastward blowing winds in winter and westward blowing winds

in summer up to about 90 km height. Above there exists a weakly pronounced semiannual wind variation with small maxima in summer and winter and minima in spring and – even if short – in fall (at the end of September). From early summer to beginning of fall the wind reverses in sign beginning in mesopause heights and shifting downward into the mesosphere during summer. The vertical flux of zonal momentum shows small values around zero up to about 85 km throughout the year and increases in mesopause heights, i.e., at heights where in general gravity waves break due to their amplitude growth with height and impose their momentum onto the background. From wave theory it is widely known that gravity waves can only propagate upward in the atmosphere when they move against the background wind. This can on the one hand be seen in the summer mesopause where the summer wind minimum (maximum westward (negative) wind) around 80 km height corresponds approximately to a weak (positive) maximum in the summer zonal momentum flux. On the other hand it is obvious that around the breaking height of the waves above about 85 km the momentum flux changes in sign during summer and the zonal wind reversal appears at almost exactly the same height and time, but with the sign change in opposite direction to the momentum flux. Furthermore the mesopause momentum flux shows also a (stronger pronounced) semiannual variation opposite to that of the zonal wind with the minima in summer and winter and maxima around the equinoxes. These observations confirm the theory for gravity wave propagation related to the background wind field and show the direct coupling between waves and winds.

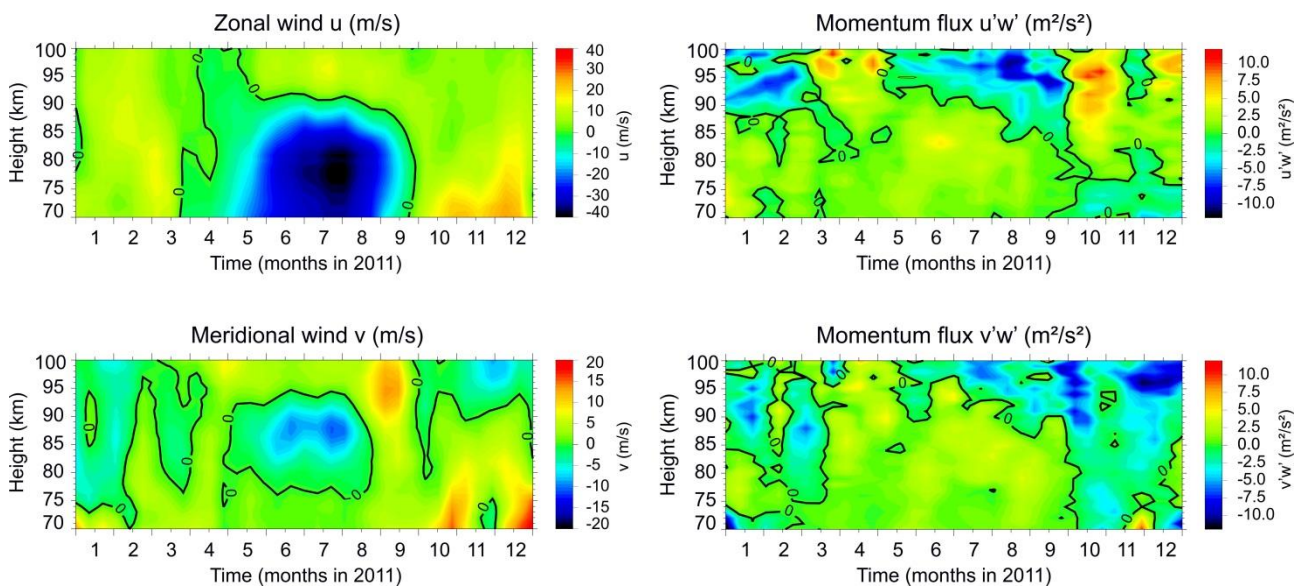


Figure 1: MF radar height-time cross-sections of zonal (left top) and meridional (left bottom) wind and vertical flux of zonal (right top) and meridional (right bottom) momentum for the year 2011.

The meridional wind has a pronounced minimum (maximum southward (negative) wind) in the summer months between about 80 and 90 km whereas in the rest of the year a more indifferent structure dominates. Again a direct comparison of the wind and the momentum flux in meridional direction shows that gravity waves only propagate upwards when they move against the background wind. For instance during summer positive momentum flux values correspond to the mentioned negative wind values and at the beginning and the end of the year there occur opposite signs in wind and momentum flux in general especially below 90 km. In the upper regions the vertical flux of meridional momentum increases due to gravity wave breaking, but reaches not

such high values as the zonal momentum flux. Furthermore the agreement between wind and momentum flux is in these heights not as good as for the zonal components.

Figure 2 shows the corresponding results for the meteor radar. Note that the height range is just a section of the one from the MF radar. Extremes of the wind and momentum flux values in the lower and uppermost height gates (82 and 97 km) should not be regarded as they appear due to small meteor count rates and hence statistically less reliable calculations as discussed, e.g., in *Placke et al. (2011)*. The data at the beginning of 2011 (January, February, March) cannot be regarded as well because of gaps in the measurements during that period which allow no acceptable calculations. In general, especially the zonal wind and zonal momentum flux have very similar patterns as the results discussed before from the MF radar. The summer zonal wind reversal appears at almost identical time and height as seen for the MF radar and is analogous to the change in zonal momentum flux sign. The latter appears just a few kilometers higher for the meteor radar than for the MF radar. Also the meridional wind pattern shows a general good agreement to that from the MF radar, but with a noticeable overestimation of the summer minimum. The biggest differences for both radar instruments are visible in the meridional momentum flux. Here the correlation is poor, but a general tendency to positive values in summer below about 90 km and a change to more negative values at the end of the year can be seen.

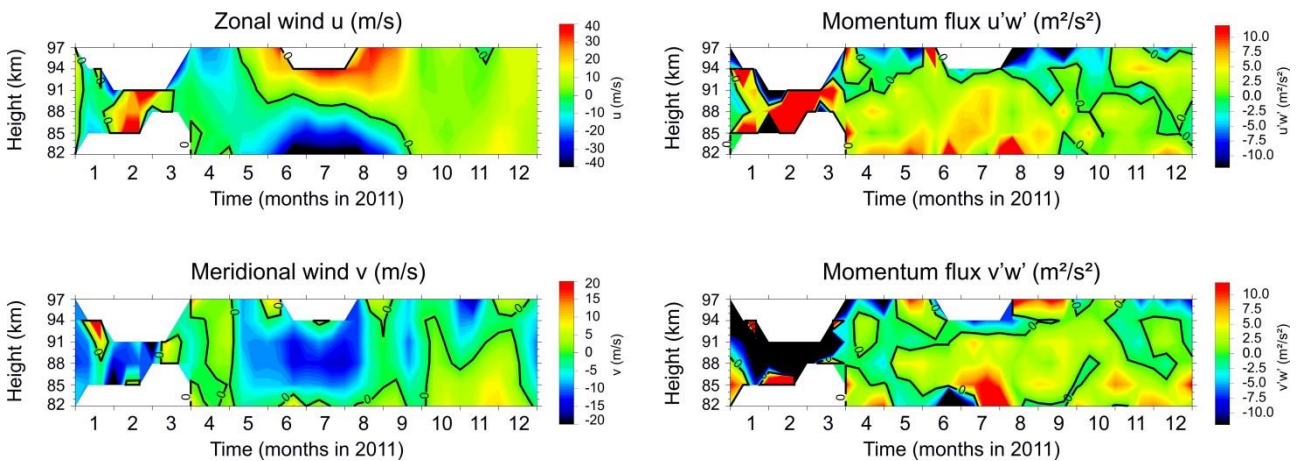


Figure 2: Meteor radar height-time cross-sections of zonal (left top) and meridional (left bottom) wind and vertical flux of zonal (right top) and meridional (right bottom) momentum for the year 2011.

4. Conclusions

An analysis of mesospheric winds and momentum fluxes has been carried out with a narrow beam and an all-sky radar instrument. Different applied methods and selection criteria lead to similar structures in the annual cycles of 2011. The zonal results agree for both instruments very good whereas for the meridional components bigger discrepancies occur. Furthermore the coupling processes between gravity waves and the background circulation can very clearly be seen in the zonal components. The coupling between the meridional components is not as obvious as for the zonal ones, but is observable nevertheless.

References:

- Hocking, W.K., A new approach to momentum flux determinations using SKiYMET meteor radars. *Ann. Geophysicae*, 23, 2433-2439, 2005.
- Placke, M., G. Stober, Ch. Jacobi, Gravity wave momentum fluxes in the MLT – Part I: Seasonal variation at Collm (51.3°N, 13.0°E), *J. Atmos. Solar-Terr. Phys.*, 73, 904-910, 2011.
- Singer, W., R. Latteck, D. Holdsworth, A new narrow beam Doppler Radar at 3 MHz for studies of the high-latitude middle atmosphere. *Adv. Space Res.*, 41, 1487-1493, 2008.
- Vincent, R.A., and I.M. Reid, HF Doppler measurements of mesospheric gravity wave momentum fluxes. *J. Atmos. Sciences*, 40, 1321-1333, 1983.

Main Characteristics of Polar Mesosphere Summer Echoes Observed with the MST Radar ESRAD, Kiruna, Sweden During 1997- 2011

E. Belova¹, M. Smirnova¹, S. Kirkwood¹

¹Swedish Institute of Space Physics, Kiruna, Sweden

1. Introduction

Since the 1980s it has been known that extremely strong radar echoes can be detected from altitudes of 80-90 km, in high latitude regions, during summer. These echoes were termed as Polar Mesosphere Summer Echoes (PMSE) and they are closely related to the visible phenomenon noctilucent clouds (NLCs). While NLCs indicate the presence of ice particles with sizes of several tens of nm (Hervig et al, 2009) formed at extremely low summer mesopause temperatures (~130 K), PMSE occur due to scattering from fluctuations in electron density caused by a combination of electrically charged ice particles, including those of smaller sizes, and atmospheric turbulence. Since NLCs are sensitive to temperature and water vapour concentration, it has been proposed that they might serve as an indicator of long-term climate change (Thomas and Olivero, 2001). PMSE observations by the radar have several advantages: they are continuous, round-the-clock and weather/observer independent, and are attractive for derivation of possible trends.

In this paper we evaluate long-term variations and trend in PMSE strength expressed in terms of volume reflectivity as well as PMSE aspect sensitivity using ESRAD data from 1997-2011. This is a 2 year extension of our previously published results covering 1997-2009 (Smirnova et al., 2011; Smirnova et al., 2012).

2. Observations

Since 1997 measurements of PMSE have been carried out with the 52 MHz ESRAD MST radar located near Kiruna in Northern Sweden (see Table 1 for the ESRAD main parameters). Importantly, these measurements have been made using the same experimental settings. In this paper we use the ESRAD data from 'fca_4500' experiment (8-bit complementary code, 600 m resolution, 25/98 ms data sampling time) for PMSE reflectivity calculations and 'fca_150' experiment (no coding, 150 m resolution, 55 ms data sampling time) for aspect sensitivity study.

Geographic coord./ Height	67.9° N 21.1° E; 295m
Geomag. latitude / Geomag. midnigh	64.82° N ; 22:50 LT
Peak power	72 kW
Max. duty cycle	5%
No. of receivers	6
Array effective area	3740 m ² (1870 m ² before 2004)
e ⁻¹ half-beam-width	2.65° (3.98° before 2004)
Galactic noise daily variation	1680-4500 K

Table 1: The main parameters of the ESRAD radar.

3. Calibration

Radar volume reflectivity η can be calculated according to the formula (e.g. Gage, 1990):

$$h = \frac{P_r}{P_t} \frac{64(2 \ln 2) r^2}{\rho L A_e V_f \Delta r}$$

where P_t is power delivered to the radar, P_r is power received by the radar, r is the distance to the scattering volume, Δr is the range resolution along the radar beam, L is the antenna feed loss, V_f is the fraction of the scattering volume which is filled with scatterers ($V_f=1$ was assumed) and A_e is the effective area of the receiving antenna. ESRAD has been calibrated against radiosondes as described by Smirnova et al. (2011) which allows us to calculate PMSE volume reflectivity corrected for changes in transmitter output and antenna feed losses from year to year (Fig. 1).

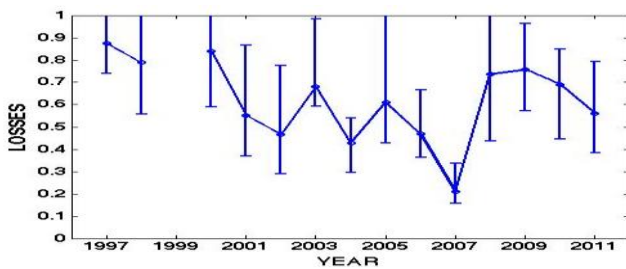


Figure 1: Variations of the effective losses in the antenna feed together with their quartiles for 1997-2011.

4. PMSE long-term variations and trend

We calculated annually means of PMSE volume reflectivities for 1997-2011 by averaging 1-hour data for the time interval from 1 June to 31 July each year and correcting them for the antenna losses. For the PMSE detection we applied a threshold of 10^{-15} m^{-1} . The results together with variations of solar UV radiation in Lyman α band and daily mean geomagnetic K -index averaged over the same time interval are presented in Fig. 2.

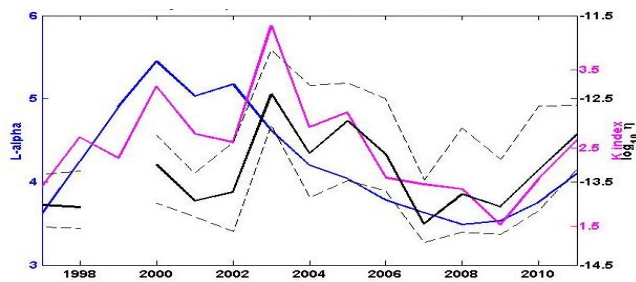


Figure 2: Year-to-year variations of \log_{10} PMSE volume reflectivities (black solid line) together with their quartiles (grey dashed lines), K -index (magenta line) and solar Lyman α (blue line).

PMSE are determined by both neutral and ionized parts of the mesosphere. Therefore, in order to assess any secular trend associated with neutral atmosphere alone, one needs to eliminate any variations related to solar and geomagnetic activity. To accomplish this we have calculated the multi-parameter linear regression of the PMSE annual volume reflectivity VR as follows:

$$VR = A_0 + A_1 \times (\text{year} - 1997) + A_2 \times (\text{Lyman}_\alpha - \text{Lyman}_\alpha_{\text{mean}}) + A_3 \times (K - K_{\text{mean}}),$$

where Lyman_α and K are mean values of Lyman α radiation and geomagnetic K-index for June-July each year, respectively; Lyman_α_{mean} and K_{mean} are their mean values for 1997-2011. The results of the regression for each 3-hour interval and for 24 hours are presented in Table 2.

Interval UT (h)	Trend × 10 ⁻¹⁴	Lyman α × 10 ⁻¹⁴	K-index × 10 ⁻¹⁴	P	R ²
00 - 03	-	-7±2	10±2	3×10 ⁻⁴	0.77
03 - 06	-	-10±4	20±4	1×10 ⁻⁴	0.80
06 - 09	0.2±0.06	-2±0.5	6±0.5	8×10 ⁻⁶	0.92
09 - 12	0.3±0.08	-	5±0.8	1×10 ⁻⁴	0.81
12 - 15	0.5±0.1	-	4±1	3×10 ⁻³	0.66
15 - 18	0.2±0.08	-	2±0.6	2×10 ⁻²	0.54
18 - 21	-	-	0.8±0.3	1×10 ⁻²	0.43
21 - 24	0.3±0.1	-	4±0.8	2×10 ⁻³	0.68
00 - 24	-	-10±2	18±2	4×10 ⁻⁵	0.84

Table 2: The coefficients of multi-parameter regression for year-to-year variation of PMSE VR together with their 95% confidence intervals. *P* is the probability that all coefficients are zero for the final fit and *R*² is the determination coefficient, which determines the proportion of VR year-to-year variability explained by variations of all predictors.

PMSE VR shows positive trend of $(2-5) \times 10^{-14} \text{ m}^{-1}$ per decade for some time intervals, but not when averaged over the whole day.

5. PMSE aspect sensitivity

Echo aspect sensitivity describes how scattered power varies with incidence angle and can be characterized by the width of the angular polar diagram of the scatterers. Larger widths are associated with more isotropic scatter and a narrow scattering polar diagram is a signature of quasi-specular scatter. We have used the full correlation analysis based on the spaced antenna technique for calculation of PMSE aspect sensitivity as described by e.g. Holdsworth (1995). The histograms for the width of the scatterers' polar diagram for PMSE in June-July for 2011-1997 are shown in Fig. 3. Yearly median values were found to be 2.9-3.7° and the proportion of the echoes with the aspect angle less than 10° is 50-52% of all detected PMSE. Fig. 4 presents the distributions of PMSE aspect (sensitivity) angles averaged over 1997-2011 at different altitudes. PMSE aspect angle increases with increase of altitude.

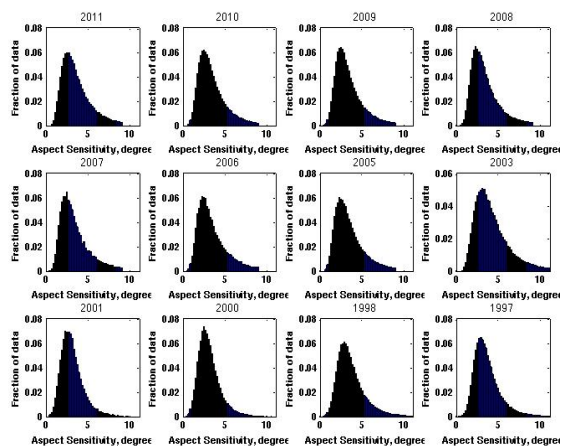


Figure 3: The distributions of the widths of the scatterers' polar diagram for PMSE.

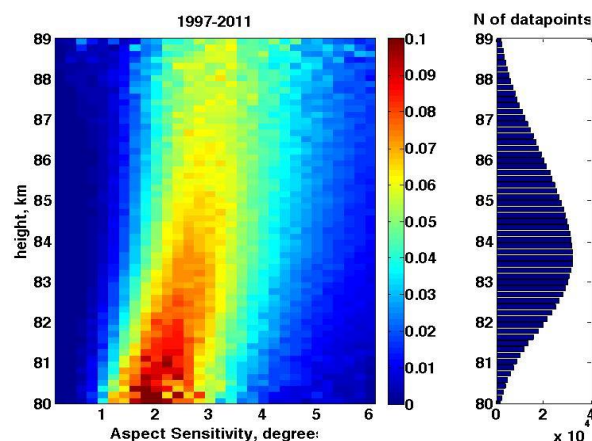


Figure 4: The distributions of the widths of the scatterers' polar diagram for PMSE averaged over 1997-2011 for each 150-m altitude interval (left panel) and number of data points at each altitude.

6. Summary

PMSE have been studied on the basis of ESRAD MST radar observations in 1997-2011. We found that:

- Over 80% of year-to-year PMSE VR variability (daily averaged) can be explained by corresponding variations in Lyman α and geomagnetic activity.
- VR correlates negatively with Lyman α and positively with geomagnetic K-index.
- Correlation of VR averaged over PMSE season and geomagnetic activity is perhaps due to long-lived changes in mesospheric chemistry caused by variations in geomagnetic activity. Probably, ionospheric electric field contributes to this correlation (to be further studied).
- Lyman α statistically significantly contributes to yearly PMSE variability during night and morning hours (01-10 LT). It may be an effect of increase of mesospheric temperature & decrease of water vapour on ice particle formation.
- No trend in yearly mean PMSE VR (daily averaged) for 1997-2011 was identified.
- 50% of all PMSE detected by ESRAD in 1997-2011 are highly aspect sensitive (with median aspect angle = 2.9-3.7°). It results in underestimation of PMSE VR by a factor of 2. These PMSE become more isotropic with increasing altitude and do not show dependence of aspect angle on backscatter power (Smirnova et al, 2012). Further study is needed to make a conclusion what mechanism (specular scatter or scatter from anisotropic turbulence) is responsible for such aspect sensitive PMSE.

References:

Hervig, M.E., Gordley, L.L., Stevens, M., Russell, J.M., Bailey, S., Baumgarten, G.: Interpretation of SOFIE PMC measurements: Cloud identification and derivation of mass density, particle shape, and particle size. *J. Atmos. Sol.-Terr. Phys.* 71, 316–330. doi:10.1016/j.jastp.2008.07.009, 2009.

- Holdsworth, D. A.: Signal analysis with applications to atmospheric radars, Ph.D. thesis, University of Adelaide, 1995.
- Smirnova, M., Belova, E., Kirkwood, S.: Polar mesosphere summer echo strength in relation to solar variability and geomagnetic activity during 1997-2009. *Annales Geophysicae* 29, 563–572, 2011.
- Smirnova, M., Belova, E., Kirkwood, S.: Aspect sensitivity of polar mesosphere summer echoes based on ESRAD MST radar measurements in Kiruna, Sweden in 1997-2010. *Annales Geophysicae* 30, 457–465, 2012.
- Thomas, G. E. and Olivero, J.: Noctilucent clouds as possible indicators of global change in the mesosphere, *Adv. Space Res.*, 28, 937–946, 2001.

Eureka meteor radar temperatures compared with AuraMLS

Chris Meek¹, Alan Manson¹, and Wayne Hocking²

¹ Institute of Space and Atmospheric Studies, University of Saskatchewan, 116 Science Pl., Saskatoon, Canada S7N 5E2.

² Department of Physics and Astronomy, University of Western Ontario, 1151 Richmond St., London, Ontario, Canada N6A 3K7.

Abstract

The Eureka (80°N, 86°W) meteor trail echo decay times, τ , are analysed on site to provide daily temperature near 90Km. In order to get absolute temperature, T , either knowledge of the pressure, or of the background temperature height gradient near 90Km is required (Hocking, 1999). Hocking et al. (2004) have developed an empirical gradient model which is used in situ in the SKiYMET meteor analysis. The gradient is assumed to just depend on latitude and time of year. The sensitivity of the resulting temperature to the assumed gradient is estimated, and the gradient model is compared with that calculated from AuraMLS data. The original SKiYMET daily temperatures and those employing the pressure method (average daily pressures at 90 Km geopotential height, GPH, from AuraMLS, at 79.9°N, within 12.5 degrees longitude of Eureka) are plotted against average AuraMLS, similarly selected, temperatures.

1. Data and analysis

Dependence of temperature on temperature and decay time gradients

The diffusion coefficient, D_a relates Temperature, Pressure, and trail decay time, $\tau_{1/2}$:

$$K_0 \frac{2kT}{q_e} \frac{T}{T_0} \frac{P_0}{P} = C_a \frac{T^2}{P/P_0} = D_a = \lambda^2 \ln 2 / (16\pi^2 \tau_{1/2}) = C_b \frac{1}{\tau_{1/2}} \quad (1)$$

where K_0 is $2.5 \times 10^{-4} m^2 s^{-1} V^{-1}$, k is the Boltzmann constant, q_e electron charge, λ is the radio wavelength, T_0, P_0 are 273°, and 101300 Pa respectively. Substitute for

$$P = P_0 \exp\left\{ \int_0^z -\frac{mg}{kT_z} dz \right\}, \quad (2)$$

take logs for both sides and let

$$S = -d \log_{10} \tau_{1/2} / dz \quad (3)$$

Then

$$T = \frac{\log_{10} e}{S} \left(\frac{mg}{k} + 2 \frac{dT}{dz} \right) \quad (4)$$

To take an original analysed T (°K) and the used gradient (K°/Km) and change the gradient without going back to the meteor decay times (and using $mg/k = 34.09^\circ/Km$):

$$T_{\text{new}} = \frac{T_{\text{orig}}}{\left[34.09 + 2 \frac{dT}{dz} \Big|_{\text{orig}} \right]} \cdot \left[34.09 + 2 \frac{dT}{dz} \Big|_{\text{new}} \right] \quad (5)$$

—————XXXX—————

If the pressure at 90 Km is available *a priori*, e.g. from satellites, equation (1) can be usefully re-arranged as:

$$T = \sqrt{\frac{C_1 P}{\tau_{1/2}}} \quad (6)$$

where

$$C_1 = \frac{q_e}{2k} \cdot \frac{T_0}{P_0} \cdot \frac{\ln 2 \lambda^2}{16\pi^2 K_0} \quad (7)$$

Figure 1: The theory behind the use of temperature gradients and pressures in analyzing meteor data for temperatures.

Figure 1 shows the theory relating temperature pressure and meteor trail decay time, (e.g. Hocking, 1999). This assumes that ambipolar diffusion (ions) is the only dispersing agent, which applies best near 90 Km; other effects may become significant above (e.g. magnetic field, plasma) and below (e.g. atmospheric turbulence). Further potential factors have also been proposed, e.g. capture of free electrons by aerosols, turbulence created by the meteor itself, etc. Note that despite the appearance of T under the integral in equation (2) of Fig. 1, the required derivative is just dependent on the pressure gradient, dP/dz at z , not on the T profile from the ground up.

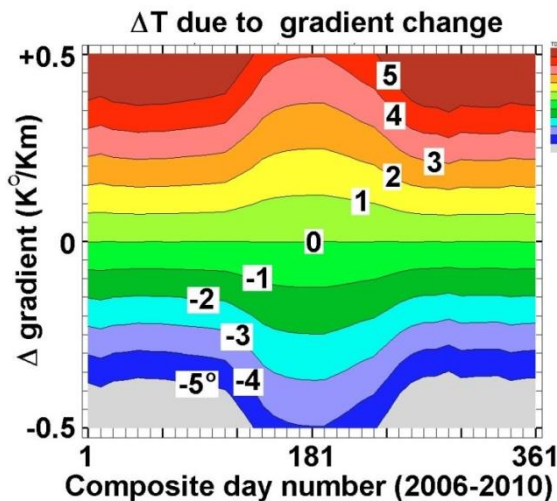


Figure 2: Sensitivity of calculated temperature to small changes in gradients from empirical model.

Figure 2, for which equation (5) of Fig. 1 was applied to real data, shows the sensitivity of calculated temperature to small changes in gradient from the original empirical model at 80°N. It can be seen that temperature (K°) change is ~10 times the gradient change (K°/Km) and in the same sense.

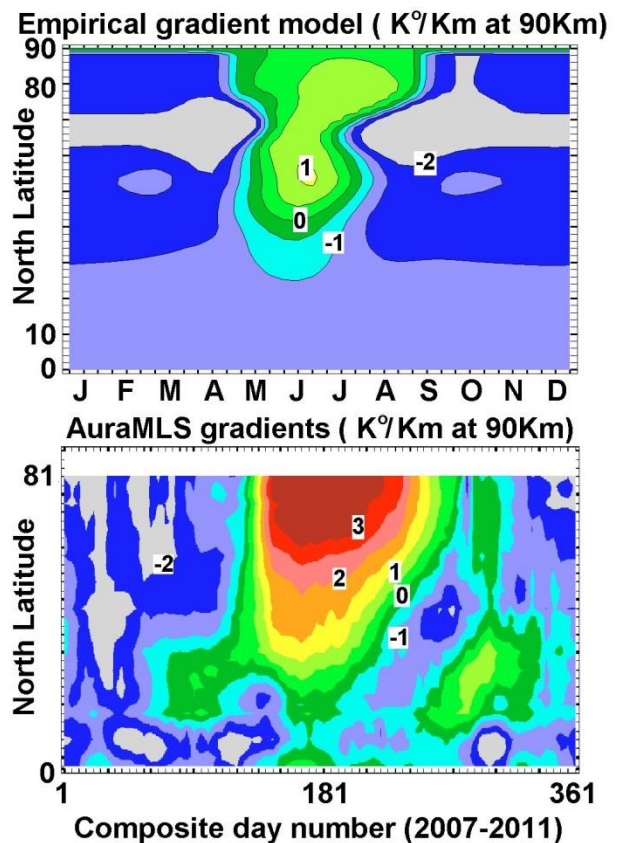


Figure 3: Compare empirical gradient model and AuraMLS multi-year gradients at 80°N.

Fig 3 compares empirical model and average AuraMLS gradients. Here the satellite temperatures and GPH levels were fitted by a second order polynomial to the lowest three GPH levels that included 89Km (~90Km geometric). Quite often, to satisfy the inclusion of 90 Km, a

pressure level beyond the recommended 0.001 mb limit had to be used. Comparison (not shown) of interpolated temperatures at 88 Km (always occurring at $P > 0.001\text{mb}$) and 90 Km displayed no sign of degradation at the latter level.

In winter, the 80°N gradients are small ($\sim -2 \text{ K}^\circ/\text{Km}$) so the choice of gradient is not critical to the absolute temperature. In summer the mesopause near 85 Km has a sharp minimum in temperature. Above this, as the temperature recovers, the gradient is quite variable, and large. AuraMLS mid-summer temperature gradients become greater than $+4 \text{ K}^\circ/\text{Km}$ at 90 Km (GPH, 3 level 2nd order fit) these are very sensitive to height and drop to $+2$ at 89Km (GPH). Another potential problem with the rapid height variations in temperature is that the log 10 τ slope, employing a large range of heights, say 85 – 94 Km,, might be a poor representation of that at 90Km. It may be that the empirical gradient model has at least partially corrected for this possibility.

For the pressure method (e.g. Holdsworth et al., 2004; Dyrlund et al., 2010), each non-ambiguous trail, with decay time $9 \text{ sec} > \tau > 0.015 \text{ sec}$ and within the height interval 89-91 Km, is converted directly to a temperature according to equation (6) of Fig. 1 using interpolated multiyear AuraMLS 5 day log10 pressure averages at 90Km. The average and median T results were quite similar, except for a small consistent offset, so the average was chosen for further use.

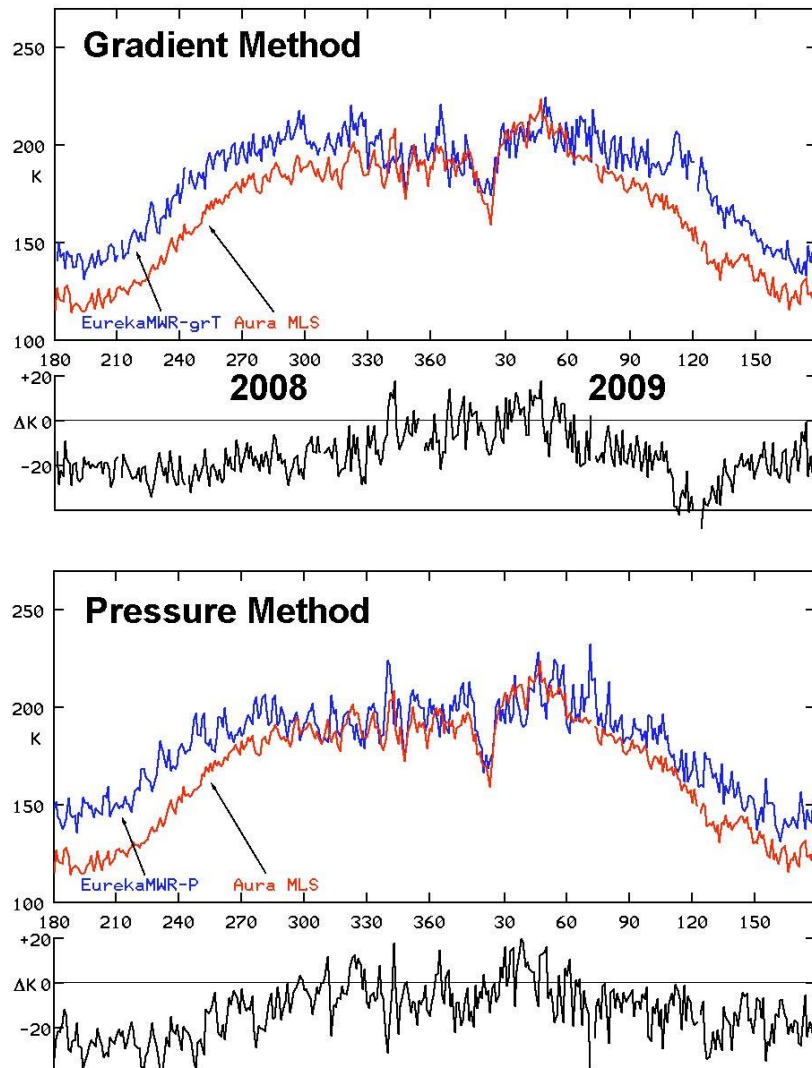


Figure 4: Compare meteor radar gradient and pressure method daily temperatures with AuraMLS data.

Fig 4 compares both meteor methods with AuraMLS 2008/2009 split year. In winter short term fluctuations from both meteor methods agree well with AuraMLS especially during the very major stratwarm (Jan 20 2009), but outside mid-winter there are large discrepancies leading to meteor temperatures about 20° K greater than AuraMLS in mid-summer, a season with higher mesospheric turbulence (e.g. Muellmann et al.,2002). For these data in spring and fall the pressure method matches absolute AuraMLS temperatures somewhat better than the gradient method. This is not always the case (other years, not shown). The year to year variability in agreement might be a result of using a multi-year average pressure for all years.

2. Discussion

The fact that the winter short term variations match quite well for AuraMLS and the two meteor-trail analyses suggests that precise knowledge of daily temperature gradient or pressure is not an important factor in determining these variations. A separate analysis, not shown, which, in conjunction with Fig 1, examined how the use of *calculated* AuraMLS gradients (instead of those from the empirical model), if they were correct, would affect temperature, produced fluctuations of similar magnitude to what we see in winter. That is, their use would destroy the apparent agreement we see. The conclusion we must draw is that the actual gradient variations are quite small; and it is sufficient to use a model for that parameter if we are just interested in short term changes, not absolute temperatures.

References

- Dyrland, M.E., et al., 2010, Improved estimates for neutral air temperature at 90 km and 78°N using satellite and meteor radar data, Radio Science, RS4006, doi:10.1029/2009RS004344
- Hocking W.K. et al. 1999, Temperatures using radar meteor decay times. Geophys. Res. Lett., 26, 3297-3300
- Hocking, W.K., et al. 2004, Meteor radar temperatures at multiple sites derived with SKiYMET radars and compared to OH, rocket, and LIDAR measurements, J. Atmos. Sol-Terr. Phys, 66, 585-593
- Holdsworth D., et al., 2004, Buckland Park all-sky interferometric radar, Radio Science 39, RSS009, doi:10.1029/2003RS00301
- Muellmann, A., et al., 2002, In situ measurements of mesospheric turbulence during spring transition of the Arctic mesosphere, Geophys. Res. Lett., 29, No. 10, 1477, doi:10.1029/2002GL014841

Climatology of the 8-hour solar tide over Central Europe, Collm (51.3°N; 13.0°E)

Ch. Jacobi¹, T. Fytterer¹

¹ Institute for Meteorology, University of Leipzig, Stephanstr. 3, 04103 Leipzig, Germany

1. Introduction

The dynamics of the mesosphere and lower thermosphere (MLT) are strongly influenced by atmospheric waves, including the solar tides. In the past the diurnal tide (DT) and the semidiurnal tide (SDT) have attracted more attention. But recently, also the terdiurnal tide (TDT) has been considered to play an important role as well, because occasionally their amplitudes are as large as the ones of DT and SDT.

Observations of the TDT are relatively rare. Global characteristics at 95 km, derived from Upper Atmosphere Research Satellite/High Resolution Doppler Imager (UARS/HRDI) measurements, have been presented by Smith (2000). The characteristics of the TDT observed by radar have been described on few occasions (e.g. Thayaparan, 1997; Namboothiri et al., 2004; Beldon et al., 2006; Jacobi, 2011).

The forcing mechanism of the TDT is still under debate, and both direct solar heating in the lower and middle atmosphere and nonlinear interaction between the DT and SDT (Teitelbaum et al., 1989) or gravity waves are also thought to excite the TDT. Model analyses gave partly inconclusive results, showing that both direct forcing and nonlinear interaction may play a role in forcing the TDT (Akmaev, 2001; Smith and Ortland, 2001; Du and Ward, 2010).

In this paper some features of the TDT measured at Collm, Germany (51.3°N; 13.0°E) are presented, using the dataset from August 2004 to June 2011. This data represents an update of the one presented by Jacobi (2011).

2. Collm meteor radar wind measurements and tidal analysis

The data used have been measured by VHF meteor radar at Collm Observatory, Germany (51.3°N, 13°E). It is operating since July 2004, and the 7-year dataset from August 2004 – July 2011 is analysed here to investigate the peculiarities of the TDT. Radial winds are observed by the Doppler shift of signals reflected from meteor trails (e.g., Jacobi, 2011). The observed height interval is divided in six not overlapping height gates centred at 82, 85, 88, 91, 94 and 97 km. The amplitudes and phases of the TDT within each height interval in a given 15-day time interval are calculated by a multiple regression analysis of half-hourly zonal or meridional wind components, which includes the mean wind as well as the 8-, 12-, and 24 h oscillations.

3. 7-year mean tidal amplitudes and phases

Figure 1 presents TDT zonal (a) and meridional amplitudes (b), and zonal (c) and meridional phases (d). Note that the scaling of the meridional phase is shifted by 2 hours with respect to the zonal one to more clearly indicate seasons and regions where the TDT components are in quadrature. On an average, zonal and meridional amplitudes are of similar order of magnitude. They both maximise in autumn, while a second maximum is found in spring. Generally, amplitudes tend to increase with altitude during the entire year. An exception is seen in the region below about 90 km in midsummer, where a slight tendency for constant or decreasing amplitudes with

height is visible. Figure 2(e) presents relative amplitude differences, i.e. the difference of zonal and meridional amplitudes divided by their half sum. Throughout the year, on an average the zonal components increase the meridional ones. An exception is observed during the March maximum, where the meridional amplitudes dominate in upper height gates. The differences in summer are insignificant, due to the generally small amplitudes.

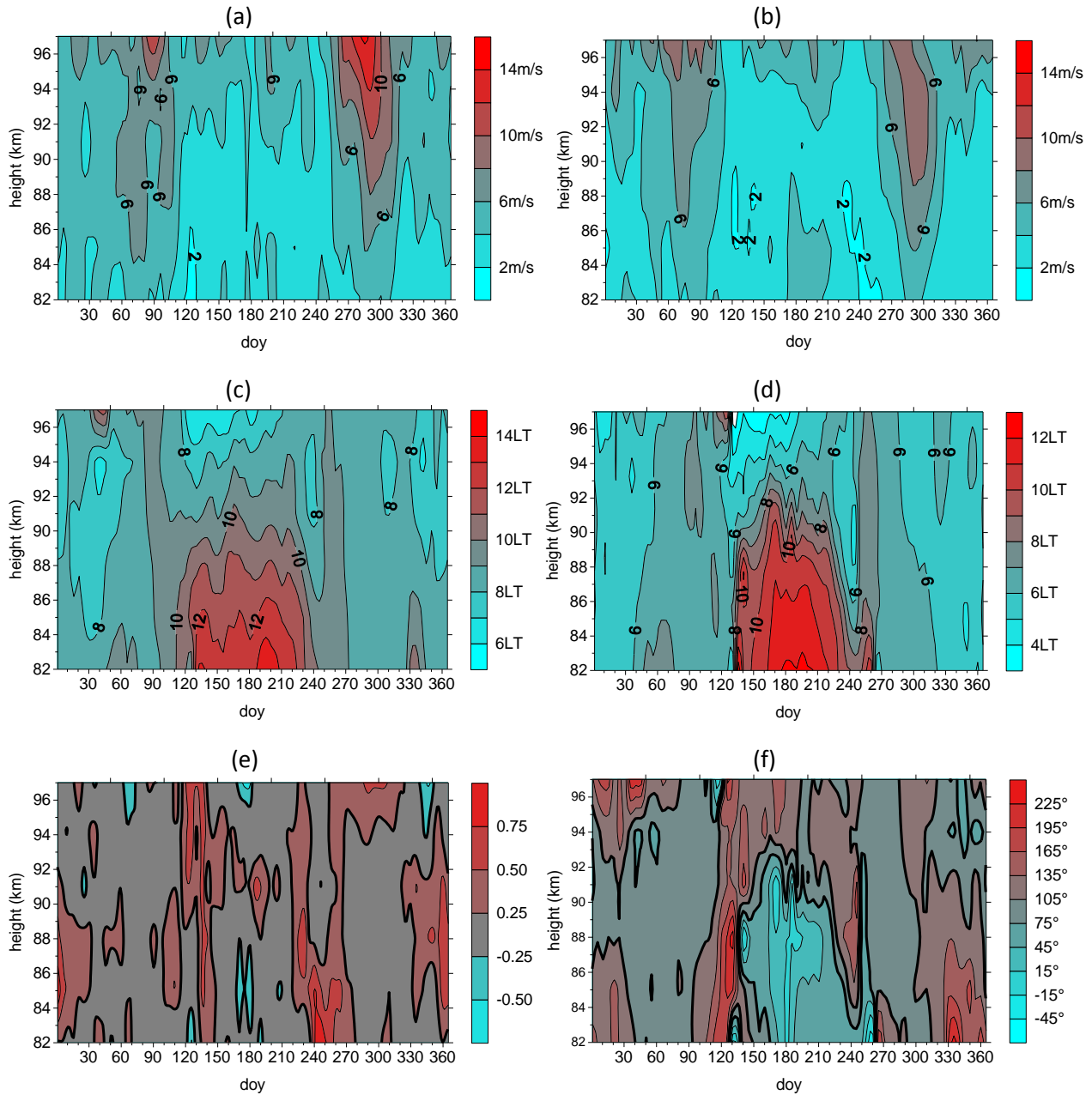


Figure 1: Zonal amplitudes (a) and phases (c), meridional amplitudes (b) and phases (d) of the terdiurnal tide over Collm. Relative amplitude differences are shown in panel (e). Phase differences $\Delta\phi$ in degrees are given in panel (f).

TDT phases take two positions in winter and summer. The phase is nearly constant with height during winter. Therefore the vertical wavelength, calculated from the phase change with altitude, is very long, generally exceeding 200 km. This result is in agreement with the ones by Namboothiri et al. (2004). In summer, there is a strong phase change with height, resulting in wavelengths of about 20 km, even shorter than those reported by Namboothiri et al. (2004) and

Thayaparan (1997). The zonal and meridional phases are close to being in quadrature, at least when the amplitude is strong in autumn and late winter/early spring. During summer, the phase difference shows a sharp change around 90 km, indicating at least two different TDT modes.

4. Interannual variability

Interannual variability of the TDT amplitudes and phases at 91 km is shown in Figure 2. Here the 7-year mean, calculated from individual data each based on 15 days of measurements, is represented as the solid line. The dots show the respective amplitudes (left panel) and phases (right panel) of single years. In most months, the amplitude variability is very strong, and occasionally some amplitudes of less than 1 m/s are found. An exception is observed during the autumn maximum (a multi-year average of ~9 m/s), which has considerably large amplitudes in every year. On the contrary, the spring maximum (~7 m/s on an average) is less stable. Beldon et al. (2006) showed for the case of the U.K. radar, that the spring amplitudes are not larger than the winter ones. The phases generally range within about 3 hours from year to year, but the interannual variability is smaller in March and October, when the amplitudes are larger.

Du and Ward (2010) have used correlation analysis between the TDT and the DT or SDT, respectively, from CMAM model results in order to explain possible coupling processed between tides. They found significant correlation between TDT and SDT amplitudes, which, however, change with height and latitude and show a rather complicated pattern in the MLT near 50°N. In Figure 3 correlation coefficients of monthly mean amplitudes are shown for each month. In April and during autumn there is a generally negative correlation between TDT and SDT amplitudes, while usually the correlation is positive. However, the time series used is too short to draw substantial conclusions, and the correlations are not significant at the 95% level. The same analyse has been performed for a TDT and mean wind dependence (not shown here), but the results are inconclusive.

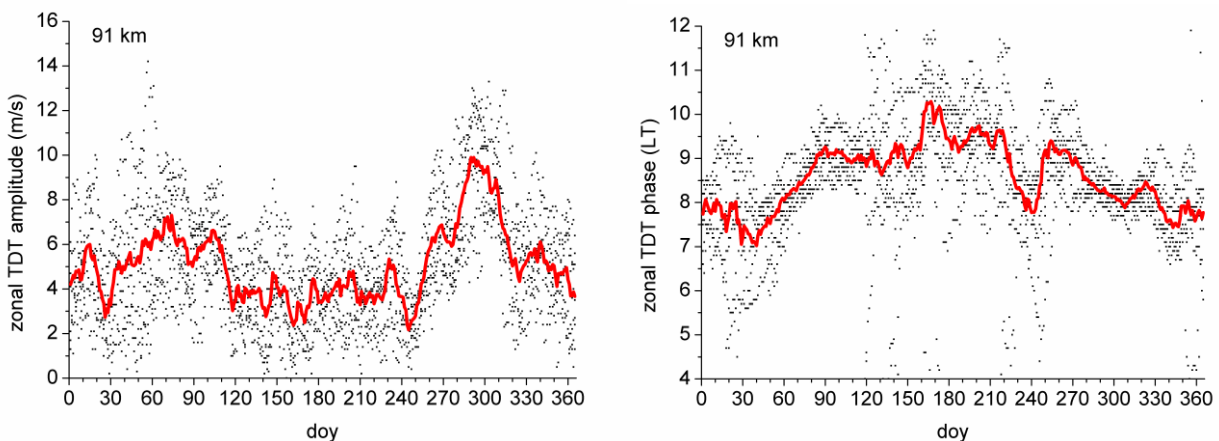


Figure 2: Zonal amplitudes (left panels) and phases (right panels) of the TDT over Collm at 91 km. The solid line denotes the 7-year mean while the dots represent data from individual years.

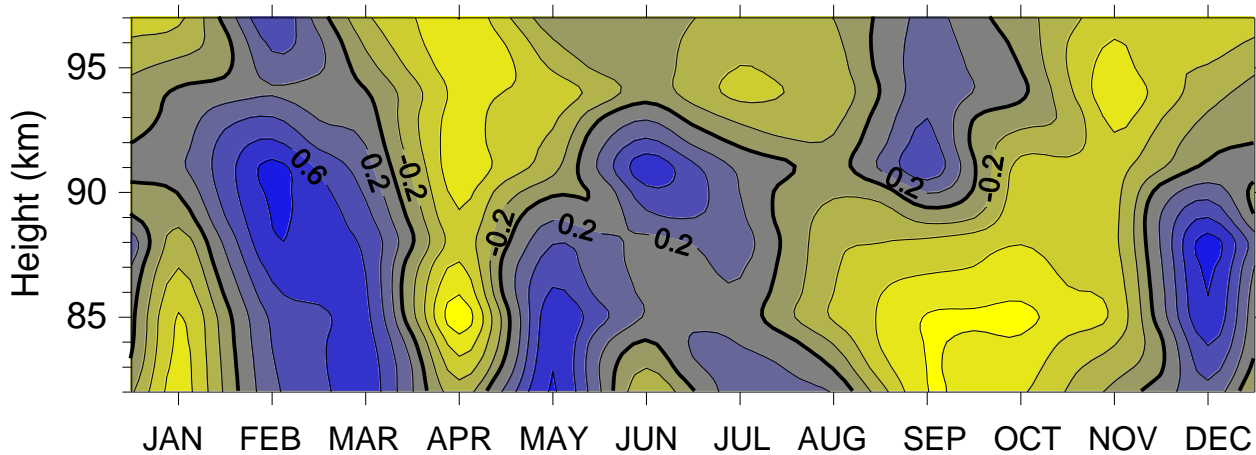


Figure 3: Correlation coefficients of monthly mean TDT and SDT amplitudes.

5. Conclusions

A 7-year climatology of the TDT as observed by the Collm meteor radar is presented. The amplitudes reach largest values in autumn, show a secondary peak in spring, and are small during summer. The autumn maximum is quite stable, while the spring maximum is broader and less stable, so that during some years small amplitudes are found then. Vertical wavelengths are short (~20 km) in summer, but very long in winter.

Interannual variability of amplitudes has been analysed for March and October, when the phases are only weakly varying from year to year. TDT amplitudes are positively correlated with SDT ones in spring, but negatively in autumn. This indicates a possible interaction between TDT and SDT, but the underlying process is not clear and probably different in different seasons.

References

- Akmaev, R.A., 2001: Seasonal variations of the terdiurnal tide in the mesosphere and lower thermosphere: a model study, *Geophys. Res. Lett.*, 28, 3817-3820.
- Beldon, C.L., Muller, H.G., and Mitchell, N.J.: The 8-hour tide in the mesosphere and lower thermosphere over the UK, 1988–2004, *J. Atmos. Sol.-Terr. Phys.*, 68, 655 - 668, 2006.
- Du, J., and Ward, W. E.: Terdiurnal tide in the extended Canadian Middle Atmospheric Model (CMAM), *J. Geophys. Res.*, 115, D24106, doi:10.1029/2010JD014479, 2010.
- Jacobi, Ch.: 6 year mean prevailing winds and tides measured by VHF meteor radar over Collm (51.3°N, 13.0°E), *J. Atmos. Sol.-Terr. Phys.*, doi:10.1016/j.jastp.2011.04.010, 2011.
- Namboothiri, S.P., Kishore, P., Murayama, Y., and Igarashi, K.: MF radar observations of terdiurnal tide in the mesosphere and lower thermosphere at Wakkanai (45.4°N, 141.7° E), Japan, *J. Atmos. Sol.-Terr. Phys.*, 66, 241 – 250, 2004.
- Smith, A.K.: Structure of the terdiurnal tide at 95 km, *Geophys. Res. Lett.*, 27, 177-180, 2000.
- Smith, A.K., and Ortland, D.A.: Modeling and analysis of the structure and generation of the terdiurnal tide, *J. Atmos. Sci.*, 58, 3116-3134, 2001.

Teitelbaum, H., Vial, F., Manson, A.H., Giraldez, R., and Masseur, M.: Non-linear interactions between the diurnal and semidiurnal tides: terdiurnal and diurnal secondary waves, *J. Atmos. Sol.-Terr. Phys.*, 51, 627–634, 1989.

Thayaparan, T.: The terdiurnal tide in the mesosphere and lower thermosphere over London, Canada (43°N, 81°W), *J. Geophys. Res.*, 102, 21695–21708, 1997.

Characteristics of the “Hiccup” in the fall transition

V. Matthias¹, T.G. Shepherd², P. Hoffmann¹, M. Rapp^{1,3}

¹ Leibniz Institute for Atmospheric Physics at the Rostock University, Schlosstr. 6, 18225 Kuehlungsborn, Germany

² University of Reading, Department of Meteorology, Earley Gate, Reading RG6 6BB, UK

³ German Aerospace Center, Institute of Atmospheric Physics, Muenchener Strasse 20, 82234 Oberpfaffenhofen-Wesslingen, Germany

1. Introduction

The equinoxes are expected to reveal rapid changes in the Mesosphere/Lower Thermosphere (MLT) dynamics since the mean flow has to reverse from westward to eastward or vice-versa. But for a long time it has been considered as a smooth transition between summer and winter and vice-versa because of the methods of measurement at that time. During the vernal equinox of 1992 and 1993, G.G. Shepherd et al. (1999) found for the first time a large perturbation of a few days in the oxygen airglow emission rates at mid latitudes. Two years later, Taylor et al. (2001) considered a similar disturbance of the fall transition of 1997 in the mesospheric temperature measurements over Ft. Collins (41°N, 105°W). Liu et al. (2001) assumed that the large local temperature variability is caused by fast changes of phase and amplitude of planetary waves (PWs) due to the interaction of wave transience and the transition of the mean flow.

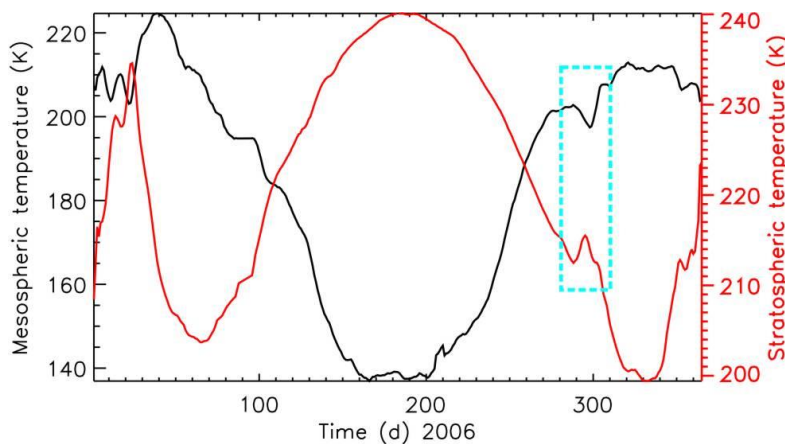


Figure 1: Seasonal variation of zonal mean temperature at 86 km (black) and 32 km (red) at 70°N from MLS for 2006.

Figure 1 shows the seasonal variation of zonal mean temperature at 86km (black) and 32km (red) at polar latitudes of 2006 from the Microwave Limb Sounder (MLS) onboard the Aura satellite. During the fall transition a large perturbation occurs with a warming in the stratosphere and a cooling in the mesosphere (dashed rectangle). This perturbation is called “Hiccup” in the following. Such Hiccups occur in the fall and spring transition but is better observable in the fall since the atmosphere is relatively quiet in the summer compared to the winter months. Therefore we will here concentrate on the autumnal Hiccup. We assume that the Hiccup is induced by the sudden turning on of PW propagation in the stratosphere during the fall transition and can then be communicated up to the MLT region through filtering of gravity wave propagation, as in the case

of SSWs (Holton 1983). Here we analyze the latitudinal and altitudinal expansion as well as the average behavior of this perturbation using model data.

2. Results and discussion

We study the behavior of the Hiccup in the fall transition using the CMAM20 data set. This data set is produced by running the Canadian Middle Atmosphere Model (CMAM, Scinocca et al. 2008) in a nudged configuration where the meteorological fields are nudged towards ERA-Interim in the troposphere and stratosphere, but the mesosphere evolves according to the internal model dynamics, which provides the vertical coupling (Ren et al. 2008). The CMAM20 results are validated by comparing them with temperature data from the MLS instrument (Waters et al. 2006) on board the Aura satellite.

Figure 2a) shows the zonal mean zonal wind from CMAM20 during the fall transition of the year 2006 at 32 km depending on the latitude. Around day 290 the zonal mean zonal wind starts to reverse at polar and a little later also at mid latitudes. Most of the previous analysis (e.g. G.G. Shepherd et al. (1999) and Taylor et al. (2001)) found this effect at mid latitudes due to their locality of their instruments. Only the TIME-GCM model data of Liu et al. (2001) induced also a disturbance at polar latitudes. Since the Hiccup appears stronger at high latitudes we will concentrate on the latitudinal region between 60 – 70°N in the following.

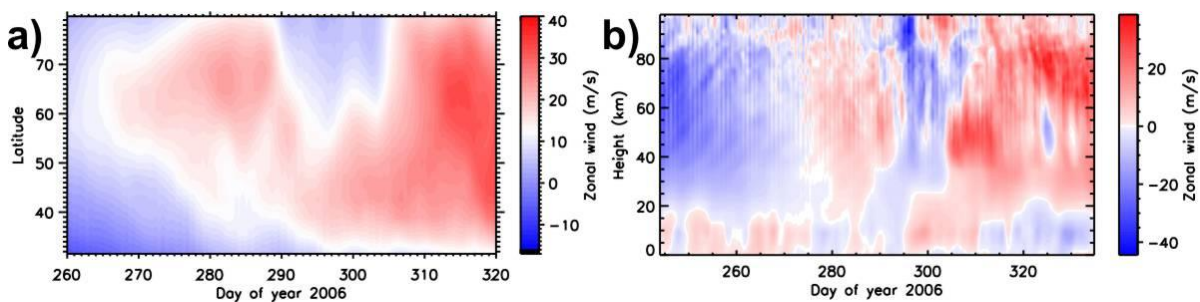


Figure 2: Zonal mean zonal wind from CMAM20 during autumnal equinox a) at 32 km as a function of time and latitude and b) averaged between 60 – 70°N depending on time and altitude.

Figure 2b) shows the altitudinal dependence of the polar zonal mean zonal wind. It seems that the Hiccup starts in the troposphere and propagates almost directly upwards to the mesosphere with a little shift in the upper stratosphere. Taylor et al. (2001) and Liu et al. (2001) for example described this perturbation only as a mesospheric phenomenon.

Similar to a sudden stratospheric warming the Hiccup can be categorized into minor and major. For the superimposed epoch analysis we define the Hiccup onset day as follows: It is the first day where at 10hPa

- i) zonal mean zonal wind is larger than 15m/s,
- ii) $du/dt < 0$ for at least 3 days and
- iii) mean zonal wind increases after Hiccup again.

These criteria are satisfied by 9 perturbations during the fall transitions between 1989 and 2009 and will now be used for the composite analysis.

Figure 3 shows the composite of the anomaly of the zonal mean zonal wind (left) and temperature (right) relative to the Hiccup. The zonal wind increases strongly before the Hiccup in the stratosphere and indicates a vertical wave structure around the Hiccup onset day which is also visible in the temperature anomaly. In the stratosphere the temperature changes seem to lag the wind changes by a few days while in the troposphere the temperature increase right after the Hiccup onset day (dashed line) is simultaneous with the zonal wind decrease. The temperature anomaly shows also an upward propagating wave with time after the Hiccup onset day in the strato- and mesosphere.

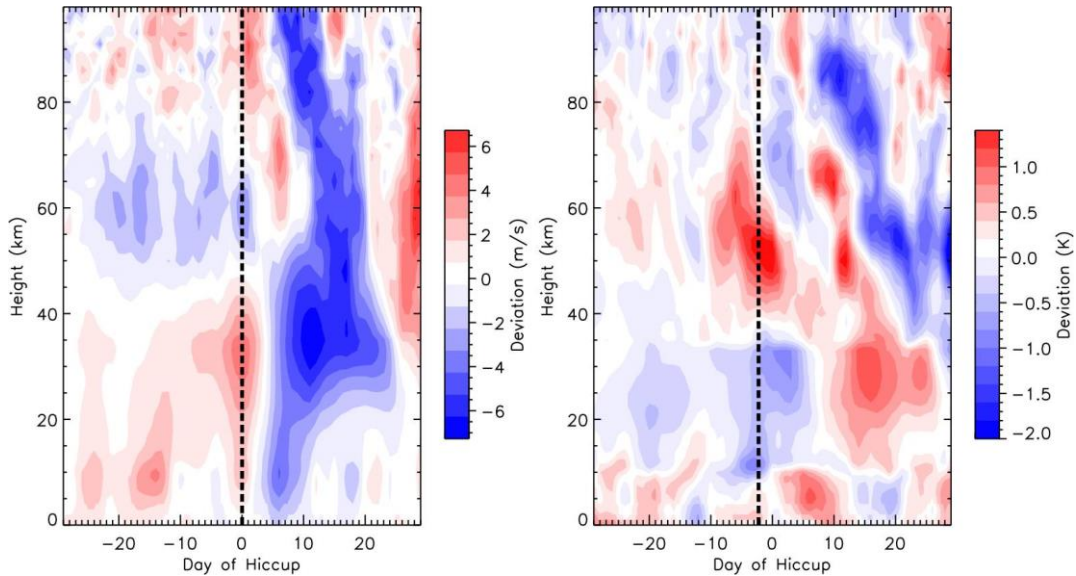


Figure 3: Composite of the zonal mean zonal wind (left) and temperature (right) anomaly from CMAM20 between 60 – 70°N.

Our assumption that the Hiccup is induced by the sudden turning on of PW activity is supported by Figure 4 where the averaged activity of the stationary wave 1 starts around the Hiccup onset day. This result is in a good agreement with model results of Liu et al. (2001) where a rapid increase of the planetary wave 1 in the mesosphere around the fall equinox occurs. They assume that the wave transience together with the transition can lead to fast changes of the amplitude and phase of PWs and cause therefore a large variability of the temperature.

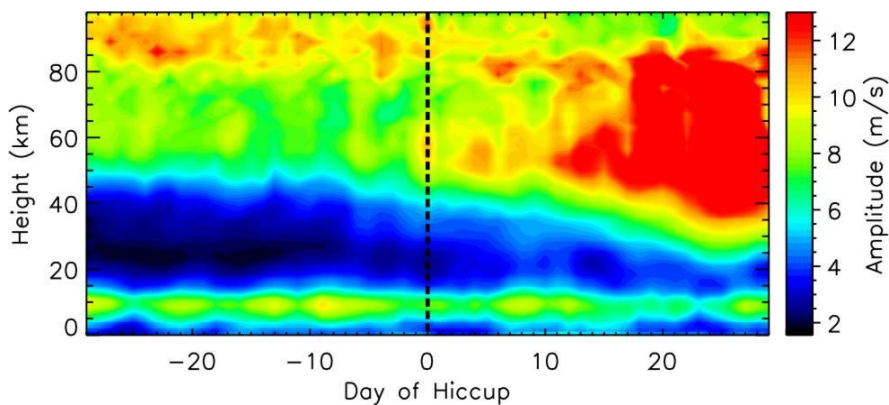


Figure 4: Composite of the stationary wave 1 activity of the zonal wind from CMAM20.

3. Conclusions

The middle atmosphere fall transition at mid and high latitudes is perturbed by the Hiccup which is strongest at polar latitudes. The Hiccup ranges from the troposphere up to the mesosphere with an indication of an upward movement due to vertical wave propagation. An increase of the zonal mean zonal wind occurs before the Hiccup in the stratosphere where the temperature changes seem to lag the wind changes by a few days. On the other hand, the tropospheric temperature increase coincides with the beginning of the wind reversal in the troposphere.

These results support our assumption that vertically propagating planetary waves are responsible for the Hiccup of the fall transition in the middle atmosphere. Nevertheless, there is a year-to-year variation of the Hiccup similar to the stratospheric warmings.

The next steps will be to have a look at the composite of the E-P-flux and at the upward propagating planetary waves.

4. Acknowledgements

This work was supported from the Canadian Space Agency through the CMAM20 project.

5. References

- Holton, J. R., 1983: The influence of gravity wave breaking on the general circulation of the middle atmosphere, *J. Atmos. Sci.*, 40, 2497–2507.
- Liu, H.-L., R. G. Roble, M. J. Taylor, and W. R. Pendleton Jr. (2001), Mesospheric planetary waves at northern hemisphere fall equinox, *Geophys. Res. Lett.*, 28(9), 1903–1906, doi:10.1029/2000GL012689.
- Ren, S., S. Polavarapu, and T. G. Shepherd, 2008: Vertical propagation of information in a middle atmosphere data assimilation system by gravity-wave drag feedbacks. *Geophys. Res. Lett.*, 35, L06804, doi:10.1029/2007GL032699.
- Scinocca, J. F., N. A. McFarlane, M. Lazare, J. Li, and D. Plummer, 2008: The CCCma third generation AGCM and its extension into the middle atmosphere. *Atmos. Chem. Phys.*, 8, 7055–7074, doi:10.5194/acp-8-7055-2008.
- Shepherd, G. G., J. Stegman, P. Espy, C. McLandress, G. Thuillier, and R. H. Wiens (1999), Springtime transition in lower thermospheric atomic oxygen, *J. Geophys. Res.*, 104(A1), 213–223, doi:10.1029/98JA02831.
- Taylor, M.J., Pendleton, W.R., Liu, H.-L., She, C.Y., Gardner, L.C., Roble, R.G., Vasoli, V., 2001. Large amplitude perturbations in mesospheric OH Meinel and 87-km Na lidar temperatures around the autumnal equinox. *Geophysical Research Letters* 28, 1899–1902.
- Waters, J. W., Froidevaux, L., Harwood, R. S., Jarnot, R. F., Pickett, H. M., Read, W. G., Siegel, P. H., Cofield, R. E., Filipiak, M. J., Flower, D. A., Holden, J. R., Lau, G. K., Livesey, N. J., Manney, G. L., Pumphrey, H. C., Santee, M. L., Wu, D. L., Cuddy, D. T., Lay, R. R., Loo, M. S., Perun, V. S., Schwartz, M. J., Stek, P. C., Thurstans, R. P., Boyles, M. A., Chandra, K. M., Chavez, M. C., Chen, G.-S., Chudasama, B. V., Dodge, R., Fuller, R. A., Girard, M. A., Jiang, J. H., Jiang, Y., Knosp, B. W., LaBelle, R. C., Lam, J. C., Lee, K. A., Miller, D., Oswald, J. E., Patel, N. C., Pukala, D. M., Quintero, O., Scaff, D. M., Van Snyder, W., Tope, M. C., Wagner, P. A., Walch, M. J., 2006. The Earth Observing System Microwave Limb Sounder (EOS MLS) on the Aura Satellite. *IEEE Trans. Geosci. Remote Sensing* 44, 5, D18108, doi:10.1109/TGRS.2006.873771, 1075–1092.

Mesospheric vertical velocity and tilts

Chris Meek, Alan Manson

Institute of Space and Atmospheric Studies, University of Saskatchewan, 116 Science Pl., Saskatoon, Canada S7N 5E2

Abstract

Saskatoon (52N,107W) MF radar (MFR) analysis includes angle of arrival (AOA) phase and Doppler velocity (V_z). The criteria for these are based on Signal/noise only. We have been interested in vertical velocity for years (Meek and Manson, 1989) but dissuaded by the difficulty in assuring that it is a vertical value, not due to a Tx beam or ionospheric scatterer tilts. With the wide beams necessary at MF, an ionospheric tilt is the more likely cause of horizontal motion contamination. The "best" tilt is defined as that which minimizes the mean squared difference between measured and predicted (by tilt zenith, azimuth: α, β , and horizontal wind: V_n, V_e) Doppler velocities, and can be found by a least squares fit: $V_z = V_n \sin \alpha \cos \beta + V_e \sin \alpha \sin \beta + V_{z0}$. Multi-year statistics show that the tilts are seasonal and quite consistent year to year: about 4 degrees zenith westward in summer and 2-3 degrees southward in winter at 91Km (corroborated to some extent by AOA phase, which show NW and SE respectively). In spring, especially, and fall, the tilts are small. Platteville MFR data (not shown) exhibit similar features, which rules out individual antenna array characteristics as a cause. Gravity waves travelling against the wind (their tilt is up in the direction of propagation) may be an explanation, at least for the summer feature.

1. Data and analysis

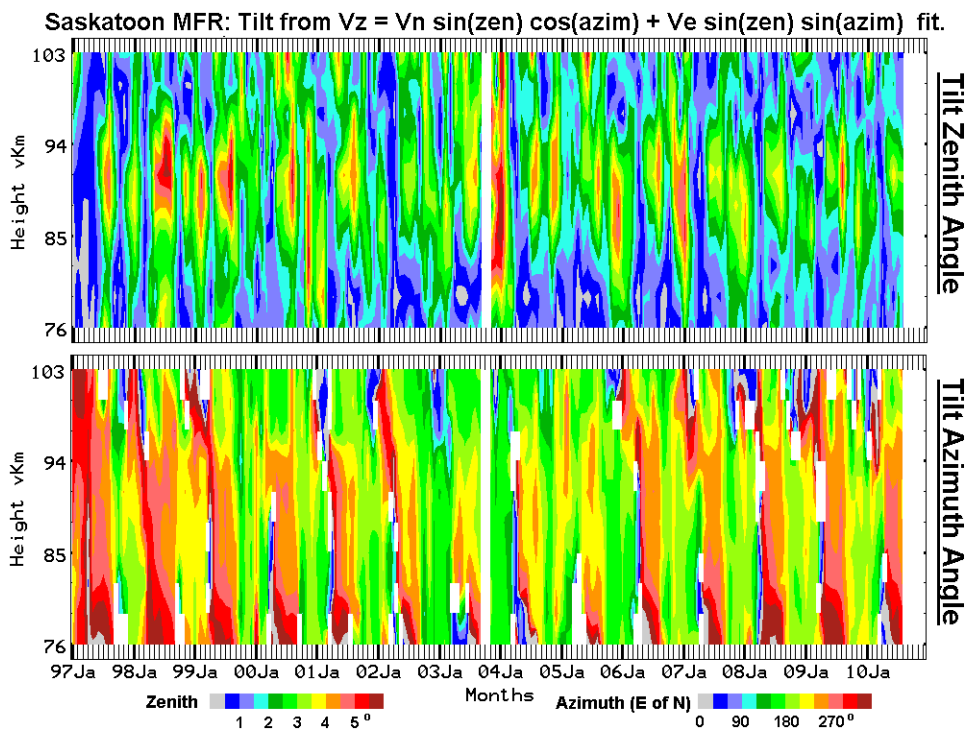


Figure 1: Monthly $V_z = f(V_n, V_e)$ method tilt zenith and azimuth vs. height for 14 years.

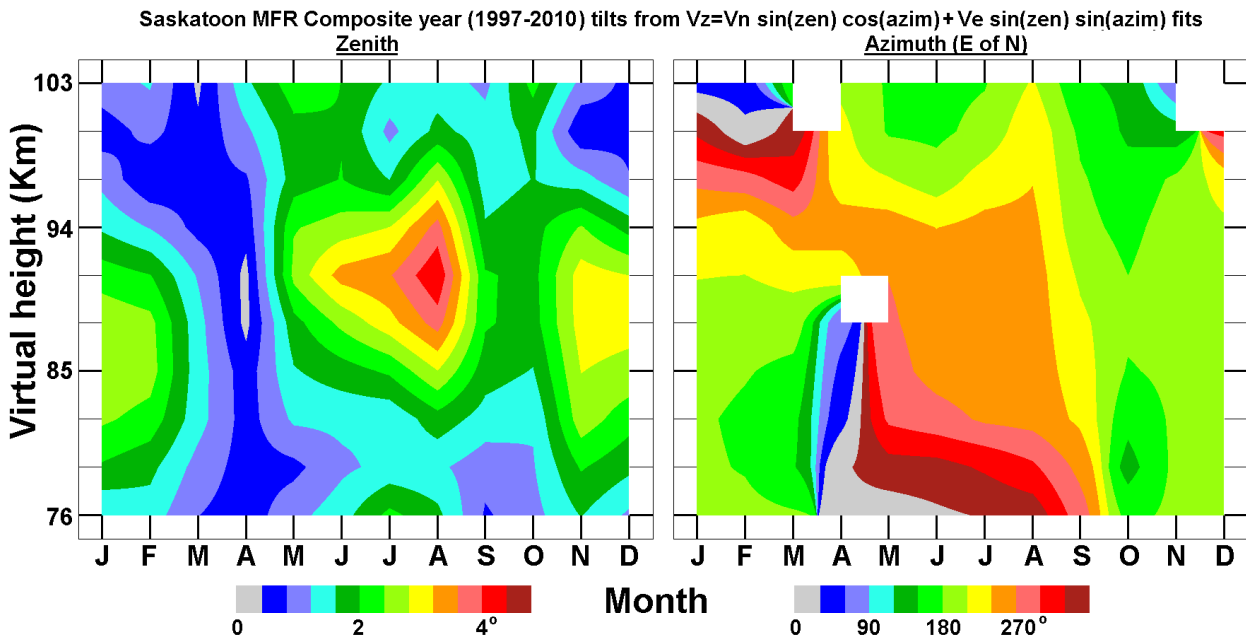


Figure 2: Composite monthly zenith and azimuth for the data in Fig. 1.

Figure 1 shows Saskatoon MFR tilt zenith (top panel) and azimuth (bottom panel) from the least squares fit with $V_{z0}=0$. Year-to-year repeatability is apparent with winter showing the largest tilts southward, and summer a weaker westward tilt.

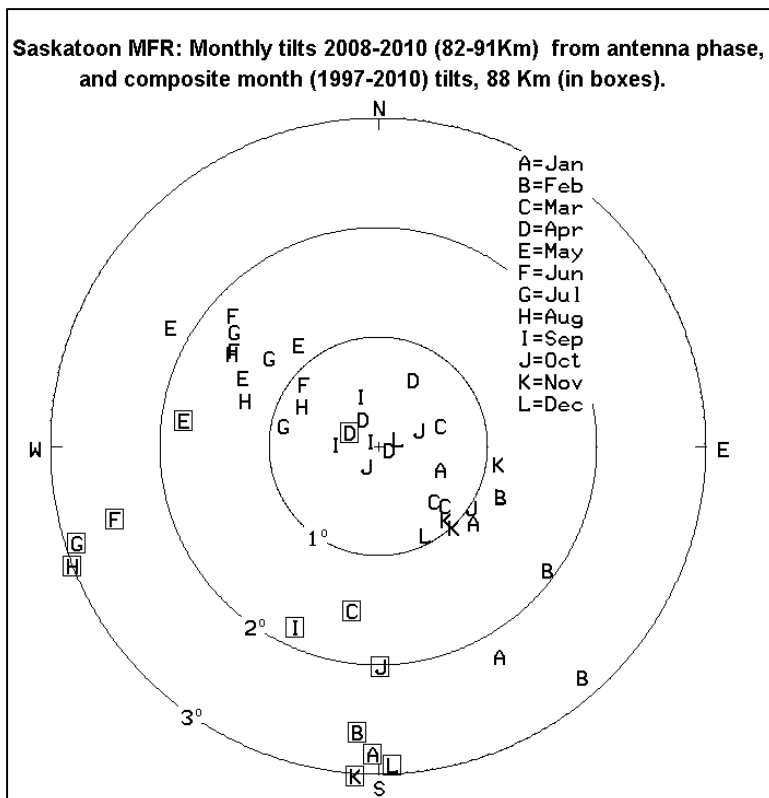


Figure 3: Monthly angle of arrival at 88 Km for the composite year in Fig. 2 (boxed) and for separate months of 2008-2010 (82-91Km layer) calculated from antenna pair phase difference data.

Fig. 2 combines the data in Fig. 1 to give a composite year; which confirms the observations made on Fig. 1. An independent method of finding the tilt is to use zero-lag cross-correlation phases (i.e. average antenna pair phase difference) from FCA data. These represent average angle of arrival (AOA) over the record time (5 min). Calibration of these phases requires long term stability of the antennas and feeders; years 2008-2010 were chosen. For this presentation fits of Gaussians to 10d sets of daytime phase difference (antenna/receiver 4-3, 4-2, 4-1, see Fig. 3) histograms in 12Km layers determine the most probable difference (MPV). This would represent the zenith if there were no seasonal variation – i.e. these phases would have to be subtracted to correct for differential cable length and receiver phases. Our best signals

(good signal/noise) are in the 12Km layer, 82-91 Km. The yearly mean MPV was subtracted and the residual 10d phases were averaged in threes (i.e. months). Ideally if there is a single tilt over an interval, these phases should sum to zero. Since many of the sums looked relatively small, we did a least squares fit to find the tilt zenith and azimuth. These are plotted in Fig. 3, one per month per year. The 88 Km zenith, azimuth tilts from Fig 2 are added. It appears that the summer westward, winter southward, and minimal equinox tilt tendencies mentioned previously are confirmed, but the two independent tilt determinations are not identical.

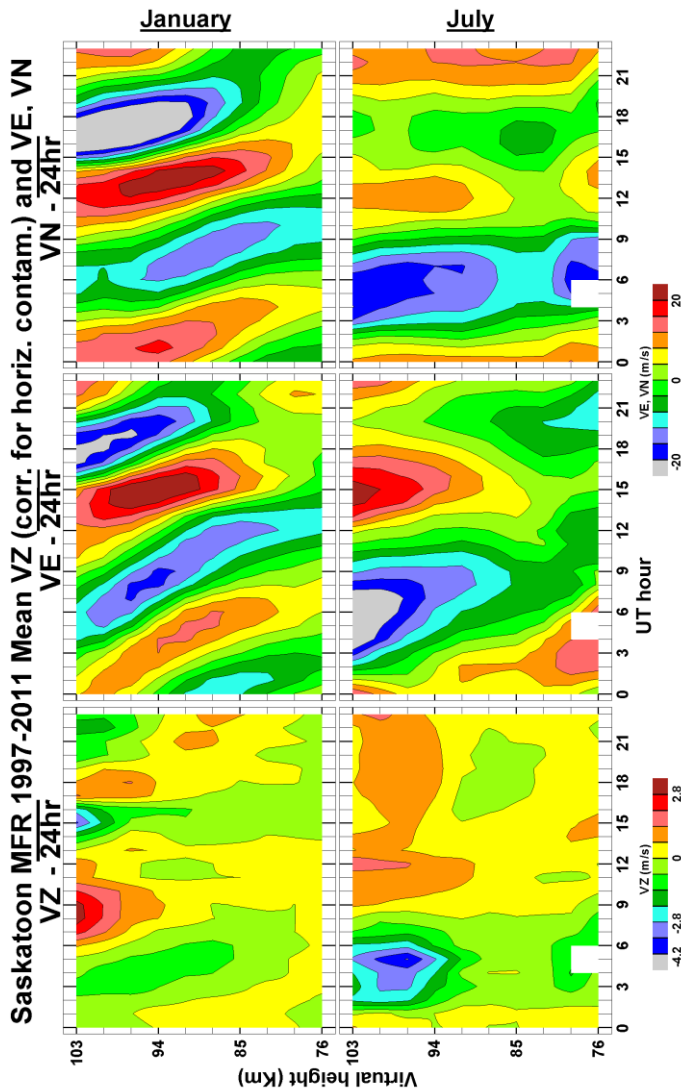


Figure 4: Contours of January and July monthly means of Vz (corrected For tilt), and Vn, Ve UT hourly data vs. height. The 24 hr means of each month have been subtracted to emphasize diurnal variations.

References

CE Meek, AH Manson Vertical Motions in the upper middle atmosphere for the Saskatoon (52N,107W) M.F. radar, J. Atmos. Sci. 46, 849-858, 1989)

Finally we have subtracted the calculated horizontal wind “contamination” [which is $V_n \sin \alpha \cos \beta + V_e \sin \alpha \sin \beta$] in composite monthly fits (1997-2011) to get “vertical” velocity versus height and hour of day for January and July. Since we have an interest in tides, the 24 hour mean has been removed at each height to show diurnal changes more clearly. It should also be noted that the scale is virtual height. Actual echo Heights above 94 Km are liable to be smaller than labelled in the summer because of extra time delay through increased ionization.

Taken at face value, Vz seems to have a similar character as Vn, Ve, viz. semi-diurnal in the winter, diurnal in the summer. Winter: out of phase with Ve (eastward wind) and leading Vn (northward wind) by ~4hr (at 94 Km), but Vz vertical wavelength doesn’t quite match Vn, Ve, though it does seem to be negative (i.e. downward phase propagation). In summer Ve seems diurnal while Vn is semi-d; Vz seems to be a distorted diurnal, maybe holds a bit of both. Harmonic processing (i.e. tidal fits) might clarify these features.

Long-Term Trends of Upper Mesosphere Gravity Waves at Midlatitudes

Ch. Jacobi¹, P. Hoffmann²

¹ University of Leipzig, Institute for Meteorology, Stephanstr. 3, 04103, Leipzig, Germany

² Leibniz-Institute of Atmospheric Physics at the University of Rostock, Schloßstr. 6, 18225 Kühlungsborn, Germany

1. Introduction

Gravity waves (GWs) play a crucial role in maintaining the dynamics of the mesosphere/lower thermosphere (MLT) region. They transport energy and momentum to the middle atmosphere, leading to a coupling between atmospheric layers. Changes of GW parameters and amplitudes may thus give insight into changes of the atmosphere as a whole. Acceleration of the mean flow through GWs mainly occurs in the MLT. This region is characterised by the wind reversal in summer, i.e. the change of the mesospheric easterly jet to the lower thermosphere westerly jet through GW momentum deposition.

Some effort has been undertaken to analyse GW variability in the MLT also in connection with background wind (Jacobi et al., 2006; Hoffmann et al., 2010, 2011). GWs are filtered in the mesosphere through the zonal wind jets. Eastward/westward travelling GWs usually encounter critical lines in the winter/summer mesosphere, where the phase speed equals the wind speed. Therefore, essentially westward/eastward travelling GWs remain in the upper mesosphere. According to linear theory, in the case of wave saturation the GW amplitudes equal the intrinsic phase speed, so that in summer/winter stronger mesospheric easterlies/westerlies should be connected with larger GW amplitudes.

Jacobi et al. (2006) has found a positive correlation of solar activity and GW proxies derived from Collm, Germany, MLT wind measurements. They attributed this correlation to the possible effect of a solar cycle variation of the mesospheric jet, which is stronger during solar maximum both in winter and in summer. Hoffmann et al. (2011), analysing medium frequency (MF) radar wind data over Juliusruh, Germany, showed a long-term increase of the mesospheric wind jet and consequently an increase of GW kinetic energy in summer. Both of these findings can be explained by filtering effects and linear theory. Here we present analyses of the Collm dataset, updated from Jacobi et al. (2006). Comparison of summer GW trends of Collm and Juliusruh data will be presented.

2. Measurements

MLT winds have been measured at Collm using the spaced receiver method in the low-frequency (LF) range at oblique incidence using a commercial transmitter (frequency 177 kHz), at a distance to Collm of 165 km. Thus, the reflection point of the registered sky wave at Collm is at 52.1°N, 13.2°E. The reflection height has been measured through comparison of the phase of the ground wave and sky wave on a side-band frequency near 1.8 kHz. The resulting altitudes represent virtual heights, exceeding the real heights by several kilometres. A correction, based on the comparison of semidiurnal tidal phase positions at corresponding heights using meteor radar (Jacobi, 2011) has been applied. Monthly prevailing winds have been calculated from one month of half-hourly mean zonal and meridional winds and reflection heights each using least-squares fitting of the prevailing wind and the semidiurnal tide to these data. Long-term mean prevailing

winds over Collm are presented in Figure 1. The results are similar to those that have been presented, e.g., by Jacobi (2011), but with a different time interval under consideration and with the height correction applied.

Gravity wave proxies over Collm have been calculated as squared differences of subsequent half-hourly mean winds at the same altitude. This is equivalent to a filter with the period band 0.7-3h (e.g. Jacobi et al., 2006). Long-term mean GW variances are presented in Figure 2. Generally, there are maximum amplitudes found in the summer upper mesosphere, and decreasing amplitudes with height. In the upper height gates, there is a tendency for increasing zonal amplitudes in winter.

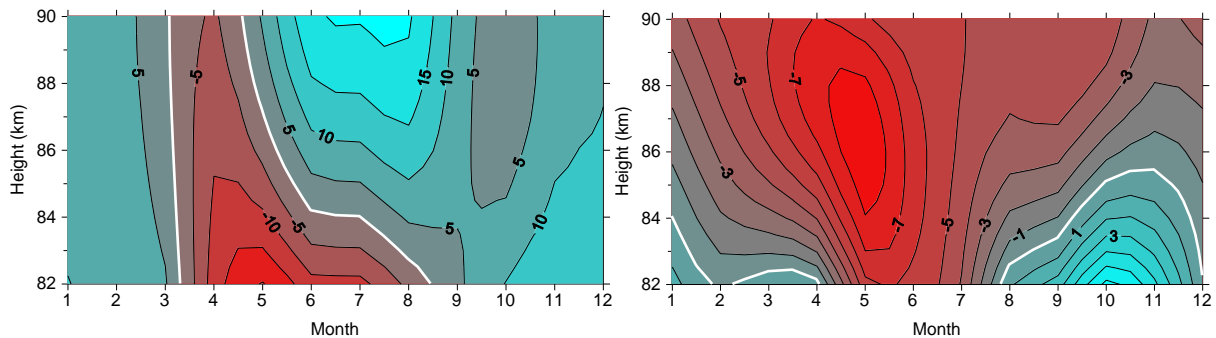


Figure 1: 1984-2006 mean zonal (left panel) and meridional (right panel) prevailing winds over Collm, according to a multiple least squares fit with quadratic height dependence and circular polarised tidal components assumed.

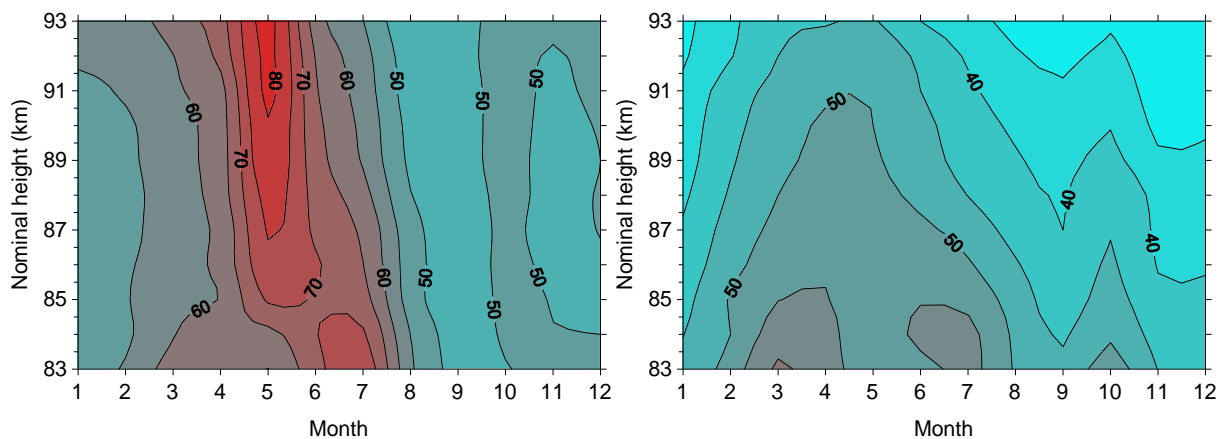


Figure 2: 10/1983-9/2007 mean zonal (left panel) and meridional (right panel) variances over Collm, calculated from half-hourly wind differences (updated from Jacobi et al., 2006).

At Juliusruh (55°N, 13°E), wind measurements have been continuously carried out with a MF radar at a frequency of 3.18 MHz since 1990. The FM-CW technique was applied until spring 2003. Afterwards, the normal pulse technique has been used by a new radar operating at the same frequency. Horizontal winds are determined from 70–94 km by the spaced antenna method. For Juliusruh, variances of hourly wind values in the period band 3-6h after removing tides have been used as GW proxies (for details see Hoffmann et al., 2010).

3. Results for GW trends over Collm

Jacobi et al. (2006) have already pointed out that there is a possible solar cycle effect visible in both zonal and meridional variances over Collm. Regarding long-term changes, Hoffmann et al.

(2011) presented long-term (22 years) trends of GW variances over Juliusruh, Germany, and found that summer GW variances have increased during that time interval, connected with an increase of the mesospheric wind jet. Therefore, here the Collm GW variance time series are analysed with respect to a possible long-term change and a solar cycle by:

$$\sigma^2 = a + b \cdot yr + c \cdot F10.7, \quad (1)$$

with σ^2 as the sum of the zonal and meridional variance and $F10.7$ given in solar flux units. The coefficients b and c are presented in Figure 3. For comparison, the same kind of analysis has been applied to the zonal prevailing winds, and the resulting regression coefficients are presented in Figure 4. Broadly, long-term trends of GW are negative in summer and positive in winter. The solar signal is positive throughout the year. The long-term trends of the prevailing wind are weakly positive in winter. In summer, they are negative at lower altitudes and change sign at greater heights. For both seasons, this indicates a strengthening of the mesospheric jet with time. The solar cycle effect is negative in spring/summer and positive in winter, both indicating a stronger mesospheric jet during solar maximum. Since due to the filtering effects stronger jets are connected with larger GW amplitudes, this is in accordance with the GW solar cycle in Fig. 3.

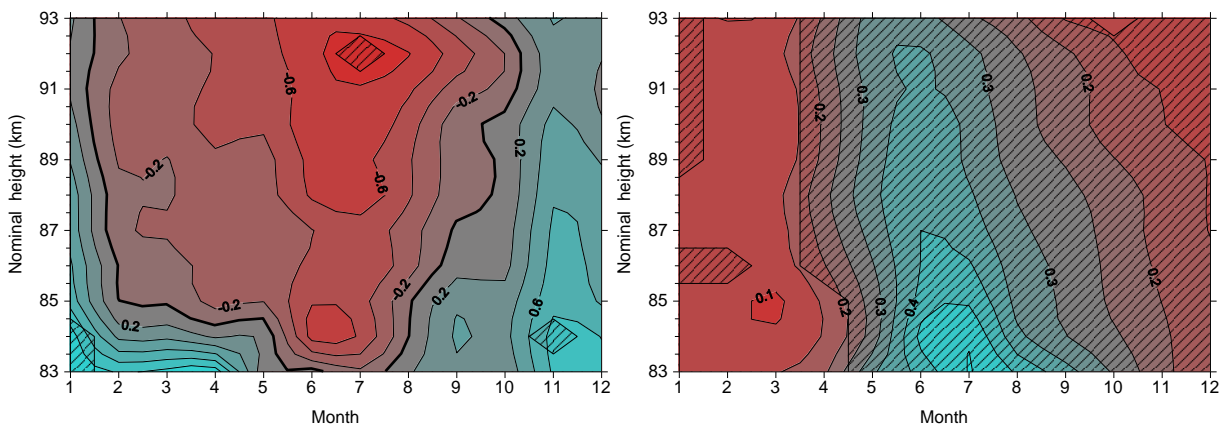


Figure 3: Linear trend b ($\text{m}^2\text{s}^{-2}\text{yr}^{-1}$) (left) and solar effect c ($\text{m}^2\text{s}^{-2}\text{sfu}^{-1}$) (right) of GW variance according to a regression analysis $\sigma^2 = a + b \cdot yr + c \cdot F10.7$ based on 1984 - 2007 3-monthly means over Collm. Significant values according to a t-test are hatched.

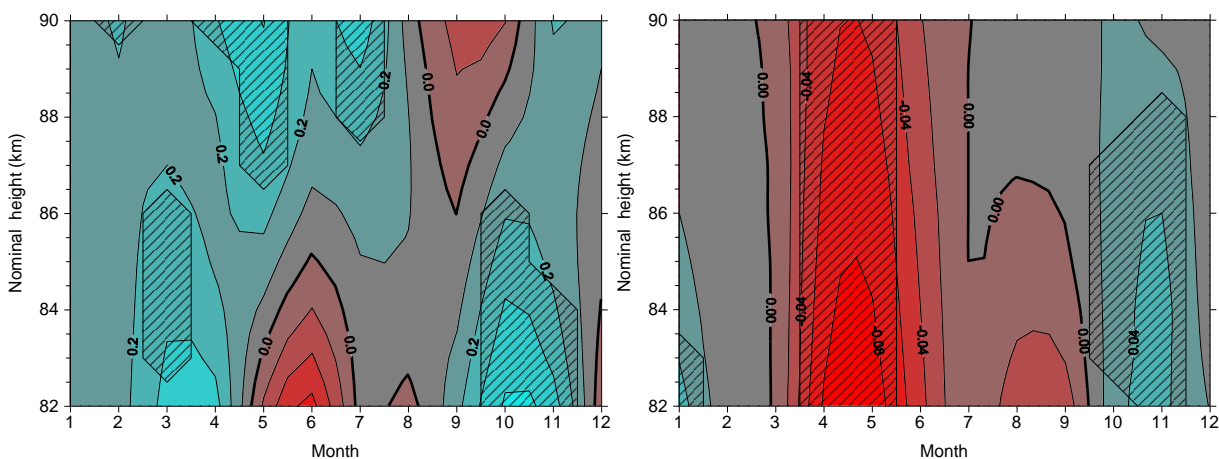


Figure 4: As in Fig. 3, but for the zonal prevailing wind over Collm.

4. Comparison of summer long-term trends over Collm and Juliusruh

Hoffmann et al. (2011) have reported increasing GW variance with time. For summer, this is shown in Figure 5 presenting time series of zonal and meridional variance over Juliusruh. GW

proxies over Collm show different absolute values, which is owing to the different methods of calculation. However, positive trend tendencies after 1995 are visible in both time series.

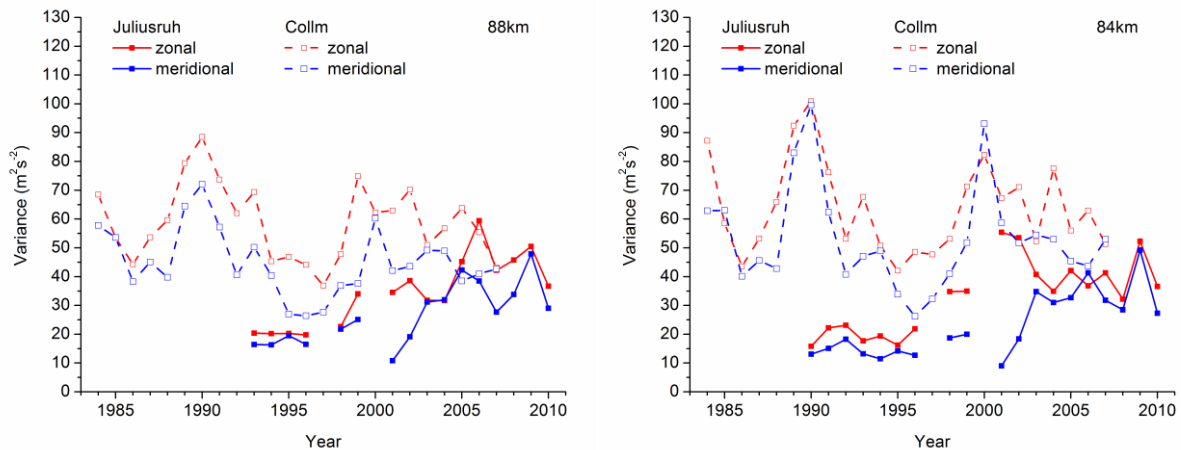


Figure 5: June-August mean time series of zonal and meridional variances over Collm and Juliusruh at two different altitudes.

5. Conclusions

GW variances and mean winds exhibit trends that may be explained by linear theory and a strengthening of the mesospheric wind jet during the last decades. However, the long-term trend coefficients presented are in most cases not significant, so that the conclusions drawn must be considered as preliminary. But, the results for summer are consistent with MF radar analyses in Fig. 5 and also by Hoffmann et al. (2011) so that the overall picture of long-term trends over Collm drawn here may be qualitatively correct.

During both summer and winter the mesospheric jets as seen over Collm increase with solar activity. These increased jets are connected with increased GW amplitudes. Thus, as is the case with the long-term trends, solar cycle effects of GW may be explained by linear theory.

6. Acknowledgements

This study was supported by Deutsche Forschungsgemeinschaft under grant JA 836/22-1 and under grant SI 501/5 in the frame of the CAWSES priority program SP1176.

7. References

- Hoffmann, P., Becker, E., Singer, W., Placke, M., 2010: Seasonal variation of mesospheric waves at northern middle and high latitudes, *J. Atmos. Solar-Terr. Phys.*, 72, 1068-1079.
- Hoffmann, P., Rapp, M., Singer, W., Keuer, D., 2011: Trends of mesospheric gravity waves at northern middle latitudes during summer, *J. Geophys. Res.*, 116, D00P08, doi:10.1029/2011JD015717.
- Jacobi, Ch., 2011: Meteor radar measurements of mean winds and tides over Collm (51.3°N, 13°E) and comparison with LF drift measurements 2005-2007, *Adv. Radio Sci.* 9, 335-341.
- Jacobi, Ch., Gavrilov, N.M., Kürschner, D., Fröhlich, K., 2006: Gravity wave climatology and trends in the mesosphere/lower thermosphere region deduced from low-frequency drift measurements 1984-2003 (52.1°N, 13.2°E), *J. Atmos. Solar-Terr. Phys.*, 68, 1913-1923.

ISBN 978-3-00-044654-2